SJKFU

المجلة العلمية لجامعة الملك فيصل

Scientific Journal of King Faisal University

2025, 26, 1

العلوم الأساسية والتطبيقية

Basic and Applied Sciences

ISSN: 1658-0311, E-ISSN 1658-8371

In this issue

Improvement and Application HPLC-UV Method for detecting of N-drugs in Pharmaceutical Formulations

وصف المجلة

المجلة العلمية لجامعة الملك فيصل: العلوم الأساسية والتطبيقية (ISSN: 1658-0311, E-ISSN: 1658-8371) مجلة علمية دولية محكمة، بدأ إصدارها منذ عام 1420هـ (2000م)، تصدرها جامعة الملك فيصل تحت إشراف المجلس العلمي للجامعة. تتبنى المجلة نهج الوصول المفتوح وتصدر في صورة مطبوعة وإلكترونيّة بدون تكاليف نشر. المجلة مفهرسة ضمن قاعده بيانات سكوبس (Scopus – CiteScore 2023 = 0.6). وتصدر بصورة نصف سنوية في شهريّ يونيو وديسمبر.

أول رئيس لهيئة التحرير أ.د. خالد سعد آل عبد السلام (12/4/1419هـ)، تلاه أ.د. عادل إبراهيم العفالق (12/6/1421هـ)، عقبه د. محمد سعد الوصالي (17/7/1432هـ)، وجاء بعده أ.د. غازي فيصل بسيوني (11/1/1433هـ)، وحالياً أ.د. عبدالرحمن عيسى الليلي (5/5/1441هـ).

رئيس الجامعة

عادل بن محمد أبوزناده ، جامعة الملك فيصل، السعودية

وكيل الجامعة للدراسات العليا والبحث العلمي

عبدالرحمن عيسى الليلي، جامعة الملك فيصل، السعودية

رئيس هيئة التحرير

بنا جويعد السبيعي، جامعة الملك فيصل، السعودية

هيئة التحرير

المحررون الاستشاريون

مدير التحرير

الحسين حماده عبد العظيم، جامعة الملك فيصل، السعودية

مساعدو التحرير

فاضل محمد العامر، جامعة الملك فيصل، السعودية
عبد رب الأمير سلمان البوعلي، جامعة الملك فيصل، السعودية
حسين معتوق الهدلق، جامعة الملك فيصل، السعودية
إبراهيم جواد العبدالله، جامعة الملك فيصل، السعودية
صلاح عبدالعزيز المحيميد، جامعة الملك فيصل، السعودية

المراسلات العامة

رئيس هيئة التحرير، المجلة العلمية لجامعة الملك فيصل
ص. ب 400 الأحساء 31982، المملكة العربية السعودية
00966135895238، 00966135895237
scijkfu@kfu.edu.sa

Description

King Faisal University Journal: Basic and Applied Sciences (ISSN: 1658-0311, E-ISSN: 1658-8371) is an international, peer-reviewed scientific journal established in 1420 AH (2000 AD). Published by King Faisal University under the supervision of the University's Scientific Council, the journal is open access, offering both print and electronic formats with no publication fees. The journal is indexed in the Scopus database, with a CiteScore of 0.6 (2023), reflecting its commitment to quality research dissemination. It is published bi-annually, with issues released in June and December.

Prof. Khalid S. Al Abdulsalam (2000-2), Prof. Adel I. Al Afaleq (2002-14), Dr Muhammed S. Al Wasli (2014-15), Prof. Ghazi F. Basiouni (2015-2020) and Prof. Abdulrahman E. Al Lily (from 2020-present).

President of the University

Adel Mohammed Abuzenadah, King Faisal University, Saudi Arabia

Vice-Rector for Higher Studies and Scientific Research

Abdulrahman Essa Al Lily, King Faisal University, Saudi Arabia

Editor-in-Chief

Bana Jawid Al Subaiei, King Faisal University, Saudi Arabia

Editorial Board

Consulting Editors

Managing Editor

Alhosein Hamada Abdelazeem, King Faisal University, Saudi Arabia

Editorial Assistants

Fadel Mohammad Al-Amer, King Faisal University, Saudi Arabia
Abd Rab Alameer S. Al-Boali, King Faisal University, Saudi Arabia
Husain Matouq Al-Hadlag, King Faisal University, Saudi Arabia
Ibrahim Jawad Al-Abdullah, King Faisal University, Saudi Arabia
Salah Abdulaziz Al-Mohameed, King Faisal University, Saudi Arabia

Correspondence

Editor-in-Chief, Scientific Journal of King Faisal University
P.O. Box 400 Al Ahsa, 31982, Saudi Arabia
00966135895238, 00966135895237
scijkfu@kfu.edu.sa

Table of Contents

جدول المحتويات

Scientific Journal of King Faisal University:
Basic and Applied Sciences

Valorizing Seed Oils for Sustainable Biodiesel Production via Transesterification Process

Souaad Chibi [1], Salah Neghmouche Nacer [2], Younes Moussaoui [3], Djamel Ghernaout [4], Noureddine Elboughdiri [4], Farid Menaa [5], Muhammad Imran Khan [6] and Djamel El Hadi [1]

[1] Department of Process Engineering, Functional Analysis Laboratory of Chemical Processes, Saad Dahlab University - Blida 1, Blida, Algeria
[2] Department of Chemistry, Faculty of Exact Sciences, University of El Oued, El Oued, Algeria
[3] Organic Chemistry Laboratory (LR17ES08), Faculty of Sciences of Sfax, University of Sfax, Sfax, Tunisia. University of Gafsa, Faculty of Sciences of Gafsa, Gafsa, Tunisia
[4] Department of Chemical Engineering, College of Engineering, University of Ha'il, Ha'il, Saudi Arabia
[5] Department of Biomedical and Environmental Engineering, Fluorotronics, Inc.-California Innovations Corporation, San Diego, USA
[6] Research Institute of Sciences and Engineering (RISE), University of Sharjah, Sharjah, United Arab Emirates

LINK	RECEIVED	ACCEPTED	PUBLISHED ONLINE	ASSIGNED TO AN ISSUE
https://doi.org/10.37575/b/eng/240046	23/10/2024	11/12/2024	11/12/2024	01/06/2025

NO. OF WORDS	NO. OF PAGES	YEAR	VOLUME	ISSUE
5981	6	2025	26	1

ABSTRACT

Biodiesel is a blend of mono-alkyl esters utilized as an alternative to traditional diesel fuel. It is produced by transesterifying vegetable oils or animal fats with light alcohol. This study valorizes two Euphorbiaceae plants, *Jatropha curcas* L. and *Ricinus communis* L., which can thrive in the most arid lands and withstand harsh weather conditions. Their mature seeds can produce a significant amount of vegetable oils through a simple heating process in methanol, resulting in biodiesel with a shallow sulfur content. Selecting these two plants as energy crops is justified by their readily available seeds containing non-edible high-energy-value oils with properties comparable to diesel. The encouraging findings show that the resulting biodiesels closely resemble petrodiesel in fuel characteristics, making them suitable substitutes for fossil diesel, meeting ASTM D6751 and EN 14214 standards.

KEYWORDS

Alternative fuels, euphorbiaceae, green revolution, renewable biofuels, sustainability, vegetable oil

CITATION

Chibi, S., Nacer, S.N., Moussaoui, Y., Ghernaout, D., Elboughdiri, N., Menaa, F., Khan, M.I. and El Hadi, D. (2025). Valorizing seed oils for sustainable biodiesel production via transesterification process. *Scientific Journal of King Faisal University: Basic and Applied Sciences*, **26**(1), 1–6. DOI: 10.37575/b/eng/240046

1. Introduction

The demand for biodiesel as a viable alternative to conventional fossil fuels and natural gas has increased drastically over the last few years, negatively affecting its price. Based on data from the International Energy Agency (IEA), the worldwide biofuel market has seen a 6% increase in 2022 compared to the previous year, resulting in a volume of 9,100 million liters per year (Razak *et al.*, 2024, Elboughdiri *et al.*, 2023). This growth is primarily attributed to the rising consumption of renewable diesel, which constitutes the highest proportion of this annual expansion (Razak *et al.*, 2024). As a result, the search for alternative renewable (organic materials) and sustainable (low-carbon) energy sources, including biofuels, has gained significant importance in most countries (Rosak-Szyrocka *et al.*, 2023, Anekwe *et al.*, 2023). Lignocellulosic plant biomass is a promising alternative to petroleum, as it is a biodegradable renewable energy source, and its production does not contribute to the increase in greenhouse gases. Lignocellulosic biomass refers to plant or plant-derived matter not used for human consumption or animal feed, mainly including agricultural residues, crops for energy production, and waste biomass (Nanda *et al.*, 2015).

Ricinus communis L. is a shrub native to Africa. The ideal growing parameters for castor beans include loamy to sandy loam soils alongside a temperature range of 20 to 30°C (Naik, 2018, Pina *et al.*, 2005). Nevertheless, this species has the potential to acclimatize, including tropical, subtropical, and semi-arid regions, demonstrating a remarkable capacity to withstand harsh environmental factors such as elevated temperatures and limited water resources. Castor oil contains a high percentage of ricinoleic acid, which imparts excellent lubricity and oxidative stability, making it ideal for biodiesel applications. Additionally, castor plants require minimal agricultural inputs, grow in marginal soils, and are not directly competing with food crops, addressing the food *vs.* fuel debate. At present, the oil derived from the seeds of this plant possesses a wide range of applications (Saadaoui *et al.*, 2017, Chakraborty and Chatterjee, 2020, Tenorio-Alfonso *et al.*, 2019, Neme *et al.*, 2022). These applications encompass various uses such as hydraulic oil, color driers, emulsifiers, varnishes, pharmaceuticals, organic soil amendments, biological pest control, and the manufacture of polymers and dyes (Glüge *et al.*, 2020, Thombare *et al.*, 2022). Additionally, it is worth noting that biodiesel production is another prominent utilization of this oil (Öner and Altun, 2009, Zhu *et al.*, 2023).

Jatropha curcas L., another oil-bearing plant species native to Central and South America, has been spread worldwide, especially in African and Asian countries (Taddese, 2014). *J. curcas* (Euphorbiaceae) can reach a height of up to 8 meters in specific regions and has a lifespan of over 50 years. The seeds of *J. curcas* are non-edible and contain 21% oil and 79% unsaturated fatty acids (UFAs). Its oil is particularly rich in UFAs, which enhance the cold flow properties of biodiesel, a critical attribute for operational efficiency in low-temperature conditions. Moreover, *J. curcas* thrives in drought-prone and nutrient-poor soils, requiring minimal water and fertilizer inputs, making it an economically and environmentally sustainable choice for biodiesel production.

The two cultivars selected for this study have the main agronomic advantage of being resistant to drought and semi-arid climates. They can also grow in relatively poor soils. Irrigation is not a problem for them as they are low-water-demanding species and require minimal fertilization and maintenance (Chakraborty and Chatterjee, 2020, Resul *et al.*, 2012, Mouahid *et al.*, 2017, Lateef and Ogunsuyi, 2021, Kibazohi and Sangwan, 2011).

Compared to first-generation biodiesel feedstocks, such as palm or soybean oils, which are associated with deforestation and high water usage, and second-generation sources, such as waste oils or animal fats, which face limitations in availability and oxidative stability, *J. curcas* and *R. communis* oils offer superior agronomic and chemical properties for sustainable biodiesel production.

Transesterified biodiesel made from *J. curcas* L. and *R. communis* L. oils could solve some problems with biofuels made from other

Corresponding Author: Noureddine Elboughdiri 00966549571015, ghilaninouri@yahoo.fr

sources, like first-generation oil, used cooking oils, and animal fat waste. These alternative sources have exhibited limitations regarding cold flow properties and oxidative stability, leading to storage complications (Keera *et al.*, 2018, Tapanes *et al.*, 2008). This research aims to formulate biodiesel from *J. curcas* and *R. communis* vegetable oils using the transesterification technique, transforming free fatty acids and triglycerides (TGs) into methyl esters (MEs) and glycerol. The resulting MEs were characterized and tested as biodiesel in diesel engines.

2. Experimental

The vegetable oils (from *J. curcas* L. and *R. communis* L.) were extracted, purified, and subsequently underwent various analyses to determine their physicochemical characteristics, including density, viscosity, water content, refractive index (RI), acid value (AV), saponification value (SV), and iodine value (IV). The analyses used the French Technical Standards (Memon *et al.*, 2024, Patil *et al.*, 2024).

2.1. Extraction and Purification of the Studied Oils:

The seeds were sorted, separated, and dried in a well-ventilated shaded area for 48 hours. They were then oven-dried at 80°C for 12 hours to remove residual moisture before grinding into a fine powder using a mortar and pestle. The powdered seeds (50 g) were placed in an extractor cartridge, and petroleum ether (250 mL, solvent-to-seed ratio 5:1 w/v) was used as the solvent. The extraction was performed using a Soxhlet apparatus at a constant temperature of approximately 60°C (near the boiling point of petroleum ether) for 6 hours. After extraction, the solvent-oil mixture was collected in a flask and evaporated using a rotary evaporator set to 50°C under reduced pressure. Based on seed weight, this process yielded approximately 36.5% and 40.2% oil for *J. curcas* L. and *R. communis* L...

2.2. Oil Extraction Performances:

Immediately after the extraction, both oils were centrifuged twice at 1300 rpm for 16 minutes each to remove debris.

2.3. Transesterification reaction:

Transesterification is the chemical conversion of ester molecules into different ester molecules by exchanging alkyl groups. This reaction is commonly used in biodiesel production, where TGs (esters) are converted into FA alkyl esters (biodiesel) and glycerol. Potassium hydroxide (KOH) is a catalyst commonly used in transesterification reactions. It helps to speed up the reaction and improve its efficiency. The optimal amount of KOH and methanol required for the transesterification reaction depends on various factors, including the type of feedstock, desired conversion rate, and reaction conditions. The catalyst concentration used was 1.5% (w/w) of the total oil weight. The molar ratio of methanol to oil used in the reaction was 6:1. The reaction temperature was set to 60°C, and the reaction time was 3 hours to ensure complete transesterification. The yield of the reaction was calculated using Equation (1):

$$R(\%) = \frac{m_b}{m_{oil}} \times 100 \quad (1)$$

where: m_b is the mass of biodiesel, and m_{oil} is the mass of oil.

2.4. Preparation of Date Palm Kernel Ash (DPKA):

Date palm kernels were soaked in water for 24 hours, thoroughly rinsed to remove impurities, and finally air-dried for a few hours (Dalila *et al.*, 2024, Badawi *et al.*, 2023, Manzoor *et al.*, 2023). The kernels were pulverized using a grinder to obtain a homogeneous mixture. Subsequently, the mixture was incinerated in an oxidizing atmosphere at 900°C using a muffle furnace of this type (Nabertherm B180, Germany) until complete combustion of the organic matter occurred. The diameter of the date palm kernel ash (DPKA) particles is approximately 100 µm. DPKA is chosen as a catalyst for its eco-friendly nature, low cost, and rich content of alkaline oxides like potassium oxide (K_2O), which are effective in catalyzing the transesterification reaction. DPKA offers several advantages over conventional catalysts, such as its sustainable production from agricultural waste and its ability to reduce the environmental impact of biodiesel production. Compared to chemical catalysts like KOH, DPKA has been shown to provide comparable biodiesel yields under milder conditions, making it a promising alternative for green biodiesel production. These ashes are used as natural catalysts in the transesterification reaction.

3. Results

3.1. Physicochemical properties of *Jatropha curcas* and *Ricinus communis* oils:

Vegetable oils, such as those of *J. curcas* and *R. communis*, exhibit diverse physicochemical properties essential for various applications. These properties encompass specific gravity (or density), kinematic viscosity (typically determined at 40°C), calorific value (CV), AV, SV, and RI. The specific gravity provides insights into the density of the oils, influencing their behavior in different environments, particularly in biodiesel production, where it affects mixing with alcohol and separation efficiency. Kinematic viscosity indicates the oil flow characteristics, which are crucial for their processing in engines or industrial machinery, influencing the efficiency of biodiesel production and other chemical applications. CV denotes the energy content of the oils, directly impacting their potential as biofuels and renewable energy sources. A higher CV indicates more excellent energy content, making the oils suitable for use in alternative fuels. The AV shows the oils' free fatty acid content, which affects their stability and suitability for consumption or industrial use. Oils with a low AV are more stable and less prone to oxidation, enhancing their shelf life and usability in food or cosmetics. SV measures the oils' average molecular weight, influencing their functionality in soap production, where a higher SV indicates better soap formation potential. RI provides information on the oils' optical properties, facilitating their identification and quality assessment in various applications, such as cosmetics and pharmaceuticals. Understanding these physicochemical properties is fundamental for optimizing the utilization of *J. curcas* and *R. communis* oils across diverse sectors, including energy, agriculture, and healthcare. The physicochemical properties of *J. curcas* and *R. communis* oils are listed in Table 1.

Table 1: Physicochemical features of *Jatropha curcas* and *Ricinus communis* oils.

Parameter	*J. curcas* oil	*R. communis* oil
Volumic mass (kg/m^3)	899.2	855
Carbon residue	0.64	-
Cetane index	51.0	53.0
Flash point (°C)	240	224
Distillation point (°C)	295	310
Sulphur (%)	0.13	-
CV (kJ/kg)	39926.38	40883.95
Pour point (°C)	8.0	2.6
Fusion point (°C)	-10	-12
Kinematic viscosity at 40°C(cSt)	50.73	226.2
Solidifying point (°C)	2.0	-10
SV (mg KOH/g)	192.64	174.6
IV (gI$_2$/100g)	97.65±1.10	87.03±3.50
Ester index	184.1±0.71	172.7±1.34
RI at 30°C	1.470	1.473
Impurities (%)	4.4331	1.0882
AV (mg KOH/g)	8.54±0.20	1.90±0.007
Palmitic acid (%)	4.2	1.8
Stearic acid (%)	6.9	0.78
Oleic acid (%)	43.1	4.2
Linoleic acid (%)	34.3	3.7
Ricinoleic acid	0.00	87.7
Other acids (%)	1.4	1.8

CV: calorific value, SV: saponification value, IV: iodine value, RI: refractive index, AV: acid value.

3.2. Biodiesel Synthesis (Transesterification Reaction):

3.2.1. Catalyst characterization

The contents of magnesium, phosphorus, sodium, potassium, and calcium were analyzed using X-ray fluorescence (XRF). The percentage of these elements in mg per 100 g sample was determined, as shown in Table 2.

Table 2: Mineral Composition of the Natural Catalyst (Date Palm Kernel Ash).

Mineral elements	Mg	P	K	Na	Ca
Content in (mg/100g of ash)	46.66	183.27	125.60	46.65	395.19

3.2.2. Reaction Yield

In transesterification reactions, the methanol quantity and the catalyst selection are critical parameters demanding precise control. These components play pivotal roles in the efficient conversion of TGs into biodiesel. Catalysts expedite the transesterification process and facilitate the formation of MEs. Various catalysts can be employed, such as KOH, potassium carbonate (K_2CO_3), and date stone ashes. The choice of catalyst is contingent upon several factors, including reaction conditions, availability, and cost.

The yield of the transesterification reaction varies depending on the plant species, the metabolite content within each species, and the solvent's nature and polarity used in extraction or fractionation processes (Figure 1).

Figure 1: Yields of (a) *Ricinus communis* methyl ester oil (RMEO), and (b) *Jatropha curcas* methyl ester oil (JMEO), obtained after transesterification in the presence of methanol and a catalyst (either K_2CO_3 or KOH).

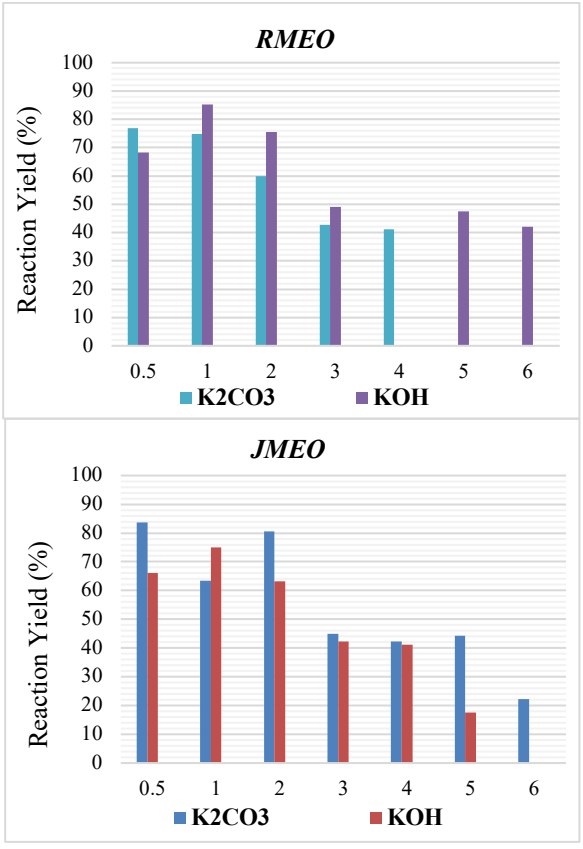

The reactions were carried out using 100 g of oil with methanol in a 6:1 molar ratio of methanol to oil, and 2 wt% K_2CO_3 or 1 wt% KOH as catalysts.

3.3. Properties of the Biodiesel Obtained from *R. communis*' and *J. curcas*' oils:

Characterizations included density, viscosity, CV, and flow rate measurements. Table 3 summarizes the characteristics of the biodiesel obtained from the transesterification of *J. curcas*' and *R. communis*' oils, including test methods, results, and comparison with ASTM D6751 and EN 14214 standards (Sidohounde *et al.*, 2018, Ahmad *et al.*, 2014, Hamdy *et al.*, 2022).

Table 3: Physicochemical features of the biofuel.

Characteristics	Test Method	Result	ASTM D6751	EN 14214
ME (% wt)	EN 14103	98.8	-	≥ 96.5
Oxidation Stability at 110°C (h)	EN 141112	30	-	≥ 6
Density at 15°C (kg/m3)	ASTM D 1298	871	860-900	820-860
Density at 30°C (kg/m3)	ASTM D 1298	862	-	-
Flash Point (°C)	ASTM D 93	> 120	> 130	> 101
Water content (ppm)	EN 12937	279	-	≤ 0.05
AV (mg KOH/g)	ASTM D 664	0.29	< 0.5	< 0.50
IV (g I2/100g)	EN 141111	56	-	< 120
Linolenic Acid ME (% wt)	EN 14103	0.08	-	12
Methanol content (% wt)	EN 14110	0.01	-	≤ 0.20
Monoglyceride (% wt)	EN 14105	0.20	-	≤ 0.80
Diglyceride (% wt)	EN 14105	0.04	-	≤ 0.20
Triglyceride (% wt)	EN 14105	0.00	-	≤ 0.20
Free Glycerin (% wt)	EN 14105	0.02	-	≤ 0.02
Total Glycerin (% wt)	EN 14105	0.07	-	≤ 0.25
Cloud Point (°C)	ASTM D 2500	20	-3 to 12	101

AV: acid value, IV: iodine value, ME: methyl ester.
The results provided apply to biodiesel obtained from *Ricinus communis* methyl ester oil (RMEO) and *Jatropha curcas* methyl ester oil (JMEO).

3.4. Fourier transform infrared (FTIR) Analysis of *R. communis*' Methyl ester Oil (RMEO) and *J. curcas*' Methyl ester Oil (JMEO):

Figure 2 and Table 4 show the Fourier transform infrared (FTIR) analysis spectra of biodiesels (RMEO and JMEO).

The peaks at 2955 and 2855 cm^{-1} are assigned to the symmetric and asymmetric stretching of CH_2 bonds, respectively. The peak at 2925 cm^{-1} shows the symmetric stretching of the CH_3 group. The absorption peaks between 1300 and 1500 cm^{-1} represent the angular deformation of CH_2 and CH_3 groups. The peak at 720 cm^{-1} is attributed to the asymmetric planar deformation of the CH_2 group. Biodiesel is a mixture of MEs with both long and short chains. Thus, the primary signature distinguishing biodiesel production from diesel is its 1743 and 1169 cm^{-1} absorption, related to the stretching modes of the ester functional groups -C=O and -COC, respectively. Another distinctive feature of biodiesel production is related to saturated and unsaturated ME compounds, whereas diesel fuel consists primarily of saturated hydrocarbons. Consequently, biodiesel displays absorption at 3018 and 1652 cm^{-1}, reflecting the alkene functional groups =C–H and –C=C, respectively.

Figure 2: Fourier transform infrared (FTIR) analysis spectrum of *R. communis*' methyl ester oil (RMEO) and *J. curcas*' methyl ester oil (JMEO).

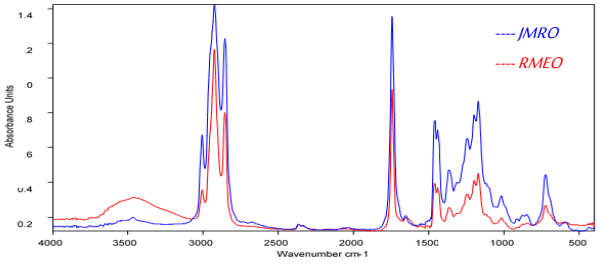

Table 4: Identified Chemical Bonds by Fourier transform infrared (FTIR).

Wavenumber (cm^{-1})	Chemical Bond
2955	Asymmetric stretching mode of CH_2
1500 and 1300	Angular deformation of CH_2 and CH_3
720	Asymmetric planar angular deformation of CH_2
3018	=C–H stretching mode in alkene
2925	Symmetric stretching of CH_3 in alkane
2855	Symmetric stretching of CH_2 in alkane
1743	Stretching of –C=O in ester
1652	Extended –C=C of alkene
1169	Stretching of –COC in ester

4. Discussion

Table 1 provides an overview of the composition of *J. curcas* crude oil, revealing that it contains 11.1% saturated fatty acids (SFAs) and 77.4%

UFAs. On the other hand, *R. Communis*'s oil seeds contain approximately 50 to 70% oil, specifically TGs, which consist of 2.3% SFAs and 87.7% UFAs (Fatma *et al.*, 2023). *R. communis*'s oil has a high viscosity, a moderately high density, and moderate saponifiability. It may be kept at 0°C and 10°C (refrigeration). According to the results presented in Table 2, the ashes of Deglet-Nour date palm kernels are rich in mineral matter. The predominant element is calcium, which is present as calcium oxide (CaO). Since CaO is essential, it reacts with methanol to make the methoxide anion (CH_3O^-). This anion acts as a nucleophile, speeding up the transesterification reaction (Kouzu and Hidaka, 2012, Avhad and Marchetti, 2015). The yield (conversion rate) of JMEO and RMEO obtained through transesterification was 85.33% and 74.9%, respectively, when KOH was used as the catalyst (1%) but was 76.89% and 83.63% when K_2CO_3 was used as the catalyst (0.5%) (Figure 1). These data mean that KOH is a better catalyst than K_2CO_3 for producing biodiesel from *J. curcas*'s oil, whereas K_2CO_3 is a better catalyst than KOH for producing biodiesel from *R. communis*'s oil. Density measurements reveal that both biodiesels exhibit lower densities than crude oil, indicating successful transesterification and a potential reduction in viscosity (Table 3). This reduction in density suggests improved flow characteristics, which is desirable for efficient fuel usage. The cetane index (CI) denotes the ignition quality of a fuel, typically increasing with the number of carbons and decreasing with the number of unsaturated carbon bonds (Ramalingam *et al.*, 2023, Achille *et al.*, 2023). Variations in the CI between JMEO and RMEO reflect differences in the number of carbons and unsaturated carbon bonds in each biodiesel. Other properties, such as oxidation stability, flash point, water content, AV, and glyceride content, fall within the acceptable range according to ASTM D6751 and EN 14214 standards. These results indicate the suitability of both biodiesels as alternative fuels and the potential of *J. curcas* and *R. communis* oils as renewable sources for biodiesel production, contributing to sustainable energy solutions.

The reaction mechanism of transesterification using KOH and K_2CO_3 as catalysts can be described in several steps:

- **Catalyst Activation:** The reaction begins with the activation of the catalyst in the reaction medium, typically methanol. For KOH, it dissolves in methanol to form CH_3O^-. In the case of K_2CO_3, it reacts with methanol to form CH_3O^- as well, but the reaction also produces carbonic acid (H_2CO_3), which decomposes into carbon dioxide (CO_2) and water. CH_3O^- is the crucial active species in the reaction that attacks the TG.
- **Acyl Exchange Reaction:** In this step, CH_3O^- acts as a nucleophile, attacking the glyceride molecule (TG). The nucleophilic attack occurs at the carbonyl carbon of the ester group in the TG, displacing the fatty acid chain (RCOOH). This leads to the formation of a ME (biodiesel) and the release of glycerol as a byproduct.
- **Reverse Reaction:** The glycerol produced in the previous step can sometimes react with another methanol molecule. This can lead to a TG molecule regeneration and water formation. However, this reverse reaction is generally negligible because glycerol is only sparingly soluble in methanol, and the equilibrium favors the formation of biodiesel and glycerol.
- **Approved Catalyst Range:** Catalyst concentrations within the optimal range promote efficient catalysis. For KOH, concentrations between 1% and 2% provide the best biodiesel yield. Similarly, K_2CO_3 concentrations between 0.5% and 2% are adeqaute. These concentrations ensure optimal catalyst activation, thus increasing the rate of the acyl exchange reaction. Furthermore, the available TGs are maximally utilized, yielding higher biodiesel.
- **Catalyst Excess:** Exceeding the recommended catalyst concentrations can produce undesirable consequences. An excess of KOH or K_2CO_3 can react with free fatty acids (FFAs) in the oil, forming soap through saponification. This is an unwanted side reaction, as the soap formed can create emulsions and hinder biodiesel separation. Moreover, excess catalyst can leave residues in the final product, necessitating additional purification steps to meet quality standards.

Using Deglet-Nour DPKA as a natural catalyst in the transesterification reaction resulted in a miscible (homogeneous) mixture, with the ash powder suspended in the reaction medium. This indicates that the ash was not dissolved in the medium. Dissolving the ash allows its active compounds to fulfill their role as catalysts and promote the transesterification reaction (Saetiao *et al.*, 2023, Chutia and Phukan, 2023, Tobío-Pérez *et al.*, 2021).

5. Conclusions

Vegetable oils are prominent renewable and sustainable energy sources, though their direct use in diesel engines necessitates specific modifications due to unique physicochemical properties deviating from standard parameters. In contrast, biodiesels derived from these oils closely emulate petrodiesel regarding physicochemical characteristics, offering advantages such as lower toxicity, biodegradability, high calorific values, and reduced greenhouse gas emissions.

The physicochemical properties of *J. curcas* and *R. communis* oils prove suitable for energy use, except for viscosity, which remains high. Nonetheless, this limitation can be mitigated through transesterification. Basic or acid transesterification is the most common process for converting vegetable oils into biodiesel due to its simplicity and cost-effectiveness. However, meticulous control of methanol quantity and catalyst type is pivotal for efficiently converting TGs into biodiesel.

In transesterification, methanol reacts with TGs in vegetable oils or animal fats, transforming them into methyl esters (biodiesel). The stoichiometric ratio of methanol to TGs, typically 3:1, ensures complete conversion and minimizes unreacted methanol in the final biodiesel product. While date seed ashes may exhibit catalytic activity during combustion, their efficiency as transesterification catalysts may be lower than that of conventional catalysts such as strong bases or enzymes.

The resulting biodiesels closely resemble petrodiesel in fuel characteristics, making them suitable substitutes for fossil diesel, meeting ASTM D6751 and EN 14214 standards. Limitations include the lower efficiency of date seed ash as a catalyst than conventional catalysts, the persistence of high viscosity in oils despite transesterification, and the high consumption of methanol, which can increase costs and environmental impact. Future research should focus on enhancing catalyst efficiency, optimizing reaction conditions, and exploring alternative feedstocks like waste oils. Investigating alternative alcohols for biodiesel production and conducting life cycle assessments would further improve sustainability and cost-effectiveness.

Biographies

Souaad Chibi

Department of Process Engineering, Functional Analysis Laboratory of Chemical Processes, Saad Dahlab University - Blida 1, Blida, Algeria, 00213673620082, chibi_souaad@univ-blida.dz

Souaad is a lecturer in the Department of Process Engineering at Saad Dahlab University, Blida 1, Algeria, and a researcher in the Functional Analysis Laboratory of Chemical Processes. Her work centers on chemical process analysis and engineering, emphasizing optimization, functional materials, and sustainable engineering solutions.

ORCID: 0009-0002-5703-321X

Salah Neghmouche Nacer

Department of Chemistry, Faculty of Exact Sciences, University of El Oued, El Oued, Algeria, 00213669444009, neghmouchenacer-salah@univ-eloued.dz

Salah is a lecturer in the Department of Chemistry, Faculty of Exact

Sciences, University of El-Oued, Algeria. He earned his Licence and Master's degrees from ENS Kouba, and his Ph.D. and accreditation diploma (HDR) in applied organic chemistry from Constantine 1 University. In 2018, he joined the Environmental and Structural Molecular Chemistry Research Unit at Constantine 1 University. His research covers organic chemistry, organometallic synthesis, electrochemical analysis, instrumentation, and bioelectrochemistry.

ORCID: 0000-0002-9381-8973

Younes Moussaoui

Organic Chemistry Laboratory (LR17ES08), Faculty of Sciences of Sfax, University of Sfax, Sfax, Tunisia, 0021697623805, y.moussaoui2@gmail.com

Prof. Younes is a Professor at the Faculty of Sciences of Gafsa, University of Gafsa. He graduated from the Faculty of Sciences of Sfax in 2000, where he also earned his Master's degree in 2002 and completed his Ph.D. in 2007. In 2012, he received his research supervision accreditation (HDR) from the University of Sfax. His research focuses on biomass valorization and its application as raw materials in biomaterials, papermaking, polymeric materials, composites, and nanocomposites.

ORCID: 0000-0003-0329-2443

Djamel Ghernaout

Department of Chemical Engineering, College of Engineering, University of Ha'il, Ha'il, Saudi Arabia, 00966534626675, djamel_andalus@yahoo.fr

Djamel is a researcher and faculty member in the Department of Chemical Engineering at the University of Ha'il, specializing in Environmental and Chemical Engineering. With over 30 years of experience in water treatment, he has extensively studied and developed treatment processes at laboratory and industrial scales. He has authored 95 ISI and 117 non-ISI publications and was recognized among the Top 2% of World Scientists in Stanford University and Elsevier's rankings for 2023 and 2024.

ORCID: 0000-0002-0806-3810

Noureddine Elboughdiri

Department of Chemical Engineering, College of Engineering, University of Ha'il, Ha'il, Saudi Arabia, 00966549571015, ghilaninouri@yahoo.fr

Prof. Noureddine is a full Professor in the Chemical Engineering Department at Hail University, Saudi Arabia. He earned his BSc, Master's, and PhD in Chemical Engineering from the University of Gabes, Tunisia. Previously, he worked at the Central Laboratory for Analysis and Testing (LCAE-Tunisia) in 2004 and joined the SGS Group in 2008. He has held various teaching and administrative roles, specializing in statistical analysis and academic accreditation. His research focuses on wastewater treatment and environmental pollution, and he is recognized among the Top 2% of World Scientists by Stanford University.

ORCID: 0000-0003-2923-3062

Farid Menaa

Department of Biomedical and Environmental Engineering, Fluorotronics, Inc.- California Innovations Corporation, San Diego, USA, 008582742728, menaateam@gmail.com

Menaa is a graduate of renowned institutions worldwide, including the University of Paris. A polyglot fluent in seven languages (French, English, Portuguese, Spanish), he has over 20 years of experience in academia and industry. With more than 220 peer-reviewed publications in top journals, Dr. Menaa serves as Consulting Director at CIC. His holistic approach offers tailored, practical insights to address the unique needs of scientific and medical collaborators across the globe.

ORCID: 0000-0002-0258-7322

Muhammad Imran Khan

Research Institute of Sciences and Engineering (RISE), University of Sharjah, Sharjah, United Arab Emirates, 00971563404827, raoimranishaq@gmail.com

Khan earned his Ph.D. from the University of Science and Technology of China (USTC), Hefei. Since December 2020, he has been a Research Scientist at the Research Institute of Sciences and Engineering (RISE), University of Sharjah, UAE. His research focuses on fabricating polymeric ion exchange membranes for water purification and fuel cell applications. In 2021, Stanford University named him among the World's Top 2% Scientists, recognizing his significant contributions to his field.

ORCID: 0000-0003-1886-8687

Djamel El Hadi

Department of Process Engineering, Functional Analysis Laboratory of Chemical Processes, Saad Dahlab University - Blida 1, Blida, Algeria, 00213779796827, elhadi64djamel@yahoo.fr

El-Hadi is a recognized process engineering expert specializing in process simulation, modeling, and petroleum refining. At Saad Dahlab University - Blida 1, he leads the Functional Analysis Laboratory of Chemical Processes, focusing on optimizing industrial chemical processes and advancing sustainable technologies. His pioneering research has substantially impacted petroleum refining and chemical technology, positioning him as a critical contributor to enhancing efficiency and driving innovation in the chemical industry.ORCID: 0009-0004-6764-9899

References

Achille, K., Ghislain, M.M., Louis, M. and Adolphe, M.I. (2023). Determination at variable temperatures and analysis of the Physico-Thermal properties of palm kernel and castor oil methyl esters as dielectrics for power transformers. *International Journal of Heat and Technology*, **41**(1), 63–71. DOI: 10.18280/ijht.410107

Ahmad, J., Yusup, S., Bokhari, A. and Kamil, R.N.M. (2014). Study of fuel properties of rubber seed oil-based biodiesel. *Energy Conversion and Management*, **78**(n/a), 266–75. DOI: 10.1016/j.enconman.2013.10.056

Anekwe, I.M.S., Nyembe, N., Nqakala, L.C., Madikizela, M. and Isa, Y.M. (2023). Sustainable fuels: Lower alcohols perspective. *Environmental Progress and Sustainable Energy*, **42**(6), e14175. DOI: 10.1002/ep.14175

Avhad, M.R. and Marchetti, J.M. (2015). A review on recent advancement in catalytic materials for biodiesel production. *Renewable and Sustainable Energy Reviews*, **50**(n/a), 696–718. DOI: 10.1016/j.rser.2015.05.038

Badawi, A.K., Salama, R.S. and Mostafa, M.M.M. (2023). Natural-based coagulants/flocculants as sustainable market-valued products for industrial wastewater treatment: a review of recent developments. *RSC Advances*, **13**(28), 19335–55. DOI: 10.1039/d3ra01999c

Chakraborty, I. and Chatterjee, K. (2020). Polymers and Composites Derived from Castor Oil as Sustainable Materials and Degradable Biomaterials: Current Status and Emerging Trends. *Biomacromolecules*, **21**(12), 4639–62. DOI: 10.1021/acs.biomac.0c01291

Chutia, G.P. and Phukan, K. (2023). Biomass derived heterogeneous catalysts used for sustainable biodiesel production: a systematic review. *Brazilian Journal of Chemical Engineering*, **41**(1), 23–48. DOI: 10.1007/s43153-023-00371-6

Dalila, B., Chafia, S., Emna Z., Karima, R., Abir, B., Hana, F., Ahmed, H., Abir, G., Ivalina, A., Zighed, M., Vasile, I.P., Krishna, K.Y., Mudassir, H., Marina, M.S.C-P., Noureddine, E., Yacine, B. (2024). Efficient biodiesel production from recycled cooking oil using a NaOH/CoFe2O4 magnetic nano-catalyst: synthesis, characterization, and process enhancement for sustainability. *Energy Conversion and Management*, **300**(n/a), 118021. DOI: 10.1016/j.enconman.2023.118021

Elboughdiri, N., Alsenani, T.R., Singh, P.K., Albani, A., Ali, H.E., Almujibah, H., Alshahri, A., Alkhalaf, S. and Islam, S. (2024). Using response surface methodology for multi-objective optimization of an efficient/clean combined heating/power system based on

sugarcane bagasse gasification for environmental sustainability. *Process Safety and Environmental Protection*, **182**(n/a), 197–209. DOI: 10.1016/j.psep.2023.11.072

Fatma, Z.B.C., Ammar, Z., Hakim, B., Ali, D., Salah, N.N., Djamel, G., Noureddine, E. (2023). Transforming waste cooking oil into environmentally friendly biodiesel: a comparative analysis of three transesterification methods, *International Journal of Oil Gas and Coal Technology*, **34** (4), 413–27. DOI: 10.1504/IJOGCT.2023.135058

Glüge, J., Scheringer, M., Cousins, I.T., DeWitt, J.C., Goldenman, G., Herzke, D., Lohmann, R., Ng, C.A., Trier, X. and Wang, Z. (2020). An overview of the uses of per- and polyfluoroalkyl substances (PFAS). *Environmental Science Processes and Impacts*, **22**(12), 2345–73. DOI: 10.1039/d0em00291g

Hamdy, M. S., Alqahtani, F. A., Shkir, M., Fawy, K. F., Benaissa, M., Hamida, M. B. B., & Elboughdiri, N. (2022). Effect of different zeolite supports on the catalytic behavior of platinum nanoparticles in cyclohexene hydrogenation reaction. *Catalysts*, **12**(10), 1106.DOI: 10.3390/catal12101106

Keera, S., Sabagh, S.E. and Taman, A. (2018). Castor oil biodiesel production and optimization. *Egyptian Journal of Petroleum*, **27**(4), 979–84. DOI: 10.1016/j.ejpe.2018.02.007

Kibazohi, O. and Sangwan, R. (2011). Vegetable oil production potential from *Jatropha curcas*, Croton megalocarpus, Aleurites moluccana, Moringa oleifera and Pachira glabra: Assessment of renewable energy resources for bio-energy production in Africa. *Biomass and Bioenergy*, **35**(3), 1352–6. DOI: 10.1016/j.biombioe.2010.12.048

Kouzu, M. and Hidaka, J. (2012). Transesterification of vegetable oil into biodiesel catalyzed by CaO: A review. *Fuel*, **93**(n/a), 1–12. DOI: 10.1016/j.fuel.2011.09.015

Lateef, F.A. and Ogunsuyi, H.O. (2021). *Jatropha curcas* L. biomass transformation via torrefaction: Surface chemical groups and morphological characterization. *Current Research in Green and Sustainable Chemistry*, **4**(n/a), 100142. DOI: 10.1016/j.crgsc.2021.100142

Manzoor, S., Aziz, K., Raza, H., Manzoor, S., Khan, M.I., Naz, A., Shanableh, A., Salih, A.A.M. and Elboughdiri, N. (2023). Tailoring Vanadium-Based magnetic catalyst by in situ encapsulation of tungsten disulfide and applications in abatement of multiple pollutants. *ACS Omega*, **8**(51), 48966–74. DOI: 10.1021/acsomega.3c06580

Memon, H.D., Mahesar, S.A., Sirajuddin, N., Kara, H., Sherazi, S.T.H. and Talpur, M.Y. (2024). A review: Health benefits and physicochemical characteristics of blended vegetable oils. *Grain and Oil Science and Technology*, **7**(2), 113–23. DOI: 10.1016/j.gaost.2024.05.001

Mouahid, A., Bouanga, H., Crampon, C. and Badens, E. (2017). Supercritical CO2 extraction of oil from *Jatropha curcas*: An experimental and modelling study. *The Journal of Supercritical Fluids*, **141**(n/a), 2–11. DOI: 10.1016/j.supflu.2017.11.014

Naik, B. (2018). Botanical Descriptions of Castor Bean. In: Kole, C., Rabinowicz, P. (eds) *The Castor Bean Genome. Compendium of Plant Genomes*. Switzerland : Springer, Cham DOI: 10.1007/978-3-319-97280-0_1

Nanda, S., Azargohar, R., Dalai, A.K. and Kozinski, J.A. (2015). An assessment on the sustainability of lignocellulosic biomass for biorefining. *Renewable and Sustainable Energy Reviews*, **50**(n/a), 925–41. DOI: 10.1016/j.rser.2015.05.058

Neme, I., Gonfa, G. and Masi, C. (2022). Preparation and characterization of activated carbon from castor seed hull by chemical activation with H3PO4. *Results in Materials*, **15**(n/a), 100304. DOI: 10.1016/j.rinma.2022.100304

Öner, C. and Altun, Ş. (2009). Biodiesel production from inedible animal tallow and an experimental investigation of its use as alternative fuel in a direct injection diesel engine. *Applied Energy*, **86**(10), 2114–20. DOI: 10.1016/j.apenergy.2009.01.005

Patil, S.P., Bhalerao, S.A., Rajput, Y.N. and Pratap, A.P. (2024). Production of Rhamnolipids using WFSO and its application in the development of antifungal nanoemulsion using Hydnocarpus Wightiana, Garcinia Cambogia - Seed oils. *Industrial Crops and Products*, **219**(n/a), 118885. DOI: 10.1016/j.indcrop.2024.118885

Pina, M., Severino, L.S., Beltrão, N.E., Villeneuve, P. and Lago, R. (2005). De nouvelles voies de valorisation pour redynamiser la filière ricin au Brésil. *Cahiers Agricultures*, **14**(1), 169–71.

Ramalingam, K., Vellaiyan, S., Venkatesan, E.P., Khan, S.A., Mahmoud, Z. and Saleel, C.A. (2023). Challenges and Opportunities of Low viscous Biofuel—A Prospective Review. *ACS Omega*, **8**(19), 16545–60. DOI: 10.1021/acsomega.3c00387

Razak, N.A.A., Taufiq-Yap, Y.H. and Derawi, D. (2024). Catalytic deoxygenation of waste cooking oil for sustainable bio-jet fuel: A comparative study of Ni-Co/SBA-15 and Ni-Co/SBA-15-SH catalysts. *Journal of Analytical and Applied Pyrolysis*, **178**(n/a), 106369. DOI: 10.1016/j.jaap.2024.106369

Resul, M.F.M.G., Ghazi, T.I.M. and Idris, A. (2012). Kinetic study of jatropha biolubricant from transesterification of *Jatropha curcas* oil with trimethylolpropane: Effects of temperature. *Industrial Crops and Products*, **38**(n/a), 87–92. DOI: 10.1016/j.indcrop.2012.01.012

Rosak-Szyrocka, J., Allahham, A., Żywiołek, J., Turi, J.A. and Das, A. (2023). Expectations for renewable energy, and its impacts on quality of life in European Union countries. *Management Systems in Production Engineering*, **31**(2), 128–37. DOI: 10.2478/mspe-2023-0015

Saadaoui, E., Martin, J.J., Tlili, N. and Cervantes, E. (2017). Castor bean (*Ricinus communis* L.): diversity, seedoil and uses. In, Ahmad P Ed. *Oil Seed Crops: Yield and Adaptations Under Environmental Stress*. United Kingdom : John Wiley and Sons. DOI: 10.1002/9781119048800.ch2

Saetiao, P., Kongrit, N., Cheng, C.K., Jitjamnong, J., Direksilp, C. and Khantikulanon, N. (2023). Catalytic conversion of palm oil into sustainable biodiesel using rice straw ash supported-calcium oxide as a heterogeneous catalyst: Process simulation and techno-economic analysis. *Case Studies in Chemical and Environmental Engineering*, **8**(n/a), 100432. DOI: 10.1016/j.cscee.2023.100432

Sidohounde, A., Dossa, C.P.A., Nonviho, G., Montcho, S.P. and Sohounhloue, D.C.K. (2018). Biodiesel potentials of two phenotypes of Cyperus esculentus unconventional oils. *Journal of Petroleum Technology and Alternative Fuels*, **9**(1), 1–6. DOI: 10.5897/jptaf2018.0136

Taddese, H. (2014). Suitability analysis for *Jatropha curcas* production in Ethiopia-a spatial modeling approach. *Environmental Systems Research*, **3**(n/a), 1–13. DOI: 10.1186/s40068-014-0025-7

Tapanes, N.C.O., Aranda, D.A. G., De Mesquita Carneiro, J.W. and Antunes, O.A.C. (2008). Transesterification of *Jatropha curcas* oil glycerides: Theoretical and experimental studies of biodiesel reaction. *Fuel*, **87**(10–11), 2286–95. DOI: 10.1016/j.fuel.2007.12.006

Tenorio-Alfonso, A., Sánchez, M.C. and Franco, J.M. (2019). Synthesis and mechanical properties of bio-sourced polyurethane adhesives obtained from castor oil and MDI-modified cellulose acetate: Influence of cellulose acetate modification. *International Journal of Adhesion and Adhesives*, **95**(n/a), 102404. DOI: 10.1016/j.ijadhadh.2019.102404

Thombare, N., Kumar, S., Kumari, U., Sakare, P., Yogi, R.K., Prasad, N. and Sharma, K.K. (2022). Shellac as a multifunctional biopolymer: A review on properties, applications and future potential. *International Journal of Biological Macromolecules*, **215**(n/a), 203–23. DOI: 10.1016/j.ijbiomac.2022.06.090

Tobío-Pérez, I., Domínguez, Y.D., Machín, L.R., Pohl, S., Lapuerta, M. and Piloto-Rodríguez, R. (2021). Biomass-based heterogeneous catalysts for biodiesel production: A comprehensive review. *International Journal of Energy Research*, **46**(4), 3782–809. DOI: 10.1002/er.7436

Zhu, C.Z., Samuel, O.D., Elboughdiri, N., Abbas, M., Saleel, C. A., Ganesan, N., ... & Fayaz, H. (2023). Artificial neural networks *vs.* gene expression programming for predicting emission & engine efficiency of SI operated on blends of gasoline-methanol-hydrogen fuel. *Case Studies in Thermal Engineering*, **49**(n/a), 103109. DOI: 10.1016/j.csite.2023.103109

Scientific Journal of King Faisal University:
Basic and Applied Sciences

Enhancing Interoperability in the Web of Things: A Reference Architecture Approach

Khalied M. Albarrak
Department of Management Information Systems, College of Business Administration, King Faisal University, Al-Ahsa, Saudi Arabia

LINK	RECEIVED	ACCEPTED	PUBLISHED ONLINE	ASSIGNED TO AN ISSUE
https://doi.org/10.37575/b/sci/240034	02/08/2024	18/12/2024	18/12/2024	01/06/2025

NO. OF WORDS	NO. OF PAGES	YEAR	VOLUME	ISSUE
5327	6	2025	26	1

ABSTRACT

The concept of the Internet of Things (IoT) has fundamentally redefined the connectivity landscape by integrating physical devices with the Internet for data exchange. The Web of Things (WoT) takes this integration a step further by embedding IoT devices within the web, thus facilitating their interoperability. However, the inherent complexity of WoT architecture requires a layer of abstraction to simplify development and integration. Patterns and reference architectures (RAs) provide such an abstraction, modeling solutions for recurrent problems within this domain. In this paper, we aim to develop an RA for the WoT ecosystem. We use architectural patterns to build the RA of the WoT. Here, we present the WoT gateway pattern, which provides a clear and adaptable framework for integrating diverse IoT devices, ensuring seamless communication and functionality within the broader web ecosystem. The purpose of this pattern is twofold: to ensure the interoperability of WoT implementations and to serve as a foundational guide for developers navigating the multifaceted challenges of WoT system design. The pattern also paves the way for building an RA for IoT environments.

KEYWORDS
Architectural patterns, Internet of Things, reference architecture, web development, web science, WoT

CITATION
Albarrak, K.M. (2025). Enhancing interoperability in the web of things: A reference architecture approach. *Scientific Journal of King Faisal University: Basic and Applied Sciences*, **26**(1), 7–12. DOI: 10.37575/b/sci/240034

1. Introduction

The Internet of Things (IoT) has revolutionized how we interact with the physical world through interconnected devices and systems. It encompasses a wide array of technologies that enable devices to collect, exchange, and act on data, often with minimal human intervention. However, as the IoT landscape expands, it has also become a complex web of proprietary systems with significant interoperability challenges. To address these issues, the Web of Things (WoT) has emerged as a unifying layer designed to enable interoperability across various IoT platforms and domains by leveraging web technologies.

The WoT seeks to create a cohesive ecosystem where IoT devices can communicate seamlessly, regardless of the diverse protocols and standards they may employ. Its integration into IoT architecture introduces a new level of standardization and interaction, allowing devices to effectively communicate, share, and act upon data. This approach is expected to mitigate existing IoT challenges, such as siloed ecosystems (Nedeltcheva and Shoikova, 2017) and lack of uniformity (Achirei *et al.*, 2020), by providing a common ground that fosters innovation and simplifies the development of IoT solutions. The application of WoT is particularly significant in ensuring that as the number of IoT devices grows, they can operate in harmony, creating more intelligent and responsive environments.

This paper introduces a pattern for WoT architecture as a foundational step toward building a reference architecture (RA) for the WoT ecosystem. The intended audience includes system architects and system designers. Patterns have been instrumental in modeling various virtualized environments (Alnaim *et al.*, 2019; Alwakeel *et al.*, 2019a; Syed and Fernandez, 2018), offering solutions to recurring design and architectural challenges. They address common problems such as flexibility (Alnaim *et al.*, 2019), heterogeneity (Fernandez and Hamid, 2015), and elasticity (Syed *et al.*, 2016). Furthermore, RAs have proven effective as tools for abstracting complex systems that often lack clear semantics.

Implementing an RA for WoT aids in understanding the system's functionality and identifying potential vulnerabilities. Over time, this RA could evolve into a security reference architecture (SRA) by incorporating misuse and security patterns addressing potential threats and vulnerabilities within the system. Despite this potential, a noticeable gap exists in the application of patterns to WoT. While IoT architectures provide general frameworks, WoT's unique challenges require more precise modeling.

The primary contribution of this paper is the development of a comprehensive RA for the WoT. This RA simplifies the integration and management of IoT devices across different platforms and protocols while enhancing interoperability and scalability. The WoT architecture defines an abstract architecture based on modular building blocks applicable across diverse application domains. This abstract architecture, as described by the World Wide Web Consortium (W3C), is not prescriptive but descriptive, emphasizing interoperability and complementing existing IoT standards rather than replacing them (Lagally *et al.*, 2023).

The remainder of the paper is structured as follows: Section 2 provides the background of WoT architecture, patterns, and RA. Section 3 presents a pattern for WoT. The paper concludes with insights and directions for future research.

2. Background

2.1. Web of Things

WoT architecture, developed by the W3C, is a conceptual framework designed to foster interoperability among disparate IoT devices and platforms (Lagally *et al.*, 2023). At its core, WoT aims to integrate IoT with the World Wide Web, establishing a uniform way to communicate across various protocols and data formats. The architecture leverages web standards to create a common interface, with the goal of making IoT devices as accessible and interactive as web pages and services. This approach enables developers to build cross-platform applications and facilitates efficient communication between devices, regardless of their underlying hardware or software specifications.

The WoT architecture comprises several key components (Lagally *et*

Corresponding Author: Khalied M. Albarrak 00966135895800, kalbarrak@kfu.edu.sa

al., 2023). At the forefront are WoT Thing Descriptions (TDs), which serve as the IoT equivalent of web pages. TDs provide a standardized, machine-readable format for describing the metadata, properties, interaction affordances, security requirements, and events associated with IoT devices. Another critical component is the WoT Binding Template, which extends TD functionality by defining how the abstract interactions described in TDs are implemented over various communication protocols. This ensures that devices not only communicate but do so in a consistent and comprehensible manner across diverse network environments.

Complementing these components are WoT Discovery mechanisms, which facilitate the dynamic detection and integration of devices within the IoT ecosystem. These mechanisms enable the automatic identification and configuration of new devices as they join the network, significantly simplifying the process of expanding and maintaining IoT systems. Together, these components form the backbone of the WoT framework, promoting a seamless, standardized, and scalable approach to IoT device interoperability and management.

2.2. Patterns

A pattern is essentially a solution to a recurring problem within a specific context (Buschmann *et al.*, 2001). Software patterns, such as design and architectural patterns, are instrumental in developing systems that are both flexible and extensible. Security patterns focus on constructing secure systems by detailing methods to manage threats, address vulnerabilities, and implement necessary security measures (Fernandez *et al.*, 2016). Similarly, misuse patterns offer insights into how attacks are executed from the attacker's perspective. They specify the conditions conducive to an attack, the required security measures, and methods for gathering forensic data post-incident (Alnaim, 2022).

In this paper, patterns are used to define the principal components of the WoT. Patterns serve as a robust mechanism for articulating comprehensive solutions that encompass not only software but also hardware and physical elements that collectively form ecosystems. These patterns are typically structured as templates with designated sections. In our approach, we adopt the POSA (Pattern-Oriented Software Architecture) template (Fernandez, 2013). The documentation of these patterns may include UML modeling techniques and formal language descriptions to ensure clarity and precision.

2.3. Reference Architecture

A RA serves as a conceptual blueprint for one or more domains, focusing on architectural aspects without addressing specific implementations (Angelov *et al.*, 2012; Avgeriou, 2003 and Cloutier *et al.*, 2010). An RA is designed to outline the core components of a system and their interactions, providing an architectural framework tailored to a specific domain. Key attributes that enhance the utility of RAs include configurability, extendibility, and reusability (Avgeriou, 2003). Beyond class and sequence diagrams, an RA may include a collection of use cases (UCs) and a set of roles (R) corresponding to its stakeholders or actors (Pankowska, 2015).

RAs can be categorized into various types, such as those for the technology domain, which details platforms and design artifacts (Angelov *et al.*, 2012); those for the application domain, which describe different types of applications; and those for the problem domain, which are similar to domain models but tailored for software solutions. Stakeholders of an RA may include groups, individuals, organizations, and systems that have a vested interest in the system and influence its design and development (Avgeriou, 2003). To enhance its security features, an RA can be transformed into an SRA by integrating security patterns that address and mitigate identified threats (Avgeriou, 2003 and Alnaim *et al.*, 2022).

3. Related Work

Numerous studies have been conducted to develop and refine the architecture of WoT. Guinard *et al.* (2010) detailed a resource-oriented architecture rooted in RESTful principles. Zhang, Cheng, and Ji (2012) introduced a Social WoT framework that merges RESTful web services with social networking elements. Guinard (2011) further advanced the field by proposing a four-layered WoT application architecture aimed at streamlining the development of applications involving smart devices. He also illustrated client–thing interaction through a sequence diagram, though his proposed architecture could benefit from a deeper exploration of its components and their interconnections. Mainetti *et al.* (2015) offered an architectural approach that includes mechanisms for discovering devices and virtualizing them outside their physical network. However, these architectures tend to be conceptual and lack detailed semantics.

Additionally, Manta-Caro *et al.* (2024) discussed the new opportunities and challenges brought by IoT and WoT, particularly in the field of information retrieval. They proposed architectural solutions to manage the vast data generated by interconnected devices. The use of architectural patterns has also become prevalent in various technological contexts, providing targeted solutions within specific ecosystems. Alnaim *et al.,* (2019) and Fernandez and Hamid (2015) applied patterns to model the network function virtualization architecture. Syed *et al.* (2016a) utilized patterns within Fog Computing to address particular challenges, while Hashizume *et al.* (2012) extensively employed patterns to tackle architectural issues in cloud environments.

4. A Pattern for Web of Things Gateway

- **Intent:** To enable interoperability and standardized interaction among diverse IoT devices and services in various application domains.
- **Context:** Within the IoT ecosystem, devices and services must communicate effectively regardless of their underlying implementations and across multiple networking protocols.
- **Example:** John's home contains various IoT devices, including a Bluetooth-enabled smart door lock, a Wi-Fi-connected TV, and smart lighting that operates on ZigBee. The diversity in communication protocols means each device requires its own specific application for control, complicating the management process. Currently, there is no unified standard that allows all these devices to be controlled seamlessly through a single application or platform.
- **Problem:** IoT devices vary widely in their implementations and communication protocols, creating a heterogeneous ecosystem. To facilitate smooth and effective interaction between these devices, it is crucial to ensure interoperability across this diverse landscape.

  The solution is influenced by the following forces:

  1. **Compatibility:** Maintaining compatibility among an ever-growing number of IoT devices is a significant challenge. As new models and versions are released, they must communicate and function with older devices without requiring frequent upgrades or replacements.
  2. **Scalability:** As IoT ecosystems expand in terms of both the number of devices and the volume of data generated, scalability becomes a critical concern.
  3. **Interoperability:** IoT devices vary in their platforms and protocols. Ensuring seamless interoperability among heterogeneous devices remains a core challenge.
  4. **Discoverability:** In an IoT ecosystem, devices frequently join and leave the network. Automatic discovery and integration of new devices are essential for maintaining an up-to-date and responsive system.
  5. **Resource Constraints:** IoT devices often have limitations in processing power, memory, and energy, which complicates the implementation of complex communication protocols

and data processing tasks.

6. **Security:** IoT devices often collect and transmit sensitive data. Ensuring security and privacy is crucial, but the diversity of devices and protocols makes it difficult to implement uniform security measures.

- **Solution**: Utilize the WoT building blocks, which support describing network interfaces for IoT devices and services, define communication protocols, and facilitate the discovery, consumption, and exposure of IoT devices ("Things").
- **Structure**: Figure 1 presents a UML class diagram for WoT architecture. A "Thing" represents one or more physical IoT devices within a network responsible for collecting data and performing actions. Things can interact with other Things. A node device, which could be an edge, fog, or cloud server, manages the interactions of multiple Things. Each Thing is described by its own TD, which provides a machine-readable vocabulary for defining the physical device. TDs can be implemented over multiple protocols, each requiring a different Binding Template.
  The WoT Discovery mechanism manages TDs for various devices. When a device (Thing) is discovered, its TD is retrieved by the WoT Discovery component, allowing clients or services to understand the capabilities and interaction affordances of the discovered Thing. The WoT Discovery component also communicates with the Node to register new devices joining the network and to query devices based on specific criteria.
  In this case, the Node may act as a client to the discovery service when searching for new devices to manage or integrate. Users can send commands to Things via the API, enabling interaction and control within the IoT ecosystem.

Figure 1. Class diagram of the WoT pattern

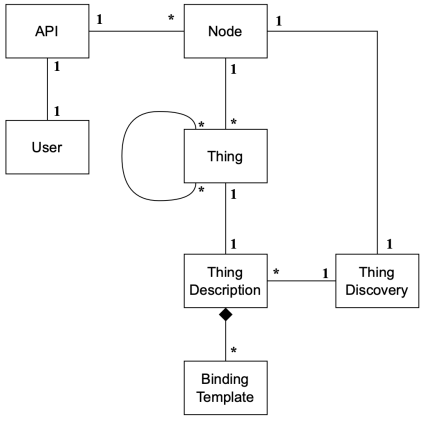

- **Dynamics**: This section delves into the operational aspects of the WoT architecture to elucidate how the various elements of the WoT architecture interact and coordinate in practical scenarios through illustrative sequence diagrams. Two UCs are presented: one in a Smart Agriculture System and the other in a Health Monitoring System.

4.1. Use Case-1 (UC1): Unified Device Management

Summary: This scenario demonstrates how diverse Thing devices are unified under a single management platform by utilizing the Node, which aggregates access to all the Things' properties. Figure 2 presents a sequence diagram for this UC.

Actor: User

Precondition: The Node is pre-configured with all connected Things.

Description: Several IoT devices are installed in a user's premises and are ready to be utilized.

1. The user launches a unified application (e.g., a mobile application) designed to communicate with the Node, which serves as the central point for device management in the home.
2. The user sends a request to a Thing device to perform a task.
3. The Node forwards the formatted commands to the Thing devices.
4. The Thing devices acknowledge the completion of the commands and send confirmation to the Node.
5. The Node relays the acknowledgment to the user.

Postcondition: Requests sent to the diverse Thing devices are fulfilled using one unified control management platform.

Figure 2. Sequence diagram for the use case "unified device management"

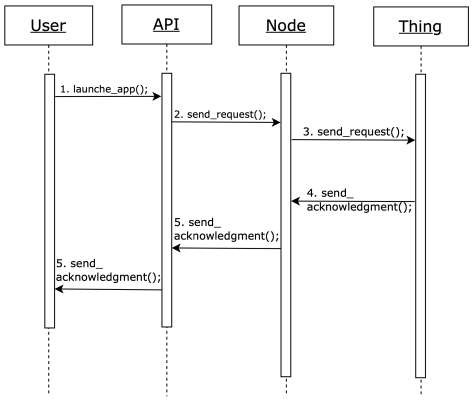

4.2. Use Case-2 (UC2): Adjust Irrigation

Summary: This scenario illustrates how an IoT moisture sensor autonomously monitors soil moisture levels and activates an irrigation process through a smart ecosystem when necessary. Upon detecting low moisture, the sensor's data prompts either user intervention or an automated response, triggering an irrigation controller to hydrate the soil. In this case, the scenario highlights how a controller initiates an irrigation request based on predefined rules within the Node. Figure 3 provides the sequence diagram for this UC.

Actor: IoT sensor

Precondition: The IoT sensor monitors soil moisture levels and detects that the soil moisture is below the predetermined threshold.

Description:

1. After measuring soil moisture, the sensor (a Thing) detects that the moisture level is below the predetermined threshold.
2. The sensor sends the measurement data to the Node.
3. The Node, utilizing WoT Discovery, identifies the sensor and retrieves its TD to interpret the data format and meaning.
4. The Node sends a command to the irrigation controller, activating the irrigation system.
5. The irrigation controller sends a confirmation or status update back to the Node.

Postcondition: The Node provides the user with reports about the soil moisture level.

Figure 3. Sequence diagram for use case "adjust irrigation"

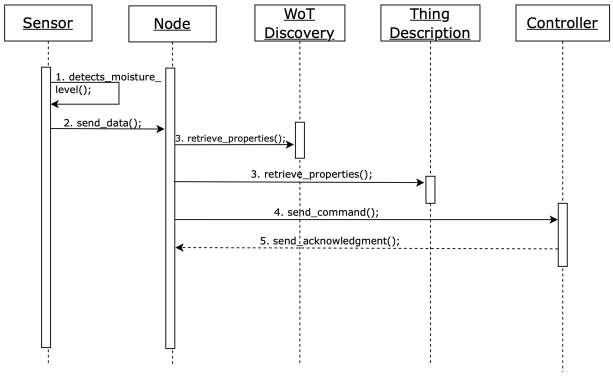

4.3. Use Case-3 (UC3): Smart Emergency Response System

Summary: This UC illustrates a Smart Healthcare Monitoring System that leverages the WoT architecture to enhance patient care by continuously monitoring health metrics through connected medical devices in a healthcare facility.

Actors: IoT sensor, medical staff

Precondition: All IoT medical devices are operational and connected to the WoT gateway, with the system configured to monitor and respond to specific health metric thresholds.

Description:

1. IoT health sensors (e.g., heart rate monitors and blood pressure sensors) continuously collect patient data and transmit it to the WoT gateway.
2. The WoT gateway analyzes the incoming data against predefined health thresholds. If abnormalities are detected, it triggers alerts to medical staff and initiates necessary medical protocols.
3. Based on the analyzed data, automated adjustments to medical devices may be performed, such as modifying oxygen levels or administering medication through connected dispensers.
4. In critical conditions, the system automatically alerts emergency medical teams and provides detailed patient data to facilitate a rapid response.

Postcondition: Appropriate medical responses are executed.

- **Implementation**

To understand the implementational aspects of WoT, we need to delve into its ecosystem and the possible scenarios where Thing devices are connected and implemented. Figure 4 shows a schema diagram of the WoT ecosystem. The ecosystem contains various heterogeneous IoT devices, some of which can be connected to each other, allowing for direct communication and collaboration.

The devices can be implemented through edge or fog computing to optimize data processing and decision-making closer to the source of data generation, while others are implemented directly in the cloud for broader data analysis and storage. Some devices are owned by companies, indicating their integration into business operations, while others are owned by individuals. All devices are connected and controlled by WoT (i.e., a web browser), ensuring standardized interactions and seamless interoperability across this diverse device environment.

Figure 4. Schema diagram of the WoT ecosystem

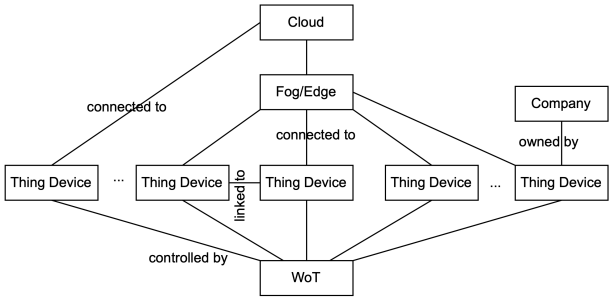

A notable example of WoT implementation is the Mozilla WebThing Gateway (Bolar, 2020), a smart IoT gateway that emphasizes interoperability and security. It plays a crucial role in connecting various IoT devices, allowing them to communicate and interact effectively in a standardized manner. The gateway serves as the central point of interaction for devices in the WoT network, resembling the Node class in our pattern.

- **Known Uses**

This section highlights real-world applications of the WoT, illustrating its practical utility and adaptability in addressing complex challenges across various domains. These examples provide insights into how the WoT pattern enhances functionality, interoperability, and efficiency in diverse IoT systems.

One example is Greenhouse Horticulture, which utilizes various sensors and facilities (such as heaters, CO2 generators, and sheet controllers) connected to a gateway and managed via the cloud. This system employs WoT architecture and WoT TDs to optimize environmental conditions, including temperature, humidity, and CO2 concentration, for plant growth. It demonstrates the application of WoT in agricultural technology (Matsukura and Kamiya, 2019).

Another example is in education, where an IoT remote lab enables students to interact remotely with various IoT devices as part of a practical course (Korkan, 2020). This setup includes robotic arms, conveyor belts, motorized sliders, and sensors for atmospheric data. The course allows students to build mashup applications, deepening their understanding of WoT technologies. These applications leverage the WoT TD and Scripting API, providing hands-on experience in controlling physical devices and verifying actions via video streams. This UC emphasizes the importance of standardized resource sharing in educational settings (Steinhorst and Korkan, 2020).

Lastly, the Eclipse Thingweb Project leverages W3C WoT standards to create IoT solutions that are both scalable and interoperable.

Key features of this implementation (Eclipse Foundation, ThingWeb) include:

1. Device Description: Utilizing standardized formats to describe device information, capabilities, and data schemas. This ensures that devices can be understood and managed consistently across different systems.
2. Device Integration: Providing connectivity for devices via various IoT protocols under a uniform interface. This approach enables diverse devices to communicate effectively, regardless of their underlying protocols.
3. Device Description Validation: Ensuring consistent metadata for devices across directories, which is crucial for maintaining the accuracy and reliability of device information.
4. Application Development: Offering a web browser-like runtime for developing portable IoT applications. This feature allows developers to create flexible, headless applications suited for various IoT scenarios.
5. Other Services: Including several libraries, tools, and services such as node-wot for building IoT devices, a playground for TD validation, and Online Things for simulating IoT devices. This project provides a comprehensive set of tools for developers to build interoperable IoT solutions while maintaining flexibility in their development choices.

- **Consequences**

This pattern provides the following advantages:

1. Compatibility: Utilizing TDs as a uniform interface allows devices with different models and versions to interact without direct compatibility issues.
2. Scalability: Employing the Node as a central point to manage connections and data flow between a vast number of Thing devices enables the system to scale effectively. By offloading device management and communication handling to Nodes, which are designed to efficiently process and route messages across the network, the architecture supports a growing ecosystem.
3. Interoperability: Leveraging Binding Templates alongside WoT TDs defines how devices communicate over various protocols. This setup ensures that devices can not only exchange data but also interpret and act on the information received, regardless of the underlying communication standards.
4. Discoverability: Implementing dynamic discovery mechanisms within the WoT Node allows it to automatically detect new devices and their services based on their TDs. This facilitates the seamless addition and integration of devices into the ecosystem, enhancing system responsiveness and user experience.
5. Security: Integrating security protocols directly into TDs and enforcing them through the Node ensures robust system protection. This includes specifying authentication mechanisms, data encryption methods, and access control policies within TDs, ensuring all interactions with and between devices adhere to predefined security standards.

- **Related Patterns**

1. Cloud Ecosystem Pattern (Syed and Fernandez, 2018): Illustrates the dynamic interaction between IoT devices and various components of ecosystem patterns within the cloud infrastructure.
2. Gateway Pattern for Integrated IoT Systems (Tekinerdogan and Köksal, 2018): Presents several gateway patterns integrated into IoT systems, including one focused on web services.
3. Design Patterns for the Industrial Internet of Things (IIoT) (Bloom *et al.,* 2018): Describes communication protocols for IIoT applications.
4. An Ontology Design Pattern for IoT Device Tagging System (Charpenay *et al.,* 2015).
5. A Pattern for Secure IoT Thing (Fernandez *et al.*, 2007): Presents a pattern for adding security to IoT devices.

5. Comparative Analysis

In this section, we present a detailed comparative analysis to examine the key components that play pivotal roles in the WoT architecture , specifically focusing on API, Node, Thing, TD, Thing Discovery, and Binding Template. This focused approach enables a direct comparison of how each architecture incorporates and supports these essential elements, highlighting areas where our architecture provides significant improvements or novel contributions.

As shown in Table 1, our architecture offers a more robust and flexible API, capable of supporting a diverse range of protocols and data formats, compared to the basic or RESTful-focused APIs in other architectures. The Node component, which is largely undefined in other works, is a key feature of our architecture. It enables sophisticated network operations and local data processing, which are crucial for real-time IoT applications.

Moreover, our architecture enhances the management and interoperability of Things by providing advanced features for autonomous operations and dynamic, detailed descriptions. This ensures seamless integration and operability within IoT ecosystems, representing a significant advancement over the simpler object management and static descriptions seen in the compared frameworks.

Additionally, the automated Thing Discovery mechanisms in our architecture support dynamic IoT environments, in contrast to the manual or socially enhanced methods in earlier models. Furthermore, the Binding Template in our architecture supports a variety of communication protocols, offering greater adaptability than the more limited implementations found in other studies.

Table 1. Comparison of the proposed architecture with the existing architecture

Architectural Component	Our Architecture	Guinard *et al.,* (2010)	Zhang *et al.,* (2012)	Guinard (2011)	Mainetti *et al.,* (2015)
API	API for device management and data interaction	RESTful API for basic device interaction	RESTful APIs integrated with social networking features	RESTful API focusing on device interaction	Limited API scope focused primarily on device discovery
Node	Node for managing network communication and processing	Not explicitly defined	Not explicitly defined	Not explicitly defined	Focus on virtualizing devices outside their physical network
Thing	Thing management with communication and control features	Basic smart Things integration	Enabled Things with limited control features	Basic Thing management	Basic Thing integration without extensive management features
Thing Description	Thing descriptions to facilitate interoperability and automation	Basic static description	Descriptions integrated with social profiles	Structured descriptions for application development	Not emphasized
Thing Discovery	Discovery mechanisms with support for dynamic environments	Discovery mechanisms based on RESTful services	Enhanced discovery through social interactions	Not emphasized	Advanced discovery mechanisms for virtualized environments
Binding Template	Templates supporting multiple protocols and data formats	Basic binding using web standards	Moderate binding capabilities with a focus on web integration	Not explicitly defined	Not emphasized

6. Conclusions and Future Works

This research presents an architectural pattern for the WoT, an area that has, until now, lacked precision in its modeling approach. The framework developed here not only aligns with the intricate requirements of the WoT environment but also enhances its interoperability and efficiency. The architecture proposed in this study is intended to serve as a foundational guide for future WoT architectures, providing a replicable and scalable approach for integrating the vast array of IoT devices into the web ecosystem. Additionally, the pattern lays the groundwork for creating a comprehensive RA for the IoT/WoT ecosystem.

Biography

Khalied M. Albarrak

Department of Management Information Systems College of Business Administration, King Faisal University, Al-Ahsa, Saudi Arabia, 00966135895800, kalbarrak@kfu.edu.sa

Dr. Albarrak, an Assistant Professor in the MIS department at King Faisal University, holds a B.Sc. in Computer Science (2009) from King Faisal University, an M.Sc. from King Abdullah University of Science and Technology (2012), and a Ph.D. from the University of Southampton (2019). His research areas include web sciences, open data, data analytics, artificial intelligence, e-governance, and digital transformation.

ORCID: 0000-0001-9224-5926

Acknowledgment

This study could not have been initiated or completed without the encouragement and continued support of King Faisal University.

References

Achirei, S.D., Zvoristeanu, O., Alexandrescu, A., Botezatu, N.A., Stan, A., Rotariu, C. and Caraiman, S. (2020). Smartcare: On the design of an IoT-based solution for assisted living. In: *International Conference on e-Health and Bioengineering (EHB),* **n/a**(n/a), 1–4. IEEE. DOI: 10.1109/EHB50910.2020.9280185

Alnaim, A.K. (2022). Misuse patterns from the threat of modification of non-control data in network function virtualization. *Future Internet*, **14**(7), 201. DOI: 10.3390/fi14070201

Alnaim, A.K., Alwakeel, A.M. and Fernandez, E.B. (2019). A Pattern for an NFV virtual machine environment. In: *13th Annual IEEE International Systems Conference*, **n/a**(n/a), 1–6. IEEE. DOI: 10.1109/syscon.2019.8836847

Alnaim, A.K., Alwakeel, A.M. and Fernandez, E.B. (2022). Towards a security reference architecture for NFV. *Sensors*, **22**(10), 3750. DOI: 10.3390/s22103750

Alwakeel, A.M., Alnaim, A.K. and Fernandez, E.B. (2019a). A Pattern for a virtual network function (VNF). In: *14th International Conference on Availability, Reliability and Security (ARES)*. 1–7. Canterbury, UK. DOI: 10.1145/3339252.3340519

Angelov, S., Grefen, P. and Greefhorst, D. (2012). A framework for analysis and design of software reference architectures. *Information and Software Technology*, **54**(4), 417–31. DOI: 10.1016/j.infsof.2011.11.009

Avgeriou, P. (2003). Describing, instantiating and evaluating a reference architecture: A case study. *Enterprise Architecture Journal*, **3**(n/a), 1–24.

Bloom, G., Alsulami, B., Nwafor, E. and Bertolotti, I.C. (2018). Design patterns for the industrial Internet of Things. In: *14th IEEE International Workshop on Factory Communication Systems (WFCS)*, **n/a**(n/a), 1–10. DOI: 10.1109/wfcs.2018.8402353

Bolar, T. (2020, August 18). *Web of things Over IOT and its Applications*. *InfoQ*. Available at: https://www.infoq.com/articles/web-of-things-iot-apps/ (accessed on 30/11/2024).

Buschmann, F., Meunier, R., Rohnert, H., Sornmerlad, P. and Stal, M. (2001). *Pattern-Oriented Software Architecture: A system of Patterns*. Volume 1. Wiley.

Charpenay, V., Kabisch, S., Anicic, D. and Kosch, H. (2015). An ontology design pattern for IoT device tagging systems. In: *5th International Conference on the Internet of Things (IOT)*, **n/a**(n/a), 138–45. DOI: 10.1109/iot.2015.7356558

Cloutier, R., Muller, G., Verma, D., Nilchiani, R., Hole, E. and Bone, M. (2009). The concept of reference architectures. *Systems Engineering*, **13**(1), 14–27. *Portico*. DOI: 10.1002/sys.20129

Eclipse Foundation (n/a). *Eclipse ThingWeb*. Available at: https://thingweb.io/ (accessed on 30/11/2024).

Fernandez, E.B. and Hamid, B. (2015). A pattern for network functions virtualization. In: *20th European Conference on Pattern Languages of Programs*, **n/a**(n/a), 1–9. DOI: 10.1145/2855321.2855369

Fernandez, E., Pelaez, J. and Larrondo-Petrie, M. (2007). Attack patterns: A new forensic and design tool. *Advances in Digital Forensics III*, **n/a**(n/a), 345–57. DOI: 10.1007/978-0-387-73742-3_24

Fernandez, E.B. (2013). *Security Patterns in Practice: Designing Secure Architectures Using Software Patterns*. John Wiley and Sons. DOI: 10.5555/2531565

Guinard, D. (2011). *A web of Things Application Architecture: Integrating the Real-World into the Web*. PhD Theiss, ETH Zurich. DOI: 10.3929/ethz-a-006713673

Guinard, D., Trifa, V. and Wilde, E. (2010). A resource-oriented architecture for the Web of Things. In: *Internet of Things (IOT)*, **n/a**(n/a), 1–8. DOI: 10.1109/iot.2010.5678452

Hashizume, K., Fernandez, E.B. and Larrondo-Petrie, M.M. (2012). A Pattern for Software-as-a-Service in Clouds. In: *ASE/IEEE International Conference on Biomedical Computing (BioMedCom)*, **n/a**(n/a),140–4. DOI: 10.1109/biomedcom.2012.29

Korkan, E. (2020). *Wot-Architecture Use Cases: Shared Devices*. Available at: https://github.com/w3c/wot-architecture/blob/main/USE-CASES/education.md (accessed on 30/11/2024).

Lagally, M., Matsukura, R., McCool, M., Toumura, K., Kajimoto, K., Kawaguchi, T. and Kovatsch, M. (2023). Web of things (WoT) architecture 1.1. *PR-wot-architecturell-202307111*.

Mainetti, L., Mighali, V. and Patrono, L. (2015). A software architecture enabling the web of things. *IEEE Internet of Things Journal*, **2**(6), 445–54. DOI: 10.1109/biomedcom.2012.29

Manta-Caro, C. and Fernández-Luna, J.M. (2024). IR.WoT: An architecture and vision for a unified web of things search engine. *Sensors*, **24**(11), 3302. DOI: 10.3390/s24113302

Matsukura, R. and Takuki, K. (2019). *Smart Agriculture: Greenhouse Horticulture*. Available at: https://github.com/w3c/wot-architecture/blob/main/USE-CASES/smart-agriculture.md (accessed on 30/11/2024).

Nedeltcheva, G.N. and Shoikova, E. (2017). Models for innovative IoT ecosystems. In: *International Conference on Big Data and Internet of Thing*. DOI: 10.1145/3175684.3175710

Pankowska, M. (2015). Stakeholder Oriented Enterprise Architecture Modelling. In: *12th International Conference on E-Business (ICETE15)*, **n/a**(n/a), 72–79. DOI: 10.5220/0005544700720079

Steinhorst, S. and Ege, K. (2020). *IoT Remote Lab*. Available at: (https://campus.tum.de/tumonline/ee/ui/ca2/app/desktop/#/slc.tm.cp/student/courses/950504601?$ctx=lang=en&$scrollTo=toc_overview&$scrollto=toc_overview (accessed on 30/11/2024).

Syed, M.H. and Fernandez, E.B. (2016). A pattern for a virtual machine environment. In: *The 23rd Conference on Pattern Languages of Programs*, **n/a**(n/a), 1–8. DOI: 10.5555/3158161.3158172

Syed, M.H. and Fernandez, E.B. (2018). A reference architecture for the container ecosystem. In: *The 13th International Conference on Availability, Reliability and Security*, **n/a**(n/a), 1–6. DOI: 10.1145/3230833.3232854

Syed, M.H., Fernandez, E.B. and Ilyas, M. (2016a). A Pattern for fog computing. In: *The 10th Travelling Conference on Pattern Languages of Programs*, **n/a**(n/a), 1–10. DOI: 10.1145/3022636.3022649

Tekinerdogan, B. and Köksal, Ö. (2018). Pattern based integration of internet of things systems. In: *Internet of Things–ICIOT 2018: Third International Conference, Held as Part of the Services Conference Federation, SCF 2018, Seattle, WA, USA, Springer International Publishing*, **3** (n/a). 19–33. DOI: 10.1007/978-3-319-94370-1_2

ThingWeb. (n/a). *Eclipse ThingWeb: Web of Things Components*. Available at: https://www.thingweb.io/ (accessed on 30/11/2024).

Zhang, C., Cheng, C. and Ji, Y. (2012). Architecture design for social web of things. In: *1st International Workshop on Context Discovery and Data Mining (ContextDD '12)*, **n/a**(n/a), 1–7. DOI: 10.1145/2346604.2346608

Scientific Journal of King Faisal University:
Basic and Applied Sciences

Using Order Texture Statistics to Classify Multi-Class Malware

Raaed Fadhil Mohammed
Department of Accounting, College of Administration and Economics, University of Mustansiriyah, Baghdad, Iraq

LINK	RECEIVED	ACCEPTED	PUBLISHED ONLINE	ASSIGNED TO AN ISSUE
https://doi.org/10.37575/b/sci/240048	05/11/2024	21/01/2025	21/01/2025	01/06/2025

NO. OF WORDS	NO. OF PAGES	YEAR	VOLUME	ISSUE
6525	7	2025	26	1

ABSTRACT

The most significant challenge in the security of information and communication networks is the escalating number of malware types, followed by the search for appropriate methods to protect systems against them, which is one of the most critical concerns of programmers and information security specialists, along with the prompt recognition and identification of methods to combat malicious effects, such as malware. The purpose of this study is to use static and dynamic analytic approaches, as well as first- and second-order texture statistics, to detect and classify multi-class malware. The most important conclusions reached were that the order texture statistics approach provides better results than traditional methods (decision tree algorithm and naïve Bayes algorithm) in terms of improving precision, detection rate and false alarm rate, indicating the algorithm's efficacy in cyberattack detection systems.

KEYWORDS
statistics approach, naïve Bayes, decision tree, cyberattack, static analysis, machine learning

CITATION
Mohammed, R. F. (2024). Using order texture statistics to classify multi-class malware. *Scientific Journal of King Faisal University: Basic and Applied Sciences*, **26**(1), 13–19. DOI: 10.37575/b/sci/240048

1. Introduction

In recent years, one of the most significant challenges in the security of information and communication networks has been the escalating number of malware types, followed by the search for appropriate methods to protect systems against them, which is one of the most important concerns of programmers and information security specialists. Malware consists of viruses, worms, trojans, adware, spyware and ransomware that disrupt system function, spy, steal private information and constitute a hazard to users and operating systems (Dutta *et al.*, 2022). Malware is increasing at an alarming rate, prompting computer security specialists to develop new methods for protecting computers and networks. The builders of computer viruses utilise polymorphic strategies to create viruses with mutable internal structures. A popular technique for detecting malware is to compare the signature of the studied file to the signature of known dangerous programs (Aslan and Samet, 2020).

Nevertheless, this technique is ineffective in identifying unknown or novel malware types. Hence, traditional methodologies, including static and dynamic analysis, are used. Static analysis analyses malware without executing it and disassembles the code to find unusual actions. Typically, static analysis recovers opcodes. That indicates code functionality, function calls performed by executables or dangerous API call sequences, while dynamic analysis executes the code in a controlled environment to detect malicious behaviour. Dynamic analysis looks for system calls made by malicious programs, negative file actions, registry modification records or suspicious networks. Both static analysis and dynamic analysis are used to detect malware (Han *et al.*, 2019).

In the topic of virtual security, to create security in a computer system, intrusion detection systems (IDS) are required, in addition to firewalls and other intrusion prevention equipment, so that if an intruder gets past the firewall, antivirus and other security equipment and intrudes the system, it can be diagnosed, and a solution can be devised to deal with it. There are three ways to categorise IDS: detection technique, architecture and a response to an incursion. Methods of intrusion detection include the detection of anomalous activity and misuse (signature-based detection). There are several architectures for IDS, which may be roughly categorised into three groups: host-based, network-based and distributed IDS (Singh and Singh, 2014). In this paper, we used detection systems for computer network attacks, focusing on multi-class malware classification using order texture statistics to improve effectiveness. We used the min–max ascending method to evaluate the KDD-Cup99 dataset and analyse the accuracy of network attack detection based on device characteristics. This paper aims to examine the features of multi-class malware and identify them using first- and second-order texture statistics methods. In addition, the accuracy of multi-class malware detection is also expected to be improved compared to traditional methods, such as decision tree (DT) and naïve Bayes (NB) algorithm.

2. Order Texture Statistics

Order statistics refer to the statistics obtained from the ordered values of a sample; they are instrumental in non-parametric statistics and fundamental in various statistical analyses. Moreover, order statistics help in analysing life data and failure times; the distribution of order statistics can be derived from the parent distribution of the sample. Order texture statistics are used in image processing and computer vision to analyse and characterise textures within images; these statistics can be categorised into different orders based on the complexity of the statistical measures (Arsenault *et al.*, 2011).

2.1. First-Order Statistics

These involve basic measures, such as mean, variance and histogram of pixel intensities. They do not consider the spatial relationship between pixels. The first-order statistic or smallest-order statistic is always the minimum of the sample, that is, $X_{(1)} = \min\{X_1, \ldots, X_n\}$.

2.2. Second-Order Statistics

These include measures such as the co-occurrence matrix, which captures the frequency of pixel pairs with specific values occurring at a certain distance and orientation. It helps in understanding the texture's spatial structure. Similarly, for a sample of size n, the nth-order statistic (or largest-order statistic) is the maximum, that is, $X_{(n)} = max\{X_1, \ldots, X_n\}$ (Hung *et al.*, 2019).

Corresponding author: Raaed Fadhil Mohammed 00964 7727597446, raad@uomustansiriyah.edu.iq

2.3. Higher-Order Statistics

These involve more complex relationships between three or more pixels. They can capture intricate patterns and are useful for more detailed texture analysis. For $X_1, \ldots, X_n$ iid continuous random variables with P.D.F (f) and C.D.F (F), the density of the order statistic (k^{th}) is as follows (Arsenault *et al.*, 2011):

$$f_{(k)}(x) = nf(x)\binom{n-1}{k-1} F(x)^{k-1}\,(1-F(x))^{n-k} \quad (1)$$

To assess the performance of the order texture statistics algorithm and verify its correctness, we used the evaluation criteria outlined below.

TP: This is the number of correctly recognised features.

TN is the number of wrong features that are correctly recognised.

FP: It is the number of correct features that are incorrectly recognised as false.

False negative (FN): This is the number of false features that are falsely recognised as correct.

FN is the case where something is mistakenly classified as negative even though it is positive. In simpler terms, it is a case where a test incorrectly identifies a condition as absent when it is present.

Accuracy: It is the ratio of the number of correctly classified samples to all samples, which is calculated using the following equation:

$$Accuracy = \frac{TP + TN}{TP + FP + FN + TN} \quad (2)$$

Precision: It is the ratio of correctly classified positive samples to all available positive samples.

$$Precision = \frac{TP}{TP + FP} \quad (3)$$

Recall: It is the proportion of positively identified samples to the total number of positive samples. It should be noted that some of the samples that have been diagnosed as positive are wrong and included in the FN collection (Viswanath and Krishna, 2021).

$$Recall = \frac{TP}{TP + FN} \quad (4)$$

2.4. NB

NB, a highly adaptable probabilistic machine-learning algorithm, demonstrates remarkable efficacy across a diverse spectrum of classification tasks. From filtering spam and unwanted messages to categorising documents and predicting sentiment, this algorithm consistently delivers precise outcomes. Its robust foundation in Bayes' theorem empowers it to accurately assess the likelihood of a hypothesis based on available evidence, making it a valuable tool for various applications. According to Bayes' theorem, the posterior probability distribution is given this way:

$$P(\alpha|\beta) = \frac{P(\beta|\alpha).P(\alpha)}{P(\beta)} \quad (5)$$

The probability of (β), given that (α) is true, is denoted as $P(\beta|\alpha)$. $P(\alpha)$ and $P(\beta)$ represent the independent probabilities of (α) and (β). Assuming attributes are conditionally independent given the class, for attribute value data, this assumption results in the following:

$$P(\beta|\alpha) = \prod_{i=1}^{n} P(\beta_i|\alpha) \quad (6)$$

This is where (β_i) is the value of (i^{th}) attribute in (β), and (n) is the number of attributes.

$$P(\beta) = \prod_{i=1}^{k} P(c_i).P(\beta|c_i) \quad (7)$$

This is where (k) is the number of classes and (c_i) is the (i^{th}) class. Formula (1) can be calculated by normalising the numerators on the right-hand side of the equation (Webb *et al.*, 2010).

2.4.1. NB Classifier

The NB classifier is a probabilistic model based on Bayes' theorem. It assumes that all features are independent (hence 'naïve'). Despite this assumption, it performs remarkably well in many applications, particularly text classification. The classifier works by calculating the probability that a given feature set belongs to a particular class and then chooses the class with the highest probability. It is fast, simple and efficient for large datasets. This makes it popular in spam filtering, sentiment analysis and recommendation systems. While it may not capture all complexities, its simplicity often leads to surprisingly accurate results. There are several variants of naive Bayes, including multinomial naive Bayes, Gaussian naive Bayes and Bernoulli naive Bayes. Each variant makes certain assumptions and works for different data types (Sammut and Webb, 2017).

2.5. DT

This non-parametric, supervised learning algorithm is handy for classification and regression tasks, allowing users to visualise the decision-making process clearly and intuitively. By structuring data in this hierarchical format, DTs facilitate the identification of optimal choices based on available information. This approach enhances transparency and encourages informed decision-making, making it a valuable asset in numerous fields (Pathak *et al.*, 2018).

The fundamental structure of a DT consists of three key elements: nodes, branches and leaves, where the root node serves as the starting point, representing the initial decision or question. From there, branches extend to possible outcomes, creating a pathway for each potential decision. Each branch leads to additional nodes, which further dissect data until reaching the terminal or leaf nodes. Leaf nodes signify the final decision or classification, indicating the end of the decision-making process (Song and Ying, 2015).

DTs can be categorised into two primary types: classification trees and regression trees. Classification trees are designed to address classification-type problems, where the objective is to assign a category or label to a given input. In contrast, regression trees focus on prediction-type problems, aiming to forecast continuous outcomes. The key difference between these two types lies in how they split data; classification trees utilise Gini impurity error calculations, while regression trees employ mean squared error as their impurity metric. This distinction is crucial because it determines the appropriate application of DTs depending on the problem at hand and demonstrates their versatility in data analysis (Loh, 2011).

The DT algorithm decisively categorises a large volume of records into smaller groups using simple decision rules. This process yields a tree structure with distinct leaf nodes and decision nodes. Applying the information gain theory, the DT algorithm effectively identifies the attribute that best segregates the dataset. Information (Y) is then calculated using the following formula (8):

$$Y = \sum_{i=1}^{n} P(x_i) log_2\, P(x_i) \quad (8)$$

Formula (8) is a measure of impurity or randomness in a dataset and determines how well a feature (or attribute) divides the data. Lower values indicate more informative splits, which helps create more accurate DTs. The underlying principles behind DTs are much easier

to understand and interpret than other complex machine-learning algorithms (Ullah *et al.*, 2020).

2.6. World Wide Web

The World Wide Web functions as a database managed by humans to store and exchange vast amounts of information. However, it differs from conventional databases in its breadth, rapid dynamism and diversity. Moreover, its vast size makes it impossible to determine or measure it accurately; the number of pages is not restricted, and the data submitted by a user determine their content. Another difficulty is the quick evolution of website content (Jacksi *and* Abass, 2019).

Online documents are diverse for many reasons. Websites may also include photographs, movies and audio files in various forms, which may range in size from one byte to hundreds of gigabytes. Different versions and pages with erroneous syntax that do not adhere to W3C standards but are, nonetheless, readable by web browsers may be found among the most prevalent HTML files. Online material is often unstructured, comprising several languages, styles and varying quality (Seneviratne and Hendler, 2023). Although HTML pages contain some information, they are often unreliable, except for a few specific sites. The web graph creates a single linked component if web links are considered undirected edges. Many network nodes are inaccessible from the remaining nodes; the graph nodes can be separated into five distinct sections. The following structure is specified in web pages, as shown in Figure 1 below. The central core — strongly connected component (SCC) — is the primary element and the largest component linked to the graph. Any node in SCC can be reached in a limited number of steps from any other node in SCC. In Broder's test, the size of the SCC is 50 MB, while the second largest associated component occupies only 150 KB of the page.

Figure 1. Bowie-Tie Web Structure Described in the Article

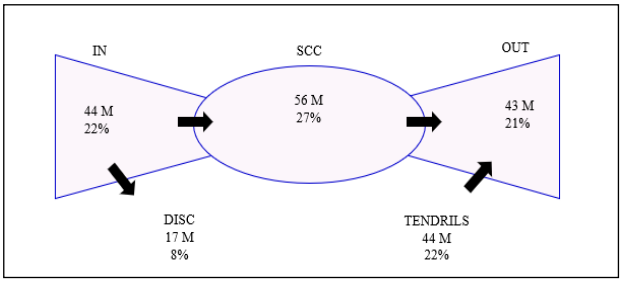

According to the given information, certain nodes are situated outside the SCC but can still be accessed through it. These nodes make up 22% of the entire graph and are categorised as both OUT and IN components. The remaining nodes can either be reached from the IN components and can also reach OUT, or they are not accessible from any of the previously mentioned nodes (DISC; Broder *et al.*, 2017).

2.7. Architecture of Web Search Engines

While the inner workings of commercial search engines remain largely confidential, it is widely believed that their overall architecture closely resembles the following diagram. This architecture comprises three distinct logical components: the browser downloads web pages to a local repository, the indexer performs operations on these pages and the query engine handles user queries using the data pre-processed and generated by the indexing process.

Researcher: Using hyperlinks, the crawler crawls the online graph and downloads newly identified pages; pages that have been downloaded are saved in a local repository. The primary obstacles in probe design are as follows:

Coverage: The crawler downloads as many pages as possible but does not permit website overhead; it also adheres to constraints that prohibit repeated queries.

Novelty: Invalid pages must be reloaded, pages that often change must be re-fetched and those that change seldom are rarely updated. The probe's mission is to simultaneously preserve freshness and coverage.

Indexing: To provide a search result in a fraction of a second, substantial precomputing is necessary. During the precomputation of various databases, indexes are built. The primary index includes the declaration list of all document IDs and their occurrence places for each word w. The notification list is parsed for each query term to provide a list of documents matching the query. This index is sometimes referred to as an inverted index since it represents a transliteration of the link between documents and words. The repository's documents are typically analysed and annotated concurrently with the index's construction. In addition to the primary index, databases and other indices are created, often utilised by the explorer or a ranking system (Arya, 2024).

2.8. Cyber Security

Cyber is a term derived from Cyberspace, which refers to the processes used to govern and regulate complex human or machine systems. Cyberspace is defined as a common delusion experienced daily by billions of operators and children who are taught mathematics. Others have characterised cyberspace as a collection of internal human conversations using computers and telecommunications equipment, independent of physical location (Azmi, 2019). It has been over three decades since the first communication on the World Wide Web, which was later renamed the Internet. Although the idea of a global village and the dominance of a particular culture over the entire world, known as globalisation, was an exaggeration, the development of communication and its rapid growth in a short period had positive outcomes. However, the negative impact on societies and the attempts of some forces to manipulate global opinion cannot be ignored. As a result of the evident danger posed by this dispersed power, several governments have attempted centralised control over such a chaotic network. In the past, the United States tried to restrict the use of cryptographic technology and control verbal communication through the Communications Decency Act and the Key Recovery Initiative, respectively. Many countries have imposed strict rules regarding these issues. However, internet users and stakeholders have strongly opposed these regulations, leading to conflicts. Cyberattacks can be defined in several ways, including illegal access to computers and data, as well as the malicious destruction of information systems, including hardware and software. Some examples of cyberattacks include spam, denial-of-service attacks and malware (Mishra *et al.*, 2022).

It is possible to identify, track and predict cyberattacks by analysing the massive volume of data collected from various sources to develop a cyber situational awareness system, where three basic subsystems of cyber assault comprehension, comprehension and visualisation are required, as seen in Figure 1. The terms *visualisation* and *prediction* are often used interchangeably, but it is important to note that these two concepts have distinct meanings. Forecasting involves making educated assumptions to predict future events, while visualisation is simply a way of representing what is currently happening or what has already happened. Forecasting is used to estimate future events with varying degrees of probability, while prediction forecasts specific future occurrences. This distinction is important because the future is not always certain and can be affected by random events (Ji *et al.*, 2019). The subsystem for comprehending cyber assaults collects signs and learns ideas. Without this subsystem, it is highly likely to develop an inaccurate picture of the cyber environment under command and control. This subsystem helps understand what is happening in the cyber

command and control area (Ding *et al.*, 2014).

Deception attacks are assaults during which the attacker's intention is to outsmart IDS using a method that is not detectable or recognisable. Network layer attacks: Network-layer attacks are carried out by modifying packet header values, such as TTL fields and packet control fields, or by breaking smaller packets. Transport layer attacks: Unauthorised users exploit protocol headers of the transmission layer, mainly TCP, to access targeted systems in this type of attack (Dipert, 2016). Denial-of-service attacks: IDS often have central logging servers that store notifications from the system. These servers are responsible for centralising alert data. However, if an intruder knows the IP address of the central register server, they may use a denial-of-service attack to slow it down or even shut it down completely. This can be dangerous, as the attack may remain hidden after the server is shut down because warning data are no longer being collected (Tan *et al.*, 2011).

3. Malware Identification Methods

Malware refers to malicious, harmful software. Cyber-attackers create malware to gain access to or harm a computer or internet network, and the victim of the assault is often unaware of its presence. Whenever malware infects a computer, it allows hackers to obtain unauthorised access to data, devices and systems. Malware was initially designed as cyber vandalism to crash computers, alter background images or gain access to personal information. However, in the hands of cybercriminals, it has become a tool for making money by stealing valuable information to blackmail businesses, hacking passwords to gain access to bank accounts or committing identity theft (Akhtar and Feng, 2022). Malware is available in several forms, such as backdoors, computer viruses, trojans, worms, cheats and logic bombs. Malware detection is difficult due to the variety of malware types and the technological tactics malware writers employ, such as encryption, obfuscation and dynamic programming. Hence, technologies such as extensive data machine learning are used to discover applications. In addition, ransomware is a sort of malware in which the malicious agent encrypts all or a portion of the victim's data and demands payment in return for the decryption key. With worldwide ransomware losses increasing, ransomware has become one of the most lucrative malware attacks for criminals (Butt *et al.*, 2010). Cyberattacks are primarily categorised into two types: targeted and non-targeted attacks. Targeted attacks are focused on a specific target, such as a particular organisation or equipment, while non-targeted attacks are opportunistic, targeting any organisation without adequate security. The speed of IDS is a significant challenge because attackers may have enough time to cause damage. Social media users generate the most data; an example is the average of 95 million photos and videos uploaded on Instagram daily. In addition, Facebook users publish an average of 510,000 comments and 293,000 status changes every hour. Other communication systems also produce vast quantities of data. With an average of 156 million emails sent each minute and 154,200 Skype calls per minute, social media users are not the only contributors to the surge in data generation. Old database systems cannot handle the massive amount and velocity of big data, so novel or improved versions of data processing algorithms are necessary. Big data comes in various forms and is rarely ready for direct analytics use. Therefore, preprocessing or staging is required to refine the massive data after data collection. Such preprocessing involves preparing a dataset for processing to make it worthwhile. These data are then used for further processing and analysis.

Statistical approaches, data mining, parallel algorithms, machine learning and soft computing are examples of data analysis techniques. The analytics application contains a query interface adapted to the needs of the application in question. This query interface functions as a dashboard that examines the data product the user wishes to create. The last step in processing is data visualisation. Visualisation entails generating visual summaries of data, which are the outcomes of information processing. This stage is regarded as the most crucial step in the process since the accurate comprehension of the data is related to their quantity, and the greater the volume of data, the more challenging it is to visualise and comprehend (Alani, 2021).

3.1. Capability-Based Malware Cyberattacks

Let x as be a Bernoulli variable that indicates the ability of the attacker to execute an attack a on the service $s \in S$. Mathematical hope $(E[X_{sa}])X_{sa}$ is calculated from the following conditional probability relation:

$$p(S|S_a) = \frac{E(S \cap S_a)}{E(S_a)} \quad (9)$$

To add the influence parameter to the above probability relation, we divide the services in the network into four types: services where the S_u attack failed, S_d services that have been discovered, services whose control s_p is partially controlled by the attacker and services whose control s_c is completely controlled by the attacker.

$$p(S|S_a) = \frac{E(S_u \cup S_d \cup S_p \cup S_c \cup S_a)}{E(S_a)} \quad (10)$$

For each service (S) and each attack (a), the credibility score $(p(s \mid S_a))$ and the reliability score (r) are calculated. A method is implemented for the network capability visualisation for each host, and this procedure begins by receiving the current attack rejection warnings (T Current), which also shows that the introduced algorithm is in real time. For all these warnings, the element that represents the target of the warning and the state change of that element S_a are stored as a binary set. To evaluate the capability of a component in a virtual environment of a cyber battle scene, the system refers to the history of attack rejections and extracts the attack rejections in which the desired component was present. Then, it calculates the ratio of the number of attack rejections in which this selected component was present and changes its state to the number of attack rejections that the desired part is a member of. This ratio serves as a measure of the desired component's capability and is calculated in a non-professional manner (Tan *et al.*, 2011).

3.2. Analysis of Problems

Using the right multi-objective, linear programming approach and the minimum–maximum climbing method, we examined and enhanced security to categorise malware, identify component behaviour during various attack diagrams and compare the resulting outcomes after explaining the software and database. In general, to solve physical problems, there are three methods:

1. exact solution method,
2. numerical method (numerical solution), and
3. experimental method.

In tackling engineering issues, numerical methods are among the most practical approaches. Among the benefits of the numerical solution over other methods are the following:

- The primary flaw of the laboratory techniques is that they are costly and time-consuming. In contrast, this is not the case with numerical solution methods.
- The exact solution approach cannot assess models with complicated geometry; in this sector, only numerical methods, particularly finite elements, are utilised.
- The exact solution cannot solve situations where boundary conditions are complex and standard numerical techniques are required.

MATLAB software was utilised in this study, enabling matrix computation and integration with other programming languages. Additionally, the MATLAB environment can be expanded by adding toolboxes for various purposes.

3.3. Dataset Description

The dataset was taken from the dependable KDD Cup 99 database, whose raw data consisted of 494,022 lines based on 40 distinct parameters examined for middleware, a particular attack. As the quantity of data is quite huge and its analysis with the intended system may be problematic, we analysed the number of 54,000 distinct modes based on the same 40 middleware characteristics to define the kind of attack. This data must clarify that eight different types of assaults are examined, whose names and the number attributed to them are presented in Table 1 (Viswanath and Krishna, 2021).

Table 1. Attacks Considered in the Database

Assigned number	Attack name
1	normal (no attack)
2	back
3	Ipsweep
4	ftp_write
5	nmap
6	smurf
7	neptune
8	multihup

3.4. Data Processing

Data preprocessing is a crucial step in preparing data for analysis, where the quality of preprocessing can significantly influence the results, potentially leading to the best or worst outcomes. Therefore, the preprocessing in this paper was carried out adhering to the following principles:

3.4.1. Elimination of Noise and Outliers

During data collection, some columns can be empty or contain illogical entries, such as question marks or Greek symbols. Identifying such anomalies is crucial in this phase. Since the dataset's target column (attack types), protocol type column (TCP, HTTP, FTP, etc.), service type (HTTP, FTP, etc.) and flag type (SF, REJ, S3, etc.) consisted of strings or words, MATLAB recognised them as noise or outliers, necessitating their conversion to a compatible format for the data.

3.4.2. Data Sorting

Data sorting is essential for the MATLAB program to understand and process information. In this research, the rows correspond to the different states of the network components under study, while the columns relate to the attributes associated with these states, facilitating the distinction between attack and non-attack types. Since MATLAB software solves numerically, all variables must be labelled numerically. During this phase, every feature from the first to the fortieth was listed, and the target column had eight modes (Numbers 1 to 8), of which seven were types of attacks, and one was expected, indicating that the middleware is not under assault. The classification of assaults is provided in Table 1.

After all of them were turned into numeric variables, we imported them into MATLAB. In addition, it is essential to note that since the data had varied scales, they had to be converted into a standard format:

$$\bar{x} = \frac{(x - xmin)(d_2 - d_1)}{xmax - xmin} + d_1 \qquad (11)$$

According to the data, $d_1 = 0$ and $d_2 = +1$ were selected. It can be observed that all the data are normalised in this standard interval. Data segmentation was done; 70% of the data was used to train the classifiers, while the remaining 30% was utilised to evaluate the model. To employ all the data for both objectives, these divisions were purely arbitrary. The (Randperm) function of the MATLAB program may generate a random index automatically, and the associated data are inserted in the appropriate matrices. Seventy per cent of the 54,000 lines of final data are 37,800. Therefore, 37,800 data lines were used to develop the classification model, while 16,200 non-educational data lines (30% of the original data) were used to test the model (Viswanath and Krishna, 2021).

4. Results and Discussion

In our research, we employed first-and second-order texture statistics to classify malware accurately. We used two additional techniques, the DT and the NB algorithm, to assess the effectiveness of the first- and second-order texture statistics (MILP). These techniques identify the type of attack using the mathematical connections established between malware classification and network attributes. The outcomes in Table 2 clearly show how feature extraction works well for malware classification using the MILP, DT and NB algorithms.

Table 2. The Evaluation Results of Feature Extraction With MILP, DT and NB algorithms

Algorithms	Parameter	Amount in the training phase	Amount in the test phase
First- and second-order texture statistics	TP	10292	4342
	TN	27508	11847
	FP	0	10
	FN	0	1
	Precision (%)	100	99.9321
	Recall (%)	100	99.977
	Accuracy (%)	100	99.7702
DT	TP	10288	4337
	TN	27508	11839
	FP	4	15
	FN	0	9
	Precision (%)	99.9894	99.8519
	Recall (%)	100	99.7929
	Accuracy (%)	99.9611	99.6553
NB	TP	10289	4346
	TN	27508	11838
	FP	3	6
	FN	0	10
	Precision (%)	99.9921	99.9012
	Recall (%)	100	99.7704
	Accuracy (%)	99.7909	99.8621

Figure 2 also shows the results of all three algorithms using a bar chart.

Figure 2. Comparison of the Results Obtained From the Performance of the Presented Algorithms

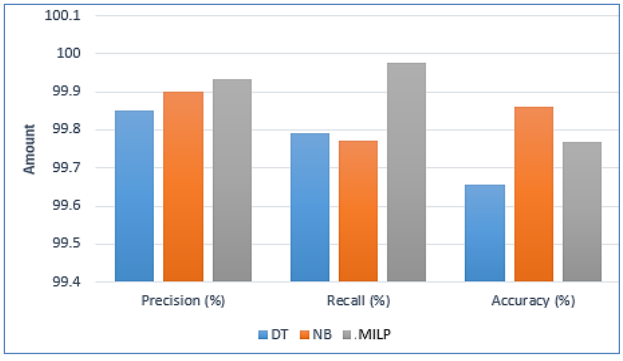

Additionally, this paper evaluated the maximum–minimum approach utilised in first- and second-order tissue statistics (MILP) with the most outstanding performance using the three criteria DR, FPR and AR, whose correlations are shown below.

DR = (the number of assaults accurately identified as attacks/number of attacks in the test dataset) x 100.

FPR = (the number of incorrectly categorised normal/total number of ordinary in the test database) x 100.

AR = (the number of accurate sample classifications/total number of samples in the test dataset) times 100.

The classification and evaluation performance of IDS improve with increasing DR and AR values and decreasing FPR values. Therefore, we checked the above criteria for the first- and second-order texture

statistics algorithms.

The acquired values for the aforementioned criteria are shown in Table 3.

Table 3. The Findings of the Maximum–Minimum Approach Used in the First- and Second-Order Texture Statistics Method

The number of features	DR	AR	FRP
5	95.214	94.323	2.689
10	98.632	97.6524	2.457
15	97.6587	96.02	2.021
20	99.021	97.874	2.3365
25	89.963	89.365	2.465
30	74.524	82.547	0.978
35	75.698	80.3321	2.0142
40	78.996	78.547	15.224

Based on the data, it was determined that as the number of features in this approach increases, the AR and DR criteria decrease, while the FPR criteria increase. This investigation was conducted using 40 parts, and it was discovered that the maximum DR and AR values were achieved by analysing 20 features because some characteristics have little bearing on selecting the sort of assault.

Now that the accuracy of the necessary approach to identify attacks has been defined, it is viable to detect network assaults and victims.

Table 4. A High and Low Impact Level Attack Scenario

Level	A high-impact level attack scenario		A low-impact level attack scenario	
	The address of the attacker	The address of the victim	The address of the attacker	The address of the victim
1	9.5.231.72	192.168.1.3	9.5.231.72	192.168.1.3
2	237.22.202.140	192.168.1.3	237.22.202.140	192.168.1.3
3	178.87.46.91	192.168.1.3	178.87.46.91	192.168.1.3
4	192.168.1.3	192.168.2.8	192.168.1.3	192.168.2.6
5	192.168.1.3	192.168.2.9	192.168.1.3	192.168.2.6
6	192.168.1.3	192.168.2.18	192.168.1.3	192.168.2.9
7	192.168.1.3	192.168.2.18	192.168.2.9	192.168.4.35
8	192.168.2.18	192.168.4.22	192.168.2.9	192.168.4.16
9	192.168.4.22	192.168.6.111	192.168.2.9	192.168.2.2
10	192.168.6.111	192.168.7.9	192.168.2.2	192.168.5.5

In Table 4 above, we provide two instances of assault scenarios with high and low degrees of effect. The stealthiness of an attack suggests that the attacker may have utilised many intermediary sites end routes to the victim, but the exploits of these hosts have not been uncovered. Our results showed that this combination, based on the belief transfer model, can achieve high accuracy against high-impact attacks, especially in networks with strict firewalls and limited services. Although low-impact attacks may undermine this approach, the belief transfer model is still effective.

The next table (Table 5) shows an attack scenario with a hidden parameter.

Table 5. An Attack Scenario with Stealth Parameter

Level	The address of the Attacker	The address of the victim
1	9.5.231.72	192.168.1.3
2	237.22.202.140	192.168.1.4
3	192.168.1.3	192.168.2.7
4	192.168.2.9	192.168.4.20

According to the assaults, based on the scenarios provided in Tables 4 and 5, the performance of each of the two techniques without and with the combination of capability and opportunity for attacks with various parameters was assessed. Rather than pinpointing the next target of an assault, the primary function of cyberattack visualisation systems is to produce a prioritised list of viewable targets. To specify method efficacy, we must examine the percentage of probability acquired for the attacked host one step before the assault.

5. Conclusions

- Using the maximum–minimum approach utilised in first- and second-order tissue statistics (MILP), three crucial method assessment criteria – DR, AR and FPR – were examined. A comparison of the findings revealed that the MILP approach is superior to the other methods, indicating the algorithm's efficacy in cyberattack detection systems.
- The NB algorithm, DT and the order texture statistics approach were compared, and it was found that the order texture statistics approach provided better results with improved precision, detection rate and false alarm rate.
- The findings indicate that combining capability and opportunity based on the belief transfer model has a high degree of accuracy against high-impact attacks in normal mode and is more effective when the network has a firewall with rigorous regulations and restricted auxiliary services.

6. Recommendations

- In the topic of virtual security, IDS are required – in addition to firewalls and other intrusion prevention equipment – to create complete security in a computer system so that if an intruder gets past the firewall, antivirus and other security equipment and invades the system, it can be diagnosed, and a solution can be devised to deal with it.
- Using enormous amounts of data, it will be necessary to examine the efficacy of architecture and the parameters incorporated in the confidence-meter algorithms at each step of the assault. Future concerns may include presenting algorithms to measure the influence of current and future scenarios and combining belief meter algorithms more effectively.

Data Availability Statement

The dataset used in this study is called KDD CUP 99, which contains various simulated intrusion attempts into a military network environment. It includes features such as connection duration, number of failed login attempts and type of service accessed. This dataset was used in the 5th International Conference on Knowledge Discovery and Data Mining; it is freely available on the Internet (https://kdd.ics.uci.edu/databases/kddcup99/kddcup99.html).

Acknowledgements

The author is grateful to the University of Mustansiriyah for its research facilities and to the Administration and Economic Faculty Laboratories and Science Faculty Laboratories (University of Mustansiriyah).

Conflicts of Interest

The author declares no conflict of interest.

Biography

Raaed Fadhil Mohammed

Department of Accounting, College of Administration and Economics, University of Mustansiriyah, Baghdad, Iraq, +964 7727597446, raad@uomustansiriyah.edu.iq

Raaed completed his Master of Science in Applied Statistics from the prestigious University of Baghdad. Currently, he serves as an assistant teacher in Iraq, where he has accumulated over 5 years of valuable experience in the fields of teaching and academia. His extensive expertise encompasses a diverse range of subjects, including mathematical statistics, computer science, neural networks, econometrics and predictive modelling. Raaed is passionate about educating others and contributing to the growth of knowledge in these areas.

ORCID ID: 0000-0002-7309-8702

References

Akhtar, M.S. and Feng, T. (2022). Malware analysis and detection using machine learning algorithms. *Symmetry*, **14**(11), 2304. DOI: 10.3390/sym14112304

Alani, M.M. (2021). Big data in cybersecurity: A survey of applications and future trends. *Journal of Reliable Intelligent Environments*, **7**(2), 85–114. DOI: 10.1007/s40860-020-00120-3

Arsenault, E., Yoonessi, A. and Baker, C. (2011). Higher order texture statistics impair contrast boundary segmentation. *Journal of Vision*, **11**(10), 1. DOI: 10.1167/11.10.14

Arya, U. (2024). Digital Tools for effective web searching. In: *Handbook of Digital Journalism: Perspectives from South Asia* (217–228). Singapore: Springer Nature Singapore. DOI: 10.1007/978-981-99-6675-2_19

Aslan, Ö.A. and Samet, R. (2020). A comprehensive review on malware detection approaches. *IEEE Access*, **8** (n/a), 6249–71. DOI: 10.1109/ACCESS.2019.2963724

Azmi, R. (2019, July). Revisiting cyber definition. In *European Conference on Cyber Warfare and Security,* (22–30). Academic Conferences International Limited. Available at: https://www.proceedings.com/content/049/049816webtoc.pdf (accessed on 13/12/2024)

Broder, A., Kumar, R., Maghoul, F., Raghavan, P., Rajagopalan, S., Stata, R. and Wiener, J. (2000). Graph structure in the web. *Computer Networks*, **33**(1-6), 309–20. DOI: 10.1016/S1389-1286(00)00083-9

Butt, U.J., Abbod, M.F. and Kumar, A. (2020). Cyber threat ransomware and marketing to networked consumers. In: *Handbook of Research on Innovations in Technology and Marketing for the Connected Consumer*, (155–185). IGI Global. DOI: 10.4018/978-1-7998-0131-3.ch008

Ding, Y., Dai, W., Yan, S. and Zhang, Y. (2014). Control flow-based opcode behavior analysis for malware detection. *Computers and Security*, **44** (n/a), 65–74. DOI: 10.1016/j.cose.2014.04.003

Dipert, R.R. (2016). The ethics of cyberwarfare. In: *Military Ethics and Emerging Technologies* (159–185). Routledge. DOI: 10.4324/9781315766843

Dutta, N., Jadav, N., Tanwar, S., Sarma, H.K.D., Pricop, E., Dutta, N. and Pricop, E. (2022). Introduction to malware analysis. *Cyber Security: Issues and Current Trends*, **995**, 129–41. DOI: 10.1007/978-981-16-6597-4_7

Han, W., Xue, J., Wang, Y., Huang, L., Kong, Z. and Mao, L. (2019). MalDAE: Detecting and explaining malware based on correlation and fusion of static and dynamic characteristics. *Computers and Security*, **83**(n/a), 208–33. DOI: 10.1016/j.cose.2019.02.007

Hung, C.C., Song, E., Lan, Y., Hung, C.C., Song, E. and Lan, Y. (2019). *Image Texture, Texture Features, and Image Texture Classification and Segmentation. Image Texture Analysis: Foundations, Models and Algorithms*, 3–14. Springer. DOI: 10.1007/978-3-030-13773-1_1

Jacksi, K. and Abass, S.M. (2019). Development history of the world wide web. *Int. J. Sci. Technol. Res*, **8**(9), 75–9. Available at: https://www.ijstr.org/final-print/sep2019/Development-History-of-The-World-Wide-Web.pdf (accessed on 13/12/2024)

Ji, L., Zhi, X., Zhu, S. and Fraedrich, K. (2019). Probabilistic precipitation forecasting over East Asia using Bayesian model averaging. *Weather and Forecasting*, **34**(2), 377–92. DOI: 10.1175/WAF-D-18-0093.1

Loh, W.Y. (2011). Classification and regression trees. *Wiley Interdisciplinary Reviews: Data Mining and Knowledge Discovery*, **1**(1), 14–23. DOI: 10.1002/widm.8

Mishra, S., Alotaibi, W.B., Alshehri, M. and Saxena, S. (2022). Cyber-attacks visualisation and prediction in complex multi-stage network. *International Journal of Computer Applications in Technology*, **68**(4), 345–56. DOI: 10.1504/ijcat.2022.125180

Pathak, S., Mishra, I. and Sweta Padma, A. (2018). An assessment of decision tree-based classification and regression algorithms. In: *2018 3rd International Conference on Inventive Computation Technologies (ICICT)* (92–95). IEEE. DOI: 10.1109/ICICT43934.2018.9034296

Sammut, C. and Webb, G.I. (2017). *Encyclopedia of Machine Learning and Data Mining*. Springer Publishing Company, Incorporated. Available at: https://link.springer.com/referencework/10.1007/978-1-4899-7687-1 (accessed on 13/12/2024)

Seneviratne, O. and Hendler, J. (Eds.). (2023). *Linking the World's Information: Essays on Tim Berners-Lee's Invention of the World Wide Web*. New York, USA: ACM Books. DOI: 10.1145/3591366

Singh, A.P. and Singh, M.D. (2014). Analysis of host-based and network-based intrusion detection system. *International Journal of Computer Network and Information Security*, **6**(8), 41–7. DOI: 10.5815/ijcnis.2014.08.06

Song, Y.Y. and Ying, L.U. (2015). Decision tree methods: applications for classification and prediction. *Shanghai Archives of Psychiatry*, **27**(2), 130. DOI: 10.11919/j.issn.1002-0829.215044

Tan, Y., Sengupta, S. and Subbalakshmi, K.P. (2011). Analysis of coordinated denial-of-service attacks in IEEE 802.22 networks. *IEEE Journal on Selected Areas in Communications*, **29**(4), 890–902. DOI: 10.1109/JSAC.2011.110419

Ullah, F., Javaid, Q., Salam, A., Ahmad, M., Sarwar, N., Shah, D. and Abrar, M. (2020). Modified decision tree technique for ransomware detection at runtime through API calls. *Scientific Programming*, **2020**(1), 8845833. DOI: 10.1155/2020/8845833

Viswanath, G. and Krishna, P.V. (2021). Hybrid encryption framework for securing big data storage in multi-cloud environment. *Evolutionary Intelligence*, **14**(2), 691–8. DOI: 10.1007/s12065-020-00404-w

Webb, G.I., Keogh, E. and Miikkulainen, R. (2010). Naïve Bayes. *Encyclopedia of Machine Learning*, **15**(1), 713–4. DOI: 10.1007/978-0-387-30164-8

Scientific Journal of King Faisal University:
Basic and Applied Sciences

Improvement and Application HPLC-UV Method for detecting of N-drugs in Pharmaceutical Formulations

Safanah M. Alkulaib, Ahmed O. Alnajjar and Esam M. Bakir
Department of Chemistry, College of Science, King Faisal University, Al Ahsa, Saudi Arabia

LINK	RECEIVED	ACCEPTED	PUBLISHED ONLINE	ASSIGNED TO AN ISSUE
https://doi.org/10.37575/b/sci/240055	19/12/2024	09/02/2025	09/02/2025	01/06/2025
NO. OF WORDS	**NO. OF PAGES**	**YEAR**	**VOLUME**	**ISSUE**
4095	5	2025	26	1

ABSTRACT

The ultraviolet-visible high-performance liquid chromatography (HPLC–UV) coupled method was developed to detect five pharmaceutical compounds: indapamide (INDP), clomipramine (CMI), promethazine HCl (PMH), lisinopril (LSP) and trifluoperazine HCl (TFPH). The mobile phase consisted of 70% acetonitrile and 30% water, ensuring specific retention times (tR) for each compound. Analytical validation parameters were calculated from a calibration curve, including sensitivity, limit of detection (LOD) and linearity of the method. The LOD values of N-drugs were calculated as 6.24 µM for INDP, 2.19 for CMI, 10.57 for PMH, 6.68 for LSP and 1.25 for TFPH. Peak deconvolution or spectral deconvolution of standard solutions of drug mixtures was used to separate overlapping peaks in a dataset and extract information about individuals. Chromatographic separation of the standard mixture of pure compounds achieved a good resolution (R_s), ensuring the effective separation of the mixture components. However, other mixtures did not achieve satisfactory resolution due to retention time interference. Overall, the HPLC–UV method demonstrated good sensitivity and selectivity for the detection of the chosen pharmaceutical compounds.

KEYWORDS
Chromatogram, deconvolution, limit of detection, pharmaceutical analysis, retention time, sensitivity

CITATION
Alkulaib, S.M., Alnajjar, A.O. and Bakir, E.M. (2025). Improvement and application HPLC-UV method for detecting of n-drugs in pharmaceutical formulations. *Scientific Journal of King Faisal University: Basic and Applied Sciences*, **26**(1), 20–4. DOI: 10.37575/b/sci/240055

1. Introduction

Pharmaceutical compounds containing nitrogen atoms (N-atoms) are used to treat various diseases. Indapamide (INDP) is prescribed to manage hypertension, while lisinopril (LSP) is used for heart failure (Goa *et al.*, 1997; Thomas, 1985). Promethazine HCL (PMH) is utilized to prevent nausea and vomiting associated with certain conditions (Shearer and Miller, 1976). Trifluoperazine HCl (TFPH) is employed to help reduce hallucinations (Vardanyan and Hruby, 2006). Clomipramine (CMI) is frequently prescribed for the treatment of obsessive–compulsive disorder (Van-Scheyen and Van-Kammen, 1979). Various analytical methods have been developed to determine the concentration of pharmaceutical compounds containing N-atoms in formulations. Bakir *et al.* developed a spectrofluorometric method for assessing pharmaceutical compounds containing N-atoms, utilizing their rapid reaction with Eosin Y. The limits of detection (LODs) were found to be 2.07 µmol/L for INDP, 1.36 µmol/L for CMI, 3.02 µmol/L for PMH, 3.52 µmol/L for LSP and 2.09 µmol/L for TFPH (Alkulaib *et al.*, 2024). Reverse-phase high-performance liquid chromatography (RP-HPLC) was employed to quantify the concentration of INDP in oral antihypertensive tablets and bulk dosage forms. In a mobile phase consisting of a 60:40 ratio of methanol and phosphate buffer (pH: 5.8), the dynamic range for INDP was 0.2–1.2 µg/mL, with an R^2 value of 0.999 (Agrawal, 2021). A simultaneous quantification of CMI and its active metabolite in plasma was performed using a liquid chromatography coupled with mass spectrometry technique (Mohiuddin *et al.*, 2021). Solid-phase extraction, combined with ultra-performance liquid chromatography, was employed to detect perindopril (PP) and INDP (IP) in human plasma, with a LOD of 8.6 ng/mL for INDP (Palakeeti *et al.*, 2021). CMI and its major N-demethylated and hydroxy metabolites were detected in ng/ml using a sensitive ultraviolet-visible high-performance liquid chromatography (HPLC–UV) coupling method. The method employed a modified column to separate the compounds from the plasma. A mobile phase consisting of 10 mM K_2HPO_4, acetonitrile and methanol in a 35:25:40 v/v/v ratio was used (Pirola *et al.*, 2002). LSP and amlodipine (AML) were detected in solid tablet forms using an RP-HPLC method. The methodology achieved speed, cost-effectiveness, short response time and high resolution (Pawar *et al.*, 2021). An HPLC–UV coupled system with a modified column was used to detect TFPH and its photodegradation products. The mobile phase consisted of acetonitrile, 2-tetrabutylammonium hydroxide and o-phosphoric acid in a ratio of 50.5:0.83:0.1 (v/w/w; Shetti and Venkatachalam, 2010). An HPLC-ACE 5 C18 analytical column (12.5 × 4.6 mm) was used to analyze perindopril, INDP (IND) and AML in the TRIPLIXAM® sample. The LODs were in the ppm concentration range (Özsar and Altınöz, 2024).

Therefore, the suggested methods aimed to detect N-drug concentrations in pharmaceutical formulations using the HPLC–UV coupled system. The chemical structures of chosen pharmaceutical compounds have primary, secondary and tertiary N-atoms. The LOD values were calculated to be 6.24 µM for INDP, 2.19 for CMI, 10.57 for PMH, 6.68 for LSP and 1.25 for TFPH. Peak deconvolution was used to separate the chromatogram graphs of the mixture standard solution of N-drugs. The vision of peak deconvolution provided an approach to accurately analyze and predict the separation resolution of N-drugs in complex mixtures. The resolution for certain mixtures of pure N-drug solutions in pharmaceutical compounds was below 1.5, indicating difficulties in effectively separating and accurately detecting the concentrations of pharmaceutical compounds within complex mixtures.

2. Experimental

2.1. Reagents and Instrument:

High-grade pharmaceutical compounds, such as INDP, TFPH, LSP, CMI and PMH, were received from Sigma Aldrich. HPLC-grade solvents were used in the experiments. INDP formula was used as Normalix SR 1.50 mg per tablet (Jazeera Pharmaceutical Industries, KSA), CMI as Anafranil 10 mg/tablet (Novartis, UK), PMH as Prometin syrup 5.0/5 ml (Kuwait Saudi Pharmaceutical Industries), LSP as Zestril 5 mg/g (Astra Zeneca, UK) and TFPH as Stellasil tablet 5mg.g^{-1} (Kahira

Corresponding Author: Esam M. Bakir 00966509725364, ebakir@kfu.edu.sa

Pharmaceuticals and Chemical Industries Company, Egypt), which were purchased from the medicine market in Saudi Arabia. An HPLC–UV coupled system (Agilent 1200 series, Waldbronn, Germany) with column (Zorbax Eclipse Plus C18, 50 × 2.1 mm ID, 1.8 µm) was used for determining the retention time (t_R) of the samples. Agilent ChemStation (Ver. B 4.0.2) software was used to monitor the signals.

A Stock solution of drugs (1000 µmmol L^{-1}) was prepared by dissolving the accurate weights of drugs in 10-ml organic solvents (methanol and ethanol); then, solutions of different concentrations (5.0–50 µmmol l^{-1}) of calibration plots were prepared from this stock solution.

Chromatographic conditions used a flow rate of 1.0 ml min^{-1}. The injection volume was 10 µl. UV absorption was at 252 nm or close to 255 nm. However, INDP and TFPH had a good absorbance at 240 and 255 nm, while CMI, PMH and LSP did not have a good absorbance at 218–255 nm. This indicates that CMI, PMH and LSP have smaller molar absorptivity in the solvent used. The experiments were conducted using a mobile phase composed of acetonitrile and water in a 70:30 (v/v) ratio. The runtime was set to 10 minutes and the column temperature was maintained at ambient conditions (24°C–26°C). The column was equilibrated with the mobile phase for 30 minutes before injecting the analyte. The pre-sample was filtered through a 0.45-µm membrane filter and degassed using sonication.

The robustness of the method was assessed to evaluate the effect of small, controlled variations in chromatographic conditions on drug determination. This was achieved by adjusting the mobile phase flow rate to 0.9 and 1.1 mL/min and modifying the acetonitrile concentration in the mobile phase to 68% and 72%.

Regarding the procedure for pharmaceutical formulation, five tablets were finely grounded using a mortar. A measured portion of the powder was dissolved and sonicated in methanol for 10 minutes. The solution was then centrifuged at 1800 rpm/5 min and the residue was filtered and then washed with methanol; then, the filtrate was diluted into 100 mL of methanol. For a syrup sample, the volume of 1.0 mL was diluted with methanol into 10 mL to prepare 0.1 mg/ml. The homogenous solution was obtained by sonication for 15 mins. A 10-µL aliquot of the solution was injected into the chromatograph.

2.2. Theoretical Considerations:

Retention time (t_R) refers to the duration a solute spends in the column. It depends on the interaction of the analyte with the stationary phase (Ahuja and Dong, 2005). The retention factor (k) is the relative ratio time of the solute spent in the stationary compared with mobile phases (see Eq. 1).

$$k = \frac{t_R - t_M}{t_M}, \qquad \text{Eq. 1}$$

Where the retention times (t_R) and (t_M) of analyte and mobile phases.

Column efficiency (N) expresses the theoretical layers per column (see Eq. 2.).

$$N = 5.545\left(\frac{t_R}{W_{0.5}}\right)^2 \qquad \text{Eq. 2}$$

Where (N) is theoretical layers (N/m), (t_R) is retention time and ($w_{0.5}$) is the half-height width of a peak (Jennings *et al.*, 1997; Robards and Ryan, 2021).

3. Results and Discussion

The mobile phase was selected based on the physicochemical properties of the pharmaceutical drugs to achieve optimal separation. Various solvent mixtures, including water and acetonitrile, were evaluated for their effectiveness. A mixture of acetonitrile and water was chosen as the mobile phase to provide the best resolution and a short runtime for the N-drugs (Beasley *et al.*, 2005; Chaudhary *et al.*, 2016; Hang *et al.*, 2006; Mostafavi *et al.*, 2010; Thumma *et al.*, 2008). The mobile phase composition was selected considering the clarity and symmetry of the peaks. The pharmaceutical compounds were successfully separated in 5 minutes using gradient elution with a mobile phase composed of 30% water and 70% acetonitrile. The selected wavelengths for the N-drugs were applied in the range of 200–440 nm (Beasley *et al.*, 2005; Chaudhary *et al.*, 2016; Hang *et al.*, 2006; Mostafavi *et al.*, 2010; Thumma *et al.*, 2008).

Table 1: LODs, LOQs and Precision of the Proposed Method (n = 5)

N-drugs	λ_{max}^{abs} (nm)	LOD	LOQ	Precision %RSD		Ref,
				Repeatability (%RSD)	Reproducibility (%RSD)	LOD
INDP	240.0	6.24	18.19	1.01	1.52	0.1 ppm (Özsar and Altınöz, 2024)
CMI	252.0	2.19	6.65	1.61	1.57	0.507 µg/ml (Vijayavaani et al., 2024)
PMH	255.0	10.57	32.04	0.55	0.55	10–100µg/ml (Pippalla et al., 2024)
LSP	218.0	6.68	20.26	4.07	4.70	1.11 µg/ml (Pawar et al., 2024)
TFPH	255.0	1.25	3.79	0.91	0.94	3.41µg/ml (Chauhan et al., 2024)

*** The concentration in µmol L^{-1}; recovery, RSD (%); replicate times, n = 5.**

3.1. Validation of the Analytical Method:

Linearity of the calibration curve: The linear range of observation was 5.0–50 µmmol.L^{-1} of N-drug solutions. The calibration graphs were plotted between the peak area vs. concentration (figure. 1) and the data are represented in table 1.

Figure 1: (a) HPLC Chromatogram and (b) Calibration Curve of 5.0–50 µmol L^{-1} Pharmaceutical Compounds in Ethanol and ACN:H_2O (70:30) at 1.0 mL/min With Selected Wavelengths

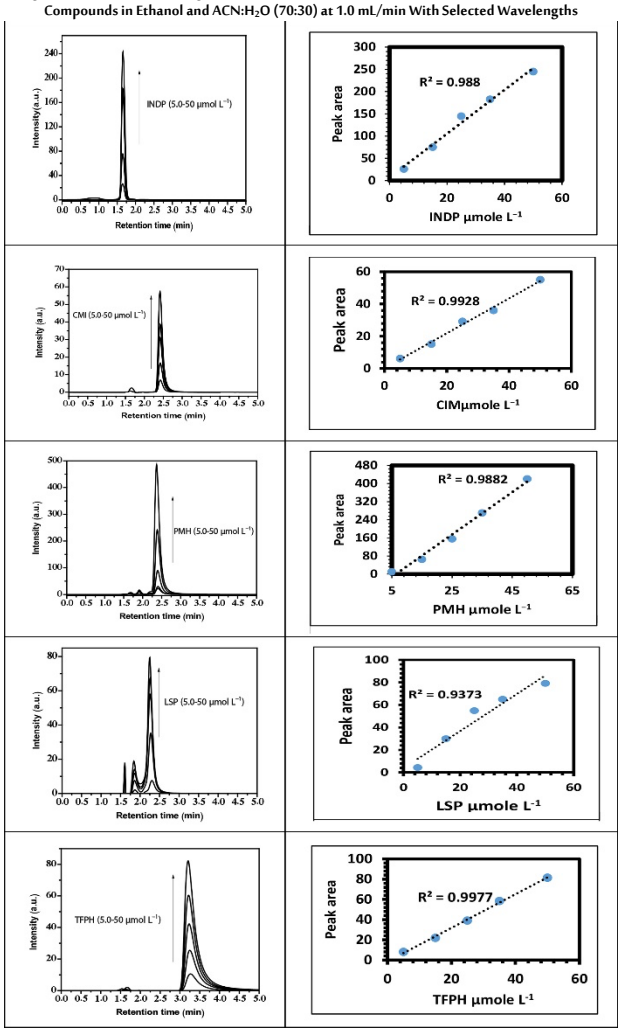

The LODs and limits of quantification (LOQs) were calculated as LOD

= 3.3σ/s and LOQ = 10σ/s, where (σ) is the standard deviation of peak area and (s) is the slope of the calibration curve.

Table 1 shows that the LOD values of N-drugs were calculated to be 6.24 µM for INDP, 2.19 for CMI, 10.57 for PMH, 6.68 for LSP and 1.25 for TFPH. The chemical structure and geometric positioning of the N-atom improved drug detection at low LODs by affecting molecular reactivity, polarity and detection system interactions. LSP showed a low LOD value due to the geometry of the N-atom in its primary, secondary and tertiary positions. Table 1 presents the reference methods for detecting N-drugs. Furthermore, the current method demonstrated good sensitivity.

To confirm that the method was suitable for sample analysis, a system suitability test was performed at optimized chromatographic conditions. The retention time, resolution (between adjacent peaks), peak symmetry and theoretical layers in the column were calculated (table 2). The effective column efficiencies were calculated as 97.37 for INDP, 103.32 for CMI, 86.57 for PMH, 61.45 for LSP and 56.61 for TFPH in the analysis of drug molecules. The column provided narrow, sharp peaks with excellent resolution. Furthermore, the low mobile phase consumption was achieved at 1.0 mL/min and 10.0 µL sample volume. The column efficiencies (N) are presented in Table 2, where the order of efficiency of CMI > INDP > PMH > LSP > TFPH was observed.

Table 2: The System Suitability for the N-Drugs

	INDP	CMI	PMH	LSP	TFPH
t_R(min)	1.65	2.42	2.40	2.30	3.24
Asymmetry S	0.29	0.06	1.4	1,2	0.07
Theoretical plates	1600	833	800	10	392
$W_{0.5}$	0.09	0.12	0.15	0.20	0.31
N	97.37	103.32	86.57	61.45	56.61

Accuracy, intraday and interday precision: For the pre-analyzed standard and sample solution, the standard solutions 30, 50 and 70 µmol L^{-1} were used. The %RSD values were 0.55%–1.61%, meeting the acceptable precision (UNODC., 2009,). The average % recoveries obtained for pure compounds were 97.90%–99.70%, while those of the pharmaceutical formulations were 82.93% and 100.03% for tablet and syrup dosage forms, which is within the acceptable range (Rao, 2018).

The robustness of the method was tested and no significant change in the retention time of N-drugs was observed when the composition and flow rate of the mobile phase were altered. The low %RSD values were below 0.05%, further confirming the robustness of the method.

The specificity of the method was examined in the presence of interferences. It is important to note that the chromatogram of the excipient solution showed no peaks, indicating that no interference from the excipients (additives in pharmaceutical formulation) was observed. The low LOD, LOQ, precision and recovery values demonstrated high sensitivity, accuracy and precision for determining N-drugs in standard solutions. Table 3 shows the good performance and acceptable levels for all the selected N-drugs. The chromatographic method achieved suitability and sensitivity.

Table 3: Results of the % Recovery Studies of the Developed HPLC Method (n = 5)

N-drugs (µmol L^{-1})	Pre-analyzed standard			Pre-analyzed tablet and syrup*		
	Spiked amount	Recovery (%)	Av. recovery ± SD (%)	Spiked amount	Recovery (%)	Av. recovery ± SD (%)
INDP	30.0	94.50	97.90 ± 4.30	30.0	81.47	84.89 ± 4.30
	50.0	96.50		50.0	83.49	
	70.0	102.70		70.0	89.70	
CIM	30.0	97.80	99.16 ± 1.60	30.0	98.1	99.46 ± 0.1.61
	50.0	98.70		50.0	99.0	
	70.0	101.0		70.0	101.3	
PMH	30.0	99.30	99.70 ± 0.55	30.0	99.61	100.03 ± 0.55
	50.0	99.50		50.0	99.84	
	70.0	100.35		70.0	100.65	
LSP	30.0	94.84	98.02 ± 3.99	30.0	79.75	82.93 ± 3.99
	50.0	96.75		50.0	81.66	
	70.0	102.49		70.0	87.40	
TFPH	30.0	98.79	99.53 ± 0.9	30.0	98.66	99.40 ± 0.91
	50.0	99.26		50.0	99.13	
	70.0	100.54		70.0	100.41	

***The concentration in µmol L^{-1}; recovery in %; mean ± SD; replicate times, n = 5.**

3.2. Analysis of the Mixture of N-drugs:

The difference in retention times between the two peaks divided by the combined widths of the elution peaks was used to measure the resolution of separation (see Eq. 3).

$$\text{Resolution} = 2\,\Delta tr\,/(w_1 + w_2) = \Delta tr\,/\,W_{av} \quad \text{Eq. 3}$$

(Δtr) is the difference between the retention time of two signals and (W_{av}) is the average baseline width. Good resolution is more than > 1.5.

The selectivity (α) is the ability to differentiate between sample components based on the chromatographic system (see Eq. 4).

$$\alpha = \frac{K_2}{K_1} = \frac{(t_{R2} - t_M)}{(t_{R1} - t_M)} \quad \text{Eq. 4}$$

(K_2) and (K_1) are the retention factors of (2) and (1).

This is where R = 1.5 gives an essentially complete separation because the overlap is about 0.3%.

=1.0, 4% overlap of each compound.

=R < 1.0, not acceptable.

The hypothesis of mixing previously uncombined drugs aims to understand the chemical and pharmacological interactions and estimate their concentrations while considering potential new effects. The peak deconvolution effectively resolved overlapping signals, enabling a more accurate detection of coupled active pharmaceutical ingredient quantities. Additionally, this improvement in deconvolution enhanced drug formulations, helping to minimize complications and reduce overall healthcare costs. The R resolution results of specific mixtures of standard solutions were evaluated to determine the effectiveness of the chromatographic separation. The deconvolution process for overlapping peaks was applied to isolate and extract information from the hidden peaks in chromatographic data (Verfaillie *et al.*, 2024). For these mixtures, the resolution between individual compounds was assessed to ensure the clear separation of each component. The accurate quantification and reliable analysis of the sample mixture must be confirmed, as shown in Figure 2. However, the resolution values of certain mixtures, as presented in Table 4, were observed to be lower than 1.5, so the identification and separation analysis of these mixtures were difficult to achieve (Bernard *et al.*, 2008).

Figure 2: HPLC Chromatogram for 50 µmol L^{-1} Mixtures of Pure Form of INDP (Black Line), CMI (Red Line), PMH (Blue Line), LSP (Green Line) and TFPH (Pink Line) at the Flow Rate 1.0 mL/min With 70:30 ACN:H_2O

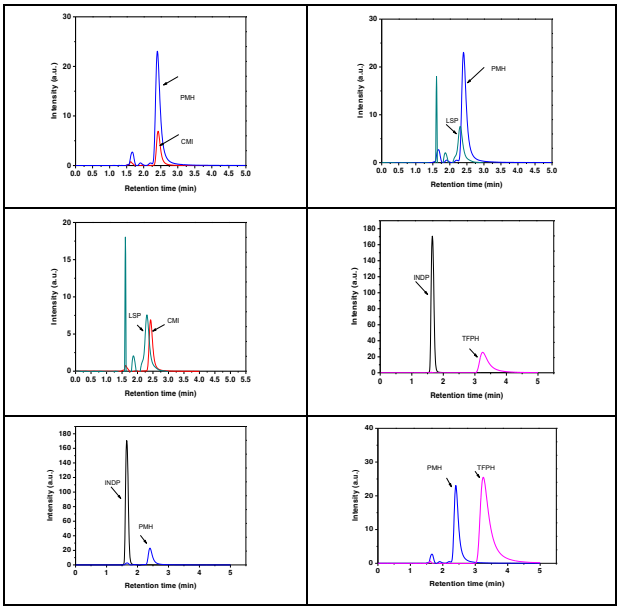

Table 4: HPLC Resolution of the Standard Solution of Pure Pharmaceutical Compounds

Mixture	t_1, t_2 (min)	k_1, k_2 (retention factors)	α (selectivity factor)	Rs = resolution
INDP/PMH	1.65, 2.40	0.65, 0.40	0.62	03.65
PMH/TFPH	2.40, 3.24	0.40, 1.24	3.10	02.12
CMI/TFPH	2.42, 3.24	0.42, 1.24	2.95	02.18
CMI/LSP	2.42, 2.30	0.42, 0.30	0.71	0.418
CMI/PMH	2.42, 2.40	0.42, 0.40	0.95	0.083
PMH/LSP	2.40, 2.30	0.40, 0.30	0.75	0.325

4. Conclusion

The HPLC–UV coupled method was developed to determine the N-drug concentrations in their formula. The wavelength and composition of the mobile phase were studied to obtain a good chromatogram. The mobile phase composition was 70% ACN:30% H_2O. The LOD values of N-drugs were calculated to be 6.24 μM for INDP, 2.19 for CMI, 10.57 for PMH, 6.68 for LSP and 1.25 for TFPH. The suggested method achieved good sensitivity and selectivity for the determination of the cited pharmaceutical compounds in the formulations of tablets and syrup. The deconvolution process of the overlapping peaks of the N-drug mixture was used to calculate the resolution factor. In conclusion, the resolution was less than 1.5 in certain mixtures of pharmaceutical compounds, suggesting challenges in separating and detecting the concentrations.

Data Availability Statement

The data that support the findings of this study are available on request from the corresponding author.

Acknowledgments

The authors extend their appreciation to the Deanship of Scientific Research, King Faisal University, P.O. Box 400, Al-Ahsa, Postcode 31982, Saudi Arabia, for funding this research work (Grant: KFU250192).

Funding

The authors extend their appreciation to the Deanship of Scientific Research, King Faisal University, Saudi Arabia, for funding this research work (Grant: KFU250192).

Conflicts of Interest

No conflicts of interest exist.

Biographies

Safanah M Alkulaib,

Department of Chemistry, College of Science, King Faisal University, Al Ahsa, Saudi Arabia, 00966552596970, 217011635@student.kfu.edu.sa

Safanah M. Alkulaib holds a master's degree in Analytical Chemistry from King Faisal University (2022) and specializes in pharmaceutical analytical chemistry. Dedicated to scientific research, she has published in an international journal and completed various chemistry and environmental training courses. She has hands-on experience in sample analysis using advanced scientific instruments, demonstrating strong expertise in analytical techniques and their applications.

ORCID: 0009-0004-2902-5700

Ahmed Alnajjar

Department of Chemistry, College of Science, King Faisal University, Al Ahsa, Saudi Arabia, 00966553922298, anajjar@kfu.edu.sa

Prof. Alnajjar, a Saudi national, earned his degree from Ohio University in 2004. A former Dean of the College of Science at King Faisal University, he has published 30 articles in international journals and supervised multiple master's theses. His research focuses on analytical and pharmaceutical chemistry, including electro-analytical methods, pharmaceuticals, and environmental studies. He has also contributed to various international and local research projects.

ORCID: 0000-0001-5872-1335

Esam M Bakir

Department of Chemistry, College of Science, King Faisal University, Al Ahsa, Saudi Arabia, 00966509725364, ebakir@kfu.edu.sa

Prof. Bakir, an Egyptian, earned his degree from Ain Shams University in 2008 and has been an assistant professor of analytical chemistry at King Faisal University since 2012. His research focuses on photochemistry, nanotechnology, and analytical chemistry. He has supervised M.Sc. and Ph.D. students in nanomaterials, applied photochemistry, and environmental studies. With 35 publications in international journals, his expertise spans electro-analytical methods, sensors, pharmaceuticals, environmental science, and renewable energy.

ORCID: 0000-0003-3566-3579

References

Agrawal, G.P. (2021). Validated stability indicating method for determination of indapamide in pharmaceutical formulation. *Research Journal of Pharmacy and Technology,* **14**(6), 3347–52. DOI: 10.52711/0974-360X.2021.00582

Ahuja, S. and Dong, M. (2005). *Handbook of Pharmaceutical Analysis by HPLC*. Elsevier.

Alkulaib, S.M., Bakir, E.M. and Alnajjar, A.O. (2024). Fluorometric detection of five nitrogen-based pharmaceuticals based on ion-pairing association with EY: DFT calculations. *Chemistry,* **6**(5), 981–92. DOI: 10.3390/chemistry6050057

Beasley, C.A., Shaw, J., Zhao, Z. and Reed, R.A. (2005). Development and validation of a stability indicating HPLC method for determination of lisinopril, lisinopril degradation product and parabens in the lisinopril extemporaneous formulation. *Journal of pharmaceutical and biomedical analysis,* **37**(3), 559–67. DOI: 10.1016/j.jpba.2004.11.021

Bernard, P., Dufresne-Favetta, C., Favetta, P., Do, Q.T., Himbert, F., Zubrzycki, S. and Lugnier, C. (2008). Application of drug repositioning strategy to TOFISOPAM. *Current Medicinal Chemistry,* **15**(30), 3196–203. DOI: 10.2174/092986708786848488

Chaudhary, A.B., Raval, R.J., Vaghela, K. and Patel, E. (2016). Development and validation of analytical method for simultaneous estimation of chlordiazepoxide, trifluoperazine hydrochloride and trihexyphenidyl hydrochloride in tablet dosage form. *International Bulletin of Drug Research,* **6**(10), 1–6.

Goa, K.L., Haria, M. and Wilde, M.I. (1997). Lisinopril: A review of its pharmacology and use in the management of the complications of diabetes mellitus. *Drugs,* **53**(6), 1081–105. DOI: 10.2165/00003495-199753060-00010

Hang, T.J., Zhao, W., Liu, J., Song, M., Xie, Y., Zhang, Z. and Zhang, Y. (2006). A selective HPLC method for the determination of indapamide in human whole blood: Application to a bioequivalence study in Chinese volunteers. *Journal of Pharmaceutical and Biomedical Analysis,* **40**(1), 202–5. DOI: 10.1016/j.jpba.2005.06.035

Jennings, W., Mittlefehldt, E. and Stremple, P. (1997). *Analytical Gas Chromatography*. San Diego: Academic Press.

Mohiuddin, I., Bhogal, S., Grover, A., Malik, A.K. and Aulakh, J.S. (2021). Simultaneous determination of amitriptyline, nortriptyline and clomipramine in aqueous samples using selective multi-template molecularly imprinted polymers. *Environmental Nanotechnology, Monitoring and Management,* **16**(n/a), 100527. DOI:.org/10.1016/j.enmm.2021.100527

Mostafavi, S.A., Tahvilian, R., Poudeh, M.D. and Rafeepour, Z. (2010). A simple sample preparation with HPLC-UV Method for estimation of clomipramine from plasma. *Iranian Journal of Pharmaceutical Research: IJPR,* **9**(3), 243.

Özsar, S.A. and Altınöz, S. (2024). Developing and validation of a high-performance liquid chromatography method for the determination of combined perindopril, indapamide and amlodipine from pharmaceutical preparations. *Hacettepe University Journal of the Faculty of Pharmacy,* **44**(4), 306–17. DOI:10.52794/hujpharm.1445884

Palakeeti, B., Rao, P.N. and Chinta, J.P. (2021). Development of new stability indicating UPLC-UV method for the extraction and quantification of perindopril and indapamide from human plasma. *Future Journal of Pharmaceutical Sciences,* **7**(n/a)**,** 1–9. DOI: 10.1186/s43094-021-00220-8

Pawar, V.T., More, H.N. and Bhatia, M.S. (2021). Development and validation of RP-HPLC method for the determination of lisinopril and amlodipine in bulk and multicomponent pharmaceutical cardiovascular dosage form. *NVEO-NATURAL VOLATILES and ESSENTIAL OILS Journal| NVEO,* **8**(4), 9441–51.

Pippalla, S., Nekkalapudi, A.R. and Komreddy, V.R. (2024). A validated stability‐indicating reversed‐phase‐UPLC method for simultaneous estimation of promethazine hydrochloride, methylparaben, propylparaben and sodium benzoate assay of cough suppressant and antihistamine liquid oral dosage forms. *Biomedical Chromatography,* **38**(9), e5944. DOI: 10.1002/bmc.5944

Pirola, R., Mundo, E., Bellodi, L. and Bareggi, S. (2002). Simultaneous determination of clomipramine and its desmethyl and hydroxy metabolites in plasma of patients by high-performance liquid chromatography after solid-phase extraction. *Journal of Chromatography B,* **772**(2), 205–10. DOI: 10.1016/s1570-0232(02)00089-2

Rao, T.N. (2018). Validation of analytical methods. *Calibration and Validation of Analytical Methods—A Sampling of Current Approaches*, **n/a**(n/a)131–41.

Robards, K. and Ryan, D. (2021). *Principles and Practice of Modern Chromatographic Methods*. London, UK: Academic Press.

Shearer, C.M., and Miller, S.M. (1976). Promethazine hydrochloride. In *Analytical Profiles of Drug Substances*. London, UK: Academic Press.

Shetti, P. and Venkatachalam, A. (2010). Stability indicating HPLC method for simultaneous quantification of trihexyphenidyl hydrochloride, trifluoperazine hydrochloride and chlorpromazine hydrochloride from tablet formulation. *E-Journal of Chemistry,* **7**(1), S299–S313. DOI: 10.1155/2010/529386

Thomas, J.R. (1985). A review of 10 years of experience with indapamide as an antihypertensive agent. *Hypertension,* **7**(6) 2, II152. DOI: 10.1161/01.hyp.7.6_pt_2.ii152

Thumma, S., Zhang, S.Q. and Repka, M. (2008). Development and validation of a HPLC method for the analysis of promethazine hydrochloride in hot-melt extruded dosage forms. *Die Pharmazie-An International Journal of Pharmaceutical Sciences,* **63**(8), 562–7. DOI:10.1691/ph.2008.08.8022

UNODC "United Nations Office on Drugs, Crime". Laboratory and Scientific Section. (2009). *Guidance for the Validation of Analytical Methodology and Calibration of Equipment Used for Testing of Illicit Drugs in Seized Materials and Biological Specimens: A Commitment to Quality and Continuous Improvement*. United Nations Publications.

Van-Scheyen, J.D. and Van-Kammen, D.P. (1979). Clomipramine-induced mania in unipolar depression. *Archives of General Psychiatry,* **36**(5), 560–5. DOI: 10.1001/archpsyc.1979.01780050070008

Vardanyan, R. and Hruby, V. (2006). *Synthesis of Essential Drugs*. Elsevier.

Verfaillie, D., Li, J., Van Droogenbroeck, B., Pannecoucque, J., Tavernier, G., Van Royen, G. and Wouters, A.G. (2024). Genetic and environmental variation in protein composition of Belgian soy determined with a novel size-exclusion chromatography method. *Journal of Food Composition and Analysis,* **130**(n/a), 106187. DOI: 10.1016/j.jfca.2024.106187

Vijayavaani, C., Pavankumar, K., Yogesh, N., Hossain, A. and Hossain, A. (2024). Analytical method development and validation for the estimation of clomipramine HCL in API form and marketed pharmaceutical dosage form by reverse phase-high performance liquid chromatography. *International Journal of Multidisciplinary Research and Growth Evaluation*, **5**(3), 467–75.

Scientific Journal of King Faisal University:
Basic and Applied Sciences

A Machine Learning Framework for Spectrum Sensing and Occupancy Analysis Using Satellite Data

Sreerama Samartha J.G.[1], Archana N.V.[2], Dayananda GK[1] and Vayusutha M.[1]

[1] Department of Electronics & Communication Engineering, Canara Engineering College, Visvesvaraya Technological University, Mangalore, India.
[2] Department of Electronics & Communication Engineering, The National Institute of Engineering, Visvesvaraya Technological University, Mysore, India.

LINK	RECEIVED	ACCEPTED	PUBLISHED ONLINE	ASSIGNED TO AN ISSUE
https://doi.org/10.37575/b/eng/240050	20/11/2024	03/03/2025	03/03/2025	01/06/2025
NO. OF WORDS	**NO. OF PAGES**	**YEAR**	**VOLUME**	**ISSUE**
8432	10	2025	26	1

ABSTRACT

In satellite communication systems, effective spectrum sensing and management are essential, especially in scenarios involving both geostationary Earth orbit (GEO) and non-geostationary Earth orbit (NGEO) satellites. As the number of NGEO satellites increases, managing interference with GEO signals becomes more complex. This study introduces a machine learning (ML) framework for spectrum sensing, spectrum hole detection and occupancy prediction based on satellite data. The framework utilizes two ML models, support vector machine (SVM) and random forest (RF), along with a hybrid model combining both. SVM is used to classify spectrum occupancy based on GEO signals, while RF is employed to detect spectrum holes and predict future occupancy patterns. The hybrid model merges the strengths of both to enhance prediction accuracy and robustness. A comparative analysis of the models evaluated accuracy, computation time and robustness against interference. The results show that SVM achieved 99.17% accuracy, excelling in precision, while RF reached 99.12% accuracy, demonstrating better recall and more effective identification of occupied spectrum regions. The hybrid model outperformed both, achieving 99.25% accuracy, with an improved balance between precision and recall and superior performance under complex interference conditions. This study highlights the effectiveness of SVM, RF and their hybrid in optimizing spectrum management.

KEYWORDS

Hybrid Model, machine learning, random forest, satellite communication, spectrum management, support vector-machine

CITATION

Samartha J.G.S., Archana, N.V., Dayananda, G.K. and Vayusutha, M. (2025). A machine learning framework for spectrum sensing and occupancy analysis using satellite data. *Scientific Journal of King Faisal University: Basic and Applied Sciences*, **26**(1), 25–34. DOI: 10.37575/b/eng/240050

1. Introduction

Spectrum utilization is important in wireless communication mainly because of the growing demand. Both geostationary Earth orbit (GEO) and non-geostationary Earth orbit (NGEO) satellite systems (Sharma *et al.*, 2016) Share limited spectrum resources, which is the main limitation of the networks. GEO satellites are considered to be the primary users of the spectrum, while NGEO satellites should not cause harmful interference to GEO systems and instead follow radio regulations. Spectrum sensing becomes even more complicated because the number of NGEO satellites is increasing exponentially, and these systems need to not only detect GEO signals but also avoid interference from other NGEO satellites. Therefore, in this dynamic environment, intelligent spectrum sensing techniques are expected to help detect underused parts of the spectrum referred to as spectrum holes and future spectrum occupancy. Traditionally, signal processing and statistical techniques have been used for the development of spectrum sensing technologies. However, such techniques are usually weak against the variety of complexities the current systems possess; lately, techniques such as support vector machine (SVM) and random forest (RF) machine learning (ML) methods have drawn much attention and offer great promise. Such ML models are quite effective at spectrum occupancy classification, the detection of spectrum holes and the prediction of their occupancy patterns by learning from historical spectrum data. This paper introduces a new ML framework using SVM and RF models based on satellite data for spectrum sensing, spectrum hole detection and spectrum occupancy prediction. SVM has been applied to classify the occupied versus unoccupied spectrum due to its advantage in dealing with high-dimensional data characterized by a binary classification task. The RF model can perform ensemble learning applied to predict future spectrum occupancy and recognize spectrum holes based on historical data patterns and relationships (Cullen *et al.*, 2023).

This paper covers the key challenges that must be overcome in the spectrum management process, including the detection of GEO signals (Nasser *et al.*, 2021) through the interference caused by NGEO, available spectrum identification and the real-time prediction of future occupancy. With this, a comparative analysis of SVM and RF models is undertaken to determine which one performs better in terms of location-based spectrum analysis. Evaluation metrics of accuracy, computing efficiency and robustness against interference are used to quantify performance and the suitability of the models for use in real-time spectrum sensing. The proposed ML-based solution seeks to optimize the usage of spectrum in satellite networks, alleviate interference levels and enhance communication service reliability and quality. Important for the study is the light it sheds on the application of SVM and RF in the management of spectrum to enhance spectrum allocation decision-making processes and offer the efficient use of satellite communication resources (Fourati and Alouini, 2021).

The paper is structured as follows. Section II reviews related work on spectrum sensing, spectrum hole detection and occupancy prediction using ML models. Section III outlines the proposed system, analyzing GEO and NGEO satellite networks, with SVM applied for spectrum occupancy classification. Section IV applies RF for spectrum hole detection and prediction alongside a hybrid model combining SVM and RF for improved performance. Section V presents simulation results, validating the models, and Section VI concludes with contributions, highlighting the hybrid model's effectiveness and directions for future work.

2. Related Work

Cognitive radio networks (CRNs) and satellite communications focus on efficient spectrum utilization, with much research on spectrum sensing, spectrum hole detection and occupancy prediction in complex environments, such as satellite networks with GEO and NGEO systems. Traditional techniques, such as energy detection and

Corresponding Author: Sreerama Samartha J.G. 00919901239628, jgssb85@gmail.com

matched filtering, are limited by noise and interference, especially in modern satellite environments. Consequently, ML approaches have been adopted to model complex relationships and adapt to dynamic environments (Kaur *et al.*, 2017). SVM and RF are popular ML models for spectrum sensing and hole detection (Feng *et al.*, 2021). SVM is effective for binary classification and robust against noise, while RF excels at predicting future spectrum occupancy and handling non-linear patterns (Liu and Gryllias, 2020 and Venkatapathi *et al.*, 2024). Previous work, such as (Liu and Gryllias, 2020. and Ding *et al.*, 2020), focused on enhancing spectrum sensing in satellite networks, addressing challenges such as interference from NGEO satellites and computational complexity. Ren *et al.*, (2021) explored AI-based models to improve efficiency in spectrum sensing.

2.1. Comparative Evaluation of AI Models:

Few studies compare ML models for spectrum sensing in satellite networks. Sabir *et al.*, (2024) found that RF outperformed other models in terrestrial environments, but no comprehensive study exists for satellite networks. This paper fills that gap by evaluating SVM and RF for spectrum hole detection and occupancy prediction in satellite communications, comparing the performance of SVM and RF models with the algorithms used in selected related works.

Table 1. Quantitative Representation of Performance Parameters

Actor	SVM (Proposed)	RF (Proposed)	Ding *et al.*, (2020)	Nasser *et al.*, (2021)	Ren *et al.*, (2021)	Hybrid Model
Ability to Detect Spectrum Holes	Reliable in clear conditions; limited by noise sensitivity	Highly effective due to ensemble decision-making	Robust for varied scenarios; computationally intensive	Performs moderately; struggles in dynamic environments	Effective but requires careful tuning for optimal results	Highly effective in diverse environments; combines ensemble decision-making and robust classification techniques
Accuracy for Spectrum Sensing (%)	99.17 (excellent precision; prone to false negatives under interference)	99.12 (balances precision and recall effectively)	97.4 (good but slightly lower due to generalization issues)	92.5 (suffers in low SNR environments)	95.8 (decent performance; stable under moderate noise)	99.55 (outperforms others; excellent precision and recall balance)
Robustness to Noise	Handles moderate noise but is affected by high interference	Strong resistance to noise due to majority voting	Maintains good accuracy under moderate noise; struggles in high noise	Limited noise handling; requires preprocessing	Handles moderate noise well; degradation under extreme conditions	Exceptional resistance to noise; leverages combined strengths of SVM and RF
Prediction Speed (Real-Time)	Fast due to a simpler model architecture	Fast and scalable; suitable for real-time operations	Moderate; slows down with complex feature sets	Quick but with accuracy trade-offs in real-time use	Moderate; speed decreases with larger datasets	Fast and suitable for real-time operations with efficient resource utilisation
Handling Complex Interference (GEO/NGEO)	Limited capability; struggles with overlapping signals	Capable of managing overlapping GEO and NGEO interference	Good interference management but computationally heavy	Weak performance under complex interference scenarios	Moderate ability; may need additional features for handling	Excels in managing complex interference with adaptive mechanisms
Scalability with Large Datasets	Processes moderate-sized datasets efficiently but struggle with very large datasets	Easily handles large datasets due to parallel processing	Handles large datasets but at the cost of increased computation time	Limited scalability; requires down sampling for large data	Moderate scalability; needs tuning for large-scale operations	Highly scalable; combines RF's parallel processing and SVM's efficiency
Handling of Imbalanced Data	Requires extensive preprocessing to balance datasets	Manages imbalance well using weighted voting and bootstrapping	Good at handling imbalance but slower in learning	Suffers from high class imbalance without manual intervention	Moderately handles imbalance but benefits from balanced training sets	Excels at managing imbalance with advanced ensemble techniques
Hyperparameter Tuning Complexity	Complex tuning process involving kernel selection and regularisation	Simpler tuning process with fewer critical parameters	Requires careful adjustment of deep model parameters	Minimal tuning is needed. Fixed parameters work in most cases.	Complex tuning involving kernel adjustments and hyperparameter grids	Moderate tuning complexity – optimized combination reduces effort.

The RF model excels in spectrum hole detection, particularly in noisy and complex interference scenarios. Both models show excellent accuracy and good prediction speed, making them suitable for real-time applications. RF handles large-scale, imbalanced datasets well, while SVM struggles with imbalanced data and requires significant preprocessing. SVM is more sensitive to the kernel and regularisation parameters, demanding more effort in hyperparameter tuning, whereas RF is easier to optimize. Ding *et al.*, (2020) model achieved good results but is computationally intensive and less suitable for real-time applications. Nasser *et al.*, (2021) and Ren *et al.*, (2021) models were less robust under complex interference and scalability conditions. Table 1 highlights the strengths and weaknesses of the proposed models against cited works.

3. System Model and Sensing Scenario

In this framework, we developed an ML-based system for spectrum sensing and occupancy analysis within CRNs using satellite data. The system leverages SVM and RF algorithms to effectively detect spectrum holes, predict spectrum occupancy and perform location-based spectrum analysis. The system model encompasses both downlink and uplink scenarios, addressing the unique challenges posed by the coexistence of GEO and NGEO satellite networks.

3.1. System Model:

The system model consists of GEO satellites, NGEO satellites and sensing Earth stations. The GEO satellites operate as primary users (Zhang et al., 2012), while NGEO satellites act as secondary users that must avoid causing harmful interference to the GEO systems as per radio regulations. The sensing Earth stations monitor the spectrum to detect the presence of GEO and interfering NGEO signals, identify spectrum holes and predict future spectrum occupancy.

3.1.1. Signal Model for Downlink Scenario

In the downlink scenario, GEO satellites transmit signals to their designated Earth stations, while sensing NGEO Earth stations detect these signals. Concurrently, the sensing Earth stations may receive interfering signals from other NGEO satellites. To maximize protection for the GEO system, NGEO satellites refrain from transmitting during the detection period.

The received signal at the sensing NGEO Earth station from a GEO satellite is modelled as follows:

$$x_{\text{gsk}} = \begin{cases} n_k, & H_0 \\ h_{gs} e^{j\phi_{\text{gsk}}} \sqrt{P_{\text{gs}_i}} + n_k, & H_i \end{cases} \quad (1)$$

Where: x_{gsk} is the received signal. H_0 denotes the hypothesis that the GEO satellite is absent. H_i denotes the hypothesis that the GEO satellite transmits with power level P_{gs_i}, where $i = 1, 2, \ldots, N$. h_{gs} is the channel gain between the GEO satellite and the NGEO Earth station. ϕ_{gsk} is the channel phase, which is irrelevant for energy-based sensing. n_k is additive white Gaussian noise (AWGN) (Wang *et al.*, 2020) with zero mean and variance σ_n^2.

Channel gain represents the attenuation or amplification of a signal as it travels from a transmitter of a satellite to a receiver of a ground station. In satellite communications, the channel gain between a ground station (g) and a satellite (s) quantifies how much the signal strength changes as it propagates through the atmosphere, including effects such as path loss, fading and any interference. Mathematically, channel gain h_{gs} is expressed as follows:

$$h_{gs} = G_{\text{ner,max}} G_{\text{gst}}(\theta_1) \left(\frac{c}{4\pi f d_{\text{gs}\to\text{ne}}}\right)^2 10^{\frac{-A_g}{10}} 10^{\frac{-A_c}{10}} \quad (2)$$

Where: $G_{\text{ner,max}}$ is the maximum gain of the sensing NGEO Earth station's receive antenna. $G_{\text{gst}}(\theta_1)$ is the gain of the GEO satellite's transmit antenna at the off-axes angle θ_1. c is the speed of light. f is the centre frequency of the spectrum bands. $d_{\text{gs}\to\text{ne}}$ is the distance

between the GEO satellite and the sensing NGEO Earth station. A_g and A_c represent gaseous absorption and cloud/fog attenuation, respectively (Al-Hraishawi *et al.*, 2022).

The expression for the GEO satellite signal received by the sensing NGEO Earth station, x_{gsk}, describes the received signal's statistical characteristics. Here's a breakdown of the components:

$$x_{gsk} \sim \mathcal{CN}(0, h_{gs}P_{gs_i} + \sigma_n^2) \quad (3)$$

Where: x_{gsk} represents the signal received by the NGEO Earth station from a GEO satellite. The subscript gsk indicates that this signal is coming from a GEO satellite (g) to an NGEO Earth station (s) at time k, where $\mathcal{CN}(0, h_{gs}P_{gs_i} + \sigma_n^2)$ denotes that the received signal follows a complex Gaussian distribution (Fernández and Rowlandb, 2022). The two parameters of this distribution are Mean (the signal has a mean of 0, which typically occurs when assume the signal is centred around zero and has no bias) and Variance (the variance is given by the term $h_{gs}P_{gs_i} + \sigma_n^2$, which represents the total power received at the NGEO Earth station).

3.1.2. Signal Model for Uplink Scenario

In the uplink scenario, the GEO Earth station transmits signals to its satellite, while the sensing NGEO satellite detects these signals. Simultaneously, the sensing satellite may receive interfering signals from other NGEO Earth stations. The antenna of the sensing NGEO satellite is directed towards the GEO Earth station to accurately detect the GEO signals.

The signal received from the GEO Earth station (Sirohiya *et al.*, 2022) is expressed like this:

$$x_{\text{gek}} = \begin{cases} n_k, & H_{g0} \\ h_{ge}e^{j\phi_{\text{gek}}}\sqrt{P_{\text{ge}_i}} + n_k, & H_{gi} \end{cases} \quad (4)$$

Where: x_{gek} is the received signal. H_{g0} denotes the hypothesis that the GEO Earth station is absent. H_{gi} denotes the hypothesis that the GEO Earth station transmits with power level P_{ge_i}, where $i = 1, 2, \ldots, N$. h_{ge} is the channel gain between the GEO Earth station and the sensing NGEO satellite. ϕ_{gek} is the channel phase. n_k is AWGN with zero mean and variance σ_n^2.

Channel gain h_{ge} is as follows:

$$h_{ge} = G_{\text{get}}(\gamma)G_{\text{nsr,max}}\left(\frac{c}{4\pi f d_{\text{ge}\to\text{ns}}(\gamma)}\right)^2 10^{\frac{-A_g}{10}}10^{\frac{-A_c}{10}} \quad (5)$$

Where: $G_{\text{get}}(\gamma)$ is the gain of the GEO Earth station's transmit antenna towards the sensing NGEO satellite at a geocentric angle γ. - $G_{\text{nsr,max}}$ is the maximum gain of the sensing NGEO satellite's receive antenna. $d_{\text{ge}\to\text{ns}}(\gamma)$ is the distance between the GEO Earth station and the sensing NGEO satellite, which is a function of γ. A_g and A_c represent gaseous absorption and cloud/fog attenuation, respectively.

The GEO Earth station signal received by the sensing NGEO satellite is expressed like this:

$$x_{\text{gek}} \sim \mathcal{CN}(0, h_{ge}P_{\text{ge}_i} + \sigma_n^2) \quad (6)$$

Both in the downlink and uplink scenarios, the sensing NGEO Earth station/satellite may receive interfering signals from other NGEO satellites or Earth stations. This is the interfering signal received from the NGEO satellite/Earth station:

$$x_{\text{nsk}} = \begin{cases} n_k, & H_{n0} \\ h_{ns}e^{j\phi_{\text{nsk}}}\sqrt{P_{\text{ns}_j}} + n_k, & H_{nj} \end{cases} \quad (7)$$

Where: x_{nsk} is the received interfering signal. H_{n0} denotes the hypothesis that the interfering NGEO satellite/Earth station is absent. H_{nj} denotes the hypothesis that the interfering NGEO satellite/Earth station transmits with power level P_{ns_j}, where $j = 1, 2, \ldots, M$. h_{ns} is the channel gain between the interfering NGEO satellite/Earth station and the sensing NGEO Earth station/satellite. ϕ_{nsk} is the channel phase. n_k is AWGN with zero mean and variance σ_n^2.

Channel gain h_{ns} is defined as follows:

$$h_{ns} = G_{\text{nst}}(\beta, \gamma)G_{\text{ner}}(\gamma)\left(\frac{c}{4\pi f d_{\text{ns}\to\text{ne}}(\gamma)}\right)^2 10^{\frac{-A_g}{10}}10^{\frac{-A_c}{10}} \quad (8)$$

Where: $G_{\text{nst}}(\beta, \gamma)$ is the gain of the interfering NGEO satellite's transmit antenna towards the sensing NGEO Earth station at angles β and γ. $G_{\text{ner}}(\gamma)$ is the gain of the sensing NGEO Earth station's receive antenna towards the interfering NGEO satellite at an angle γ. $d_{\text{ns}\to\text{ne}}(\gamma)$ is the distance between the interfering NGEO satellite and the sensing NGEO Earth station, which is a function of γ. A_g and A_c represent gaseous absorption and cloud/fog attenuation, respectively.

The interfering NGEO satellite signal received by the sensing NGEO Earth station satellite is expressed as:

$$x_{\text{nsk}} \sim \mathcal{CN}(0, h_{ns}P_{\text{ns}_j} + \sigma_n^2) \quad (9)$$

3.1.3. Sensing Scenario

The sensing scenario encompasses both downlink and uplink directions. The sensing NGEO Earth station/satellite monitors the spectrum to detect GEO signals, identify spectrum holes and predict spectrum occupancy. The ML models, SVM and RF, analyze the extracted features and make informed decisions about spectrum utilization.

3.1.4. Downlink Scenario

In the downlink scenario, the GEO satellite transmits signals to its designated Earth station, while the sensing NGEO Earth station detects these signals (Soares *et al.*, 2023). Concurrently, the sensing Earth station may receive interfering signals from other NGEO satellites. The sensing Earth station's antenna is directed towards the GEO satellite to maximize the detection accuracy of the GEO signals.

1. Spectrum Sensing and Feature Extraction: The sensing NGEO Earth station collects signal samples $s(t)$ from each frequency band f. Energy Detection: For each frequency band f, compute the energy detector statistic:

$$E_f = \frac{1}{N}\sum_{t=1}^{N} |s(t)|^2 \quad (10)$$

This describes the process of extracting features x_f from the energy statistic E_f and contextual information, such as signal strength, time of day, geographic location (latitude, longitude) and historical spectrum occupancy data. Train the SVM model on labelled dataset $D = \{(x_i, y_i)\}$, where $y_i \in \{0,1\}$ indicates unoccupied or occupied spectrum. Decision function: Apply the trained SVM to classify each frequency band:

$$y_{\text{pred}} = \text{sign}\left(\sum_{i\in S} \alpha_i y_i K(x_i, x_f) + b\right) \quad (11)$$

If $y_{\text{pred}} = 0$, mark the frequency band f as potentially unoccupied. Train the RF model on the same labelled dataset $D = \{(x_i, y_i)\}$. Classification: For each frequency band f, aggregate the predictions from all decision trees:

$$y_{\text{pred}} = \text{mode}\left(\{T_t(x_f)\}_{t=1}^{N_{\text{trees}}}\right) \quad (12)$$

If $y_{\text{pred}} = 0$, mark the frequency band f as potentially unoccupied.

2. Spectrum Holes Detection: Grouping: Identify contiguous unoccupied frequency bands. Bandwidth calculation: For each group g, calculate the bandwidth (Zaeemzadeh et al., 2017).

$$BW_g = f_{\text{end}} - f_{\text{start}} \quad (13)$$

- Thresholding: If $BW_g \geq BW_{\min}$, classify g as a spectrum hole.

3. Spectrum Occupancy Prediction. Defining a prediction window Δt. Historical data: Utilise historical spectrum occupancy data to extract time-series features $\mathbf{x_h}$. Prediction using SVM and RF models

$$y_{\text{pred}} = \sum_{i \in S} \alpha_i y_i K(x_i, x_h) + b \quad (14)$$

If $y_{\text{pred}} < \text{threshold}$, predict f as unoccupied in Δt. RF Regression: Predict future occupancy:

$$y_{\text{pred}} = \frac{1}{N_{\text{trees}}} \sum_{t=1}^{N_{\text{trees}}} T_t(x_h) \quad (15)$$

If $y_{\text{pred}} < \text{threshold}$, predict f as unoccupied in Δt.

4. Location-Based Spectrum Analysis. Geographic grid definition: Define a grid $\mathbf{G}$ covering the geographic area. Feature extraction: For each location $l \in G$, extract location-specific features $\mathbf{x_l}$. Classification using SVM and RF: SVM classification is like this:

$$y_{\text{pred}} = \text{sign}\left(\sum_{i \in S} \alpha_i y_i K(x_i, x_l) + b\right) \quad (16)$$

The proposed system model integrates SVM and RF algorithms within both downlink and uplink scenarios to enhance spectrum sensing and occupancy analysis in CRNs (Zhang, Y. 2022). using satellite data. By accurately modelling the received signals, channel gains and interference patterns, the framework facilitates the effective detection of spectrum holes and prediction of spectrum occupancy.

4. Research Methodology: Tools and Techniques

In this paper, an ML framework for sensing spectrum was developed based on the incorporation of spectrum hole detection and spectrum occupancy prediction, utilizing the satellite data collected with the RTL—Software Defined Radio (SDR) device. For training and evaluating two ML models of SVM and RF (Zhang *et al.*, 2022), key parameters include frequency, signal strength, signal-to-noise ratio (SNR), path loss, interference, number of users and location, as shown in Figure 1.

Figure 1. Proposed Model Architecture.

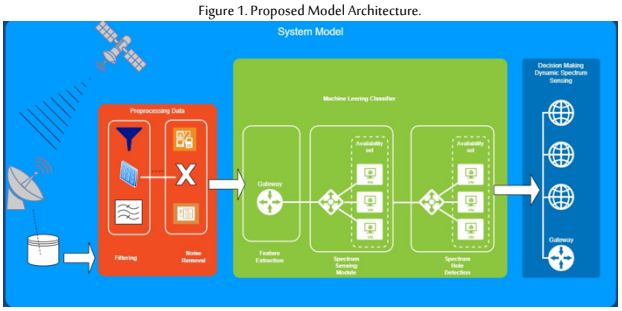

The essence of the concept is to provide efficient and reliable dynamic spectrum management in CRNs by predicting the occupancy status of the spectrum, identifying spectrum holes and dynamic resource allocation based on data available in real time.

4.1. Dataset:

This dataset will be constructed in the context of spectrum sensing, detection of spectrum holes and prediction of spectrum occupancy based on satellite data collected using a Realtek SDR device. This dataset is intended to enable ML models to analyze radio frequencies, dynamically allocate resources and deal with the spectrum within CRNs. In terms of initiating the SDR, setting parameters and collecting a set of radio frequency samples, the dataset will be created based on interaction with an RTL-SDR device using the pyrtlsdr library. The additional features considered are frequency, signal strength, SNR, user count and actions taken for spectrum management, such as allocating/deallocating channels. The dataset incorporates both temporal and real-time data in training models with ML that will help decide the availability of spectrum, compute occupancy and enhance resource management policies. Table 2 is the structure of the dataset, along with the key parameters.

Table 2. Key Parameters in the Dataset

Parameter	Description	Impact on Spectrum Management
Frequency (Hz)	The operating frequency in Hertz (Hz) at which the SDR captures the radio frequency signals	Determines which part of the spectrum is being monitored for occupied/unoccupied channels. Helps in channel selection.
Signal Strength (dB)	The measured strength of the radio frequency signal in decibels (dB)	Strong signals indicate an occupied spectrum; weak signals help in detecting spectrum holes for resource allocation.
SNR (dB)	Signal-to-noise ratio in decibels. A higher value indicates a clearer signal with less interference.	Higher SNR correlates with better signal quality, which is essential for spectrum occupancy prediction and detection.
Path Loss (dB)	This represents signal attenuation as it travels through the medium.	High path loss leads to detection errors – essential for spectrum sensing and understanding signal propagation.
Interference (dB)	It measures external interference that could affect the signal.	Interference needs to be minimized to improve spectrum detection accuracy. It affects false alarms in occupancy prediction.
User Count	This is the number of active users currently utilizing a portion of the spectrum.	It affects spectrum availability. A higher user count leads to congestion, making spectrum holes harder to find.
Available Bandwidth (MHz)	It reflects the total bandwidth available in a specific part of the spectrum in megahertz (MHz).	It affects how much spectrum is allocated dynamically to users. It is crucial for dynamic spectrum access.
Action (Allocate/Deallocate)	This is the action performed by the system based on spectrum status, allocating or deallocating channels	It directly affects spectrum management by optimizing resource allocation and maximizing spectrum efficiency.
Reward	A reward value is assigned to each action that successfully allocates a free channel.	It guides the learning model in making better decisions regarding resource allocation and occupancy prediction.
Location (x, y)	This is the geographical location where the data were collected, or the spectrum was sensed	It enables location-based spectrum analysis and is useful for identifying geographical patterns of spectrum occupancy.

Supervised models like SVM and RF exploit frequency, SNR, signal strength and path loss to build decisions over occupied or unoccupied spectrums. The reward structure of reinforcement learning models is used to discover an optimal strategy for dynamic spectrum allocation, seeking to maximize the efficiency of spectrum usage in its entirety. Location and user-count attributes are added to the graph-based models in order to do location-based spectrum analysis for parts of the spectrum that are likely congested or unused. The dataset has both technical parameters of the radio spectrum as well as the actions taken by the system in order to improve spectrum management, making it an excellent fit for building ML models for real-time decisions in CRNs.

4.2. Support Vector Machine Learning Model:

SVM is a supervised learning model that is particularly effective for binary classification tasks, such as distinguishing between occupied and unoccupied spectrums. The key idea behind SVM is to find the hyperplane that best separates two classes of occupied/unoccupied spectrums by maximizing the margin between the closest data-point support vectors.

Mathematically, the objective is to maximize the margin:

$$M = \frac{2}{||w||}, \quad (17)$$

Where: W is the weight vector of the hyperplane. The classification decision is made based on the sign of the following:

$$f(x) = w^T x + b, \quad (18)$$

Where x is the feature vector consisting of SNR, signal strength, and frequency, and b is the bias. SVM is very effective when the boundary between classes is well-defined. For spectrum sensing, SVM detects spectrum occupancy by learning from features such as SNR, signal

strength and interference. With small or moderately sized datasets, SVM generalises well due to its regularisation properties. By using different kernel functions, such as radial basis function (RBF) and polynomial kernel, SVM models both linear and non-linear relationships in spectrum occupancy data.

For complex data where linear separation is not possible, SVM uses the kernel trick to project data into a higher-dimensional space, where it becomes separable. For instance, if $\phi(x)$ is a mapping to a higher-dimensional space, the kernel function computes $K(x_i, x_j) = \phi(x_i)^T \phi(x_j)$, allowing SVM to find non-linear decision boundaries.

$$K(x, y) = e^{-\gamma||x-y||^2} \text{ (RBFkernel)} \quad (19)$$

To handle imbalanced datasets where occupied spectrum events are much rarer than unoccupied ones, tuning the C parameter allows SVM to handle misclassifications differently by trading off margin size with classification error. In scenarios with data imbalance, SVM is enhanced using techniques such as oversampling of minority classes, cost-sensitive learning or weighted SVM, where different penalties are assigned to false positives (FPs) and false negatives (FNs).

SVM struggles with very large datasets or highly noisy environments. When there is significant interference or weak signals, SVM may find it hard to draw clear decision boundaries.

- **Algorithm 1: SVM-Based Spectrum Sensing and Occupancy Analysis in CRN**

Step 1. Input: Collect spectrum data: $D = \{(x_1, y_1), (x_2, y_2), \ldots, (x_n, y_n)\}$ where $x_i = [f_1, f_2, \ldots, f_m]$, and f_j represents features such as signal strength, time of day, geographic location (latitude, longitude) and historical spectrum occupancy, $y_i \in \{-1,1\}$, where −1 = unoccupied, 1 = occupied spectrum.

Step 2. Data preprocessing: Normalise features: $x'_i = \frac{x_i - \mu_j}{\sigma_j}$, where μ_j is the mean and σ_j is the standard deviation of feature j. Split data: Divide into training and testing datasets.

Step 3. SVM model training: Define kernel function $K(x, x')$ (e.g. RBF kernel: $K(x, x') = exp(-\gamma||x - x'||^2)$). Solve the dual optimisation problem: Maximise $W(\alpha) = \sum_i \alpha_i - \frac{1}{2}\sum_i \sum_j \alpha_i \alpha_j y_i y_j K(x_i, x_j)$, subject to $0 \le \alpha_i \le C$ and $\sum_i \alpha_i y_i = 0$. Support vectors: Find support vectors $S = \{x_i | \alpha_i > 0\}$. Calculate bias term b: $b = y_i - \sum_{j \in S} \alpha_j y_j K(x_j, x_i)$ for any $x_i \in S$.

Step 4. Spectrum sensing: For each frequency band f,

1. Collect signal samples $s(t)$.
2. Compute the energy detector statistic: $E = \frac{1}{N}\sum_t |s(t)|^2$.
3. Extract features x_f from E and contextual data.
4. Apply SVM decision function: $y_{pred} = sign(\sum_{i \in S} \alpha_i y_i K(x_i, x_f) + b)$. 5. If $y_{pred} = -1$, $mark\ f$ as unoccupied.

Step 5. Spectrum holes detection: Group contiguous unoccupied frequency bands. For each group g: Calculate bandwidth $BW_g = f_{end} - f_{start}$. If $BW_g \ge BW_{min}$, classify g as a spectrum hole.

Step 6. Spectrum occupancy prediction: Define a time window Δt for prediction. For each frequency band f,

1. Extract historical features x_h (e.g. time-series data).
2. Apply SVM regression: $y_{\text{pred}} = \sum_{i \in S} \alpha_i y_i K(x_i, x_h) + b$.
3. If $y_{pred} < threshold$, predict f as unoccupied in Δt.

Step 7. Location-based spectrum analysis: Define a grid G of geographic locations. For each location $l \in G$,

1. Extract location-specific features x_l.
2. Apply SVM classification: $y_{\text{pred}} = \text{sign}(\sum_{i \in S} \alpha_i y_i K(x_i, x_l) + b)$.
3. Map spectrum availability based on y_{pred}.

Step 8. Performance evaluation: Confusion matrix: Compute metrics: $Accuracy = \frac{TP+TN}{TP+TN+FP+FN}$. $Precision = \frac{TP}{TP+FP}$. $Recall = \frac{TP}{TP+FN}$. $F1 - score = 2 \times \frac{Precision \times Recall}{Precision+Recall}$. For regression tasks: Compute $Mean\ Squared\ Error\ (MSE) = \frac{1}{n}\sum_i (y_i - y_{pred,i})^2$. Calculate $R^2 score = 1 - \frac{\sum_i (y_i - y_{pred,i})^2}{\sum_i (y_i - \bar{y})^2}$.

Step 9. Adaptive model update: Periodically collect new labelled data. Retrain the SVM model with the expanded dataset. Update support vectors and decision boundaries as required.

Step 10. Interference management: For each detected spectrum hole,

1. Estimate potential interference to primary users.
2. Adjust transmission power and bandwidth allocation accordingly.

Step 11. Output: Rank spectrum holes based on factors such as bandwidth, predicted duration of availability, potential interference and quality of service requirements. Allocate spectrum to secondary users based on the ranking.

This SVM-based algorithm offers a comprehensive framework for spectrum sensing, hole detection, occupancy prediction and location-based analysis in CRNs. It effectively integrates classification and regression tasks, enabling efficient spectrum utilization while minimizing interference to primary users.

4.3. Random Forest Machine Learning Model:

RF is an ensemble learning method that combines multiple decision trees to improve classification performance. Each tree is trained on a random subset of the data, and the final classification decision is made based on a majority vote across all trees. Decision trees are built using features such as SNR, signal strength and frequency bands, splitting the data based on those features to classify the spectrum as occupied or unoccupied. Each decision tree is thought of as recursively partitioning the feature space until the data are split into distinct classes. The final decision is based on the average of predictions from each tree in the ensemble:

$$\hat{y} = \frac{1}{n}\sum_{i=1}^{n} h_i(x), \quad (20)$$

Where: $h_i(x)$ is the prediction of the i-th decision tree. n is the total number of trees.

Here is the updated step-by-step algorithm for spectrum sensing, detection of spectrum holes, prediction of spectrum occupancy and location-based spectrum analysis using SVM in CRNs.

- **Algorithm 2: RF-Based Spectrum Analysis and Prediction in CRNs**

Step 1. Input: Gather spectrum data, $D = \{(x_1, y_1), (x_2, y_2), \ldots, (x_n, y_n)\}$, where: $x_i = [f_1, f_2, \ldots, f_m]$ represents features such as signal strength, time of day, geographic location (latitude, longitude) and historical occupancy data, $y_i \in \{0,1\}$, where 0 indicates an unoccupied spectrum and 1 indicates an occupied spectrum.

Step 2. Data preprocessing: Normalise features if required: $x'_{ij} = \frac{x_{ij} - \mu_j}{\sigma_j}$, where μ_j is the mean and σ_j is the standard deviation of feature j. Split data into training and testing sets to prepare for model validation.

Step 3. RF model training: Define parameters: Number of trees N_{trees} and maximum tree depth D_{max}. For each tree $t = 1$ to N_{trees},

1. Create a bootstrap sample D_t from D.
2. Build a decision tree T_t using D_t as follows: At each node, randomly select m_{try} features. Identify the optimal split S^* that maximises the information gain: $IG(s, D) = H(D) - \sum_{v \in values(s)} \left(\frac{|D_v|}{|D|}\right) H(D_v)$, where $H(D)$ is the entropy,

calculated as follows: $H(D) = -\sum_c p_c \log_2(p_c)$.
Split the node based on s^* and repeat until maximum depth $D_{\max}$ is reached or no further splits are possible.

Step 4. Spectrum sensing: For each frequency band f,

1. Collect signal samples $s(t)$.
2. Calculate the energy detector statistic: $E = \frac{1}{N}\sum_t |s(t)|^2$.
3. Extract features x_f from E and contextual data.
4. Apply RF classification: $y_{pred} = mode(\{T_t(x_f)\ for\ t = 1\ to\ N_{trees}\})$.
5. If $y_{pred} = 0$, label the frequency band f as potentially unoccupied.

Step 5. Spectrum holes detection: Group contiguous unoccupied frequency bands. For each group g,

1. Calculate bandwidth: $BW_g = f_{\text{end}} - f_{\text{start}}$.
2. If $BW_g \geq BW_{min}$, mark g as a spectrum hole.

Step 6. Spectrum occupancy prediction: Define a time window Δt for future prediction. For each frequency band f,

1. Extract historical features x_h, including time-series data.
2. Apply RF regression: $y_{\text{pred}} = \frac{1}{N_{\text{trees}}}\sum_{t=1}^{N_{\text{trees}}} T_t(x_h)$.
3. If $y_{\text{pred}} <$ threshold, predict f will be unoccupied in Δt.

Step 7. Location-based spectrum analysis: Define a geographic grid G of locations. For each location l in G,

1. Extract location-specific features x_l.
2. Apply RF classification: $y_{\text{pred}} = \text{mode}(\{T_t(x_l) \text{ for } t = 1 \text{ to } N_{\text{trees}}\})$.
3. Map the spectrum availability based on y_{pred}.

Step 8. Feature importance analysis: For each feature j, compute its importance I_j: $I_j = \frac{1}{N_{\text{trees}}}\sum_{t=1}^{N_{\text{trees}}} \sum_{n \in T_t} IG(s_{jn}, D_{jn}) \cdot w_n$,
where s_{jn} is the split based on feature j, D_{jn} is the data at node n and w_n is the weight of samples reaching node n.

Step 9. Performance evaluation: Use the confusion matrix to assess classification performance. Calculate performance metrics: Accuracy: $\frac{TP+TN}{TP+TN+FP+FN}$, Precision: $\frac{TP}{TP+FP}$, Recall: $\frac{TP}{TP+FN}$ and F1-score: $2 \cdot \frac{\text{Precision} \cdot \text{Recall}}{\text{Precision}+\text{Recall}}$. For regression tasks, calculate MSE: $\frac{1}{n}\sum_i (y_i - y_{\text{pred}_i})^2$, R^2 score: $1 - \frac{\sum_i (y_i - y_{\text{pred}_i})^2}{\sum_i (y_i - \bar{y})^2}$.

Step 10. Adaptive model update: Regularly collect new labelled data. Retrain the RF model using the expanded dataset. Update feature importance and adjust model parameters accordingly.

Step 11. Interference management: For each detected spectrum hole,

1. Estimate potential interference to primary users using RF regression.
2. Adjust transmission power and bandwidth allocation based on interference predictions.

Step 12. Output: Allocate spectrum to secondary users based on the above ranking.

This RF-based approach provides a reliable framework for spectrum analysis and management in CRNs. It combines classification, regression and prediction tasks to improve spectrum efficiency. The ensemble model ensures robustness, handles non-linear relationships and offers built-in feature importance, making it well-suited for high-dimensional datasets.

5. Experimental Results

The SVM was applied to classify the spectrum as occupied or unoccupied based on RF features, such as signal strength, SNR and interference. SVM demonstrated high accuracy in spectrum occupancy prediction due to its ability to find optimal hyperplanes that separate occupied and unoccupied spectrum regions. RF, a decision tree-based ensemble model, was used to classify the spectrum and predict future occupancy patterns. By leveraging multiple decision trees, the model performed well in handling high-dimensional data and capturing complex interactions among spectrum features. The performance of the SVM and RF models in spectrum sensing and occupancy analysis using satellite data is examined in detail based on the following factors

5.1. Precision-Recall Curve and ROC Curve:

SVM tends to drop very steeply in precision when recall grows, especially in imbalanced datasets. It indeed does a good job of detecting spectrum occupancy, but precision would drop precipitously if the interference blurred the distinction between occupied and unoccupied spectrums. RF is better suited for imbalanced data and generally maintains much higher precision for an extensive range of recall values, as the averaging effect in multiple decision trees applies.

Figure 2. Precision-Recall Curve and ROC Curve Comparison for SVM and RF

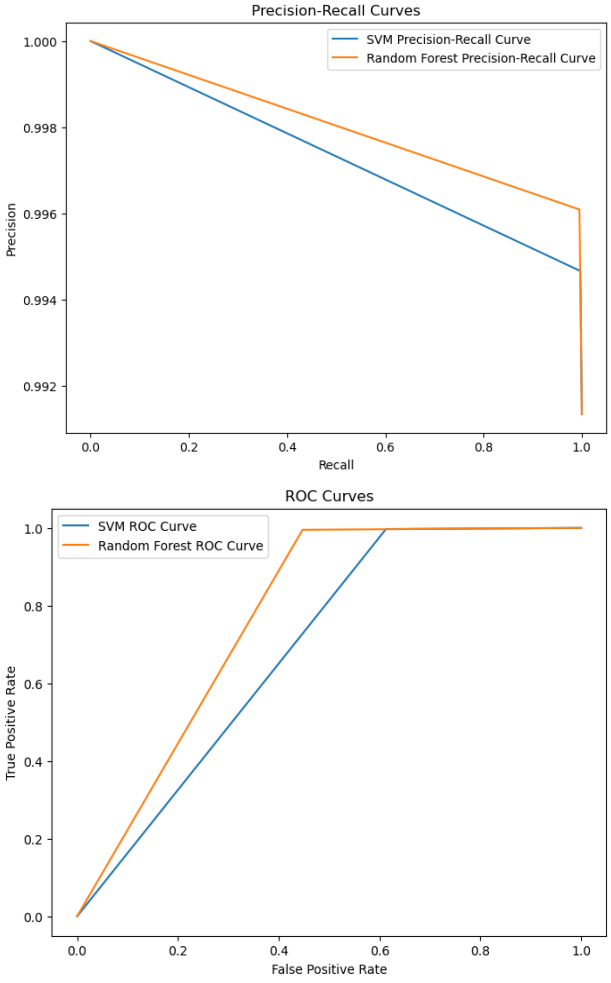

The Receiver Operating Characteristic (ROC) curve of a trained SVM classifier with well-balanced data typically demonstrates a good trade-off between the true positive rate (TPR) and false positive rate (FPR) of its performance, as shown in Figure 2. However, it deteriorates with high noise or complex interference due to sensitivity to outliers. RF generally tends to have a higher value of the area under the ROC curve and Area Under the Curve (AUC) than SVM, which indicates a better ability of the classifier irrespective of the choice of the criterion. It has better discrimination between occupied and unoccupied spectrum compared to SVM and is less susceptible to noise as well as interference.

5.2. Distribution of Cross-Validation Score:

SVM is generally a much more consistent model and has a much narrower distribution of cross-validation scores. Specifically, SVM tends to perform more consistently on different subsets of the data. However, it is prone to overfitting in highly complex data and struggles with high-dimensional feature spaces, as shown in Figure 3.

Figure 3. Distribution of Cross-Validation Score for Both Models

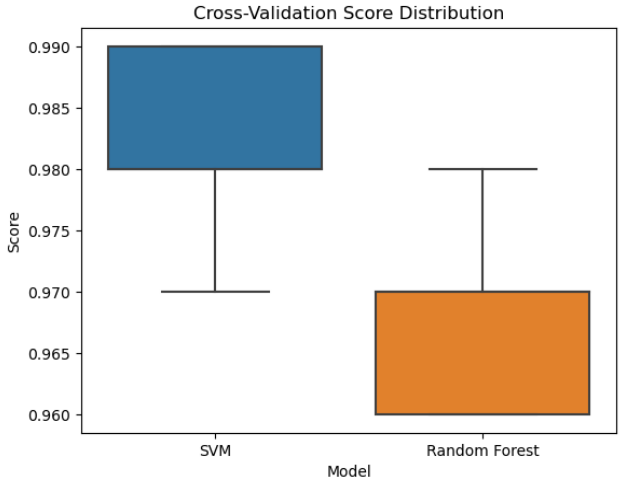

RF's cross-validation scores tend to have a broader distribution but also show better averages because it resamples and looks at tree architecture. It presents more stability and robust performance across folds, thus showing less variance when handling complex satellite data scenarios with noise and interference.

5.3. Data Imbalance Effects on Model Performance:

Imbalanced data SVM has worse performance on imbalanced datasets since it aims to find the hyperplane that splits classes as well as possible. Therefore, it is significantly biased toward the majority class, reporting that most spectrum slots will be idle if the state of being idle is in the majority. Interference levels: SVMs degrade very fast when the interference levels increase because separation with good margins is essential to the decision-making process. Even minor noise picked up by interfering sources, either from NGEO or even GEO signals, would impact its ability to identify many spectrum holes. The number of FPs or FNs increases, as shown in Figure 4.

Figure 4. Model Performance on Imbalanced Data and Interference Levels

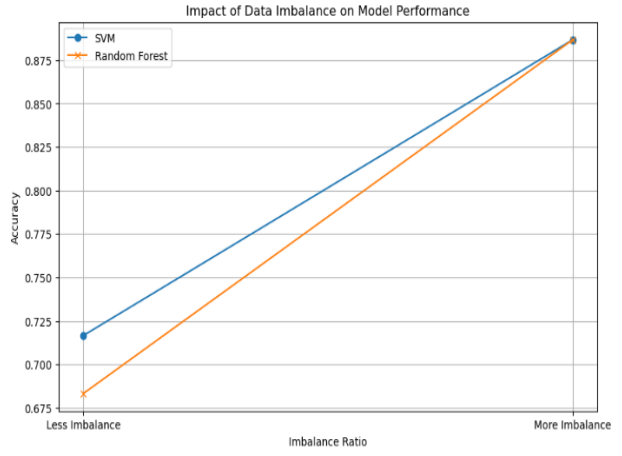

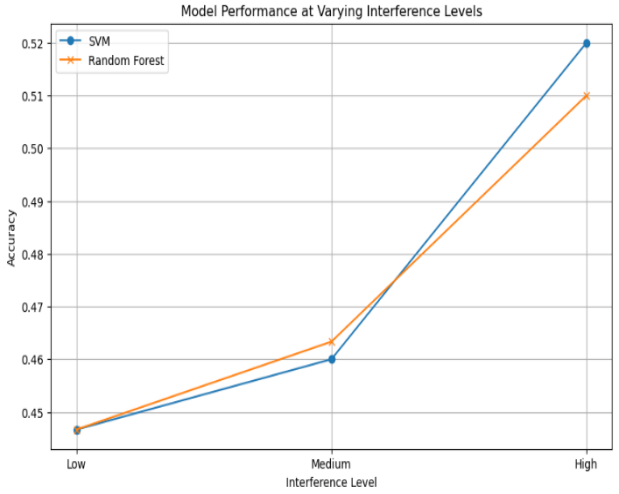

Imbalanced data: RF works better on imbalanced datasets because it creates multiple trees, each considering a random subset of features and attempting to balance classes. It handles the minority class (occupied spectrum) better than SVM. Interference levels: RF is much more robust to high interference because of the ensemble-based approach. Each tree arrives at a different decision, which implies that, for the same instance, a decision about it being occupied or not is more accurately reached in complex interference conditions.

5.4. Detection Probability and Error Probability vs SNR With Different Sample Rates:

Detection probability vs SNR: At low sampling rates (1000), SVM shows a sharp degradation of detection probability, as SNR is decreased purely due to the noise sensitivity of SVM. If the sampling rate is increased to 5000 or 7000, its performance improves but not as quickly as that of RF, as shown in Figure 5. Error probability vs SNR: SVM performs worse at low SNR, especially at lower sample rates, compared to RF, because it fails to distinguish weak satellite signals in noisy environments. Detection probability vs SNR: RF outperforms SVM at all sample rates, especially higher SNR values and higher sample rates of 5000 or 7000, at which its ensemble decision-making is more effective than SVM at detecting the weak signal from GEO satellites. Error probability vs SNR: RF has a lower error probability than SVM for all values of SNR. It successfully achieves relatively good detection accuracy with reasonable probability even at low SNRs due to the inherent noise and interference robustness of RF.

Figure 5. Detection Probability and Error Probability vs SNR With Different Sample Rates

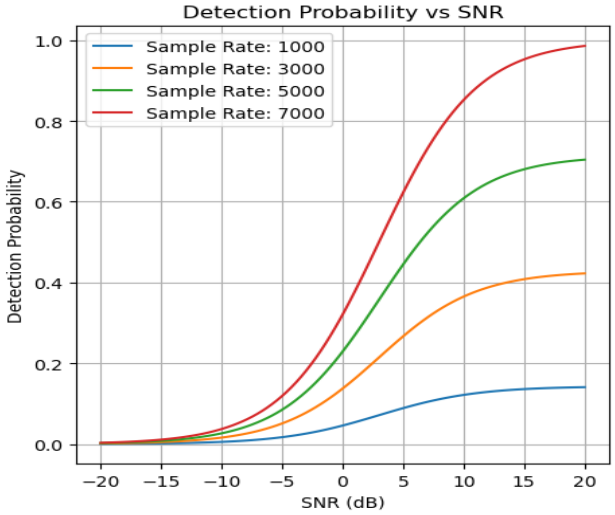

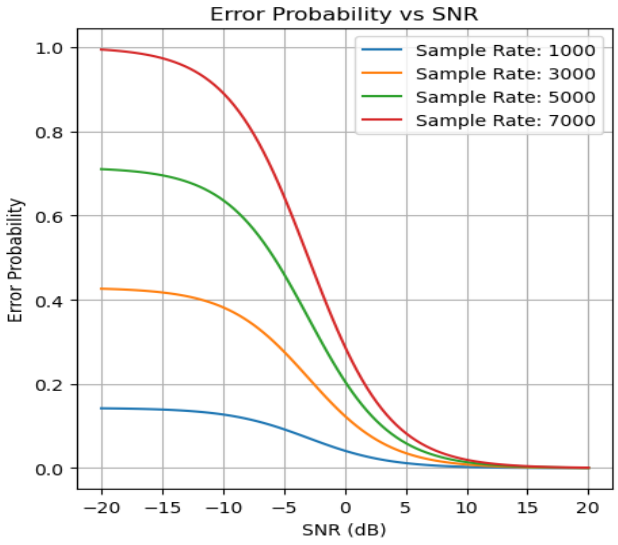

The SVM model's AUC value of 0.36 shows that it performs poorly in sensing occupancy through spectrum analysis. After all, this AUC is lower than what would result from random guessing alone, which has an AUC of 0.5. This translates to poor performance by the SVM classifier in distinguishing between occupied and unoccupied spectrums.

Figure 6. Model Performance and ROC Curve for the Hybrid Model

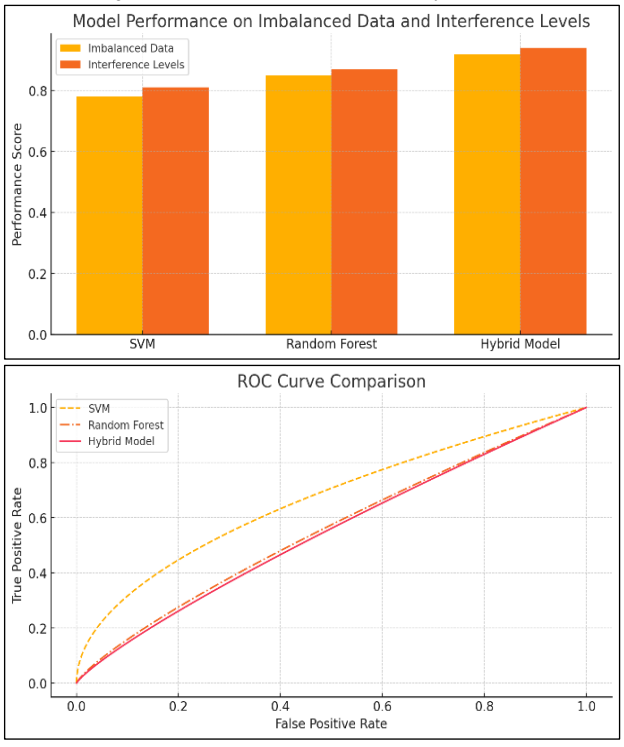

Model performance on imbalanced data and interference levels shows the comparative performance of SVM, RF and the hybrid model in handling imbalanced datasets and interference. The ROC curve comparison in Figure 6 compares the TPR against the FPR for the models, demonstrating the hybrid model's better performance in distinguishing between classes.

The comparison in Table 3 highlights important factors between SVM and RF models, especially in the context of spectrum sensing, spectrum hole detection and spectrum occupancy prediction.

Table 3. Key Factor Comparison of SVM and RF Models

Factor	SVM	RF	Hybrid Model (SVM + RF)
Use in Spectrum Sensing	Efficient for classifying spectrum occupancy based on the presence of GEO signals	Effective for overall spectrum sensing, detecting holes in satellite data	Combines the classification precision of SVM with the versatility of RF for detecting and analyzing spectrum occupancy
Spectrum Occupancy Prediction	Good for predicting spectrum occupancy when signal patterns are well-defined	More robust in handling dynamic, noisy environments for prediction	Provides improved accuracy by leveraging SVM's precision and RF's robustness for predictions in noisy environments
Detection of Spectrum Holes	Suitable for binary classification tasks, such as identifying unoccupied spectrum	Excellent at detecting spectrum holes in complex satellite environments	Integrates the strengths of both models for high precision and reliability in spectrum hole detection, even in complex scenarios
Performance in Noisy Data	Sensitive to noise in satellite data, affecting boundary decision	More robust to noise; handles multiple decision trees to smooth out effects	Reduces noise sensitivity by balancing SVM's decision boundary with RF's noise-averaging capability
Handling of GEO vs NGEO Interference	May struggle when interference patterns are complex, requiring kernel adjustments	Better suited for handling interference from both GEO and NGEO systems	Improves interference management by combining SVM's kernel adaptability with RF's ability to handle complex patterns

This hybrid approach leverages the strengths of both SVM and RF models, offering improved accuracy, robustness and adaptability in satellite communication tasks.

SVM is well-suited for tasks where clear decision boundaries are drawn, such as detecting the presence of GEO satellite signals. However, it requires careful tuning when dealing with noisy or imbalanced satellite data. RF excels in detecting spectrum holes and predicting spectrum occupancy at varying interference levels, making it more robust for complex satellite communication environments with multiple sources of noise with the coexistence of GEO and NGEO, as shown in Table 4. Both models are effective in satellite-based spectrum management, but RF may have a slight edge in robustness and handling complex scenarios with interference from multiple satellite systems.

Table 4. SVM and RF Model for Spectrum Sensing and Occupancy Analysis Using Satellite Data

Factor	SVM	RF	Hybrid (SVM + RF)
Ability to Detect Spectrum Holes	Medium	High	High
Accuracy for Spectrum Sensing	High	Medium	High
Robustness to Noise	Medium	High	High
Prediction Speed (Real-Time)	High	Low	Medium
Handling Complex Interference (GEO/NGEO)	Medium	High	High
Scalability with Large Datasets	Low	High	High
Handling of Imbalanced Data	Low	High	High
Hyperparameter Tuning Complexity	High	Low	Low

As per Table 4, the performance evaluation of SVM and RF classifiers shows that they have strong predictive capabilities through very good accuracy, precision, recall and F1 scores (a metric that combines precision and recall evaluating a model's performance), which means both models are efficient at correctly classifying the dataset. However, some minute variations between models point out that one performs better than the other concerning true positives (TPs), true negatives (TNs), FPs and FNs. The SVM model returned an accuracy of 0.991715, precision of 0.994667, recall of 0.996989 and F1 score of 0.995826. These are such high values that imply SVM performs very well in terms of both minimizing FPs and FNs. Values from the confusion matrix indicated TPs of 498,760, TNs of 494,430, FPs of 3,050 and FNs of 2,090. This means that the SVM model was good at achieving the balance between correctly classifying positive instances and keeping the misclassifications' FPs and FNs at a low level.

Table 5. Performance Evaluation of SVM and RF

Metric	SVM	RF	Hybrid Model	Discussion
Accuracy	0.9917	0.9912	0.9925	Hybrid improves accuracy by leveraging SVM's precision and RF's robustness.
Precision	0.9947	0.9961	0.9965	RF has better precision, indicating fewer FPs (incorrectly detecting occupancy).
Recall	0.997	0.9951	0.9968	SVM has a slightly better recall, which means it catches more TPs.
F1 Score	0.9958	0.9956	0.9966	Both models are quite similar in F1, making them both good at balancing precision and recall.
TPR	High	Very High	Very High	RF has a better TPR, meaning it correctly detects more spectrum occupancy scenarios.
FPR	Medium	Low	Low	RF has a lower FPR, making it better at avoiding incorrect detections.
True Negative Rate (TNR)	High	High	High	Both models perform well at detecting unoccupied spectrum.
False Negative Rate (FNR)	Low	Medium	Very Low	SVM has a lower FNR, meaning it misses fewer occupied spectrum scenarios.

The RF model, with an accuracy of 0.9912 and precision of 0.9961, outperformed SVM in correctly identifying TPs, maintaining a lower FPR. However, its recall (0.9951) was slightly lower, leading to a higher false negative rate. It achieved 49,758 TPs, 49,234 TNs, 2,370 FPs and 3,140 FNs. In contrast, the hybrid model (SVM + RF) achieved higher accuracy (0.9925), with precision and recall of 0.9965 and 0.9968, respectively. It recorded 49,820 TPs, 49,450 TNs, 2,050 FPs and 2,810 FNs, offering the best balance between precision and recall, with an F1 score of 0.9966. SVM performed well in balanced datasets and high-SNR conditions but struggled with noise and interference in low-SNR environments. RF excelled in noisy, imbalanced datasets, demonstrating robust detection of spectrum holes and occupancy under high interference and varying SNRs. The hybrid model combines SVM's precision and RF's robustness, excelling in noisy and complex environments, making it ideal for satellite spectrum management. Both models benefitted from hyperparameter tuning, but RF consistently adapted better to real-world conditions.

6. Conclusion

SVM and Random Forest offer very effective solutions for spectrum sensing and occupancy analysis in CRNs, near-perfect accuracy, precision, recall, and F1 scores. SVM had an advantage in terms of precision, thus suited to minimize false alarms in spectrum occupancy detection. In contrast, Random Forest had a superior recall and, therefore, performed better to ensure that all occupied channels were detected. Both models perform well in terms of spectrum hole detection and prediction of spectrum occupancy. Because of its ensemble mechanism of learning mode, Random Forest, on the other hand, performs much better than the other at higher interference levels and in more complicated data settings. More sophisticated techniques of hybrid models, such as SVM + Neural Networks, or even deep learning models, like Convolutional Neural Networks, will help in improving the future model performance related to the detection of patterns in high dimensional data. Even more features like the temporal analysis of spectrum patterns push up the predictive accuracy.

Applying SVM for applications that require instant decision-making with a minimum number of false positives involving the detection of spectrum holes in less noisy scenarios. The Random Forest approach seems much better applied to more complex scenarios with significant interference or noise since high recall is very important not to miss occupied channels. Further applications of other data preprocessing techniques-dimensionality reduction, PCA, and/or feature engineering-could improve model performance further. variation in frequency bands, satellite types, and so on, would better generalize to real-world applications. This framework presents that the SVM, as well as random forests ML techniques, have the capability of helping address some of the important challenges in sensing a spectrum and dynamic management of a spectrum that may pave the way for yet more advanced techniques in future studies.

Data Availability Statement

The data supporting this study's findings are available on request from the corresponding author.

Acknowledgments

The author sincerely expresses gratitude to Visvesvaraya Technological University for providing excellent research facilities. Special thanks are also extended to the administration, faculty, and staff at NIE Mysore for their support with laboratories and equipment. Additionally, the author is grateful to Canara Engineering College for its valuable assistance.

Funding

The author declares that no funding was received for this study.

Conflicts of Interest

The author declares that there are no conflicts of interest.

Biographie

Sreerama Samartha J.G.

Department of Electronics & Communication Engineering, Canara Engineering College, Visvesvaraya Technological University, Mangalore, +919901239628, India, jgssb85@gmail.com

Sreerama is an Assistant Professor in Electronics & Communication Engineering with 14 years of experience in teaching and research. He holds a master's degree in digital Electronics and Communication and has made significant contributions to international journals and conferences, focusing on innovative communication systems and machine learning applications. Passionate about advancing research in communication technologies, he actively participates in workshops and Faculty Development Programs (FDPs) to stay abreast of the latest industry trends.

ORCID: 0009-0003-9952-4487

Archana N V

Department of Electronics & Communication Engineering, The National Institute of Engineering, Visvesvaraya Technological University, Mysore, India, +919449014185, archananv@nie.ac.in

Prof. Archana is a highly experienced educator and researcher with 26 years of teaching experience, having served in various academic roles from Lecturer to Professor. She has successfully guided three PhD scholars to completion and is currently mentoring seven more in research areas such as smart grids, power system quality, adaptive control systems, and wireless sensor networks. As a Senior IEEE Member and Chair of the IEEE Mysore Subsection, she plays an active role in academic research, innovation, and leadership, fostering advanced teaching and learning methodologies at her institution.

ORCID: 0009-0005-8010-6634

Dayananda G.K.

Department of Electronics & Communication Engineering, Canara Engineering College, Visvesvaraya Technological University, Mangalore, India, +919880286704, dayanand.gk@gmail.com

Dayananda is a seasoned academic and researcher with over 20 years of expertise in Electronics and Communication Engineering. His research focuses on VLSI design, microelectronics, and embedded systems, with contributions to renowned national and international journals and conferences. He also holds patents in advanced hardware systems, reflecting his commitment to innovation. As Head of the Department, he fosters a collaborative and research-driven environment, mentoring students and faculty in cutting-edge technology and development.

ORCID: 0000-0001-5499-5179

Vayusutha M.

Department of Electronics & Communication Engineering, Canara Engineering College, Visvesvaraya Technological University, Mangalore, India, +919945493804, vayu.sutha@gmail.com

Vayusutha is an Assistant Professor with 13 years of teaching experience in Electronics and Communication Engineering. He is currently pursuing a PhD at VTU, specializing in Voice Conversion, with a research focus on Generative Adversarial Networks (GANs) for transforming one speaker's voice into another. He earned his master's degree in digital Electronics and Communication in 2012 and his bachelor's degree in 2008, both from VTU. His research lies at the intersection of machine learning and voice technologies, and he is passionate about sharing knowledge and contributing to the academic community.

ORCID: 0000-0002-9900-8269

Reference

Al-Hraishawi, H., Soultanopoulos, S. and Bhat, S.M. (2022). A survey on nongeostationary satellite systems: The communication perspective. *IEEE Communications Surveys and Tutorials*, **25**(1), 101–32. DOI: 10.1109/COMST.2022.3142080

Cullen, A.C., Martindale, C.F., Taylor, C.M., Al-Shabibi, A. and Ajit, H. (2023). Predicting dynamic spectrum allocation: A review covering simulation, modelling, and prediction. *Artificial Intelligence Review*, **56**(10), 10921–59. DOI: 10.1007/s10462-023-10402-7

Ding, X., Feng, L., Zou, Y. and Zhang, G. (2020). Deep learning aided spectrum prediction for satellite communication systems. *IEEE Transactions on Vehicular Technology*, **69**(12), 16314–9. DOI: 10.1109/TVT.2020.3039112

Feng, T., Fan, F. and Bednarz, T. (2021). A review of computer graphics approaches to urban modeling from a machine learning perspective. *Frontiers of Information Technology and Electronic Engineering*, **22**(7), 915–25. DOI: 10.1631/FITEE.2000065

Fernández-Rodríguezа, E. and Rowlandb, Z. (2022). Current status and future trends in radio link interference research for the planning of sustainable geocentric satellite constellations. In: *73rd International Astronautical Congress (IAC),* Paris, France, 18-22 /9/ 2022.

Fourati, F. and Alouini, M.S. (2021). Artificial intelligence for satellite communication: A review. *Intelligent and Converged Networks*, **2**(3), 213–43. DOI: 10.23919/ICN.2021.0014

Kaur, R., Goyal, N., Goyal, D. and Goyal, N. (2017). Analysis of energy detection and cyclostationary feature detection under fading channels in CRNs. *Communication and Computing Systems*, **n/a**(n/a) 327–34. DOI: 10.1201/9781315152651-45

Liu, C. and Gryllias, K. (2020). A semi-supervised support vector data description-based fault detection method for rolling element bearings based on cyclic spectral analysis. *Mechanical Systems and Signal Processing*, **140**(n/a), 106682. DOI: 10.1016/j.ymssp.2020.106682

Nasser, A., Hosseini, S.A., Zargari, M.D. and Duong, T.Q. (2021). Spectrum sensing for cognitive radio: Recent advances and future challenges. Sensors, **21**(7), 2408. DOI: 10.3390/s21072408

Ren, S., Wang, Q., Wang, M. and Yu, C. (2021). An adaptive compressive wideband spectrum sensing algorithm based on least squares support vector machine. *IEEE Access*, **9**(n/a), 116594–603. DOI: 10.1109/ACCESS.2021.3104162.

Sabir, B., Yang, S., Nguyen, D., Wu, N., Abuadbba, A., Suzuki, H. and Nepal, S. (2024). Systematic Literature Review of AI-enabled Spectrum Management in 6G and Future Networks. *arXiv preprint arXiv,* **2407**(n/a). 10981. DOI: 10.48550/arXiv.2407.10981

Sharma, S.K., Chatzinotas, S. and Ottersten, B. (2016). In-line interference mitigation techniques for spectral coexistence of GEO and NGEO satellites. *International Journal of Satellite Communications and* Networking, **34**(1), 11–39. DOI: 10.1002/sat.1127

Sirohiya, S., Baghel, A. and Bhatia, V. (2022). Enhancement of Spectrum Efficiency in Satellite Communication Applying Prediction Model of Machine Learning Technique. In: *Second International Conference on Advances in Electrical, Computing, Communication and Sustainable Technologies (ICAECT).* Bhilai, India 21-22 /4/ 2022. DOI:10.1109/ICAECT54875.2022.9808054

Soares, M.D., Passos, D. and Castellanos, P.V.G. (2023). Cognitive Radio with Machine Learning to Increase Spectral Efficiency in Indoor Applications on the 2.5 GHz Band. *Sensors*, **23**(10), 4914. DOI:10.3390/s23104914

Venkatapathi, P., Khan, H., Rao, S.S. and Immadi, G. (2024). Cooperative spectrum sensing performance assessment using machine learning in cognitive radio sensor networks. *Engineering, Technology and Applied Science Research*, **14**(1), 12875–9. DOI: 10.48084/etasr.6639

Wang, Y., Ding, X. and Zhang, G. (2020). A novel dynamic spectrum-sharing method for GEO and LEO satellite networks. *IEEE Access*, **8**(n/a), 147895–906. DOI: 10.1109/ACCESS.2020.3015705

Zaeemzadeh, A. (2017). Reliable Spectrum Hole Detection in Spectrum-Heterogeneous Mobile CRNs via Sequential Bayesian non-Parametric Clustering. MSc Thesis, University of Central Florida, Florida, US. Available at: https://stars.library.ucf.edu/cgi/viewcontent.cgi?article=6687&context=etd (accessed on 01/02/2025).

Zhang, C., Hu, Z., Guo, T.N., Qiu, R.C. and Currie, K. (2012). Cognitive Radio Network as Wireless Sensor Network (III): Passive target intrusion detection and experimental demonstration. *IEEE Radar Conference*, **n/a**(n/a), 0293–8. DOI: 10.1109/RADAR.2012.6212173

Zhang, Y. (2022). *Machine Learning-Based Full-Duplex Communications and CRNs*. PhD Thesis, King's College, London, UK.

Scientific Journal of King Faisal University:
Basic and Applied Sciences

Modified Efficient Net of Chest X-Ray Images for Lung Disease Classification Using Transfer Learning Approach

Sonia Verma[1], Ganesh Gopal Devarajan [1] and Pankaj Kumar Sharma [2]

[1]Department of Computer Science and Engineering, Faculty of Engineering and Technology, SRM Institute of Science and Technology, Delhi - NCR Campus, Delhi - Meerut Road, Modinagar, Ghaziabad, Uttar Pradesh 201204, India

[2]Department of Computer Science ABES Engineering College, Ghaziabad, UP, India

LINK	RECEIVED	ACCEPTED	PUBLISHED ONLINE	ASSIGNED TO AN ISSUE
https://doi.org/10.37575/b/eng/240032	29/07/2024	04/03/2025	04/03/2025	01/06/2025
NO. OF WORDS	**NO. OF PAGES**	**YEAR**	**VOLUME**	**ISSUE**
5703	8	2025	26	1

ABSTRACT

Chest X-ray (CXR) studies can be automatically detected, and their locations can be identified using artificial intelligence in healthcare. The World Health Organization reports that lung diseases such as COVID-19, pneumonia, tuberculosis, and lung opacity contribute significantly to global mortality. The overlapping symptoms of these diseases make accurate identification difficult. To accelerate the process and enable early detection, machine learning (ML) and traditional approaches are combined to improve disease detection. CXR images are used in this study to classify lung disease using ML and transfer learning (TL). The study primarily consists of three parts: firstly, the data augmentation technique addresses class imbalance; secondly, the image enhancement and pre-processing technique improves image quality; and finally, the TL approach EfficientNetB1 extracts features and uses weighted binary cross-entropy loss to handle a large number of false positive cases. Fine-tuning hyperparameters significantly enhance performance. AUC-PR, ROC-AUC, F1-score, and precision are among the metrics that demonstrate the proposed method to be more accurate and effective than other TL models.

KEYWORDS

Computer vision, COVID-19, deep learning, efficientNetB1, pneumonia, transfer learning

CITATION

Verma, S., Devarajan, G.G. and Sharma, P.K. (2025). Modified efficient net of chest x-ray images for lung disease classification using transfer learning approach. *Scientific Journal of King Faisal University: Basic and Applied Sciences*, **26**(1), 35–42. DOI: 10.37575/b/eng/240032

1. Introduction

Radiologists are instrumental in diagnosing and treating medical conditions by utilizing various imaging techniques, including computed tomography (CT) and positron emission tomography scans, magnetic resonance imaging, and chest X-ray (CXR). Nevertheless, using such a wide range of medical equipment presents challenges, the most difficult of which is interpreting chest radiographs (Cheng *et al.,* 2021). As modern industry and transportation have developed rapidly, air pollution has become a serious problem, leading to a significant increase in the prevalence of lung disease. Even highly qualified radiologists invariably commit 3%–6% of clinical errors in CXRs, and between 20% and 50% of reports are faulty (Wang *et al.,* 2019). According to a World Health Organization report, chronic obstructive pulmonary disease (COPD) is the third leading cause of death globally. Reports from various parts of the world have recently highlighted numerous cases of lung infections, including pneumonia, COVID-19, and lung opacity. Figure 1a shows the last three years' data of confirmed cases, while Figure 1b depicts the mortality rate of lung-affected COVID-19 patients (Mathieu *et al.*, 2020). Similar lung conditions, such as pneumonia, COVID-19, lung cancer, and lung opacity, are currently affecting several people worldwide. The healthcare sector has undergone a digital transformation that includes early diagnosis, virtual consultation, and remote access to reduce disease transmission (Kasinathan and Jayakumar, 2022). Due to the shortage of physicians and radiologists, the pandemic has brought about a new wave of complications in the healthcare sector, increasing the mortality rate of patients with chronic conditions, particularly those affected by cancer, diabetes, and heart disease.

Machine learning (ML) can be highly beneficial to healthcare informatics in terms of disease prognosis, classification, and screening. CT scans and CXR images are frequently used for lung disorders. CXRs provide a straightforward and affordable imaging method for grading and diagnosing lung conditions. The radiation exposure for a 2D projection image of the chest and lungs produced by X-rays is relatively low. Despite its limitations in 3D lung visualization, chest CT, which provides 3D imaging, is steadily gaining ground. Chest CTs are routinely used to identify lung nodules, although they expose individuals to more radiation than usual (Chowdhury *et al.,* 2020). However, in less developed countries, CXR continues to be the primary tool for diagnosing or screening tuberculosis. According to Tan *et al.,* (2018), radiologists can use these radiological imaging techniques in screening settings to identify lung problems or recommend additional testing. As a result, early lung disease identification and classification have become increasingly critical. ML and deep learning (DL) (Kumar, 2020) play an important role in handling and accelerating such processes.

This research aims to improve object detection in CXR for disease identification. The three models – YOLOv5, EfficientDet, and Faster R-convolutional neural network (CNN) – each contributed to the study in different ways. In Faster R-CNN (Ravi *et al.,* 2023), a ResNet50 backbone is used, along with a region proposal network (RPN) and classifier. RPNs generate region proposals, while classifiers utilize ResNet50 (Geddes, 2020) to classify objects based on predicted bounding box coordinates. Models with anchor boxes of varying sizes and aspect ratios can handle objects in various shapes and sizes. In YOLOv7 (Syed *et al.,* 2023), bounding boxes and class probabilities are predicted by considering one object at a time. This version allows users to choose between different network architectures, including CSPDarknet53 and CSPResNeXt50. For specific datasets, K-means clustering enhances the model's efficiency and accuracy by optimizing anchor box sizes (Li *et al.,* 2022) and aspect ratios.

1.1. Paper Contribution:

This paper makes the following substantial contributions:

1. Image enhancement and pre-processing are applied to enhance and standardize images.
2. A data augmentation technique is used to balance the dataset.

Corresponding Author: Sonia Verma 0091 8218634036, sonverma@gmail.com

However, this approach may reduce the number of generalization errors, particularly for classes with smaller sample sizes.
3. Feature extraction is performed using the transfer learning (TL) approach, EfficientNetB1, along with weighted binary cross-entropy loss to manage the high number of false positive cases.
4. The effectiveness of mEffCxrNet is evaluated in comparison to ResNet155v2, DenseNet-121, VGG-19, Mask R-CNN, bidirectional LSTM, MobileNetV2 with exponential fine-tuning, wavelet transformation, and EfficientNet, among others.

2. Literature Review

The lungs are among the most exposed organs in the body and have been a leading cause of death and disability for the past 200 years (Geddes, 2020). Developing a model that effectively analyses medical images is challenging because medical images are inherently more complex and heterogeneous than standard images. Numerous studies have explored the use of CXR images to identify various lung infections, including but not limited to pneumonia and COVID-19 (Ravi *et al.,* 2023).

TL and CNNs have proven effective in automatically extracting features from unstructured data, such as images, due to their advanced feature extraction capabilities. This research presents a comparative analysis of lung diseases in Table 1. The study focuses on a realistic dataset of patients with COPD (Hemdan *et al.,* 2020) to demonstrate the model's effectiveness in detecting COVID-19 and other lung diseases (Singh *et al.,* 2021).

Table 1. Literature summary and limitations

Author	Methodology	Features	Challenges
Syed *et al.,* (2023).	Optimised ResNet50v2	PF-positive individuals can be automatically classified using chest CT images based on the diagnostic model.	Did not conduct cross-validation experiments to confirm the reliability of the findings.
Li *et al.,* (2022)	Inception-ResNet v2	The prediction model combines Attention-U-Net and Inception-ResNet to improve the accuracy of CXR predictions.	Model complexity can be optimized due to insufficient computational training data.
Raza et al., (2023).	Inception-ResNet-v2	Achieves high classification accuracy.	The dataset is limited.
Yaseliani *et al.,* (2022).	VGG16 + VGG19	Displays improved performance metrics.	Requires fine-tuning.
Souid *et al.,* (2021).	MobileNet V2	Incorporates extra global average pooling and a dense layer.	AUC = 0.762 and F1-score = 0.652 are too low.
Cheng *et al.,* (2021).	DSAE	Effectively removes noise from the input signal.	Training is expensive due to complex data.
Hussain *et al.,* (2021)	CNN	The proposed method creates a sizable dataset to evaluate classification algorithms.	Model performance is low due to a limited number of images.
Ismael and Şengür (2021)	CNN	Achieves better classification accuracy using the kernel function.	Does not consider various lung diseases.
Karthik *et al.,* (2021).	CNN	Pneumonia classes can be optimally distinguished based on learning differentiating patterns.	Ineffective in learning definite patterns to assist radiologists in disease identification.
Cheng *et al.,* (2021).	BAT	Enhances local search capabilities and algorithm stability.	The dataset is small.
Bharati *et al.,* (2020).	ResNetv2	Uses ResNetv2 to categorise and locate abnormal regions.	Precision = 0.64, Recall = 0.62, and Accuracy = 70.8% – all relatively low.
Panwar *et al.,* (2020).	Grad-CAM	CXR images received a strong response.	Classification accuracy was not very high.
De Moura *et al.,* (2020).	DL	Provides reliable and rigorous analysis to assist clinical decision-making.	Deep learning is difficult and expensive in practice.
Arias-Londoño *et al.,* (2020).	DNN	Aims to improve specificity and classification accuracy.	Error distribution among classes remains an issue.
Rajaraman *et al.,* (2020).	CNN	Trimmed techniques precisely pinpoint the prominent ROI.	Requires an enormous amount of training data.

The literature review identified several gaps:

1. Effectively analyzing medical images is challenging due to limited data availability and their complexity.
2. Most TL methods overlook challenges such as improving X-ray image quality and handling class imbalance, which hinder the accurate identification of infected areas during feature extraction.
3. Existing approaches often extract features from complete lung images, disregarding the relevance of infected lung regions.
4. High training times pose significant challenges for CXR image classification and detection. The proposed model addresses this by achieving efficient classification on large datasets with reduced training time.

3. Methodology

The methodology aims to improve the accuracy and reliability of the CXR model by enhancing and standardizing images. Image enhancement and pre-processing techniques are applied to reduce noise and ensure uniformity across datasets. A data augmentation technique is used to address data imbalance by enlarging underrepresented classes and reducing overfitting risks. This approach minimizes generalization errors for smaller classes, ensuring balanced learning. Feature extraction is performed using the EfficientNetB1 TL model, which captures intricate patterns in medical images. A weighted binary cross-entropy loss function is integrated into the model to effectively manage the disproportionately high number of false positives that arise in medical diagnosis.

3.1. Pre-processing: Image Enhancement:

3.1.1. Standardisation

Standardizing an image involves subtracting its mean pixel value and dividing the result by its standard deviation. This process converts all images from the original grayscale into a standard grayscale, where similar intensities correspond to similar tissue characteristics, correcting inter-subject intensity variance (Hassan *et al.,* 2022).

Standardization normalizes a random variable by assigning it an expected mean value of 0 and a standard deviation of 1 (Dzierżak, 2019). The Z-test formula guides this procedure:

$$Z = \frac{x-\mu}{\sigma} \quad (1)$$

Based on Equation (1), the standardization formula calculates the value Z using the observed value x, the expected mean μ, and the standard deviation σ.

3.1.2. Class Imbalance

Class imbalance (Muljo *et al.,* 2023) occurs when a dataset contains a disproportionate number of examples from a single class, making it a prominent issue. This may appear as a classification problem with a distinct majority-minority class distinction or as a multiclass classification problem.

Table 2. Augmentation parameters for class balancing

Transformation	Techniques
Flip-horizontally	TRUE
Flip-vertically	TRUE
Rotational-range	20
Shift-width-range	0.2
Shift-height-range	0.2
Zoom-range	0.2
Shear transformation	20

Due to imbalance, the model skews toward predictions for the majority class, making imbalanced datasets problematic. Accuracy also becomes a misleading performance metric in such cases. A data augmentation technique is employed to balance the class distribution. A dataset containing an uneven ratio of samples between the majority and minority classes is referred to as class imbalance.

Shear transformation is a method that fixes one axis of an image while stretching the other at a predetermined angle, for example, a 0.2 shear angle. Random zoom transformation was performed using the zoom range argument; a value greater than one indicates that the images were zoomed in, while a value less than one indicates that they were zoomed out. To balance the dataset, augmented images were created for minority classes based on the maximum size of the majority class. Out of four classes, the majority class, 'Normal,' has 7,146 samples; thus, the other minority classes were sampled to match this number. The augmentation process increased the number

of images by 13,737, bringing the total training dataset size to 28,584. Table 2 presents the data augmentation transformation techniques applied to balance the data.

3.1.3. EfficientNet Model

The EfficientNetB1 method was introduced by Google AI (Raza *et al.,* 2023) to solve the problem of accurate prediction using an efficient approach. The EfficientNet algorithm was initially developed by Tan and Le in 2019. This TL algorithm performs well on both common and ImageNet image classification tasks.

To classify lung diseases from CXR images, we fine-tuned the EfficientNetB1 architecture. Figure 1 depicts the model architecture of mEffCxrNet. Optimizing the network's depth, width, and resolution can improve performance by scaling the network model.

Figure 1. Architecture of model

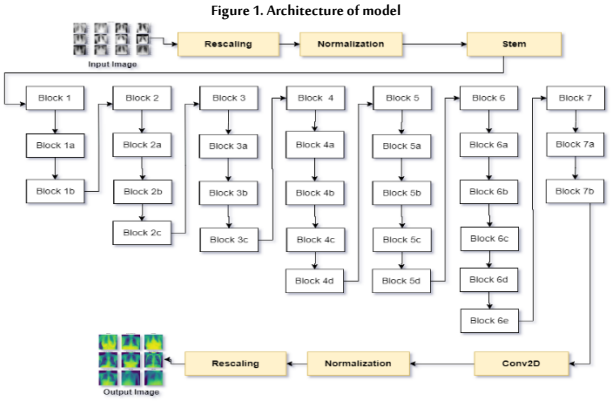

It can enhance local search capabilities and guarantee algorithm stability. It achieves excellent accuracy and performs better than other methods with a huge amount of data. The CXR images receive a strong response; COVID-19 cases are not identified in the present scenario, and the cropped techniques precisely identify the prominent ROI. The amount of data needed for training is enormous.

In order to scale EfficientNet (Tan and Le, 2020) in three aspects — width (w), depth (d), and resolution (r) — it includes a fixed set of scaling coefficients that follow predefined guidelines. For n output classes, the likelihood distribution is computed using the SoftMax function, given in Equation (2). Here, x, y, and z are constants computed through a hyperparameter tuning process known as grid search, where φ is user-specified and manages computational resources accordingly.

$$d = x^{\varphi}$$
$$w = y^{\varphi}$$
$$r = z^{\varphi}$$
$$s.t\ \alpha.\beta^2.\gamma^2 \approx 2$$
$$\alpha \geq 1, \beta \geq 1, \gamma \geq 1 \quad (2)$$

Scaling coefficients were applied to the baseline network to achieve the desired target model size. The accuracy of images increases marginally as the image width or resolution increases. To solve this problem, it is important to adjust all these dimensions simultaneously.

It is possible to express the CNN using the following expression:

$$O_i = f_i$$

Where f_i represents the operator, t_o represents the output image and X_i represents the input image. The input CXR image X_i has the shape (H_i, W_i, C_i), where spatial dimensions are H_i, W_i, and the channel dimension is C_i so the ConvNet of the EfficientNet-B1 model is represented as a series of layers: $L = f_k \ldots \ldots \ldots \ldots f_1(X_i)$ and finally, ConvNet is represented as:

$$N = \bigcirc_{i=1}^{s} f_{Li}(X_{H_i,W_i,C_i}) \quad (3)$$

Here, the shape of the input image X_i is represented by H_i, W_i, C_i, and f_{Li} *represents* f_i applied l_i times in stage i. To optimize the outcome, it is important to scale the model by adjusting the network length (L_i), and with shape H_i, W_i.

$$s.t.\ N(d, w, r) = \bigcirc_{i=1}^{s} f_{d.Li}(X_{r.H_i, r.W_i, w.C_i}) \quad (4)$$

In Equation (4), N illustrates the network with predefined baseline model parameters F_i, L_i, H_i, W_i, C_i, where i is the stage number. These parameters are scaled with width, resolution, and depth d, r, w. EfficientNet-B1 has 344 layers with three color channels (R, G, and B), with each input image having a size of 400 × 400 pixels. The resolution of subsequent layers is scaled down to reduce the feature map size while the width is increased for accuracy. For instance, the second convolution (CNN) layer consists of W = 16 filters, and the following convolution layer has W filters. For example, Conv2D has W = 16 filters, while the third CNN layer has W = 24 filters. The final layer, which is fed to the fully connected layer, has an upper limit of D = 1469 filters.

By combining Plateau, Early Stopping, and Model Checkpoint Keras callbacks, the model effectively addresses some of their drawbacks.

Algorithm: Pseudo-Code for mEffCxrNet

Input: Covid19-Radiography-Database

Output: A model for lung disease classification

```
Begin
1   data ← load dataset
2   check_ims_in_folder ← data
3   Check_label_distribution ← x
4   Found:
5       Class_imabalace ← dataset(positive sample>>negative sample)
        b_x ← balance dat (data_augmentation)
6       Add: train_ ata(x) and test_dat (y)
7   x,y ← spli (x1,x2,y1,y2)
8   Standardization ← Z = (x − μ)/σ
9   img_gen:
        img_size = (300,300,1)
        b_size = 64
        t_size = (300,300)
10  img_merge ← x,y
    img_split ← x,y
11  L_cross_entropy ← cross_w − loss_entropy
12      Restore_be t_weight = True
13      classifier ← train_model using b_x
        model.fit ← EfficientNetB1(mEffCxrNet)+additional layer
            Activation ← Softmax, relu
            k_r ← l2(l = 0.016)
            a_r ← l1(0.006)
            b_r ← l1(0.006)
            momentum ← 0.99
            optimizer ← Adamax
14      Predict ← cross_validation with model
        computes evaluation_metrics
End
```

Early stopping based on user-specified accuracy criteria and dynamic learning rate modifications is possible due to the weighted cross-entropy loss. The cross-entropy loss contribution from the i^{th} training dataset is computed as follows for each CXR image in this study:

$$L_{cross\_entropy(x_i)} = -(\ y_i\ \log(f(x_i)) + (1 - y_i\ )\log(1 - f(x_i))) \quad (5)$$

Where $f(x_i)$ represents the model output or the likelihood of a

correct classification while (x_i) and (y_i) denote the input characteristics and corresponding label, respectively. In each training scenario, where $(y_i) = 0\ or\ (1 - y_i) = 0$, only one of these terms contributes to the loss (as the other term is divided by zero and becomes equal to zero).

The average cross-entropy loss across a training set of N instances, denoted as D, can be expressed in the following manner:

$$L_{cross\_entropy} = -\frac{1}{N}\left(\sum_{n_{pos}} \log\left(f(x_i)\right) + \sum_{n_{neg}} \log\left(1 - f(x_i)\right)\right) \quad (6)$$

In scenarios where positive training instances are significantly fewer, the negative class dominates the loss. Whether each class contributes positively or negatively is determined based on its total contribution across all training cases related to the pathological condition:

$$freq_p = \frac{n_{pos}}{w_{pos}}, \text{and} \quad freq_n = \frac{n_{neg}}{w_{neg}} \quad (7)$$

Where n_{pos} and n_{neg} represent the number of positive and negative examples, respectively. To equalize the overall contribution of each class, each instance is multiplied by the class-specific weight factors w_{pos} and w_{neg}. The desired balancing condition is:

$$w_{pos} * freq_p = w_{neg} * freq_n \quad (8)$$

which we can achieve simply by applying the weightings. The positive and negative labels within each class would have the same overall contribution to the loss function, as seen in the above image if these weightings were applied. Now, let us implement such a loss function. The final weighted loss for each training case after calculating the weights is:

$$L_{cross\_entropy(x_i)} = -\left(w_{pos} y \log\left(f(x)\right) + w_{neg}(1 - y)\log(1 - f(x))\right) \quad (9)$$

By reducing the weighted cross-entropy loss, the model becomes less biased towards the majority class and improves its ability to classify all classes accurately, particularly those underrepresented in the dataset.

4. Results

4.1. Dataset Description:

Evaluation of the proposed framework is conducted using publicly available Kaggle Mathieu *et al.*, (2020) that is, the COVID-19 Radiography Dataset (Nguyen *et al.*, 2020). The dataset contains 21,212 images. Upon the initial release, our database contained 219 CXR images of COVID-19, along with 1,341 CXR images of standard pneumonia and 1,345 CXR images of viral pneumonia.

Figure 2: A visualization of the dataset's class distribution and description

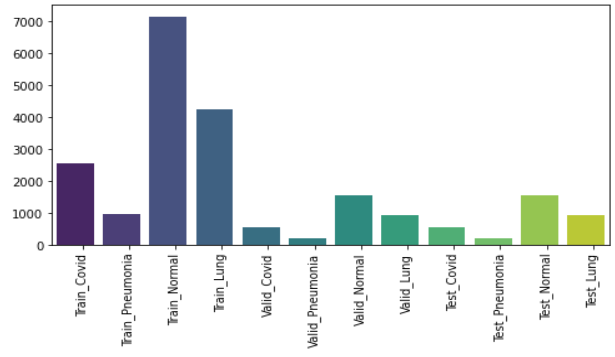

Figure 2 illustrates the basic distribution of the proposed dataset, which combines data sources into a single dataset repository containing raw CXR image data from a lung-infected patient. Each folder was checked for available data and label distributions. After the distribution, it was noticed that the positive samples were significantly more significant than the negative samples, indicating an imbalance in the class.

Therefore, we applied class balancing and measured the intensity distribution of pixels before and after standardization for image enhancement. To build the model, an augmentation layer, a pre-processing layer, and a custom lambda layer were added using EfficientNetB1 with the pre-trained image. We use weighted binary cross-entropy loss to handle false positives, aiming to achieve the best result.

Since there are many more X-ray images of pneumonia, the model weighs these cases heavily, leading to incorrect classifications. Thus, we adjust this bias and attempt to force the model to balance normal and pneumonia images. The performance metrics evaluate the model's effectiveness.

4.2. Performance Measures:

The hardware and software environment used in the experiment are as follows: Windows 10 Pro edition with a 64-bit operating system, x64-based processor, Intel(R) Core(TM) i5-8250U CPU @ 1.60GHz–1.80GHz, 8 GB memory, and GPU100 with 16 GB memory. Python was used as the primary programming language to execute the work.

Performance metrics, including accuracy, specificity, recall, precision, false positive rate (FPR), false negative rate (FNR), and F1-score, were calculated to assess the TL models. Each unique model's confusion matrix was used to derive these parameters. The most commonly used metrics in image annotation were employed to evaluate the effectiveness of the proposed model, including:

Accuracy: Accuracy is a metric used to evaluate the effectiveness of classification and regression methods. It is defined as the ratio of correct predictions to the total number of predictions:

$$Accuracy = \frac{t_p + t_n}{t_p + t_n + f_p + f_n} \quad (10)$$

Here, t_p, t_n, f_p and f_n represent true positives, true negatives, false positives, and false negatives, respectively.

Precision (p): Based on the number of predicted values that are actually correct, precision indicates the proportion of accurately made positive predictions. It is calculated as follows:

$$p = \frac{t_p}{t_p + f_p} \quad (11)$$

Recall(r): Recall measures the proportion of correct positive predictions among all actual positive cases:

$$r = \frac{t_p}{t_p + f_n} \quad (12)$$

$F1 - score$: F1-score is a metric used to evaluate binary classification models based on the predictions made for the positive class. It is calculated by combining precision and recall while assigning equal weight to both. The formula is:

$$F1 - score = \frac{2 * t_p}{2 * t_p + f_p + f_n} \quad (13)$$

Specificity (S_p): Specificity measures the percentage of patients correctly identified as normal (having no lung disease). Patients with any lung disease, such as lung opacity, are categorized as TN and FP – those who are actually not suffering from lung opacity. This metric determines which lung disease belongs to which class:

$$S_p = \frac{t_n}{t_n + f_p} \quad (14)$$

Table 3 presents the performance measures and their values, demonstrating the effectiveness of the proposed model.

Table 3. Performance measures

Measure	Value(%)
Precision	99.44
Recall	99.26
Sensitivity	99.26
Specificity	99.89
Positive Predictive Value (Precision)	99.45
Negative Predictive Value	99.85
False Positive Rate	0.11
False Discovery Rate	0.55
False Negative Rate	0.74
Accuracy	99.78
F1 Score	99.35
Matthews Correlation Coefficient	99.22

Matthews Correlation Coefficient (MCC): According to the confusion matrix, MCC yields a high score only if the model performs well in all four categories (TP, TN, FP, FN), maintaining a balance between the size of positive and negative variables in the dataset:

$$\frac{t_p * t_n - f_p * f_n}{\sqrt{(t_p+f_p) * (t_p+f_n) * (t_n+f_p) * (t_n+f_n)}} \quad (15)$$

4.3. Result Analysis

An Adamax optimizer was used for learning rate optimization over 20 epochs with 75% training data, 15% validation data, and 15% testing data. The Adamax optimizer significantly enhanced model performance, and fine-tuning with optimized learning rates further improved accuracy.

Figure 3. Training and validation curve

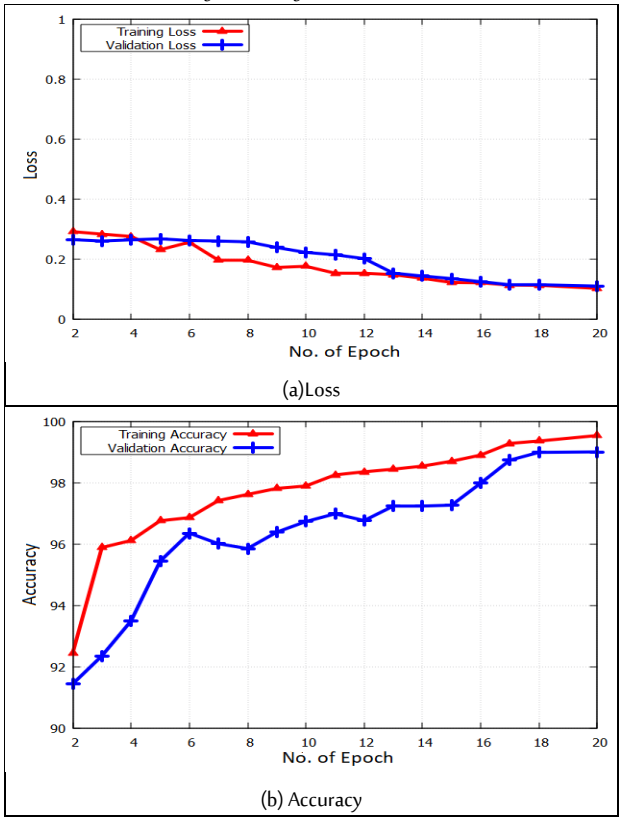

(a)Loss

(b) Accuracy

Figure 4. Precision and recall curve

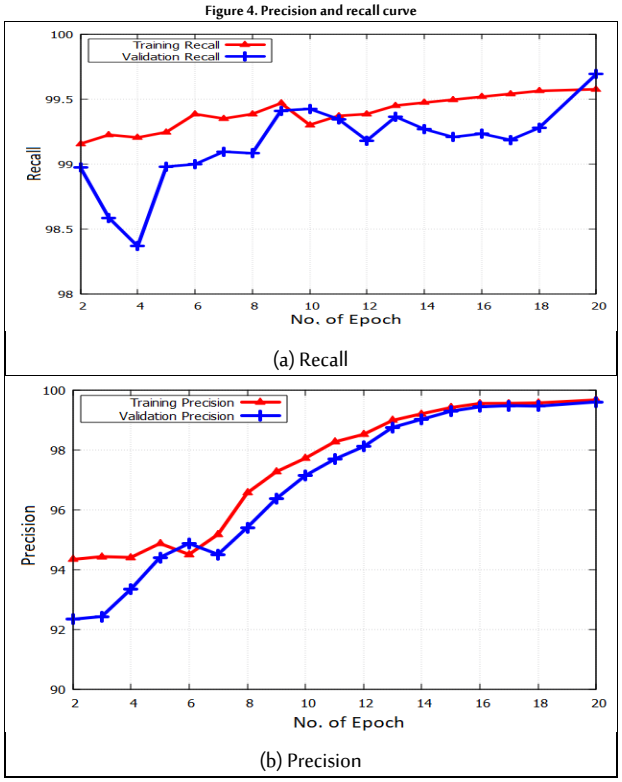

(a) Recall

(b) Precision

Figure 5: Performance Measure Graph

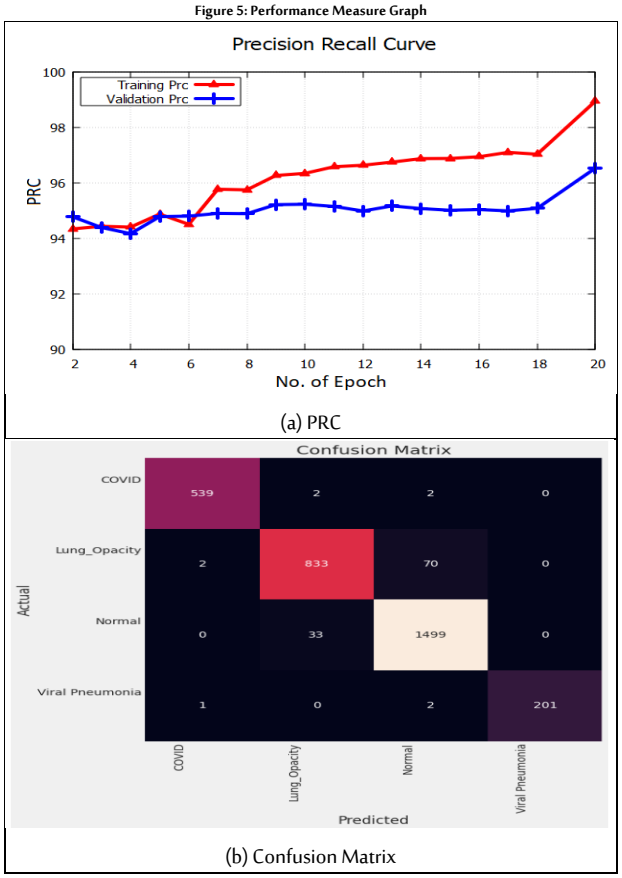

(a) PRC

(b) Confusion Matrix

Figure 3(a–b) shows the loss and accuracy values during the validation and training phases of the proposed model. In Figure 5(a–b), the y-axis represents loss/accuracy, and the x-axis represents the number of epochs. Figure 4(a–b) shows Precision and Recall values on the y-axis with a number of epocs on the x-axis. Figure 5(a)

represents the proportion of true positive predictions among all positive predictions made, while Figure 5(b) shows the ratio of true positive predictions to the total number of actual positive cases. The classification decisions were analyzed using confusion matrices and contingency tables. Additionally, the ROC curves in Figure 6(a) illustrate the decision-making process in diagnostic tests, where the ROC graph shows the relationship between the true positive rate (Sensitivity, Y-axis) and the false positive rate (Specificity, X-axis).

4.4. Comparative Analysis:

Based on the experiment results, it can be concluded that the proposed model offers substantial improvements in terms of accuracy, speed, and cost for lung disease classification using CXR images. The suggested model outperforms other models in statistical metrics, as shown in Table 4, leading to improved generalization, better accuracy, and fewer incorrect predictions.

Table 4. Comparison with state-of-the-art methods

Reference	Method	Accuracy	Precision	Recall	F1-Score	Chest X-ray images
Chakraborty *et al.*, (2022)	VGG-19	97.11	97	97	96	3,797
Fernando *et al.*, (2022)	ResNet152V2	98.96	97.52	98.64	98.25	5,386
Kaur and Kulkarni (2024)	MobileNetV2 + Exponential Fine-Tuning	96.89	96.72	96.71	96.9	9,475
Indumathi and Siva (2023).	Mask R-CNN + Bidirectional LSTM	99.16	99.18	99.16	99.14	13,808
Al-Ahmadi and Mohammad (2023)	Wavelet Transformation and EfficientNet	97	96	89	92	5,544
Showkat and Qureshi (2022).	ResNet Model	95	95.65	94	95	1,428
Our Model		99.39	98.89	97	97	21212

Figure 6(b) shows a comparative analysis of the proposed model with other models such as VGG-19, ResNet50, MobileNetV2 + Exponential Fine-Tuning, Deep CNN + ResNet50, Mask R-CNN + Bidirectional LSTM, Wavelet Transformation and EfficientNet, ResNet Model, CoviXNet, and Wide ResNet50. The analysis shows that mEffCxrNet performed better in terms of accuracy and speed.

Figure 6. Decision-making measures

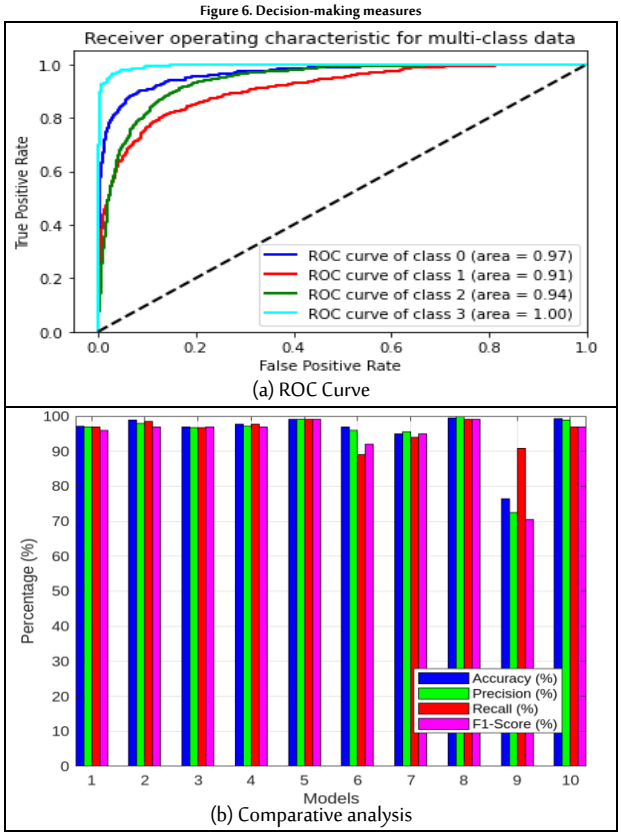

(a) ROC Curve

(b) Comparative analysis

5. Conclusion and Future Work

We can use a categorization system to compare CXR images of COVID-19 patients and those with normal pneumonia. COVID-19 significantly disrupts daily life, affecting everything from public healthcare to the global economy. This work introduced the mEffCxrNet model, which employs CXR to classify positive lung disease. The proposed model, mEffCxrNet, successfully provides precise diagnoses for four class divisions: COVID-19, lung opacity, viral pneumonia, and normal. To the best of our knowledge, the suggested framework achieves the highest accuracy on the datasets used in the experiments, with a classification accuracy of 99.70%, precision of 98.68%, recall of 98.67%, F1-score of 98.67%, and the lowest error rate of 1.33%. It consists of multiple layers, including an input layer, the primary capsule, and the first convolutional layer. Moreover, models can be retrained and reused, and image analysis can help identify further abnormalities. In this research, the use of CXR images – a practical, effective, and affordable testing method – has been investigated for the quick and accurate identification of COVID-19 in patients. Using our dataset, we experimented with and examined many pre-trained models. On the top-performing models, we also performed a 4-class classification. Future versions of this method may be implemented as a real-time CT scan by integrating high-end GPUs, cloud computing, patient data security, and appropriate software interfaces.

Biographies

Sonia Verma

Department of Computer Science and Engineering, Faculty of Engineering and Technology, SRM Institute of Science and Technology, Delhi - NCR Campus, Delhi - Meerut Road, Modinagar, Ghaziabad, Uttar Pradesh 201204, India, 0091 8218634036, sonverma@gmail.com

Sonia, an Indian researcher, holds M.Tech. in Computer Science and Engineering and is currently pursuing a Ph.D. With over 10 years of experience in academia and industry, she serves as an Assistant Professor at ABES Engineering College, Ghaziabad (U.P.). She is a reviewer for SCI-indexed journals, with research interests in Machine Learning, Artificial Intelligence, IoT, and Cloud Computing. She has published extensively in reputed SCI/Scopus-indexed journals and conferences.

ORCID: 0000-0002-2384-472X

Ganesh Gopal Devarajan

Department of Computer Science and Engineering, Faculty of Engineering and Technology, SRM Institute of Science and Technology, Delhi - NCR Campus, Delhi - Meerut Road, Modinagar, Ghaziabad, Uttar Pradesh 201204, India,

0091 9444540447, dganeshgopal@gmail.com

Prof. Ganesh (Member, IEEE) received his Ph.D. in Computer Science and Engineering from VIT University, Vellore, in 2015. With over 17 years of research and teaching experience, he is a Professor at the School of Computing Science and Engineering, SRM Institute of Science and Technology, Chennai. He has served as a Technical Program Committee member, Program Committee member, and Session Chair at prestigious international conferences and is a member of professional bodies such as ACM and CSI.

ORCID: 0000-0003-0036-7841

Pankaj Kumar Sharma

Department of Computer Science, ABES Engineering College, Ghaziabad, India, 00919899346360, pankaj.sharma@abes.ac.in

Prof. Pankaj is a distinguished scholar in Computer Science with over 18 years of experience in academia and industry. He holds a Ph.D. and an M.Tech. in Computer Science and has made significant contributions to System Modeling & Simulation, Artificial

Intelligence, Machine Learning, Data Analytics, and Wireless Mobile Ad Hoc Networks. His research expertise spans multiple cutting-edge domains, reflecting his dedication to advancing technological innovation and academic excellence.

ORCID: 0000-0003-2793-6100

Data Availability Statement

The data that support the findings of this study are available on request from the corresponding author.

Acknowledgments

The authors extend their appreciation for the continued support of SRM University.

Funding

This research received no external funding.

Conflicts of Interest

No conflicts of interest exist.

References

Al-Ahmadi, S. and Mohammad, F. (2023). Pattern recognition of omicron variants from amalgamated multi-focus EEG signals and X-ray images using deep transfer learning. *Egyptian Informatics Journal,* **24**(1), 129–38. DOI: 10.1016/j.eij.2023.01.001

Arias-Londono, J.D., Gomez-Garcia, J.A., Moro-Velazquez, L. and Godino-Llorente, J.I. (2020). Artificial intelligence applied to chest X-ray images for the automatic detection of COVID-19. A thoughtful evaluation approach. *Ieee Access*, **8**(n/a), 226811–27. DOI: 10.1109/ACCESS.2020.3044858

Bharati, S., Podder, P. and Mondal, M.R.H. (2020). Hybrid deep learning for detecting lung diseases from X-ray images. *Informatics in Medicine Unlocked*, **20**(n/a), 100391. DOI: 10.1016/j.imu.2020.100391

Chakraborty, S., Paul, S. and Hasan, K.A. (2022). A transfer learning-based approach with deep cnn for covid-19-and pneumonia-affected chest x-ray image classification. *SN Computer Science*, **3**(n/a), 1–10. DOI: 10.1007/s42979-021-00881-5

Cheng, J., Zhao, W., Liu, J., Xie, X., Wu, S., Liu, L. and Liu, J. (2021). Automated diagnosis of COVID-19 using deep supervised autoencoder with multi-view features from CT images. *IEEE/ACM Transactions on Computational Biology and Bioinformatics*, **19**(5), 2723–36. DOI: 10.1109/TCBB.2021.3102584

Chowdhury, M.E., Rahman, T., Khandakar, A., Mazhar, R., Kadir, M.A., Mahbub, Z.B. and Islam, M.T. (2020). Can AI help in screening viral and COVID-19 pneumonia?. *Ieee Access*, **8**(n/a), 132665–76. DOI**:** 10.1109/ACCESS.2020.3010287

De Moura, J., García, L.R., Vidal, P.F.L., Cruz, M., López, L.A., Lopez, E.C. and Ortega, M. (2020). Deep convolutional approaches for the analysis of covid-19 using chest x-ray images from portable devices. *Ieee Access*, **8**(n/a), 195594–1607. DOI: 10.1109/ACCESS.2020.3033762

Dzierżak, R. (2019). Comparison of the influence of standardization and normalization of data on the effectiveness of spongy tissue texture classification. *Informatyka, Automatyka, Pomiary W Gospodarce I Ochronie Środowiska*, **9**(3), 66–9. DOI: 10.35784/iapgos.62

Fernando, C., Kolonne, S., Kumarasinghe, H. and Meedeniya, D. (2022). Chest radiographs classification using multi-model deep learning: A comparative study. In: *2nd International Conference on Advanced Research in Computing (ICARC)*. Belihuloya, Sri Lanka, 23-24 /02/2022. DOI**:** 10.1109/ICARC54489.2022.9753811

Geddes, D. (2020). The history of respiratory disease management. *Medicine*, **48**(4), 239–43. DOI: 10.1016/j.mpmed.2020.01.007

Hassan, M., Shaikh, M.S. and Jatoi, M.A. (2022). Image quality measurement-based comparative analysis of illumination compensation methods for face image normalization. *Multimedia Systems*, **28**(2), 511–20. DOI: 10.1007/s00530-021-00853-y

Hemdan, E.E.D., Shouman, M.A. and Karar, M.E. (2020). Covidx-net: A framework of deep learning classifiers to diagnose covid-19 in x-ray images. *arXiv preprint arXiv:2003.11055*, **n/a**(n/a), n/a. DOI: 10.48550/arXiv.2003.11055

Hussain, E., Hasan, M., Rahman, M.A., Lee, I., Tamanna, T. and Parvez, M.Z. (2021). CoroDet: A deep learning based classification for COVID-19 detection using chest X-ray images. *Chaos, Solitons and Fractals*, **142**(n/a), 110495. DOI: 10.1016/j.chaos.2020.110495

Indumathi, V. and Siva, R. (2023). An efficient lung disease classification from X-ray images using hybrid Mask-RCNN and BiDLSTM. *Biomedical Signal Processing and Control*, **81**(n/a), 104340. DOI:10.1016/j.bspc.2022.104340

Ismael, A.M. and Şengür, A. (2021). Deep learning approaches for COVID-19 detection based on chest X-ray images. *Expert Systems with Applications*, **164**(n/a), 114054. DOI: 10.1016/j.eswa.2020.114054

Karthik, R., Menaka, R. and Hariharan, M.J.A.S.C. (2021). Learning distinctive filters for COVID-19 detection from chest X-ray using shuffled residual CNN. *Applied Soft Computing*, **99**(n/a), 106744. DOI: 10.1016/j.asoc.2020.106744

Kasinathan, G. and Jayakumar, S. (2022). Cloud-Based Lung Tumor Detection and Stage Classification Using Deep Learning Techniques. *Biomed research international*, **2022**(1), 4185835. DOI: 10.1155/2022/4185835

Kaur, S. and Kulkarni, N. (2024). FERFM: An enhanced facial emotion recognition system using fine-tuned mobilenetv2 architecture. *IETE journal of research*, **70**(4), 3723–37. DOI:10.1080/03772063.2023.2202158

Kumar, D. (2020). Feature extraction and selection of kidney ultrasound images using GLCM and PCA. *Procedia Computer Science*, **167**(n/a), 1722–31. DOI: 10.1016/j.procs.2020.03.382

Li, D., Liu, Z., Luo, L., Tian, S. and Zhao, J. (2022). Prediction of Pulmonary Fibrosis Based on X-Rays by Deep Neural Network. *Journal of Healthcare Engineering*, **2022**(1), 3845008. DOI: 10.1155/2022/3845008

Mathieu, E., Ritchie, H., Rodés-Guirao, L., Appel, C., Gavrilov, D., Giattino, C. and Roser, M. (2020). *Coronavirus (COVID-19) Cases*. Available at: https://ourworldindata.org/covid-cases (acssesd on 13/02/2025)

Muljo, H.H., Pardamean, B., Elwirehardja, G.N., Hidayat, A.A., Sudigyo, D., Rahutomo, R. and Cenggoro, T.W. (2023). Handling severe data imbalance in chest X-Ray image classification with transfer learning using SwAV self-supervised pre-training. *Commun. Math. Biol. Neurosci.*, **2023**(n/a), n/a. DOI: 1028919/cmbn/7526

Nguyen, H., Pham, H.H., Nguyen, N.T., Nguyen, D.B., Dao, M., Vu, V. and Le, L.T. (2020). *Vinbigdata Chest X-Ray Abnormalities Detection*. Available at: https://www. kaggle. com/c/vinbi gdatachest-xray-abnor malit ies-detec tion (acssesd on 13/02/2025)

Panwar, H., Gupta, P.K., Siddiqui, M.K., Morales-Menendez, R., Bhardwaj, P. and Singh, V. (2020). A deep learning and grad-CAM based color visualization approach for fast detection of COVID-19 cases using chest X-ray and CT-Scan images. *Chaos, Solitons and Fractals*, **140**(n/a), 110190. DOI: 10.1016/j.chaos.2020.110190

Rajaraman, S., Siegelman, J., Alderson, P.O., Folio, L.S., Folio, L.R. and Antani, S.K. (2020). Iteratively pruned deep learning ensembles for COVID-19 detection in chest X-rays. *Ieee Access*, **8**(n/a), 115041–115050. DOI: 10.1109/access.2020.3003810

Ravi, V., Acharya, V. and Alazab, M. (2023). A multichannel EfficientNet deep learning-based stacking ensemble approach for lung disease detection using chest X-ray images. Cluster Computing, 26(2), 1181–1203. DOI: 10.1007/s10586-022-03664-6

Raza, R., Zulfiqar, F., Khan, M.O., Arif, M., Alvi, A., Iftikhar, M.A. and Alam, T. (2023). Lung-EffNet: Lung cancer classification using EfficientNet from CT-scan images. *Engineering Applications of Artificial Intelligence*, **126**(n/a), 106902. DOI:10.1016/j.engappai.2023.106902

Showkat, S. and Qureshi, S. (2022). Efficacy of Transfer Learning-based ResNet models in Chest X-ray image classification for detecting COVID-19 Pneumonia. *Chemometrics and Intelligent Laboratory Systems*, **224**(n/a),104534. DOI: 10.1016/j.chemolab.2022.104534

Singh, R.K., Pandey, R. and Babu, R.N. (2021). COVIDScreen: explainable deep learning framework for differential diagnosis of COVID-19 using chest X-rays. *Neural Computing and Applications*, **33**(n/a), 8871–92. DOI: 10.1007/s00521-020-05636-6

Souid, A., Sakli, N. and Sakli, H. (2021). Classification and predictions of lung diseases from chest x-rays using mobilenet v2. *Applied Sciences*, **11**(6), 2751. DOI: 10.3390/app11062751

Syed, A.H., Khan, T. and Khan, S.A. (2023). Deep transfer learning techniques-based automated classification and detection of

pulmonary fibrosis from chest CT images. *Processes*, **11**(2), 443. DOI: 10.3390/pr11020443

Tan, M. and Le, Q. (2019). Efficientnet: Rethinking model scaling for convolutional neural networks. In: The 36th *International conference on machine learning*. PMLR. Long Beach, CA, USA, 10-15/06/2019.

Tan, T., Li, Z., Liu, H., Zanjani, F.G., Ouyang, Q., Tang, Y. and Li, Q. (2018). Optimize transfer learning for lung diseases in bronchoscopy using a new concept: sequential fine-tuning. *IEEE Journal of Translational Engineering in Health and Medicine*, **6**(n/a), 1–8. DOI: 10.1109/JTEHM.2018.2865787

Wang, C., Chen, D., Hao, L., Liu, X., Zeng, Y., Chen, J. and Zhang, G. (2019). Pulmonary image classification based on inception-v3 transfer learning model. *IEEE Access*, **7**(n/a), 146533–141. DOI**:** 10.1109/ACCESS.2019.2946000

Yaseliani, M., Hamadani, A.Z., Maghsoodi, A.I. and Mosavi, A. (2022). Pneumonia detection proposing a hybrid deep convolutional neural network based on two parallel visual geometry group architectures and machine learning classifiers. *IEEE access*, **10**(n/a), 62110–28. DOI**:** 10.1109/ACCESS.2022.3182498

Scientific Journal of King Faisal University:
Basic and Applied Sciences

Experimental Analysis of Oxy-Fuel Combustion in Diesel Engines with Insights on Adaptations and Performance

Raghavendra Ugraram[1], R. Meenakshi Reddy[2] and B. Chandra Mohana Reddy[1]

[1] Department of Mechanical Engineering, Jawaharlal Nehru Technological University Anantapur (JNTUA), Ananthapuramu - 515002, Andhra Pradesh, India.
[2] Department of Mechanical Engineering, G. Pulla Reddy Engineering College, Kurnool- 518007, Andhra Pradesh, India.

LINK	RECEIVED	ACCEPTED	PUBLISHED ONLINE	ASSIGNED TO AN ISSUE
https://doi.org/10.37575/b/eng/250003	13/01/2025	13/03/2025	13/03/2025	01/06/2025
NO. OF WORDS	**NO. OF PAGES**	**YEAR**	**VOLUME**	**ISSUE**
7239	8	2025	26	1

ABSTRACT

Oxy-fuel Combustion (OFC) in diesel engines is a transformative advancement, replacing traditional air intake with pure oxygen to enhance combustion efficiency and enable precise control over engine performance. This study adapted a Conventional Air Combustion (CAC) diesel engine to OFC by sealing the air intake and introducing oxygen directly into the inlet manifold. Precise oxygen injection via a Tomasetto Achille IT01 rail gas injector and enhanced sealing mechanisms ensured a stable, uncontaminated combustion environment, critical for assessing OFC performance. Experimental trials at 25% engine load demonstrated that 0.77 grams of oxygen per cycle maintained stable combustion under OFC. Introducing 40% Exhaust Gas Recirculation (EGR) reduced oxygen consumption to 0.462 grams per cycle. Performance comparisons revealed that Brake Thermal Efficiency (BTE) dropped from 20.1% under CAC to 16.2% in OFC and further to 14.8% in OFC+EGR. Brake Specific Fuel Consumption (BSFC) increased from 420.2 g/kWh in CAC to 473.5 g/kWh in OFC and 527.7 g/kWh in OFC+EGR. These findings underscore the need for optimization to recover efficiency losses. They also establish essential insights into OFC's potential as a cleaner and potentially more efficient combustion method for diesel engines, emphasizing its promise for future advancements.

KEYWORDS

Diesel combustion, engine optimization, oxygen Injection, oxygen injection, specific fuel-consumption, thermal efficiency

CITATION

Ugraram, R., Reddy, R.M. and Reddy, B.C.M. (2025). Experimental analysis of oxy-fuel combustion in diesel engines with insights on adaptations and performance. *Scientific Journal of King Faisal University: Basic and Applied Sciences*, **26**(1), 43–50. DOI: 10.37575/b/eng/250003

1. Introduction

The imperative to reduce emissions and improve fuel efficiency in diesel engines has driven substantial research into alternative combustion techniques. Among these, OFC has emerged as a promising method for achieving near-zero emissions while potentially optimizing combustion performance. In CAC, the presence of nitrogen in the intake air leads to the formation of NOx, which contributes to environmental pollution and health concerns. OFC, by introducing pure oxygen in place of air, eliminates nitrogen from the combustion environment, thereby reducing or even eliminating NOx emissions. This transformative approach could pave the way for cleaner diesel engine technologies, positioning OFC as a potentially viable pathway toward environmentally sustainable combustion systems. OFC has been mainly explored in large-scale applications like gas turbines and coal-fired power plants. Studies on OFC in gas turbines have highlighted efficiency gains and emission reductions (Liu *et al.*, 2012). Carbon capture methods, including OFC, have been assessed for IGCC plants, emphasizing emissions reduction (Kunze and Spliethoff, 2012). Reviews of closed-cycle gas turbines have discussed OFC's role in enhancing power generation efficiency (Olumayegun *et al.*, 2016). A novel combustion cycle involving oxygen and water injection has demonstrated improved thermal efficiency and emissions control (Osman, 2009). The implementation of OFC in diesel engines requires a fundamental redesign of the engine intake system, as traditional air intake setups are not compatible with the requirements for pure oxygen delivery. The air intake manifold must be completely sealed to prevent any ambient air from entering the combustion chamber, as even minor leaks could compromise the oxygen purity and disrupt the combustion process. Precision oxygen injection technology is also essential to achieve stable and efficient combustion. Research in this area emphasizes the importance of accurately metered oxygen delivery for optimizing engine performance (Serrano *et al.*, 2022). Controlled oxygen injections enable researchers to study the effects of oxygen concentration on combustion characteristics under diverse operating conditions, a factor that has been shown to influence thermal efficiency and fuel consumption. While OFC has been shown to dramatically reduce emissions, achieving optimal performance metrics, such as BTE and BSFC, poses a unique set of challenges. Managing these trade-offs requires a comprehensive approach, considering injector design, fuel-oxidizer mixing, and timing adjustments. The potential efficiency losses in OFC highlight the importance of ongoing research to develop optimization strategies that preserve fuel economy while delivering cleaner emissions. Research has discussed the trade-offs associated with OFC in diesel engines, noting that while OFC may reduce NOx and other harmful emissions, it often results in a drop in efficiency due to changes in combustion dynamics (Mobasheri *et al.*, 2020). Studies have also investigated the effects of oxygen-enriched air combustion in diesel engines, focusing on combustion characteristics, engine performance, and emissions. These investigations have demonstrated the trade-offs involved in optimizing oxygen-enriched combustion for improved engine performance and emissions control (Zhao *et al.*, 2018). The exploration of OFC in diesel engines is a crucial step toward developing combustion systems that are both efficient and environmentally responsible. As combustion science advances, it is anticipated that refinements in OFC technology will allow for improved injector designs and enhanced sealing techniques. Ensuring sealing integrity in modified OFC diesel engines is crucial, as even minimal air leaks can lead to reduced oxygen purity, significantly affecting combustion efficiency. Research has examined the thermo-mechanical stress and fatigue life of diesel engine pistons under oxy-fuel combustion conditions, highlighting that the altered combustion environment in OFC can impose different thermal and mechanical stress on engine components, necessitating careful consideration of sealing materials and engine design to maintain performance and durability (Ugraram *et al.*, 2023). Other studies have focused on the injector design for OFC, showing that high-precision injectors could increase BTE by up to 7% under controlled oxygen flow rates. These investigations highlighted the role of injector timing and pulse synchronization in achieving optimal fuel-air mixing and combustion

Corresponding Author: Raghavendra Ugraram 00919036956234, raghuugraram@gmail.com

stability (Patel and Lin, 2020). A micro-motion mass flow meter can be used to monitor oxygen intake, enabling a more precise correlation between oxygen levels and combustion parameters. Research suggests that using Coriolis technology in mass flow meters allows for accurate measurement of oxygen gas flow in real-time, which is critical for optimizing oxygen combustion and engine efficiency. This method ensures precise oxygen control, leading to enhanced combustion stability and improved engine performance in diesel applications (Emerson, 2022). Due to the use of pure oxygen and the absence of nitrogen's dilutive effect, OFC is more prone to combustion instabilities. To address this, insights from studies on knock and irregular combustion phenomena in conventional diesel engines are being explored for adaptation to OFC. Research has analyzed combustion instabilities and control strategies in compression ignition and low-temperature combustion, emphasizing the role of ignition delay, heat release fluctuations, and pressure oscillations. These findings are relevant to OFC, where high oxygen levels and nitrogen absence alter combustion kinetics, increasing instability risks. Studies suggest that injection timing optimization and EGR can enhance stability (Krishnamoorthi and Agarwal, 2022). Additionally, knock characteristics in dual-fuel diesel engines indicate that prolonged ignition delay intensifies knock, which is a key concern in OFC due to oxygen enrichment. Optimizing pilot injection can help mitigate this issue, while poor oxidizer-fuel mixing remains a crucial challenge in OFC's altered combustion environment (Nwafor, 2002). Knock in diesel engines under altitude-induced oxygen depletion has been numerically studied, showing its impact on combustion phasing. While OFC enriches oxygen, improper control can exacerbate knock. Research suggests precise oxygen injection and turbulence enhancement to ensure stable combustion in OFC (Li *et al.*, 2022).

One of the key challenges in OFC is managing the highly reactive nature of pure oxygen combustion, which can lead to issues such as engine knocking, elevated temperatures, and increased oxygen consumption. To address this, researchers have explored the integration of EGR with OFC as a strategy to moderate the oxygen content in the combustion chamber. EGR, which involves redirecting a portion of the exhaust gases back into the intake, can help stabilize combustion by reducing oxygen concentration and lowering peak temperatures. Research has analyzed the integration of EGR with alternative combustion strategies and found that EGR significantly reduced NOx emissions while maintaining combustion stability. Although the study focused on a methanol–diesel reactivity-controlled compression ignition (RCCI) engine, the findings are relevant to OFC applications where EGR plays a crucial role in moderating combustion temperatures and mitigating emissions (Huang *et al.*, 2023). Further experiments highlighted the beneficial impact of EGR on diesel engine performance, particularly in terms of reducing peak combustion temperatures by up to 10%, which helped mitigate NOx emissions (Hountalas *et al.*, 2008). In the context of OFC, integrating EGR with controlled oxygen levels can further stabilize the combustion process by moderating the thermal conditions, thereby enhancing performance and reducing harmful emissions. Similarly, combining EGR with oxygen-enriched air has been shown to reduce NOx emissions by up to 45% while maintaining stable smoke emissions (Zhang *et al.*, 2013). This combination improves combustion efficiency and reduces particulate emissions, offering insights for enhancing OFC performance by balancing oxygen concentration and EGR for better emissions control. Additionally, experimental studies on the effects of OFC and EGR in a homogeneous charge compression ignition engine demonstrated that precisely timed injection at elevated pressure and temperature effectively stabilized combustion, improving thermal efficiency (Kang *et al.*, 2018). Although these findings highlight the emission-related benefits of OFC, they also underscore the need for further experimental validation to improve efficiency and stability.

1.1. Motivation:

Despite significant advancements, current OFC research lacks comprehensive experimental validation under real-world operating conditions, particularly at partial loads where performance and stability remain challenging. Many studies emphasize emissions reduction but fall short of quantifying the efficiencies, performance metrics, and quantity of oxygen. This study aims to bridge these gaps by experimentally evaluating diesel engine performance under OFC and OFC+EGR at a 25% load, focusing on metrics such as Oxygen consumption per cycle, BTE and BSFC. This research seeks to provide new insights into OFC's practical viability, emphasizing combustion stability and performance evaluation.

2. Methods

2.1. Experimental Setup:

The experimental analysis is performed using a naturally aspirated, direct injection, single-cylinder water-cooled four-stroke engine. Table 1 presents the specifications of the engine used in the study.

Table 1. Engine specifications

Parameter	Units	Value
Engine type	%	4-Stroke, Single Cylinder Water-Cooled Diesel Engine
Rated Speed	rpm	1500
Bore Diameter	mm	87.5
Stroke	mm	110
Compression ratio	--	15.6:1
Orifice Diameter	mm	29.6
Loading	--	Electric Loading

2.2. OFC Design and Experimental Configuration:

The successful design and implementation of the OFC system for diesel engines require substantial alterations to the engine structure, specifically focusing on the integration of controlled oxygen injections for combustion enhancement. Central to this process is the modification of the air intake system, where oxygen is directly injected into the intake manifold. This oxygen injection is synchronized with the engine's crank angle, ensuring precise control to optimize combustion efficiency. A mass flow controller is used to regulate the oxygen flow rate, maintaining a stable oxygen concentration throughout the combustion cycle. This ensures that the combustion process is optimized for higher efficiency and lower emissions. Safety is paramount in the implementation of the OFC system. Flame arresters are strategically placed both upstream of the oxygen supply and before the engine to prevent any risk of flashbacks or misfires when operating under high-pressure oxygen conditions. Moreover, the intake system is rigorously sealed to eliminate the possibility of unwanted air ingress, ensuring that only the controlled oxygen enters the combustion chamber. The importance of precise oxygen flow control, system sealing, and safety protocols for successful OFC implementation has been highlighted in previous works. Controlled oxygen enrichment significantly improves combustion efficiency in diesel engines by optimizing fuel oxidation and reducing incomplete combustion. Studies have emphasized the necessity of regulating oxygen flow to maintain stable combustion characteristics (Rajkumar and Govindarajan, 2010). Additionally, safety guidelines stress the critical role of flame arresters and proper intake system sealing in preventing hazards such as flashbacks and misfires, especially in high-oxygen environments. Ensuring these measures enhance both engine performance and operational safety in OFC applications. The careful integration of these design considerations is fundamental for creating a reliable and safe experimental setup, ensuring accurate and repeatable results in OFC studies (Occupational Safety and Health Administration [OSHA], 2009).

2.3. Diesel Engine Adoption:

The diesel engine is modified to operate in OFC mode by sealing the air inlet manifold and directly injecting oxygen into the inlet pipe. This modification necessitates a thorough examination of the engine's air intake system to ensure that all potential air entry points are completely sealed, eliminating unwanted air ingress that could compromise the accuracy and reliability of the OFC process.

Oxygen is supplied from a cylinder equipped with a pressure regulator, calibrated to maintain consistent oxygen line pressure, as controlled oxygen flow is essential for optimizing combustion efficiency and performance outcomes. The Tomasetto Achille IT01 rail gas injector is used for oxygen injections and is known for its accuracy and dependability in providing consistent gas quantities. Its robust design withstands high pressures and varying flow rates, allowing for accurate combustion conditions through modulated oxygen flow, synchronized with the crank angle. To monitor the injected oxygen flow rate, a micro-motion mass flow meter is utilized. This device provides real-time, high-precision measurements crucial for evaluating OFC performance and ensuring adherence to experimental parameters. The micro-motion mass flow meter is recognized for its accuracy and sensitivity in low-flow applications, enhancing the reliability of experimental data. Safety measures include flame arresters, installed upstream of the oxygen cylinder and prior to the engine, preventing potential misfires or flashbacks during operation under high-pressure conditions. Together, these modifications and safety protocols ensure the effective implementation of OFC in the diesel engine, facilitating accurate experimentation while upholding safety standards.

Figure 1 illustrates the experimental setup used for OFC in the diesel engine. The experiments were conducted at a constant engine speed of 1500 rpm under steady-state conditions at 25% load. Before data collection, the engine was running for 6 minutes to reach a stable operating condition. Combustion data were collected only after the engine attained a steady state, ensuring the reliability, repeatability, and consistency of the experimental results. This setup ensures effective implementation of OFC by maintaining precise oxygen injection control, enabling accurate evaluation of combustion performance under OFC conditions while adhering to safety protocols and experimental parameters.

Figure 1. Schematic layout of engine setup for oxy-fuel combustion diesel engine

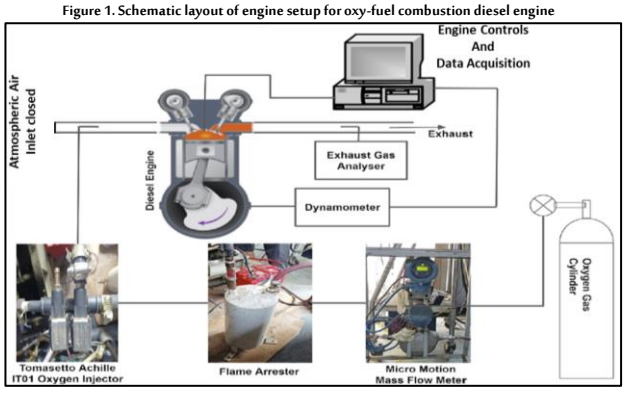

2.4. Error Analysis:

In this study, error analysis was essential to ensure the accuracy and consistency of the experimental results under OFC conditions. The primary parameters for which experimental uncertainties were considered include oxygen consumption, BTE, oxygen cylinder pressure, nozzle diameter, and end of oxygen injection.

The oxygen consumption was measured using a Micro-Motion mass flow meter with a measurement uncertainty of ±0.2% of full scale. The nozzle diameter was precisely controlled, with a tolerance of ±0.05 mm to ensure consistent oxygen flow into the combustion chamber. Oxygen cylinder pressure, recorded at various test points, was measured with an uncertainty of ±0.1 bar, and it played a crucial role in determining the mass flow of oxygen into the engine. The end of oxygen injection, defined in terms of CAD, was carefully monitored during the experiment. The uncertainty associated with this parameter was ±0.5 CAD, ensuring that the timing of oxygen injection was consistent for each experimental run.

To ensure the accuracy and reliability of the measurements, the experimental setup was designed to minimize external variables. Ambient conditions, such as temperature, pressure, and humidity, were monitored and controlled throughout the tests, although ambient temperature and pressure were not directly measured. Multiple repetitions of each experimental condition were performed to assess the repeatability and consistency of the data. For each experimental condition, the engine was allowed to stabilize to a steady-state operation before measurements were taken. The steady-state achievement duration was carefully monitored to ensure accurate readings, with a stabilization period of at least 5 minutes for each test point. The results were analyzed for consistency, and any outliers were excluded from the final dataset to ensure the reliability of the data.

Overall, using the calibration of sensors and taking appropriate precautions to mitigate error propagation, the overall uncertainty in the key experimental parameters was estimated at approximately 3.1%. This uncertainty was primarily influenced by the fuel flow measurements, oxygen consumption, uncertainties in the oxygen cylinder pressure, and nozzle diameter, all of which contributed significantly to the experimental error.

3. Results and Discussion

3.1. Engine Load Conditions:

Selecting appropriate engine load conditions is crucial for a reliable experimental analysis of OFC in diesel engines. This study carefully considers load conditions to balance meaningful data generation while considering the experimental setup's limitations. The 0% load (idle) condition is deemed unsuitable for OFC analysis due to its highly unstable combustion dynamics. At idle, minimal fuel injection and inconsistent oxidizer-fuel mixtures lead to erratic data, compounded by excess oxygen in the exhaust that exacerbates issues such as backfiring, knocking, and irregular firing pulses, resulting in significant combustion instabilities. Furthermore, the low power output at idle generates insufficient heat, complicating the calculation of performance metrics such as BTE and BSFC. Idle conditions also fail to represent typical engine operations, where engines primarily function under load.

In contrast, the 25% load condition is identified as optimal for conducting OFC experiments, offering more stable combustion dynamics. At this load, oxidizer-fuel ratios can be better controlled, ensuring consistent pressure, temperature, and fuel injection parameters. This stability enables reliable data collection and sufficient power generation for accurate performance analysis, including BTE and BSFC calculations.

Attempts to increase the load to 50%, 75%, or 100% faced operational challenges, including engine knocking, unstable pressure fluctuations, and oxidation-related safety concerns. These complications posed risks to both engine durability and experimental safety. Consequently, testing at higher loads was deemed impractical, as the conventional engine setup used was not designed to manage the unique thermal and oxidative stresses of OFC. Future research should focus on developing

specialized engines tailored to OFC conditions, with improved thermal resilience, oxidation control, and fuel injection optimization. By selecting the 25% load, this study achieves a balance between combustion stability and accurate performance data collection, minimizing risks associated with higher loads in OFC conditions.

3.2. Limitations on Data Acquisition:

A key limitation encountered in this experimental analysis was the absence of sensors for direct data acquisition. The extreme conditions associated with OFC such as rapid heat release, elevated temperatures, and increased oxidation risks, made it impractical to install sensors within the combustion chamber. The presence of pure oxygen significantly accelerates oxidation, posing a risk of damage to conventional sensors. Moreover, high temperatures in the chamber exceed the maximum operating range of standard sensors.

Another concern was sensor placement, which could inadvertently allow air to enter the engine, compromising the controlled OFC environment and introducing errors in the data collection. Consequently, performance metrics like BTE and BSFC were calculated indirectly. These metrics were derived from the applied engine load, controlled via electrical loading, and the mass of fuel injected, monitored over specific operating times. While this method yields reliable performance data, it relies on estimations for detailed combustion characteristics. Despite these limitations, the calculated BTE and BSFC are sufficient to draw conclusions regarding the feasibility of applying OFC to diesel engines. Addressing these challenges through a customized experimental setup equipped with appropriate sensors will be essential for further validating the findings and enhancing the reliability of future studies.

3.3. Experimental Data and Performance Metrics:

In this study, the performance metrics of the modified diesel engine under OFC conditions are evaluated based on three key parameters Oxygen Consumption, BTE, and BSFC. Oxygen Consumption (g/cycle) is calculated by measuring the amount of oxygen injected into the engine per cycle, which is regulated and monitored using a mass flow controller. The oxygen flow rate is synchronized with the crank angle and recorded in real-time. BSFC is calculated by dividing the fuel mass consumed by the brake power output. BSFC is a critical indicator of fuel efficiency in internal combustion engines, with lower values reflecting better efficiency. BTE is determined by the ratio of the brake power output to the total energy input, which is calculated from fuel consumption. This metric indicates the efficiency with which the engine converts the fuel's energy into useful work. These parameters are critical for assessing the impact of oxygen-enriched combustion on engine performance.

3.4. Challenges in Customization of the OFC Experimental Setup:

The diesel engine's air isolation was rigorously evaluated to facilitate an effective transition to OFC. Several potential air leak zones were identified, such as the air box inlet, hose connections, intercooler, intake manifold gaskets, and the EGR valve. The objective was to ensure the engine would shut down in the absence of air intake, indicating successful air isolation. Initially, the air box inlet was closed off, but the engine continued to operate, revealing inadequate air isolation. Figure 2. illustrates the air box inlet and its assembly designed to block air entry. Additional trials, including sealing the turbocharger intake and inspecting the crankcase ventilation system for leaks, uncovered further air entry points. Ultimately, the air inlet assembly was determined to be the primary source of leaks, necessitating its removal and replacement with an airtight system on the inlet manifold. The before and after scenarios of the air inlet assembly are depicted in Figure 3.

With the air inlet securely isolated, the engine was successfully shut down, confirming the airtight integrity required for OFC operation. This enabled the introduction of pure oxygen as the oxidizer, a critical step in transitioning from CAC to OFC. Oxygen was injected directly into the cylinder using a Tomasetto Achille IT01 rail gas injector, which precisely controlled the mass flow rate through pulsed injections synchronized with the crank angle. The engine was initially operated at 25% load under CAC, followed by a gradual reduction of air intake through the manifold cover. Upon the onset of combustion subsidence, oxygen injection was initiated, and the air manifold was fully sealed to facilitate pure oxygen combustion. The air manifold sealing used to transition from air to OFC is illustrated in Figure 4.

Figure 2. Air box inlet and its blocking assembly

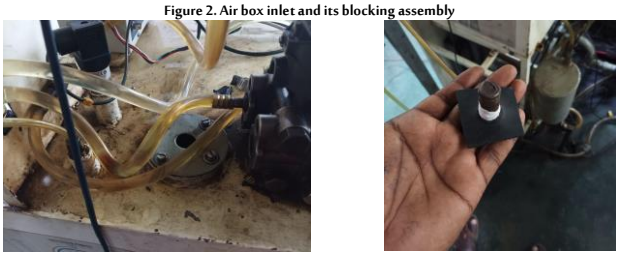

Figure 3. Air box assembly isolation

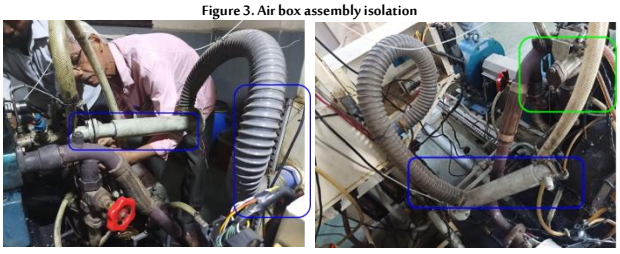

(a) (b)

(a) Air box is connected to the engine intake manifold
(b) Air box assembly is removed, and the intake manifold is closed to ensure no air entry

Figure 4. Air manifold seal

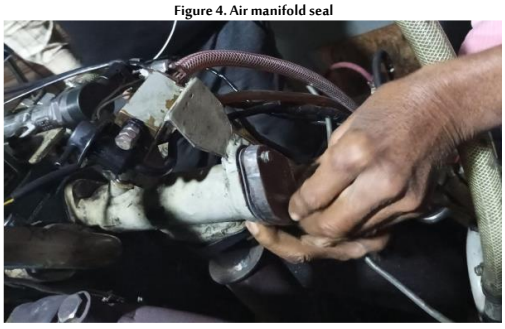

3.5. Optimization of OFC:

In the absence of direct temperature, pressure, or combustion characteristic measurements, the classification of combustion conditions in this study was based primarily on qualitative assessments derived from engine performance indicators, such as exhaust behavior, engine load stability, and fuel consumption rates. This classification approach was adapted to suit the specific limitations of the experimental setup, where traditional measurements of combustion processes were not feasible due to the extreme conditions associated with OFC, such as rapid heat release and high oxidation risks that hinder the installation of sensors within the combustion chamber. Similar classification methodologies based on performance indicators have been widely discussed in internal combustion engine studies, where the limitations of sensor-based measurements necessitate indirect assessment techniques (Heywood, 1988; Zhao, 2009).

Stable combustion was identified by consistent engine performance, where the combustion process appeared smooth, without irregularities

such as knocking, misfiring, or backfiring. This was inferred from the stability of the engine load, continuous fuel injection without interruptions, and the absence of any discernible combustion anomalies. The smooth operation of the engine, with no signs of abnormal exhaust gases, led to classifying these cycles as stable, as corroborated in studies on internal combustion systems under varying operational conditions. The combustion stability can be classified based on the uniformity of exhaust emissions and smooth engine cycles under optimized fuel-oxidizer conditions. Stable combustion in IC engines is typically marked by consistent combustion behavior, without significant fluctuations in engine performance or exhaust characteristics (Heywood, 1988; Zhao, 2009).

Unstable combustion was characterized by fluctuating engine performance, including irregular firing pulses in the exhaust and noticeable misfiring or knock events. These irregularities, observed through visual inspection and exhaust behavior, led to the classification of combustion as unstable. Since temperature and pressure data were unavailable, the focus was placed on the consistency of the combustion cycles, which in this case showed pronounced fluctuations in exhaust pulses. Studies have classified unstable combustion using similar operational indicators, where the occurrence of knock and misfiring suggested instability in the combustion process (Heywood, 1988).

Irregular combustion was identified when combustion exhibited inconsistent patterns of fuel consumption and exhaust pulse irregularities, without showing the extreme instability seen in backfiring or knock. These irregularities were quantified indirectly by observing the frequency of misfires and irregular firing pulses in the exhaust gases. Similar indicators have been used in the literature to classify irregular combustion, where variations in combustion characteristics, such as incomplete combustion or fluctuating exhaust behavior, were used to categorize it. The irregular combustion could be identified by such inconsistencies in the combustion process, where the engine exhibited occasional misfiring but did not experience the complete instability typical of knock or backfiring (Zhao, 2012; Kirkpatrick, 2020).

Partial combustion was determined when incomplete fuel combustion was evident, which manifested as an irregular engine load and excessive fuel consumption for a given engine load. In this condition, exhaust gases showed signs of inefficiency, potentially contributing to higher levels of particulate matter or unburned hydrocarbons, despite the lack of direct combustion monitoring. The classification of partial combustion has been supported in studies on IC engines, where similar methods of assessing fuel efficiency and exhaust emissions were used to evaluate the combustion process. The partial combustion can be identified by the imbalance between fuel input and engine load, as well as by inefficient exhaust gases, even in the absence of direct temperature or pressure measurements (Heywood, 1988; Kirkpatrick, 2020).

Finally, Uncontrolled Combustion was classified in cases where extreme combustion irregularities were observed, including continuous backfiring and knocking. This condition indicated a complete failure of the combustion process to stabilize, which resulted in engine instability. While direct combustion measurements were not available, the combustion was inferred to be uncontrolled through the erratic engine behavior and violent exhaust emissions. This classification is well-documented in combustion research, while identifying the uncontrolled combustion through similar symptoms of combustion instability, such as backfiring, knocking, and erratic exhaust behavior (Heywood, 1988; Zhao, 2009). The classification of combustion conditions in this study follows these established methodologies, adapted for the limitations of the experimental setup, and is supported by a body of literature that utilizes similar operational performance indicators to categorize combustion stability under IC engine conditions.

Initial trials with stoichiometric oxygen quantities at 25% load failed to maintain stable combustion. A rapid increase in oxygen supply led to challenges such as backfiring, knocking, and irregular firing pulses in the exhaust due to excess oxygen accumulation. To achieve stable combustion, various combinations of oxygen cylinder pressure, gas injector nozzle diameter, and injection timing were evaluated to optimize combustion in the OFC diesel engine setup. The primary goal was to establish stable and sustained combustion at 25% engine load by fine-tuning the oxygen delivery into the combustion chamber. Oxygen injection began at approximately 180 CAD, with its duration extended beyond the fuel injection cut-off to ensure proper mixing and combustion.

Each combination aimed to optimize the oxygen supply in relation to the dynamic combustion characteristics, thereby mitigating issues such as knocking, backfiring, and incomplete combustion that were prevalent in earlier iterations. By systematically varying the nozzle size and oxygen cylinder pressure, the effects of these parameters on combustion behavior were carefully observed. Table 2 summarizes the results, offering insights into the impact of each parameter on combustion stability. Iteration 6 emerged as the optimal configuration for sustained combustion conditions, with the required oxygen per cycle recorded at 0.77 g. This finding indicates that a significant portion of the supplied oxygen remained unused, highlighting the need to balance the cylinder volume to compensate for the absence of nitrogen in the combustion chamber.

Table 2. Iterations on oxygen injection for OFC

Iteration	O2 Cylinder Pressure (bar)	Nozzle Diameter (mm)	End of Oxygen Injection (CAD)	Combustion Status	Observations
1	1.5	1.5	350.0	Unstable Combustion	Uneven combustion, misfiring.
2	1.5	1.8	370.0	Irregular Combustion	Irregular firing and misfires.
3	1.8	1.8	360.0	Knock and Instability	Knock and unstable combustion cycles.
4	1.8	2.0	375.0	Unstable Combustion	Weak and incomplete combustion.
5	2.0	2.0	355.0	Partial Combustion	Misfiring and partial combustion.
6	2.0 (Best)	2.0	375.0	Stable and Sustained Combustion	Smooth combustion with no signs of knocking or backfiring.
7	2.0	2.3	365.0	Mild Combustion Instability	Minor instability but maintained acceptable combustion conditions.
8	2.0	2.3	385.0	Combustion Variations	Combustion irregularities, discontinuous combustion
9	2.3	2.5	355.0	Backfiring and Misfiring	Backfiring and uncontrolled combustion events.
10	2.5	2.8	365.0	Severe Backfiring and Knock	Disruptive combustion process, causing severe backfiring and knock.
11	2.5	2.8	385.0	Uncontrolled Combustion	Erratic combustion and engine instability.

3.6. EGR Integration:

The current engine setup allows for a maximum EGR rate of 40%. Exceeding this threshold reduces the engine's ability to maintain stable combustion due to the excessive buildup of residual gases, which diminishes available oxygen and hampers flame propagation, leading to incomplete combustion and instability. EGR was controlled by mass flow rather than volume to ensure accurate and precise regulation of the exhaust gas recirculated into the intake manifold. This approach is crucial since mass flow directly correlates with the combustion dynamics, as it influences the oxygen concentration and thermal capacity in the combustion chamber. The engine initially operated using CAC before transitioning to OFC. Once stable combustion in OFC was established, the EGR valve was gradually adjusted to achieve the 40% mass-based rate through a controlled

process, carefully monitored to maintain combustion stability.

To optimize oxygen consumption under the OFC+EGR configuration, a series of tests systematically varied the gas injector nozzle diameter while keeping the oxygen cylinder pressure constant at 2 bars and the oxygen injection duration fixed at 375° CAD. The nozzle diameter was reduced in increments of 0.1 mm to assess its effect on combustion stability and engine performance. The trials indicated that a nozzle diameter of 1.8 mm provided the most stable and consistent combustion under the OFC+EGR setup, facilitating optimal mixing of oxygen and fuel. Further reductions in nozzle diameter led to combustion instability, characterized by misfires and incomplete combustion due to inadequate oxygen availability, which disrupted the formation of a homogeneous oxidizer-fuel mixture.

Table 3 illustrates the reduction in oxygen consumption per cycle when implementing EGR alongside OFC. Maintaining a constant oxygen cylinder pressure at 2 bar, along with EGR introduction, increased in-cylinder pressure, which reduced the pressure differential between the oxygen cylinder and combustion chamber. This resulted in a decreased oxygen flow rate. With the optimized nozzle diameter of 1.8 mm, the oxygen required for sustained combustion was reduced to 0.462 g/cycle, a significant decrease from the 0.77 g/cycle required under OFC alone. This highlights the effectiveness of EGR and nozzle optimization in minimizing oxygen consumption while maintaining combustion stability.

Table 3. Comparison of oxygen consumption (g/cycle)

Output Variable	Units	OFC	OFC + EGR
Oxygen Consumption	g/cycle	0.77	0.462

3.7. Performance Comparison:

To ensure a fair comparison between CAC, OFC, and OFC+EGR, key engine parameters such as fuel injection pressure, mass of fuel injected, injection timing, and crank angle were kept consistent with those used during CAC trials. This approach ensured that the only variable influencing combustion was the nature of the oxidizer.

The experimental results highlight notable differences in performance across the three combustion modes at 25% load. Under sustained combustion conditions, the BTE for OFC was measured at 16.2%, significantly lower than the 20.1% observed for CAC. The efficiency further decreased to 14.8% for OFC+EGR. This decline in BTE across the combustion modes can be attributed to the absence of nitrogen in OFC and OFC+EGR, which results in elevated combustion temperatures and increased heat losses through the exhaust. While the OFC environment accelerates combustion, it also increases thermal dissipation. The lack of inert gases diminishes the dilution effect, resulting in a faster burn rate and improved heat transfer to the cylinder walls. In the OFC+EGR setup, the introduction of exhaust gases further reduces the available oxygen, negatively affecting both combustion stability and efficiency.

Similarly, BSFC showed a significant increase across the combustion modes. For CAC, the BSFC was recorded at 420.2 g/kW-hr, while OFC exhibited a higher consumption rate of 473.5 g/kW-hr. In the OFC+EGR configuration, BSFC further escalated to 527.7 g/kW-hr. This increase in fuel consumption directly correlates with the reduced thermal efficiency observed in OFC and OFC+EGR, as more fuel is required to sustain the same power output. The absence of nitrogen alters flame propagation dynamics, necessitating a higher fuel mass for stable combustion, further elevating BSFC. Additionally, in the OFC+EGR setup, the reduced oxygen availability compared to pure OFC limits combustion efficiency by lowering flame temperatures and slowing combustion reactions, leading to even higher fuel consumption and reduced thermal efficiency.

Table 4 summarizes the performance comparisons among CAC, OFC, and OFC+EGR. The results indicate a clear decline in efficiency as the system transitions from CAC to OFC and further to OFC+EGR. While EGR effectively reduces excess oxygen, it compromises the combustion process due to the increased presence of in-cylinder residual gases, impairing flame propagation and stability. As a result, while excess oxygen is reduced, this trade-off results in a marked decrease in overall efficiency and increased fuel consumption across all combustion modes.

Table 4. Performance comparison of CAC, OFC, and OFC+EGR

Output Variable	Units	CAC	OFC	OFC + EGR
BTE	%	20.1	16.2	14.8
BSFC	g/kW-hr	420.2	473.5	527.7

In the current research, the thermal efficiency and fuel consumption characteristics of a diesel engine were analyzed under CAC, OFC, and OFC+EGR conditions. The BTE dropped from 20.1% under CAC to 16.2% under OFC, and further to 14.8% with OFC+EGR, which is in line with the findings of Ugraram *et al.* (2022) who reported a significant drop in indicated brake power and indicated mean effective pressure for OFC, suggesting efficiency losses, which aligns with the present findings. These results can be attributed to the absence of nitrogen in the combustion process, which increases the combustion temperatures. Hong *et al.* (2010) explained that this effect occurs due to the altered heat capacity ratio in oxy-fuel environments. Additionally, the increased exhaust heat losses contribute to the reduction in efficiency, as observed in the present study. Similarly, the BSFC increased from 420.2 g/kW-hr under CAC to 473.5 g/kW-hr under OFC, and further to 527.7 g/kW-hr under OFC+EGR. This increase in fuel consumption aligns with the observations made by Mobasheri *et al.* (2022) who found a significant reduction in thermal efficiency, with a corresponding increase in fuel consumption under oxy-fuel combustion conditions. The elevated fuel consumption in the present study mirrors this trend, highlighting the challenges of maintaining combustion stability while compensating for the absence of nitrogen in the oxy-fuel combustion system. These findings further validate the reduction in thermal efficiency and increased fuel consumption observed in OFC and OFC+EGR conditions in comparison to CAC, underscoring the need for performance optimization to recover efficiency losses.

4. Conclusion

This study underscores the successful adaptation of oxy-fuel combustion in diesel engines, highlighting the challenges encountered, the quantitative performance outcomes, and the necessity for further optimization to enhance overall efficiency and stability.

- Engine customization efforts included rigorous testing for air isolation, leading to successful shutdowns of the engine under OFC conditions, confirming effective adaptation to pure oxygen as an oxidizer.
- Challenges such as incomplete combustion and knocking were addressed through systematic optimization of the gas injector nozzle diameter, with an optimal size of 1.8 mm identified for stable combustion.
- The introduction of EGR successfully reduced excess oxygen but resulted in compromised combustion stability and further increased BSFC.
- Significant adjustments were necessary to counter the adverse effects of reduced nitrogen levels in the combustion process, which affected flame propagation and thermal efficiency.
- The transition from CAC to OFC demonstrated a decrease in BTE from 20.1% (CAC) to 16.2% (OFC) and further to 14.8% (OFC+EGR).
- BSFC increased significantly, with values of 420.2 g/kW-hr (CAC), 473.5 g/kW-hr (OFC), and 527.7 g/kW-hr (OFC+EGR), indicating reduced thermal efficiency.
- The study's findings indicate that while initial performance metrics reveal efficiency losses, the potential for enhanced combustion stability and efficiency through ongoing modifications remains.
- A comprehensive assessment of the performance outcomes suggests a critical need for further optimization of the combustion system to recover lost performance and improve operational stability.

Further optimization is crucial to address the performance losses observed under OFC conditions. With these enhancements, OFC could become a highly effective and environmentally friendly technique for diesel engine operation, positioning it as a superior alternative to conventional combustion methods while improving both performance and emissions control.

Abbreviations

BSFC : Brake Specific Fuel Consumption

BTE : Brake Thermal Efficiency

CAC : Conventional Air Combustion

CAD : Crank Angle Degree

EGR : Exhaust Gas Recirculation

NOx : Nitrogen Oxides

OFC : Oxy-Fuel Combustion

OFC+EGR : Oxy-Fuel Combustion with Exhaust Gas Recirculation

Data Availability Statement

The data that supports the findings of this study are available from the corresponding author, upon reasonable request.

Acknowledgement

The authors would like to thank Jawaharlal Nehru Technological University Anantapur (JNTUA), Andhra Pradesh, India.

Funding

The authors declare that no funds, grants, or other support were received during the preparation of this manuscript.

Conflict of Interest

The authors declare no conflict of interest.

Biographies

Raghavendra Ugraram

Department of Mechanical Engineering, Jawaharlal Nehru Technological University Anantapur (JNTUA), Ananthapuramu - 515002, Andhra Pradesh, India, 00919036956234, raghuugraram@gmail.com

Ugraram, is a Ph.D. Research Scholar, specializes in optimizing diesel engine combustion using numerical simulations, experiments, and Digital Twin technology. He has published in 1 SCI journal, 3 Scopus-indexed journals, and 2 international journals, along with presenting at 4 international conferences. His research bridges simulation and experimental validation to drive advancements in sustainable engine technologies.

ORCID: 0000-0002-0986-621X

R. Meenakshi Reddy

Department of Mechanical Engineering, G. Pulla Reddy Engineering College, Kurnool- 518007, Andhra Pradesh, India, 0091 9000321874, rmreddy123@gmail.com

Reddy, an Associate Professor with 17 years of academic and 2 years of industrial experience, holds a Ph.D. in Energy Systems from JNTU Anantapur. He has guided 3 Ph.D. scholars and published 3 national and 35 international papers. A member of ISTE, MIE, ISESI, and ISHMT, his research focuses on Energy Engineering, Thermal Energy Storage, and Heat Transfer, contributing significantly to the field.

ORCID: 0000-0002-4899-0774

B. Chandra Mohana Reddy

Department of Mechanical Engineering, Jawaharlal Nehru Technological University Anantapur (JNTUA), Ananthapuramu - 515002, Andhra Pradesh, India, 00919000321874, rmreddy123@gmail.com

Reddy, an Associate Professor, earned his Ph.D. from Jawaharlal Nehru Technological University Hyderabad in 2009. A life member of ISTE and MIE India, his research spans IC engine combustion, Alternative Fuels, Nanofluids, and Composites, making significant contributions to these fields. With a strong academic background and impactful research, Dr. Reddy remains dedicated to advancing engineering innovation and sustainable technologies.

ORCID: 0000-0002-4738-2662

Reference

Emerson. (2022). *Measuring Oxygen Gas using Coriolis Technology: Micro Motion*. Emerson. Available at: https://www.emerson.com/documents/automation/white-paper-measuring-oxygen-gas-using-coriolis-technology-micro-motion-en-65290.pdf (accessed on 31/01/2025)

Kirkpatrick, A.T. (2020). *Internal Combustion Engines: Applied Thermosciences*. 4th edition. USA: John Wiley and Sons.

Heywood, J.B. (2018). *Internal Combustion Engine Fundamentals*. 2nd edition. USA: McGraw-Hill Education.

Hong, J., Chaudhry, G., Ghoniem, A.F., Mitsos, A. and Bolland, O. (2010). Analysis of oxy-fuel combustion power cycle utilizing pressurized coal combustion. *Energy*, **35**(12), 5391–9. DOI: 10.1016/j.energy.2009.05.015.

Hountalas, D.T., Mavropoulos, G.C. and Binder, K.B. (2008). Effect of exhaust gas recirculation (EGR) temperature for various EGR rates on heavy-duty DI diesel engine performance and emissions. *Energy*, **33**(2), 272–83. DOI: 10.1016/j.energy.2007.07.002.

Huang, F., Li, L., Zhou, M., Wan, M., Shen, L. and Lei, J. (2023). Effect of EGR on performance and emissions of a methanol–diesel reactivity-controlled compression ignition (RCCI) engine. *Journal of the Brazilian Society of Mechanical Sciences and Engineering*, **45**(9), 440. DOI: 10.1007/s40430-023-04289-5.

Kang, Z., Chen, S., Wu, Z., Deng, J., Hu, Z. and Li, L. (2018). Simulation study of water injection strategy in improving cycle efficiency based on a novel compression ignition oxy-fuel combustion engine. *SAE International Journal of Engines*, **11**(6), 935–46. DOI: 10.4271/2018-01-0894.

Krishnamoorthi, M. and Agarwal, A.K. (2022). Combustion instabilities and control in compression ignition, low-temperature combustion, and gasoline compression ignition engines. In: G. Kalghatgi, A.K. Agarwal, H. Goyal and M.B. Houidi (eds.) *Gasoline Compression Ignition Technology: Future Prospects*. Singapore: Springer Nature Singapore. **n/a**(n/a), 183–216. DOI: 10.1007/978-981-16-8735-8_7.

Kunze, C. and Spliethoff, H. (2012). Assessment of oxy-fuel, pre-and post-combustion-based carbon capture for future IGCC plants. *Applied Energy*, **94**(n/a), 109–16. DOI: 10.1016/j.apenergy.2012.01.013.

Li, H., Zhang, X., Li, C., Cao, R., Zhu, W., Li, Y. and Li, Y. (2022). Numerical study of knocking combustion in a heavy-duty engine under plateau conditions. *Energies*, **15**(9), 3083. DOI: 10.3390/en15093083.

Liu, C.Y., Chen, G., Sipöcz, N., Assadi, M. and Bai, X.S. (2012). Characteristics of oxy-fuel combustion in gas turbines. *Applied Energy*, **89**(1), 387–94. DOI: 10.1016/j.apenergy.2011.08.004.

Mobasheri, R., Aitouche, A., Peng, Z. and Li, X. (2020). Influence of oxy-fuel combustion on engine operating conditions and combustion characteristics in a high-speed direct injection (hsdi) diesel engine under homogeneous charge compression ignition (hcci) mode 2020–01–1138. *SAE Technical Paper*, **n/a**(n/a), n/a. DOI: 10.4271/2020–01–1138.

Mobasheri, R., Aitouche, A., Peng, Z. and Li, X. (2022). A numerical study of the effects of oxy-fuel combustion under homogeneous charge compression ignition regime. *International Journal of Engine Research*, **23**(4), 649–60. DOI: 10.1177/1468087421993359.

Nwafor, O.M.I. (2002). Knock characteristics of dual-fuel combustion in diesel engines using natural gas as primary fuel. *Sadhana*, **27**(n/a), 375–82. DOI: 10.1007/BF02703658.

Occupational Safety and Health Administration. (OSHA). (2009). *Internal Combustion Engines and Spark Arresters: Safety Guidelines for Hazardous Environments. U.S. Department of Labor*. Available at:

https://www.osha.gov/sites/default/files/publications/osha3589.pdf (accessed on 31/01/2025)

Olumayegun, O., Wang, M. and Kelsall, G. (2016). Closed-cycle gas turbine for power generation: A state-of-the-art review. *Fuel*, **180**(n/a), 694–717. DOI: 10.1016/j.fuel.2016.04.074.

Osman, A. (2009). Feasibility study of a novel combustion cycle involving oxygen and water 2009–01–2808. *SAE Technical Paper*, **n/a**(n/a), n/a. DOI: 10.4271/2009-01-2808.

Patel, K. and Lin, S. (2020). High-precision injectors for oxy-fuel combustion: Impacts on diesel engine efficiency. *Fuel Combustion Technology*, **95**(n/a), 1025–35. DOI: 10.1016/j.fct.2020.103456.

Rajkumar, K. and Govindarajan, P. (2010). Experimental investigation of oxygen enriched air intake on combustion parameters of a single cylinder diesel engine. *International Journal of Engineering Science and Technology*, **2**(8), 3621–7. DOI: n/a

Serrano, J.R., Bracho, G., Gomez-Soriano, J. and Fernandes, C. (2022). Development of an oxy-fuel combustion system in a compression-ignition engine for ultra-low emissions powerplants using CFD and evolutionary algorithms. *Applied Sciences*, **12**(14), 7104. DOI: 10.3390/app12147104.

Taylor, C.F. (1985). *The Internal Combustion Engine in Theory and Practice: Vol. 2. Combustion, Fuels, Materials, Design*. 2nd edition. Cambridge, Massachusetts, USA: MIT Press.

Ugraram, R., Reddy, R.M. and Reddy, B.C.M. (2022). A study on oxy-fuel diesel engine and comparison with conventional air combustion. *IEOM Society International*, **n/a**(n/a), n/a. DOI: 10.46254/IN02.20220249.

Ugraram, R., Reddy, R.M. and Reddy, B.C.M. (2023). Thermo-mechanical stress and fatigue life analysis of diesel engine piston with oxy-fuel combustion and comparison with conventional air combustion. *Journal of Failure Analysis and Prevention*, **23**(1), 1–10. DOI: 10.1007/s11668-022-01456-0.

Zhang, W., Chen, Z., Li, W., Shu, G., Xu, B. and Shen, Y. (2013). Influence of EGR and oxygen-enriched air on diesel engine NO–Smoke emission and combustion characteristic. *Applied Energy*, **107**(n/a), 304–14. DOI: 10.1016/j.apenergy.2013.02.024.

Zhao, C., Wang, K. and Huang, S. (2018). Numerical investigation on effects of oxygen-enriched air and intake air humidification on combustion and emission characteristics of marine diesel engine 2018–01–1788. *SAE Technical Paper*, **n/a**(n/a), n/a. DOI: 10.4271/2018-01-1788.

Zhao, H. (2012). *The Internal Combustion Engine Handbook: Basics, Components, Systems, and Perspectives*. USA: SAE International.

Scientific Journal of King Faisal University:
Basic and Applied Sciences

Assessing Drought Patterns Using Landsat-Derived Vegetation Health Index During Spring (2013–2024)

Almustafa Abd Elkader Ayek [1], Suzan Fathe Karmoka [2], Abdullah Taher Hasan [3] and Mohannad Ali Loho [4,5]

[1] Department of Topography, Faculty of Civil Engineering, University of Aleppo, Aleppo, 12212, Syria
[2] Department of Agricultural Studies and Research, General Organization of Remote Sensing (GORS), Damascus, Syria
[3] Department of Geography, Faculty of Arts and Humanities, University of Aleppo, Aleppo, 12212, Syria
[4] Department of Geography, Faculty of Arts and Humanities, Tartous University, Tartous, Syria
[5] Department of Geography, Faculty of Arts and Humanities, Damascus University, Damascus, Syria

LINK	RECEIVED	ACCEPTED	PUBLISHED ONLINE	ASSIGNED TO AN ISSUE
https://doi.org/10.37575/b/agr/250013	17/03/2025	21/05/2025	21/05/2025	01/06/2025
NO. OF WORDS	**NO. OF PAGES**	**YEAR**	**VOLUME**	**ISSUE**
5674	6	2025	26	1

ABSTRACT

This study aims to assess drought patterns in the Harem region of northwestern Syria during the spring seasons from 2013 to 2024, using data from Landsat 8 and 9. Drought severity was evaluated and categorized into five classes using the Vegetation Health Index, which combines the Normalized Difference Vegetation Index and the Temperature Condition Index. Monthly precipitation data were included as a supporting component to evaluate climatic conditions, and the Google Earth Engine platform was used for processing and spatiotemporal analysis. The findings revealed fluctuations in drought severity, with the 2017–2019 period being the most affected, particularly in 2019, when land surface temperature (LST) reached its highest levels and vegetation health markedly declined. The 2020–2024 period, by contrast, showed gradual improvement in vegetation health and a reduction in the extent of severe drought. The study also indicated that the relationship between precipitation and drought severity is nonlinear, with LST playing a key role in determining drought intensity. To improve the management of water and agricultural resources and reduce the effects of drought on local communities and ecosystems, this study highlights the importance of adopting advanced monitoring and forecasting strategies that incorporate artificial intelligence technology.

KEYWORDS

Abiotic stress, climate change, dissertation, prediction, water resources, weather forecast

CITATION

Ayek, A.A.E., Karmoka, S.F. Hasan, A.T. and Loho, M.A. (2025). Assessing drought patterns using landsat-derived vegetation health index during spring (2013–2024). *Scientific Journal of King Faisal University: Basic and Applied Sciences*, **26**(1), 51–6. DOI: 10.37575/b/agr/250013

1. Introduction

One of the most hazardous natural occurrences that has a significant impact on ecosystems and human communities worldwide is drought. Tracking and evaluating the impacts of drought is more challenging because, unlike other natural catastrophes that strike quickly, it develops slowly and has lingering effects that can last for months or even years (Sugg *et al.*, 2020; Wilhite and Glantz, 1985). Global climate change has worsened the issue in recent decades by increasing the frequency and severity of drought occurrences (Trenberth *et al.*, 2014). This growing threat highlights the urgent need to develop advanced and efficient tools and techniques for drought monitoring and impact analysis on both the environment and communities (Kim and Jehanzaib, 2020; Adisa, Masinde, and Botai, 2020). Syria is also frequently exposed to drought. Over the past few decades, the country has witnessed an increase in the frequency and severity of drought periods, which has exacerbated the problems of desertification and the degradation of agricultural lands. This has been reflected in living conditions and a decline in per capita income due to annual fluctuations in agricultural land productivity (Atik *et al.*, 2024). Several studies indicate that Syria has experienced multiple severe drought waves in recent decades (Karmoka *et al.*, 2019; Mathbout *et al.*, 2025), which has greatly affected water and agricultural resources (Hameed *et al.*, 2020). In this context, remote sensing technologies have played a vital role in enhancing our capacity for extensive drought monitoring (Kogan, 1995; Nepsta *et al.*, 1994). Recent years have witnessed tremendous advancements in these technologies, opening new avenues for real-time environmental change monitoring and analysis. The Landsat series of satellites stands out as one of the primary sources of space data among the crucial space tools contributing to drought studies, providing precise historical records spanning more than 40 years of continuous Earth surface observation (Belward and Skøien, 2015; Goward *et al.*, 2021; Wulder *et al.*, 2022). Landsat 8 and Landsat 9 satellites are capable of providing multispectral data at high spatial resolutions of up to 30 meters per pixel, with coverage cycles repeating every 16 days (Irons and Masek, 2006; Masek *et al.*, 2020; Roy *et al.*, 2014). These features make Landsat an ideal tool for monitoring changes in vegetation cover and land surface conditions, which helps improve our ability to track the effects of drought on the environment. The ability to analyze temporal and spatial changes using these space data provides valuable tools for researchers and planners to assess drought severity and predict potential impacts, enhancing adaptation strategies and reducing negative effects on local communities and ecosystems (Bhaga *et al.*, 2020; Zhang *et al.*, 2021). Recent studies show that remote sensing techniques can provide a thorough and precise representation of drought conditions, assisting in identifying vulnerable regions and assessing their severity (Agarwal *et al.*, 2024). Additional studies have demonstrated the value of these techniques in tracking variations in vegetation cover and understanding how drought impacts various ecosystems (Li *et al.*, 2024). With the increasing volume of available space data, there is a need for powerful platforms that can efficiently process and analyze these data. Google Earth Engine (GEE) represents a paradigm shift in this field, offering massive computing power and a vast archive of space data. The platform enables researchers and specialists to process and analyze large datasets without the need for extensive local computing resources and supports the development of interactive applications that can be shared with the scientific community (Ayek and Zerouali, 2025; Bhowmik and Bhatt, 2024; Qazvini and Carrion, 2023). The Vegetation Health Index (VHI) is an enhanced drought monitoring index (Hu *et al.*, 2020), which combines vegetation cover and land surface temperature (LST) information into a single index. The VHI integrates two main indices: the Vegetation Condition Index (VCI), based on the Normalized Difference Vegetation Index (NDVI), and the Temperature Condition

Corresponding Author: Almustafa Abd Elkader Ayek 009630959262134, almustafaayek@gmail.com

Index (TCI), based on LST, and measures plant heat stress. VHI has been applied in various environments and geographical areas. It can precisely identify agricultural drought conditions, detect early vegetation stress, and be used for studying various natural and cultivated vegetation covers (Alqadhi *et al.*, 2025; Hang *et al.*, 2024; Javan *et al.*, 2025; Karmoka and Hanjagi, 2023; Zeng *et al.*, 2022) to assess the impacts, severity, and classification of drought and to monitor the temporal and spatial changes of drought conditions. It may also be used to track actual vegetation drought across different agricultural and climatic regions while accounting for meteorological variables (Bhuiyan *et al.*, 2006). Given the increasing challenges of drought and its impacts on food security and water resources, there is an urgent need to develop user-friendly and effective drought monitoring applications. These applications can support decision-makers in water and agricultural resource management, researchers in studying drought patterns and trends, farmers in planning agricultural activities, and institutions in emergency planning and drought response. The present study aims to develop an integrated application on the GEE platform to derive and analyze the VHI using Landsat 8 and 9 data. The application focuses on areas with vegetation cover only to ensure assessment accuracy, provides an interactive user interface to select the analysis time period, calculates and analyzes drought intensity, and generates detailed reports on drought conditions. This study represents an important step toward developing effective drought monitoring tools that can be used by a wide range of users, contributing to improving our understanding and management of this complex natural phenomenon.

2. Materials and Methods

2.1. Study Area:

The Harem region is located in the northern part of the Idlib Governorate, in the far northwest of Syria. It extends between latitudes 35°55′50″ and 36°20′26″ north of the equator and longitudes 36°22′35″ and 36°49′59″ east of the Greenwich line (Figure 1). With an estimated area of 768 km², it constitutes 14.1% of the Idlib Governorate's total area. The Orontes (al-Asi) River forms its western boundary; Mount Simeon, its eastern boundary; the Amq Plain and the Afrin River, its northern boundary; and the Al-Roj Plain, its southern boundary.

Figure 1: The geographical location of the study area

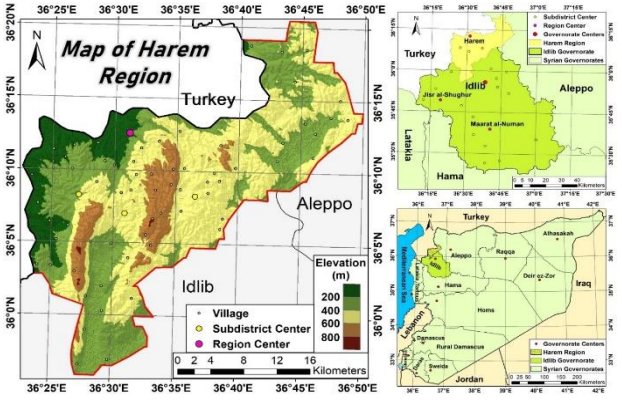

The region contains three low-lying hilly bands (Barisha, Al-A'la, Al-Wustani) that run along the north–south axis. The highest peak of Al-Wustani Mountain is 870 meters, while the lowest point is 89 meters, located north of Salqin near the Al-Omq depression. Plains and depressions such as Al-Roj, Sardin, and Al-Dana are also present and are hydrologically linked to the basin. The lower Orontes has a semi-humid Mediterranean climate with cold, rainy winters and moderate, dry summers.

2.2. Used Data:

An integrated set of satellite data from the Landsat 8 and Landsat 9 satellites was used. Together, they provide continuous coverage of Earth's surface every eight days at a spatial resolution of 30 meters. The Landsat Collection 2 Level-2 dataset was utilized, featuring advanced radiometric and geometric processing to ensure data quality and reliability. The data included the primary spectral bands for calculating the NDVI—the red band (SR_B4) and the near-infrared band (SR_B5)—as well as LST data derived from the thermal band (ST_B10) using the single channel algorithm. Additionally, monthly precipitation data from ERA5-Land were used to represent climatic conditions in the study area. The study period covered 2013 to 2024, focusing on the spring season (March to May), which represents the main vegetation growth period in the region.

2.3. Research Methodology:

The VHI was calculated and analyzed using a sequential system of related procedures (Figure 2). The process began with the preprocessing of raw data from Landsat 8 and 9. Quality masks were applied to exclude pixels affected by clouds and shadows. Spectral band values were converted to reflectance values, and thermal band data were converted to LSTs in Celsius. The red and near-infrared bands were used to calculate NDVI, and areas with vegetation cover were identified by excluding non-vegetated areas using an NDVI ≥ 0.2 threshold (Yu *et al.*, 2014).

Figure 2: Flow chart of research methodology

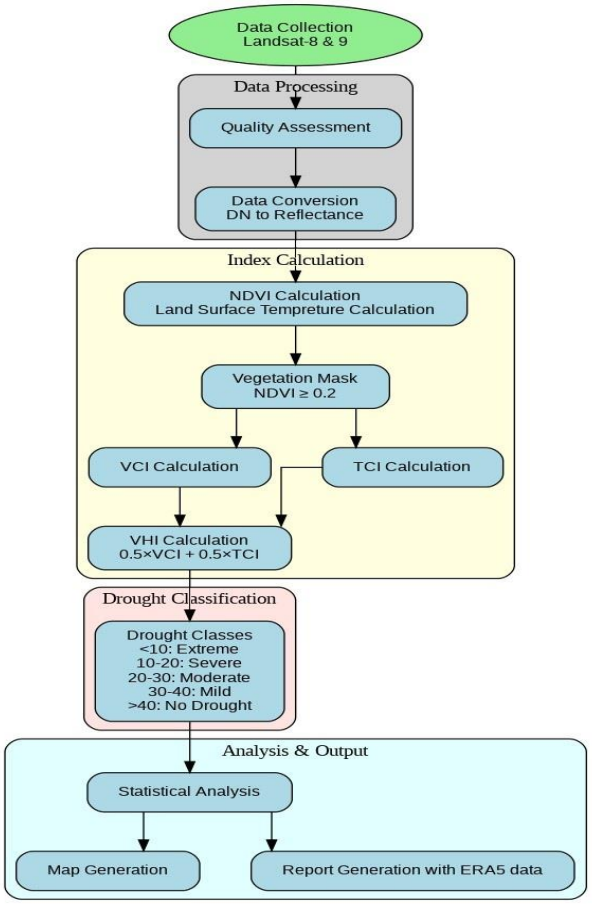

The NDVI was calculated using Equation (1) (Rouse *et al.*, 1973):

$$NDVI = \frac{NIR - RED}{NIR + RED} \quad (1)$$

Where *NIR* represents the near-infrared band surface reflectance, and *RED* represents the red band surface reflectance.

The VCI is calculated by determining the maximum ($NDVI_{max}$) and minimum ($NDVI_{min}$) values of the NDVI index for the study period by applying Equation (2) (Kogan, 1995).

$$VCI = \frac{NDVI - NDVI_{min}}{NDVI_{max} - NDVI_{min}} \times 100 \quad (2)$$

Concurrently, the TCI is calculated by applying Equation (3) (Kogan, 1995), using the maximum (LST_{max}) and minimum (LST_{min}) values of LST.

$$TCI = \frac{LST_{max} - LST_i}{LST_{max} - LST_{min}} \times 100 \quad (3)$$

Surface temperature values were extracted from Landsat Level 2 products using band ST_B10 by applying conversion factors (scale factor 0.00341802 and offset factor 149). The values were then converted from Kelvin to Celsius by subtracting 273.15 degrees (Equation 4) (USGS, 2023).

$$LST = [(ST\_B10 * 0.00431802) + 149] - 273.15 \quad (4)$$

The VCI and TCI indices are then combined with equal weights (0.5) to obtain the VHI, following Equation (5) (Kogan, 1995).

$$VHI = 0.5 \times VCI + 0.5 \times TCI \quad (5)$$

A diminished VHI value, resulting from a low NDVI and high LST, indicates suboptimal vegetative condition. In contrast, a higher VHI value, reflecting high NDVI and lower LST, suggests enhanced vegetation vitality and health (Tang *et al.*, 2020). The VHI is classified into five categories to determine drought severity: very severe drought (VHI < 10), severe drought (10–20), moderate drought (20–30), mild drought (30–40), and no drought (VHI ≥ 40).

The methodology concludes with a comprehensive statistical analysis, including calculation of the areas affected by each drought category and analysis of temporal and spatial changes. The results are presented as distribution maps and detailed statistical reports, supported by rainfall data to illustrate the relationship between drought and prevailing climatic conditions. The application, **Drought Watch**, is designed to display the VHI layer for each user analysis, showing a color gradient ranging from dark red (dry areas) to green (wet areas), within a numerical range of 0 to 50.

3. Results and Discussion

3.1. Temporal Analysis of Dry Periods:

With the exception of 2013, 2020, and 2024—when the area of the no-drought class constituted more than 50% of the study area, the results showed variation in the distribution of drought classes across the years, exceeding 50% in most years. In 2013 and 2020, the area of the no-drought category reached 570.42 km² and 527.11 km², respectively (Figure 3), reflecting the region's sensitivity to multiple climatic factors, most notably changes in precipitation amounts, LST, and human–economic impacts related to the war.

Figure 3: Drought severity trends over the years.

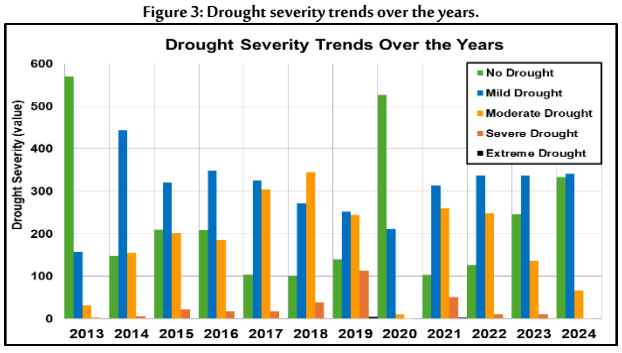

Three major phases can be distinguished within the study period:

3.1.1. Moderate to mild drought phase (2013–2016)

The extreme drought class was rare during this phase, with the area impacted by this class never exceeding 0.56 km² in any year. The percentage of regions not affected by drought (no-drought class) remained relatively high, reaching 570.42 km² in 2013 and decreasing to 208.29 km² in 2016 (Figure 3). The NDVI average fluctuated over this phase, with values ranging from 0.29 to 0.45 (Figure 5). Despite some stressful periods, the overall vegetation condition was considered good, with an index average of 0.38. During this phase, the average temperature was 31.58°C, and the average precipitation was 89.72 mm. The majority of the study area in 2013 appeared green, indicating high values of the VHI and, consequently, a vital vegetation cover and larger vegetated area. This is evident from the maps in Figure 4, which illustrate the temporal and spatial distribution of drought according to the VHI index. Although at a smaller percentage, the remaining years of this phase also displayed a spread of green (high VHI values).

Figure 4: The spatiotemporal distribution of VHI values during each phase

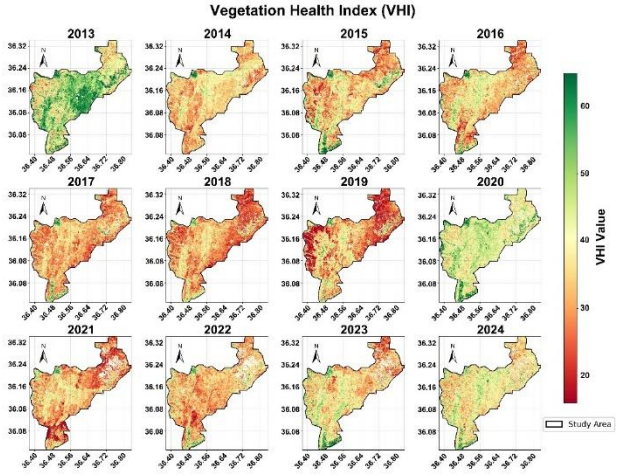

Figure 5: Standard deviation and average NDVI values for the studied time series

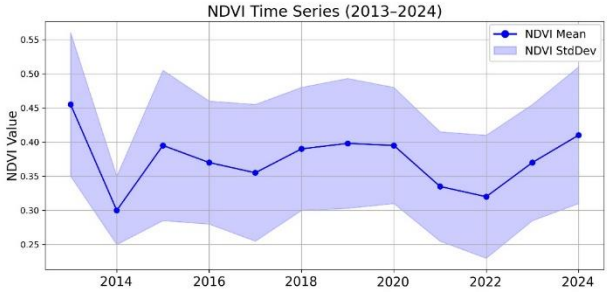

3.1.2. Severe drought phase (2016–2019)

The percentage of regions experiencing severe drought increased significantly during this phase, indicating that the vegetative cover was in an unhealthy condition with decreasing vitality. This is in line with the conclusion drawn by Mathbout *et al.* (2025), which showed that throughout the years 2008, 2010, 2016, and 2017, Syria witnessed a concentration of severe drought waves, especially in the central and northern regions. The phase was accompanied by an increase in the average LST, which recorded 32.1°C, indicating that temperature played a role in the drought condition during this period. Furthermore, it was accompanied by a notable increase in the average amount of precipitation (143.7 mm), suggesting that one of the primary causes of the drought's increased severity was the temperature rise. The highest percentage of areas experiencing severe drought in the time series,

113.54 km², was recorded in 2019. Numerous factors contributed to this, including natural ones such as high LSTs. For example, 2019 had the highest average surface temperature value during the study period at 34.9°C, indicating that the area experienced unusually high-water pressure in the spring of that year. Unnatural factors also played a role, including human activity through logging and overgrazing, particularly in areas with natural vegetation cover (FAO, 2020), as well as the consequences of the war, which affected the energy sector (fuel and electricity) required to supply irrigation water in agricultural areas (Jaafar *et al.*, 2017). This resulted in a decrease in the area of planted vegetation cover and a decline in its health and production status (Sukkar *et al.*, 2024). Based on the drought class distribution maps (Figure 4), the majority of areas appeared dark red, indicating a decline in the health and vitality of vegetation cover. This condition was due to heat stress from high LSTs and the accompanying human factors from military operations and the difficulty of accessing and maintaining agricultural lands. This indicates the state of severe drought during these years.

3.1.3. Gradual recovery phase (2020–2024)

During this phase, the areas afflicted by severe drought declined to only 1.75 km² in 2024, indicating a gradual enhancement in drought conditions and relative stability. On the other hand, the areas not impacted by drought expanded to 333.4 km² in 2024, showing that environmental conditions had generally improved. In addition, the average LST decreased to 28.56°C in 2024, reducing heat stress on plants, while the average precipitation was 114 mm during this phase. The year 2024 recorded a high rainfall of 124 mm. An obvious enhancement in vegetation cover was shown by the 2024 NDVI, which recorded one of the highest values in the time series at 0.41. Increased positive human activity and an effective precipitation–temperature balance contributed to this improvement. Due to better economic and environmental conditions, along with increased recent precipitation, the vegetation cover area (NDVI > 0.2) also expanded during this phase (Figure 6). In 2024, it increased to 741.39 km², indicating a gradual recovery of agricultural lands. Additionally, a decline in dark red–dominated regions was observed, reflecting the decrease in severe drought classes and the increase in areas showing no drought, indicated by green color shades. These areas were distributed throughout the study area (Figure 4), particularly in 2020, which witnessed a significant and rapid recovery of vegetation cover after the severe stress experienced in 2019. This recovery was attributed to the noticeable decline in average LST values by 2.95°C compared to 2019 and the accompanying improvement in precipitation, which reached 120.41 mm in 2020.

Figure 6: The vegetated cover area for the studied time series.

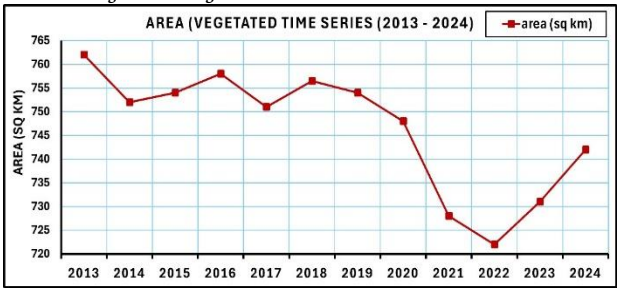

3.2. Factors that Influence Drought:

3.2.1. The relationship between surface temperatures and drought

- The findings demonstrated that high LSTs were frequently associated with severe droughts. For instance, despite relatively significant precipitation, 2019 witnessed a notable decline in vegetation health due to comparatively high temperatures.
- On the other hand, 2024 saw a temperature decrease compared to previous years, which had a positive impact on vegetation cover.

3.2.2. The role of precipitation

- Although precipitation plays a crucial role in determining the severity of drought, the results indicated that the relationship is not necessarily linear. The mean NDVI values and rainfall amounts showed a weak and insignificant correlation (R = 0.09).
- In some years, such as 2019, high precipitation did not have a clear positive effect on reducing drought due to high temperatures and their negative effects on soil and vegetation.
- In contrast, in other years, such as 2023 and 2024, precipitation played a more prominent role in improving environmental conditions, as reflected in the general enhancement of vegetation health indicators and the high value of actual precipitation in these two years.

4. Conclusions

This study assessed drought patterns and vegetation health in the Harem region from 2013 to 2024, and the main findings are summarized as follows:

- Since 2019 experienced the greatest rate of severe drought and the highest LSTs during the research period, it can be considered the peak drought year.
- In recent years (2020–2024), the study area has gradually improved, with an increase in the area of healthy vegetation and a decrease in drought intensity.
- The relationship between precipitation and drought severity is not direct, as LSTs play a crucial role in determining the extent to which vegetation is affected by drought. Therefore, the prevalence and severity of drought cannot be judged based on rainfall alone; temperature levels must also be considered. This makes monitoring climate change essential for understanding drought dynamics.
- In the long term, the results revealed a persistent pattern of mild drought in the region, with affected areas ranging between 200 and 400 km² during most of the study years. It was noted that very severe drought events, although relatively rare, remained intermittently present, indicating that the region experiences frequent cycles of stress due to high temperatures or human-induced destruction of agricultural lands and a decline in agricultural service operations.
- The results also showed significant variation in the distribution of different drought classes between years, with 2017 having a large area impacted by moderate drought (304.07 km²), while 2018 recorded the largest area of moderate drought (344.5 km²).
- Regarding vegetation cover, the area covered by vegetation progressively shrank (NDVI ≥ 0.2) from 760.97 km² in 2013 to the lowest value of 723.08 km² in 2022.

5. Recommendations

- The study area, Harem, is located within Idlib Governorate, which borders Turkey. Since the outbreak of the Syrian crisis, this area has witnessed ongoing military operations and widespread population displacement. During the study period (2013–2024), the area was outside the scope of any government support, regulation, or monitoring programs, resulting in a complete absence of data on the vegetation inventory or the state of the region's ecosystems. Furthermore, no reports were available from any governmental or non-governmental entity documenting the state of the vegetation cover during this period.
- This demonstrates the practical significance of the model, as it provides real-time and rapid data on the current state of vegetation cover and drought conditions in the region. It highlights the importance of the model and its potential to assist decision-makers in proposing necessary measures as quickly as possible after detecting an environmental problem. The model relies on the GEE platform, which provides continuous data with a long archive and near-real-time updates. It also helps decision-makers identify and navigate to affected areas to carry out rapid intervention and support operations, serving as a spatial indicator that accurately identifies areas exposed to climatic and non-climatic stresses. The model is distinguished by its potential for application in other areas, expanding its usefulness in supporting environmental and agricultural rehabilitation efforts.
- The study area urgently needs rehabilitation of existing irrigation networks and the establishment of new ones to meet agricultural development needs. Depending on the availability of groundwater resources, it is also suggested to establish a network of wells to enhance available water sources.
- To achieve resource sustainability and improve agricultural

productivity, it is recommended to implement modern irrigation projects aimed at minimizing water waste and optimizing water use. It is also suggested to expand the use of drought-resistant agricultural varieties in line with prevailing climatic conditions.

- To support farmers and enable them to replant their lands, it is essential to provide improved seeds, fertilizers, and other agricultural production inputs. Additionally, a structured pastoral program should be established to determine the appropriate seasons for opening and closing pastures, thus protecting vegetation cover while ensuring fodder needs are met.
- Based on these results, along with time series analysis approaches to forecast future developments, it is crucial to improve ongoing monitoring of LST, as it is closely associated with drought changes. Since NDVI, LST, and precipitation data can be integrated to produce more precise studies of long-term drought trends, creating AI-based models (neural networks and deep learning) is a promising first step in this direction. This will help empower decision-makers to take proactive steps to safeguard agricultural resources and reduce the detrimental effects of drought on regional ecosystems.
- Furthermore, the use and analysis of thermal sensor data in parallel with soil and moisture information can be a key component in improving the accuracy of drought assessment.
- This approach opens new avenues for understanding the impacts of drought on agricultural production and vegetation cover, helping to develop more efficient strategies to mitigate its effects and enhance the sustainability of ecosystems and agriculture in the future.

Data Availability Statement

The data that support the findings of this study are available on request from the corresponding author.

Acknowledgments

The authors extend their appreciation for the continued support of University of Aleppo, General Organization of Remote Sensing, Tartous University and Damascus University.

Funding

This research received no external funding.

Conflicts of Interest

No conflicts of interest exist.

Biographies

Almustafa AbdElkader Ayek

Department of Civil Engineering, Faculty of Civil Engineering, University of Aleppo, Aleppo, Syria, 009630959262134, almustafaayek@gmail.com

Ayek, a Syrian researcher with a Civil Engineering (Topography) degree from the University of Aleppo, specializes in remote sensing and GIS. His work focuses on water resource monitoring, land surface temperature retrieval, and spatial analysis. He publishes in peer-reviewed journals and develops applications using Google Earth Engine. Ayek also delivers GIS and remote sensing training, engaging both academics and professionals through his practical expertise and research contributions.

ORCID: 0009-0007-5952-8239

Suzan Fathe Karmoka

Department of Agricultural Research, Center for Remote Sensing Studies and Research, General Organization of Remote Sensing (GORS), Damascus, Syria, 0096399287360, karmoka.suzan@hotmail.com

Suzan is a Ph.D. scholar in Remote Sensing and Environment at Bangalore University. She holds an MSc in Renewable Natural Resources and Environment from Damascus University, Syria. She is a research assistant at GORS and formerly served as a research engineer at GCSAR. Suzan has taught remote sensing at Damascus University, Bangalore University, and NIE Mysore. She has published widely, participated in conferences, and contributed to RS/GIS training programs locally and with international organizations like the FAO.

ORCID: 0000-0003-4567-305X

Abdullah Taher Hasan

Department of Geography, Faculty of Arts and Humanities, University of Aleppo in Liberated Areas, Aleppo, Syria, 00963969154710, abdullahtaherhasan@gmail.com

Abdullah is a Syrian researcher specializing in GIS and remote sensing, with a Master's degree from the University of Aleppo in Liberated Areas. His research focuses on applying these technologies to rainwater harvesting and groundwater exploration in Syria. He is particularly interested in geo-AI for groundwater detection and karst geomorphology. Abdullah lectures part-time at the University of Aleppo, teaching climate, environment, and social geography, and is currently preparing to present his Ph.D. research proposal.

ORCID: 0009-0001-3902-1189

Mohannad Ali Loho

Department of Geography, Faculty of Arts and Humanities, Tartous University, Tartous, Syria, 00963988268102, mohannad.loho@damascusuniversity.edu.sy, mohannad609@gmail.com

Mohannad is a Syrian researcher specializing in GIS, remote sensing, and spatial AI applications. He holds a master's degree in Geography from the University of Damascus, with a focus on GIS. He has authored Syrian geography textbooks and developed hundreds of maps. As a lecturer at Tartus University, he teaches GIS, cartography, surveying, and land use. Currently pursuing a Ph.D., his research focuses on AI-driven land use monitoring and prediction. He has published and submitted several peer-reviewed studies.

ORCID: 0009-0002-5024-9798

References

Adisa, O.M., Masinde, M., Botai, J.O. and Botai, C.M. (2020). Bibliometric analysis of methods and tools for drought monitoring and prediction in Africa. *Sustainability,* **12**(16), 6516. DOI: 10.3390/su12166516.

Agarwal, V., Singh, B.V.R., Marsh, S., Qin, Z., Sen, A. and Kulhari, K. (2025). Integrated remote sensing for enhanced drought assessment: A multi‐index approach in Rajasthan, India. *Earth and Space Science,* **12**(2), e2024EA003639. DOI: 10.1029/2024EA003639.

Alqadhi, S., Mallick, J. and Hang, H.T. (2025). Assessing drought trends and vegetation health in arid regions using advanced remote sensing techniques: A case study in Saudi Arabia. *Theoretical and Applied Climatology,* **156**(1), 1–29. DOI: 10.1007/s00704-024-05301-1.

Atik, O., Kadour, A., Mahmoud, I., Al Hasan, K., Al Nabhan, A., Jazieh, H., Nijhawan, A. and Pianosi, F. (2024). Irrigation water in Northwest Syria: Impact of the recent crisis and drought. *Water,* **16**(21), 3101. DOI: 10.3390/w16213101.

Ayek, A.A. and Zerouali, B. (2025). Monitoring temporal changes of the Qttinah Lake surface area using Landsat data and Google Earth Engine. *DYSONA–Applied Science,* **6**(1), 126–33. DOI: 10.30493/das.2024.476854.

Belward, A.S. and Skøien, J.O. (2015). Who launched what, when and why: Trends in global land-cover observation capacity from civilian Earth observation satellites. *ISPRS Journal of Photogrammetry and Remote Sensing,* **103**(n/a), 115–28. DOI: 10.1016/j.isprsjprs.2014.03.009.

Bhaga, T.D., Dube, T., Shekede, M.D. and Shoko, C. (2020). Impacts of climate variability and drought on surface water resources in Sub-Saharan Africa using remote sensing: A review. *Remote Sensing,* **12**(24), 4184. DOI: 10.3390/rs12244184.

Bhowmik, S. and Bhatt, B. (2024). Drought monitoring using MODIS-derived indices and Google Earth Engine platform for Vadodara District, Gujarat. *Journal of the Indian Society of Remote Sensing,* **52**(9), 1885–900. DOI: 10.1007/s12524-024-01922-1.

Bhuiyan, C., Singh, R.P. and Kogan, F.N. (2006). Monitoring drought dynamics in the Aravalli region (India) using different indices based on ground and remote sensing data. *International Journal of Applied Earth Observation and Geoinformation,* **8**(4), 289–302. DOI: 10.1016/j.jag.2006.03.002.

Food and Agriculture Organization (FAO). (2020). *Evaluation of FAO's contribution to the Syrian Arab Republic 2012–2018* (Country Programme Evaluation Series, 12/2020). Rome. Available at: https://openknowledge.fao.org/handle/20.500.14283/cb2475en (accessed on 17/04/2025)

Ghaleb, F., Mario, M. and Sandra, A.N. (2015). Regional Landsat-based drought monitoring from 1982 to 2014. *Climate,* **3**(3), 563–77. DOI: 10.3390/cli3030563.

Goward, S.N., Masek, J.G., Loveland, T.R., Dwyer, J.L., Williams, D.L., Arvidson, T., Rocchio, L.E.P. and Irons, J.R. (2021). Semi-centennial of Landsat observations and Pending Landsat 9 launch. *Photogrammetric Engineering and Remote Sensing,* **87**(8), 533–9. DOI: 10.14358/PERS.87.8.533.

Hameed, M., Ahmadalipour, A. and Moradkhani, H. (2020). Drought and food security in the Middle East: An analytical framework. *Agricultural and Forest Meteorology,* **281**(n/a), 107816. DOI: 10.1016/j.agrformet.2019.107816.

Hang, Q., Guo, H., Meng, X., Wang, W., Cao, Y., Liu, R., De Maeyer, P. and Wang, Y. (2024). Optimizing the Vegetation Health Index for agricultural drought monitoring: Evaluation and application in the Yellow River Basin. *Remote Sensing,* **16**(23), 4507. DOI: 10.3390/rs16234507.

Hu, T., van Dijk, A.I.J.M., Renzullo, L.J., Xu, Z., He, J., Tian, S., Zhou, J. and Li, H. (2020). On agricultural drought monitoring in Australia using Himawari-8 geostationary thermal infrared observations. *International Journal of Applied Earth Observation and Geoinformation,* **91**(n/a), 102153. DOI: 10.1016/j.jag.2020.102153.

Irons, J.R. and Masek, J.G. (2006). Requirements for a Landsat data continuity mission. *Photogrammetric Engineering and Remote Sensing,* **72**(10), 1102.

Jaafar, H.H., Zurayk, R., King, C., Ahmad, F. and Al-Outa, R. (2017). Impact of the Syrian conflict on irrigated agriculture in the Orontes Basin. In: *The water-energy-food nexus in the Middle East and North Africa*, Routledge. DOI: 10.1080/07900627.2015.1023892.

Javan, F.D., Samadzadegan, F., Toosi, A. and TousiKordkolaei, H. (2025). Spatial-temporal patterns of agricultural drought severity in the Lake Urmia Basin, Iran: A cloud-based integration of multi-temporal and multi-sensor remote sensing data. *DYSONA–Applied Science,* **6**(2), 239–61. DOI: 10.30493/DAS.2025.486806.

Karmoka, S.F. and Hanjagi, D.A. (2023). Detecting the vegetation health situation of Tartus forests (Syria) and the spatio-temporal distribution of agricultural drought. In: *International Scientific Conference of Young Scientists and Specialists Dedicated to the 180th Anniversary of the Birth of K.A. Timiryazev: Collection of Articles,* **2**(n/a), 527–32. 05–07/06/2023 DOI: 10.5281/zenodo.13693241.

Karmoka, S.F., Al haj Ahmad, A. and Alkhaled, E.A. (2019). Identifying drought classes in Northwest Syria using MODIS satellite image spectral indices EVI, LAI, TVI'. *Scientific Journal of King Faisal University: Basic and Applied Sciences,* **20**(1), 27–39.

Kim, T.W. and Jehanzaib, M. (2020). Drought risk analysis, forecasting and assessment under climate change. *Water,* **12**(7), 1862. DOI: 10.3390/w12071862.

Kogan, F.N. (1995). Application of vegetation index and brightness temperature for drought detection. *Advances in Space Research,* **15**(11), 91–100. DOI: 10.1016/0273-1177(95)00079-T.

Li, T. and Zhong, S. (2024). Advances in optical and thermal remote sensing of vegetative drought and phenology. *Remote Sensing,* **16**(22), 4209. DOI: 10.3390/rs16224209.

Masek, J.G., Wulder, M.A., Markham, B., McCorkel, J., Crawford, C.J., Storey, J. and Jenstrom, D.T. (2020). Landsat 9: Empowering open science and applications through continuity. *Remote Sensing of Environment,* **248**(n/a), 111968. DOI: 10.1016/j.rse.2020.111968.

Masitoh, F. and Rusydi, A.N. (2019). Vegetation Health Index (VHI) analysis during drought season in Brantas Watershed. In: *IOP Conference Series: Earth and Environmental Science* **389**(1), 012033. IOP Publishing. DOI: 10.1088/1755-1315/389/1/012033.

Mathbout, S., Boustras, G., Papazoglou, P., Vide, J.M. and Raai, F. (2025). Integrating climate indices and land use practices for comprehensive drought monitoring in Syria: Impacts and implications. *Environmental and Sustainability Indicators*, **26**(n/a), 100631. DOI: 10.1016/j.indic.2025.100631.

Nepstad, D.C., de Carvalho, C.R., Davidson, E.A., Jipp, P.H., Lefebvre, P.A., Negreiros, G.H. and Vieira, S. (1994). The role of deep roots in the hydrological and carbon cycles of Amazonian forests and pastures. *Nature,* **372**(6507), 666–9. DOI: 10.1038/372666a0.

Rouse Jr, J.W., Haas, R.H., Schell, J.A. and Deering, D.W. (1973). *Monitoring the vernal advancement and retrogradation (green wave effect) of natural vegetation* (No. NASA-CR-132982). Available at: https://ntrs.nasa.gov/citations/19750020419 (accessed on 01/05/2025).

Roy, D.P., Wulder, M.A., Loveland, T.R., Woodcock, C.E., Allen, R.G., Anderson, M.C. and Zhu, Z. (2014). Landsat-8: Science and product vision for terrestrial global change research. *Remote Sensing of Environment,* **145**(n/a), 154–72. DOI: 10.1016/j.rse.2014.02.001.

Sugg, M., Runkle, J., Leeper, R., Bagli, H., Golden, A., Handwerger, L.H. and Woolard, S. (2020). A scoping review of drought impacts on health and society in North America. *Climatic Change,* **162**(n/a), 1177–95. DOI: 10.1007/s10584-020-02848-6.

Sukkar, A., Abulibdeh, A., Essoussi, S. and Seker, D.Z. (2024). Investigating the impacts of climate variations and armed conflict on drought and vegetation cover in Northeast Syria (2000–2023). *Journal of Arid Environments,* **225**(n/a), 105278. DOI: 10.1016/j.jaridenv.2024.105278.

Taheri Qazvini, A. and Carrion, D. (2023). A spatiotemporal drought analysis application implemented in the Google Earth Engine and applied to Iran as a case study. *Remote Sensing,* **15**(9), 2218. DOI: 10.3390/rs15092218.

Tang, J., Zeng, J., Zhang, Q., Zhang, R., Leng, S., Zeng, Y. and Wang, Q. (2020). Self-adapting extraction of cropland phenological transitions of rotation agroecosystems using dynamically fused NDVI images. *International Journal of Biometeorology,* **64**(n/a), 1273–83. DOI: 10.1007/s00484-020-01904-1.

Trenberth, K.E., Dai, A., Van der Schrier, G., Jones, P.D., Barichivich, J., Briffa, K.R. and Sheffield, J. (2014). Global warming and changes in drought. *Nature Climate Change,* **4**(1), 17–22. DOI: 10.1038/nclimate2067.

U.S. Geological Survey. (2023). *Landsat 8–9 Collection 2 Level 2 Science Product Guide* (Version 5.0). U.S. Department of the Interior. Available at: https://www.usgs.gov (accessed on 07/02/2025)

Wilhite, D.A. and Glantz, M.H. (1985). Understanding the drought phenomenon: The role of definitions. *Water International,* **10**(3), 111–20. DOI: 10.1080/02508068508686328.

Wulder, M.A., Roy, D.P., Radeloff, V.C., Loveland, T.R., Anderson, M.C., Johnson, D.M. and Cook, B.D. (2022). Fifty years of Landsat science and impacts. *Remote Sensing of Environment,* **280**(n/a), 113195. DOI: 10.1016/j.rse.2022.113195.

Zeng, J., Zhang, R., Qu, Y., Bento, V.A., Zhou, T., Lin, Y. and Wang, Q. (2022). Improving the drought monitoring capability of VHI at the global scale via ensemble indices for various vegetation types from 2001 to 2018. *Weather and Climate Extremes,* **35**(n/a), 100412. DOI: 10.1016/j.wace.2022.100412.

Zhang, Z., Xu, W., Shi, Z. and Qin, Q. (2021). Establishment of a comprehensive drought monitoring index based on multisource remote sensing data and agricultural drought monitoring. *IEEE Journal of Selected Topics in Applied Earth Observations and Remote Sensing,* **14**(n/a), 2113–26. DOI: 10.1109/JSTARS.2021.3052194.

Yu, X., Guo, X. and Wu, Z. (2014). Land surface temperature retrieval from Landsat 8 TIRS—Comparison between radiative transfer equation-based method, split window algorithm and single channel method. *Remote Sensing,* **6**(10), 9829–52. DOI: 10.3390/rs6109829.

Scientific Journal of King Faisal University:
Basic and Applied Sciences

Novel Cell-Free Suspensions of Symbiotic Bacteria for Biocontrol of Phytopathogenic Bacteria

Marwa Asad Nayef and Najwa Ibrahim Khaleel Al-Barhawee
Department of Biology, College of Education for Pure Science, University of Mosul, Mosul, Iraq

LINK	RECEIVED	ACCEPTED	PUBLISHED ONLINE	ASSIGNED TO AN ISSUE
https://doi.org/10.37575/b/sci/250009	10/03/2025	26/05/2025	26/05/2025	01/06/2025
NO. OF WORDS	**NO. OF PAGES**	**YEAR**	**VOLUME**	**ISSUE**
6289	7	2025	26	1

ABSTRACT

Biofertilizers utilize plant growth-promoting bacteria (PGPB), which are symbiotic bacteria found in the root nodules of leguminous plants that fix atmospheric nitrogen. This study utilized cell-free bacterial suspensions from several leguminous plants, including Vicia faba, Trifolium repens, Lens culinaris, Trigonella foenum-graecum, Lens culinaris subsp. orientalis and Medicago sativa. Six isolates (MA1–MA6) were tested as biocontrol agents against Agrobacterium tumefaciens RB04, Lelliottia amnigena MN1 and Xanthomonas campestris. After establishing that these bacteria are pathogenic, we evaluated their antagonistic activity using the cross method. This identified MA2 as the most effective isolate, with MA5 following closely. Among the tested isolates, MA2 was the most successful in inhibiting the growth of pathogenic bacteria, followed by MA5. The other isolates only impacted the growth of two bacterial species: L. amnigena strain MN1 and X campestris. The agar well diffusion method showed bacterial sensitivity to cell-free supernatants (CFSs) at 67%, 34% and 17% for A. tumefaciens, X. campestris and L. amnigena, respectively. CFS MA6, the most effective supernatant, was analyzed via gas chrom atography-mass spectrometry, revealing four active compounds: C7H13NO2, C11H18N2O2, C28H53NO3 and C21H39NO3, with molecular weights of 143, 210, 451 and 353, respectively.

KEYWORDS
Agrobacterium tumefaciens, antagonistic, biofertilizers, GC-MS, legume plants, PGPB

CITATION
Nayef, M.A. and Al-Barhawee, N.I.K. (2025). Novel cell-free suspensions of symbiotic bacteria for biocontrol of phytopathogenic bacteria. *Scientific Journal of King Faisal University: Basic and Applied Sciences*, **26**(1), 57–63. DOI: 10.37575/b/sci/250009

1. Introduction

In the rhizosphere, plants coexist with a diverse range of soil bacteria known as plant growth-promoting bacteria (PGPB). These bacteria have a positive influence on plant growth, development and resistance to both biotic and abiotic stresses, while also producing secondary metabolites, which explains their prevalence (Pantigoso *et al.*, 2022). Research highlights phytohormones (Egamberdieva *et al.*, 2017), organic acids and various secondary metabolites, including volatile chemicals and exopolysaccharides (Naseem *et al.*, 2018), as significant contributors. Additionally, they enhance plants' resilience against biotic threats, such as bacterial and fungal infections and abiotic stressors, including drought and salinity (Pellegrini *et al.*, 2020). Over recent decades, PGPBs have garnered substantial attention due to their sustainability and other beneficial traits. However, maintaining their activity in the root zone has proven difficult due to a decline in most PGPB species' populations and suboptimal bacterial biomass production from inoculating soil with bacterial suspensions lacking suitable carriers or formulations. Moreover, these bacteria face competition from soil microbes that have adapted to prey on them and compete with naturally occurring established microbial communities (Mokrani *et al.*, 2020). The low survival rates of PGPB bacteria in agricultural settings likely contribute to the limited mention of PGPB strains in scientific literature. To address this issue, various researchers have proposed using a cell-free suspension (CFS) as a viable alternative. A CFS can be produced through a specific protocol that includes centrifugation and microfiltration, followed by purification and an examination of the biocontrol properties of the substances it contains (Morcillo *et al.*, 2022). Although research on this topic remains limited, CFS shows promise in both the medical and food sectors, with most studies focusing on its use as a biocontrol agent in laboratory settings to combat bacterial and fungal plant diseases. Among the various genera researched for their potential biostimulant and biocontrol capabilities, considerable emphasis has been placed on Bacillus (Pellegrini *et al.*, 2020).

Having acquired this insight, we set out to utilize the conjugate filtrate system of symbiotic bacteria sourced from the root nodules of six legume plants (e.g., *Trigonella foenum-graecum, Lens culinaris subsp. orientalis* and *Medicago sativa*) as a method for biological control. Our objective was to inhibit the proliferation of three soil-borne bacterial species, *Agrobacterium tumefaciens* strain RB04, *Lelliottia amnigena MN1* and *Xanthomonas campestris*, that are harmful to various plant species. We then confirmed their pathogenicity on our target plants in vitro and identified their bioactive compounds through gas chromatography-mass spectrometry (GC-MS) analysis.

2. Materials and Methods

2.1. Symbiotic Bacteria:

Six bacterial isolates from root nodules of leguminous plants, isolated in a previous study, were used, namely: *Vicia faba, Trifolium repens, Lens culinaris, T. foenum-graecum, L. culinaris* subsp. *orientalis* and *M. sativa* (MA1, MA2, MA3, MA4, MA5 and MA6).

2.2. Pathogenic Bacteria:

Three different types of bacteria that colonize the soil and are pathogenic to plants were used in this study.

2.2.1. Agrobacterium *tumefacien* strain RB04

PhD student Rayan Salim from the University of Mosul's Department of Plant Protection, in the College of Agriculture and Forestry, conducted this research. After modifying the method outlined by Trigui *et al.* (2013), one colony of *A. tumefaciens* was transferred to Luria-Bertani (LB) broth and incubated at 30°C for 24 hours. The population was measured at 107 CFU/ml, with an absorbance of 0.96 ± 0.02 at 600 nm. Carrots (*Daucus carota L.*) were thoroughly cleaned by rinsing under running water with a brush. Subsequently, discs measuring 5 mm × 8 mm were created and sterilized in 2% sodium hypochlorite (NaClO) for 30 minutes. After three 15-minute rinses in

Corresponding Author: Marwa Asad Nayef 009647728207499, marwaasadnayef.1001@gmail.com,

sterile water, the discs were removed and dried on sterile paper towels. They were then positioned on sterile water agar medium in Petri plates. Following this, 50 µL of bacteria was applied to the discs using a small syringe. The discs were then carefully placed onto the water agar medium using sterile forceps. The plates were incubated at 25°C for 16 hours in light, followed by 8 hours in darkness. Regular monitoring of crown gall development was conducted.

2.2.2. Lelliottia amnigena (MN1)

This bacterium was obtained from the Soil Science and Water Resources Department, College of Agriculture/Mosul University. Two methods were employed to confirm its diagnosis.

The first involved assessing pathogenicity using the modified methodology of Osai *et al.* (2022), which employed mushroom plants instead of potato tubers. Healthy mushroom samples were carefully chosen, washed with tap water and subjected to surface sterilization using 75% ethanol. To eliminate any remaining alcohol, samples were rinsed three times with sterile distilled water and dried on sterile filter paper. Small incisions were made on the surface using a sterile scalpel and approximately 0.3 ml of *L. amnigena* suspension (3.5×10^1 CFU/ml) was applied. Sterile distilled water served as a negative control. The samples were then placed in a sterile plastic dish and incubated at 25°C, with daily observations of their characteristics made over 25 days.

The second method involved the molecular identification of these bacteria at the genus and species level, according to the following steps:

- A - DNA extraction: This process utilized Chelex 100 from Bio-Rad, USA. A small volume of purified colonies was collected using a loop and placed in a 1-ml tube containing 200 µl of Chelex 100 and 100 µl of TE buffer. The sample was then incubated in a water bath at 95°C. After 10 minutes, the sample was carefully lifted and centrifuged at 13,000 rpm for another 10 minutes. The resulting upper aqueous layer, which contained the DNA, was carefully removed and transferred to a 0.5-ml tube, then stored at −4°C in a refrigerator until needed.
- B-*16S rRNA* gene sequencing: As described by Rudolf *et al.* (2009), the sequencing process starts with PCR amplification of the target areas within the *16S rRNA* gene using specified primers: forward (F: GTGTAGCGGTGAAATGCG) and reverse (R: ACGGGCGGTGTGTACAA), in a total reaction volume of 25 µl. This mixture consists of 12.5 µl of master mix, 0.5 µl of forward primer, 0.5 µl of reverse primer, 6.5 µl of distilled water and 5 µl of genomic DNA. The PCR reaction involves denaturation at 95°C for 5 minutes, followed by 35 cycles of denaturation at 95°C for 30 seconds, annealing at 58°C for 1 minute and extension at 72°C for 30 seconds, concluding with an extension at 72°C for 5 minutes. Following this, PCR products are resolved on a 2% agarose gel with ethidium bromide and visualized using UV light. The sequence is then determined by sending the sample to Korea, followed by analyzing the results in the National Center for Biotechnology Information online database.

2.2.3. Xanthomonas campestris

PhD student Rayan Salim from the University of Mosul's Department of Plant Protection and College of Agriculture and Forestry obtained this bacterium. The diagnosis was validated by introducing this bacterium into cabbage (*Brassica oleracea*) plant leaves and monitoring its pathogenicity according to the methodology described by Popović *et al.* (2013). The bacteria were cultivated on a solid yeast extract-dextrose-CaCO3 medium for 48 hours at 28°C, then centrifuged and diluted in sterile distilled water to a concentration of 10^8 cfu/ml. Later, the petioles and leaves of the cabbage were injected with the inoculum to conduct the pathogenicity test. The leaves were incubated in a low-humidity environment at 25°C with a 16/8-h light cycle for a total of 24 hours. Once removed from the humid environment, the samples were kept in an incubator maintaining the same light and temperature conditions. Symptoms were visible 1-week post-inoculation.

2.2.4. Antagonistic activity test

We employed the cross-linking technique outlined by Skowronek *et al.* (2020) to evaluate whether six bacterial species isolated from legume root nodules (MA1, MA2, MA3, MA4, MA5 and MA6) can inhibit three naturally occurring soil-pathogenic bacteria (*A. tumefaciens RB04, L. amnigena MN1* and *X. campestris*). LB agar plates were prepared and inoculated with bacteria sourced from root nodules by drawing a single line down the center of each Petri dish. Following a 2-day incubation at 28°C, the plates were inoculated with phytopathogenic bacteria by creating a single line at a 90° angle to the previous line. We examined microbial interactions by measuring the size of the inhibition zone.

2.3. Testing Antibacterial Efficacy of The Cell-free Suspension:

2.3.1. Cell-free supernatant preparation

For the preparation of CFS, the procedure of El-Mokhtar *et al.* (2020) was modified slightly by adjusting the incubation conditions. The six isolated bacteria (MA1–MA6) were grown in 100 mL of LB broth for 18 hours at 28°C, then centrifuged to obtain the supernatant at 6,000 × g for 15 minutes at 4°C. The centrifuged supernatant was filtered using a sterile filter (Sigma, Germany) with a 0.22-µm pore size.

2.3.2. Agar well diffusion method

For 24 hours, each type of harmful bacteria (*A. tumefaciens RB04, L. amnigena MN1* and *X. campestris*) was cultivated in LB broth and maintained at 28°C. After 100 µL of sterile swab was used to disperse each suspension over the surface of the solid LB medium, corresponding to McFarland's standard of 0.5, the mixture was left to dry at room temperature (25°C). Then, using a sterile cork borer, holes 6 mm in diameter were punched into the agar. For each bacterial species, the holes were filled with approximately 100 µL of CFS and the plates were incubated at 28°C for 24 hours, as described by Gopal and Thirupathi (2020). A transparent graduated ruler was used to measure the inhibition area surrounding each hole in millimeters.

2.3.3. Testing pathogens' susceptibility to antibiotics

The same method described earlier was utilized to inoculate the medium with pathogenic bacteria, substituting the holes with antibiotic discs. A total of 10 different antibiotics were employed: Trimethoprim (TMP), Ceftazidime (CAZ), Erythromycin (E), Vancomycin (VA), Cefotaxime (CTX), Ampicillin (AM), Rifampin (RA), Streptomycin (S), Chloramphenicol (C), Penicillin (P), Neomycin (N) and Gentamicin (CN), all produced by Oxoid™, United Kingdom. Following incubation under identical conditions, the zone of inhibition around each disc was measured in millimeters.

2.4. Gas Chromatography-mass Spectrometry Analysis of Components of Cell-free Supernatant:

Test results indicated that the CFS from bacterial isolates of plant root nodules (AM6) was the most effective against phytopathogenic bacteria. Using a gas chromatography-mass spectrometry (GC-MS) QP210 ULTRA gas chromatograph (Shimadzu, Japan) at Basrah University, we identified chemical compounds with antibacterial properties by examining their retention times in the mass spectrometer's capillary column and then comparing them with the mass spectra from the NSTA08 library database and GC-MS Solution software (Al-Barhawee and Al-Rubyee, 2024).

2.5. Statistical Analysis:

The results were statistically analyzed according to Goad (2020) to identify significant differences between means in terms of standard deviation values at a significance level of $p = 0.05$.

3. Results and Discussion

3.1. Pathogenicity:

The pathogenicity of the bacteria from the three species in this study was confirmed through their effects on a specialized plant (Figure 1). Carrot discs, a type of dicotyledonous plant, were infected with *A. tumefaciens* strain RB04, allowing us to observe the progression of crown gall disease over 10 days and 3 weeks post-infection. *A. tumefaciens* strains collected from six distinct dicotyledonous plants on the campus of Rajshahi University in Rajshahi, Bangladesh, were identified as *A. tumefaciens*, capable of inducing crown gall disease on potato slices, when compared to the standard *A. tumefaciens* strain ATCC 23308T. These strains were assigned registration numbers based on their host plants (Islam *et al.*, 2010). According to Soriful *et al.* (2010), the number of crown galls formed on carrot discs varied with the strain, resulting in 12–16 tumors per disc, exceeding the 12 tumors per disc observed with the control *A. tumefaciens* ATCC 23308T. It is important to note that crown gall formation occurs when T-DNA from the tumor-inducing plasmid (Ti) integrates into the host plant genome (Hooykaas, 2023).

Regarding the bacterium *L. amnigena*, diagnosis was confirmed due to the infected mushroom plant exhibiting symptoms of soft mold disease. This condition is characterized by the infected plant's attachment area being submerged in a viscous solution that emits a foul, soft, mold odor, ultimately leading to the plant's demise. Molecular diagnosis was conducted using the *16S rRNA* gene primer, which revealed 95% identity with the isolate *L. amnigena* strain BW102, as documented in the gene bank with accession number PQ803913. The less than perfect match can be attributed to deletions or substitutions among some of its nitrogenous bases: C and G were deleted at two sites; G was substituted by A at five sites; A was changed to G at five sites; C was converted to both T and A at two different locations; A switched to G at four places; and T changed to A at one site (Figure 2). Consequently, it has been registered in GenBank as *L. amnigena* strain MN2, with accession number PV030017. Genome evolution occurs when there is a shift in the sequence of nitrogenous bases in a short genomic segment. This alteration is termed a mutation, caused by gene deletion or reduction (Lynch, 2006). Laboratory evolutionary studies indicate that bacterial genomes are susceptible to deletion events over brief evolutionary time frames (Nilsson *et al.*, 2005). In this study, we identified 21 independent deletion and substitution mutations occurring at varying rates, often referred to as biased mutations since they occur more frequently than others (Payne *et al.*, 2019). These mutations tend to arise at specific genomic sites, particularly those more prone to change, such as regions distant from the origin of replication (Long *et al.*, 2015). Furthermore, these mutations may occur infrequently and within a single gene (Horton and Taylor, 2023), causing damage to single-stranded sequences during replication or when used as templates for gene expression. This is frequently associated with bacterial exposure to toxic agents, such as free radicals and radiation, or variations in nutrient medium components or growth conditions (Selveshwari *et al.*, 2021). Mutations can also result from the interactions between the replication complex and mononucleotide repeats, such as CCCCC, leading to polymerase enzyme slippage that causes insertion or deletion processes (Hefetz *et al.*, 2023). Notably, this phenomenon was not observed in our study, as shown in Figure 2. However, we found a marked preference for substitutions over deletions, a tendency often associated with their simpler formation mechanisms, more efficient repair processes and generally less specific evolutionary implications (Horton and Taylor, 2023). In *Pseudomonas* sp., Danneels *et al.* (2018) reported 857 insertion and deletion mutations, with the mutations predominantly occurring in the form of deletions rather than insertions. Remarkably, this is the first record of this isolate in Iraq and other Arab countries, as per gene bank documentation. Globally, two strains have been recorded in China, the first derived from a downy mildew disease affecting potato tubers (Osei *et al.*, 2022) and the second isolated from downy mildew impacting numerous fields of purple mustard, with infection rates reaching around 20–30% across a 5-hectare agricultural area, leading to significant economic losses (Li *et al.*, 2025). Recent developments have classified *L. amnigena* as a soil-endemic bacterium and an opportunistic pathogen responsible for downy mildew in plants (Wu *et al.*, 2023). The third isolate analyzed in this study was *X. campestris*, due to its capacity to infect cabbage leaves and cause soft rot disease. Iglesias-Bernabé *et al.* (2019) reported that *B. oleracea* crops infected with *X. campestris pv. campestris* have led to significant economic damages worldwide.

Figure 1: Pathogenicity of pathogenic bacteria on carrots, mushroom and cabbage leaves

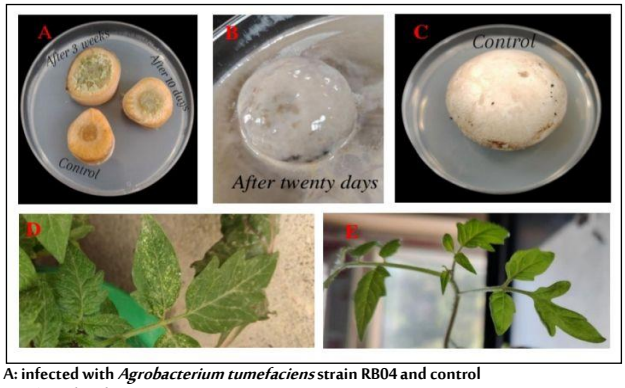

A: infected with *Agrobacterium tumefaciens* strain RB04 and control
B: infected with *L. amnigena* MN1,
C: control
D: infected with *X. campestris,*
E: control

Figure 2: The sequence of *L. amnigena* MN1 *16S rRNA* gene

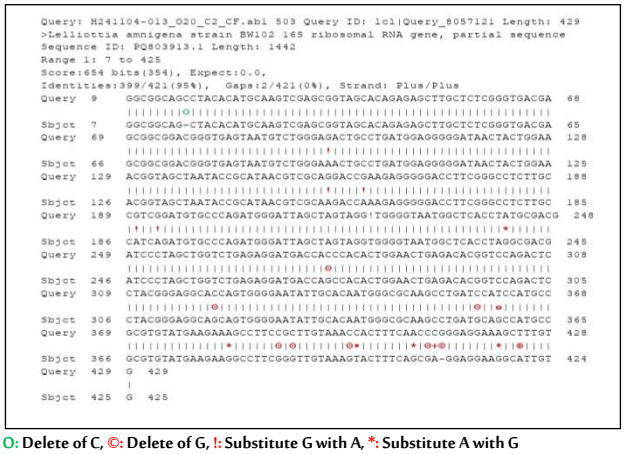

```
Query: M241104-013_020_C2_CF.ab1 503 Query ID: lcl|Query_8057121 Length: 429
>Lelliottia amnigena strain BW102 16S ribosomal RNA gene, partial sequence
Sequence ID: PQ803913.1 Length: 1442
Range 1: 7 to 425
Score:654 bits(354), Expect:0.0,
Identities:399/421(95%),  Gaps:2/421(0%), Strand: Plus/Plus
Query  9    GGCGGCAGCCTACACATGCAAGTCGAGCGGTAGCACAGAGAGCTTGCTCTCGGGTGACGA  68
            ||||||||O|||||||||||||||||||||||||||||||||||||||||||||||||||
Sbjct  7    GGCGGCAG-CTACACATGCAAGTCGAGCGGTAGCACAGAGAGCTTGCTCTCGGGTGACGA  65
Query  69   GCGGCGGACGGGTGAGTAATGTCTGGGAGACTGCCTGATGGAGGGGGATAACTACTGGAA  128
            |||||||||||||||||||||||||||!|||||||||||||||||||||||||||||||
Sbjct  66   GCGGCGGACGGGTGAGTAATGTCTGGGAAACTGCCTGATGGAGGGGGATAACTACTGGAA  125
Query  129  ACGGTAGCTAATACCGCATAACGTCGCAAGACCAAAGAGGGGGACCTTCGGGCCTCTTGC  188
            ||||||||||||||||||||||||||||!|||!|||||||||||||||||||||||||||
Sbjct  126  ACGGTAGCTAATACCGCATAACGTCGCAAGACCAAAGAGGGGGACCTTCGGGCCTCTTGC  185
Query  189  CGTCGGATGTGCCCAGATGGGATTAGCTAGTAGGTGGGGTAATGGCTCACCTATGCGACG  248
            |!|!|!||||||||||||||||||||||||||||||||||||||||||||||*||||||
Sbjct  186  CATCAGATGTGCCCAGATGGGATTAGCTAGTAGGTGGGGTAATGGCTCACCTAGGCGACG  245
Query  249  ATCCCTAGCTGGTCTGAGAGGATGACCACCCACACTGGAACTGAGACACGGTCCAGACTC  308
            ||||||||||||||||||||||||||||!|||||||||||||||||||||||||||||||
Sbjct  246  ATCCCTAGCTGGTCTGAGAGGATGACCAGCCACACTGGAACTGAGACACGGTCCAGACTC  305
Query  309  CTACGGGAGGCACCAGTGGGGAATATTGCACAATGGGCGCAAGCCTGATCCATCCATGCC  368
            ||||||||||!|||||||||||||||||||||||||||||||||||||||!|!|||||||
Sbjct  306  CTACGGGAGGCAGCAGTGGGGAATATTGCACAATGGGCGCAAGCCTGATGCAGCCATGCC  365
Query  369  GCGTGTATGAAGAAAGCCTTCGGTTGTAAACCACTTTCAACCCGGGAGGAAAGCTTTGT  428
            |||||||||||||*||||||!|!|||||||!*||||||*|||||*|!|!|||||||!|!||||
Sbjct  366  GCGTGTATGAAGAAGGCCTTCGGGTTGTAAAGTACTTTCAGCGA-GGAGGAAGGCATTGT  424
Query  429  G  429
            |
Sbjct  425  G  425
```

O: Delete of C, ©: Delete of G, !: Substitute G with A, *: Substitute A with G
Θ: Substitute C with G, ϴ: Substitute T with G, +: Substitute C with A, ▪: Substitute C with T, ®: Substitute T with A

3.2. Evaluation of The Antagonistic Activity:

3.2.1. Symbiotic bacteria by cross-streak assay

The potential antagonistic properties of symbiotic isolates were assessed using cross-line assays against three phytopathogenic bacteria: *A. tumefaciens* strain RB04, *L. amnigena* strain MN1 and *X. campestris* (Figure 3). Six isolates, labeled MA1 through MA6, successfully inhibited the growth of these bacterial species (Table 1). Among them, the isolate MA2 exhibited the strongest inhibitory effect on pathogenic bacteria, followed by MA5. In contrast, the

remaining isolates (MA1, MA3, MA4 and MA6) only affected the growth of two species: *L. amnigena strain* MN1 and *X. campestris*. This variation can be attributed to the release of secondary metabolites during the biocontrol process, which are often toxic to other microorganisms yet not critical for the cell functions of the producing organisms. The ability to generate such metabolites can vary significantly across different strains and isolates (Tariq *et al.*, 2020). The antagonistic effects of these aerobic nitrogen-fixing bacteria might stem from competition for space and nutrients rather than antimicrobial substances (Esteban-Herrero *et al.*, 2023). Alternatively, these bacteria may produce biocontrol enzymes, such as protease, lipase, amylase and DNase, or generate stable antimicrobial substances that permeate the medium and remain active throughout the analysis (Riseh *et al.*, 2024). Additionally, resistance may arise from the production of virulence factors by pathogenic bacteria, especially Gram-negative types, including efflux pumps that are crucial for expelling diverse compounds, thus lowering their concentration and effectiveness in the cell (Gaurav *et al.*, 2023).

Figure 3: Cross-tests between the six isolates (MA1–MA6)

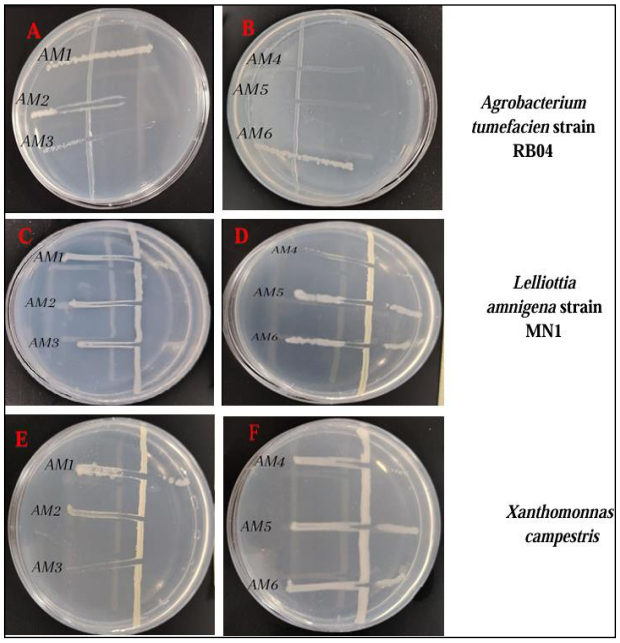

Plant symbionts are represented by the horizontal lines and the vertical lines represent the three plant pathogenic isolates.

Table 1: Determination of the antagonistic activity of the six plant symbiotic isolates against the pathogenic isolates using cross-validation tests.

Symbiotic bacteria	Size of Inhibition Zones (mm)		
	Pathogenic bacteria		
	A. tumefacien strain RB04	*L. amnigena* strain MN1	*X. campestris*
MA1	R (0) c	25 ± 1.00 c	17 ± 1.528 d
MA2	40 ± 2.000* A	45 ± 1.000 a	40 ± 1.732 a
MA3	R (0) c	30 ± 2.517 b	27 ± 2.082 b
MA4	R (0) c	26 ± 3.000 bc	23 ±1.732 c
MA5	20 ± 2.517 B	20 ± 3.464 d	12 ± 2.000 e
MA6	R (0) c	15 ± 2,646 e	10 ± 2.646 e
Resistance (%)	67	0.0	0.0
Sensitivity (%)	33	100	100

R: Resistance, *: value of standard deviation, **p-value: < 0001. Data is the average of three replicates. Similar letters indicate no significant differences, while different letters indicate significant differences.**

3.2.2. Symbiotic bacterial cell-free supernatants

When assessing the inhibitory effects of six CFSs on plant pathogens known for their drug resistance, 16% for *A. tumefaciens* RB04 and *L. amnigena* MN1 and 25% for *X. campestris* (see Figure 4 and Table 2), most tested pathogens generally exhibited varying resistance levels to all types of CFS, with complete resistance noted for CFS from MA3 and MA5. Conversely, the CFS from AM6 demonstrated the greatest inhibitory effect against plant pathogenic bacteria, showing inhibition zones of 20 mm for *A. tumefaciens* RB04, 17 mm for *X. campestris* and 16 mm for *L. amnigena* MN1, compared to the other CFS types (refer to Figure 5 and Table 3). Statistical analysis revealed significant differences among the variables, as indicated by a probability level of <0.05.

Regarding the resistance of Gram-negative bacteria, the studied plant pathogens are resistant to the following antibiotics: *X. campestris* (CAZ), *L. amnigena* MN1 and *X. campestris* (CTX) and *A. tumefaciens* RB04 (P). This resistance likely arises from their production of the beta-lactamase enzyme, which effectively cleaves the beta-lactam ring in antibiotic structures (Vivekanandan *et al.*, 2025). *A. tumefaciens* RB04's resistance to the antibiotic E is presumably due to modifications in the 23S ribosomal RNA within the 50S ribosomal subunit, which obstructs E's binding to the ribosome and allows continued protein synthesis (Liang and Han, 2013). Meanwhile, the resistance of *L. amnigena* MN1 and *X. campestris* to S could result from alterations in the genes encoding the 16S ribosomal RNA (Spagnolo *et al.*, 2016). Regarding the sensitivity of these three types of pathogenic bacteria to trimethoprim, this may stem from its inhibition of the reduction of dihydrofolate to tetrahydrofolate, the active form of folic acid, as suggested by Gleckman *et al.* (1981). On the other hand, the sensitivity to chloramphenicol may be attributed to its ability to inhibit protein synthesis by binding to the 50S subunit of the bacterial 70S ribosome (Yu and Zeng, 2024).

Furthermore, Jumaah *et al.* (2022) observed that CFS from bacteria isolated from the root nodules of leguminous plants inhibited the growth of certain plant pathogenic fungi, suggesting their potential as biological control agents. This antimicrobial action from these bacteria potentially suppresses the growth of plant pathogens by degrading compounds secreted by them and inhibiting the germination of pathogenic fungal spores (Al-Ani *et al.*, 2012). In a recent study, the cell-free supernatant of *P. aeruginosa*, isolated from soil, was found to play a role in preventing biofilm formation by *A. tumefaciens*, a plant pathogenic bacterium that attaches to plant wounds and forms crown galls (Al-Barhawee and Al-Rubyee, 2024).

Figure 4: Antimicrobial activity of antibiotics against the pathogenic isolates

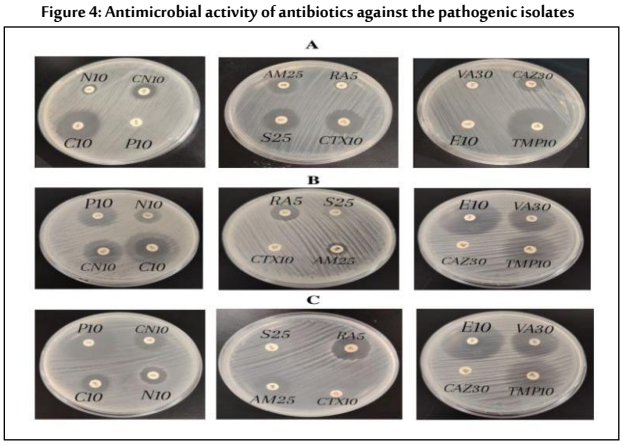

A: A. tumefaciens, B: L. amnigena, C: X. campestris.

Table 2: Effect of antibiotics on pathogenic bacteria by the diameter of the inhibition zone (mm)

Antibiotics (µg/disk)	Size of Inhibition Zones (mm)		
	Pathogenic bacteria		
	A. tumefacien strain RB04	*L. amnigena* strain MN1	*X. campestris*
TMP (10)	31 ± 2.082* a**	27 ± 3.055 bc	22 ± 2.082 b
CAZ (30)	16 ± 1.732 b	34 ± 2.517 a	R (0) e
E (10)	R (0) e	26 ± 2.309 bc	23 ± 3.055 b
VA (30)	6 ± 0.000 c	24 ± 2.000 cd	30 ± 2.082 a
CTX (10)	19.33 ± 1.528 b	R (0) e	R (0) e
AM (25)	17 ± 2.887 b	11 ± 2.000 f	16 ± 1.000 cd
RA (5)	8 ± 1.155 c	15 ± 0.000 e	19 ± 2.646 c
S (25)	18 ±1.732 b	R (0) e	R (0) e
C (10)	30 ± 4.619 a	28 ± 4.041 b	15 ± 1.155 d
P (10)	R (0) e	24 ± 1.732 cd	29 ± 1.000 a
N (10)	7 ± 1.732 c	16 ± 1.732 e	14 ± 0.000 d
CN (10)	17 ± 2.646 b	20 ± 3.215 d	17 ± 3.512 cd
Resistance (%)	16	16	25
Sensitivity (%)	84	84	75

R: Resistance, *: value of standard deviation, p-value: < 0001. Data are an average of three replicates. **: Similar letters indicate no significant differences between the variables and different letters indicate significant differences between the variables.

Figure 5: Antagonistic activity of six CFSs against three pathogenic bacteria

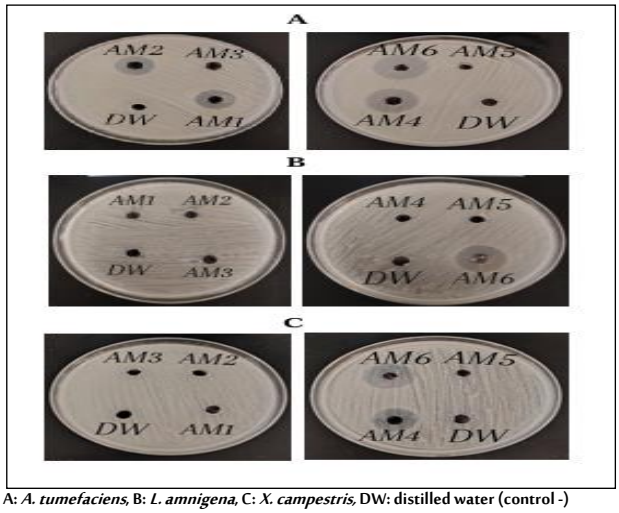

A: *A. tumefaciens*, B: *L. amnigena*, C: *X. campestris*, DW: distilled water (control -)

Table 3: Effect of CFS of Symbiotic bacteria on pathogenic bacteria by the diameter of the inhibition zone (mm).

CFS of Symbiotic bacteria	Size of Inhibition Zones (mm)		
	Pathogenic bacteria		
	A. tumefacien strain RB04	*L. amnigena* strain MN1	*X. campestris*
AM1	16 ± 1.732* bc**	R (0) e	R (0) e
AM2	13 ± 1.155 c	R (0) e	R (0) e
AM3	R (0) e	R (0) e	R (0) e
AM4	18 ± 3.464 ab	R (0,0,0)	16 (14, 17,17)
AM5	R (0) e	R (0) e	R (0) e
AM6	20 ± 3.215 a	16 ± 1.732 a	17 ± 2.517 a
Resistance (%)	33	83	66
Sensitivity (%)	67	17	34

R: Resistance, *: value of standard deviation, p-value: < 0001. Data are an average of three replicates. **: Similar letters indicate no significant differences between the variables and different letters indicate significant differences between the variables.

3.2.3. Gas chromatography-mass spectrometry analysis

Isolate MA6 CFS was chosen for GC-MS analysis due to its strong effectiveness in inhibiting pathogenic bacteria growth, as indicated by the size of the inhibition zone (mm). Table 4 shows the presence of four chemical compounds: (3-Pyrrolidin-2-yl-propionic acid), (Pyrrolo[1,2-a] pyrazine-1,4-dione hexahydro), (L-Proline, N-valeryl-, octadecyl ester) and (L-Leucine, N-cyclopropylcarbonyl-, undecyl ester). Several studies have identified these chemical compounds in various bacterial sources. For example, GC-MS analysis of an ethyl acetate extract from *Streptomyces sp.* revealed several compounds, including 3-pyrrolidin-2-yl-propionic acid, which demonstrated a notable antibacterial effect against a range of pathogenic bacteria (Veilumuthu, 2022). According to Kiran *et al.* (2018), an antibiotic called pyrrolo[1,2-a]pyrazine-1,4-dione, hexahydro was found to be effective against methicillin-resistant *Staphylococcus aureus* after being isolated from the marine bacterium *Bacillus tequilensis* MSI45. Additionally, Ser *et al.* (2015) reported its antioxidant properties when extracted from *Streptomyces* bacteria sourced from soil. Conversely, laboratory tests demonstrated that *Aspergillus oryzae* YRA3 could completely inhibit the growth of *Rhizoctonia solani*. The chemical composition of the secondary metabolites produced by this fungus, as analyzed by GC-MS, revealed the presence of 32 distinct compounds. L-Proline, N-valeryl and octadecyl esters were found to be the most effective, while no antagonistic effects were observed for Leucine, N-cyclopropylcarbonyl- and undecyl esters throughout the experiment (Rashad *et al.*, 2023).

Table 4: The four chemical compounds and their structure from the GC-MS analysis of AM6 CFS

Compound Name	Formula	Molecular Weight(g/mol)	Structures
3-Pyrrolidin-2-yl-propionic acid	$C_7H_{13}NO_2$	143	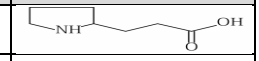
Pyrrolo[1,2-a]pyrazine-1,4-dione hexahydro	$C_{11}H_{18}N_2O_2$	210	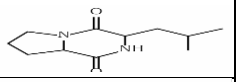
L-Proline, N-valeryl-, octadecyl ester	$C_{28}H_{53}NO_3$	451	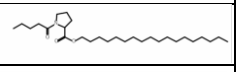
L-Leucine, N-cyclopropylcarbonyl-, undecyl ester	$C_{21}H_{39}NO_3$	353	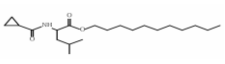

4. Conclusions

Symbiotic bacteria associated with legume plants, particularly those isolated from the root nodules of beans, can inhibit the development of bacterial plant diseases by producing bioactive compounds. Therefore, these bacteria show promise as biological agents to control bacterial infections in economically valuable crops and future research should promptly evaluate them in real-world settings as novel, environmentally safe antibacterial agents. Investigating this topic could lead to the development of new and more effective antibacterial agents based on the active compounds and diverse secondary metabolites produced by these environmentally friendly bacteria, thereby illuminating the complex relationships among different microbes coexisting in the soil. Additionally, the data stored in the gene bank indicate that *L. amnigena* has been isolated in only two previous studies conducted in China and was recently isolated for the third time in this study by the Laboratory of Molecular Genetics, Department of Biology, College of Pure Sciences, University of Mosul, Iraq. This marks the first registration in Iraq and the first time this bacterium has been used for in vitro biocontrol. We anticipate that future field applications will support sustainable agriculture efforts in producing healthy crops free from microbial diseases.

Data Availability Statement

The data that support the findings of this study are available on request from the corresponding author.

Acknowledgments

We extend our sincere appreciation to the University of Mosul for providing us with the opportunity to conduct this research and for publishing the results in your esteemed publication.

Funding

This research received no specific grant from any funding agency in the public, commercial, or not-for-profit sectors.

Conflicts of Interest

No conflicts of interest exist.

Biographies

Marwa Asad Nayef

Department of Biology, College of Education for Pure Science, University of Mosul, Mosul, Iraq, 009647728207499, marwaasadnayef.1001@gmail.com, or marwa.22esp17@student.uomosul.edu.iq

Marwa is an Iraqi lecturer and master's researcher earned her bachelor's degree in Life Sciences from the University of Mosul in 2007 and began her master's studies in 2022. In addition to her academic work, she currently teaches biology to fifth-year students at Seville Girls' High School, where she also serves as an assistant and a member of the examination committee. Her research interest lies in the fields of biological sciences and educational methodologies.

ORCID: 0009-0003-9019-3036

Najwa Ibrahim Khaleel Al-Barhawee

Department of Biology, College of Education for Pure Science, University of Mosul, Mosul, Iraq, +9647715546335, dr.najwa@uomosul.edu.iq

Najwa is an Iraqi holds a Ph.D. in Nitrogen Fixation (1999) and has authored over 30 research papers, including Scopus-indexed publications. Her expertise spans microbiology, nitrogen fixation, and pathogenic microorganisms. She has supervised eight master's and nine Ph.D. students, holds three patents, and has received prestigious honours, including a gold medal from Kuwait and a scientific shield from Iğdır University, Turkey.

ORCID: 0000-0001-8547-0316

References

Al-Ani, R.A., Adhab, M.A., Mahdi, M.H. and Abood, H.M. (2012). *Rhizobium japonicum* as a biocontrol agent of soybean root rot disease caused by fusarium solani and macrophomina phaseolina. *Plant Protection Science*, **48**(4), 149. DOI: 10.17221/16/2012-PPS.

Al-Barhawee, N.I.K. and Al-Rubyee, S.S. (2024). Inhibition of biofilm formation in *Agrobacterium tumefaciens* by cell-free supernatants of Pseudomonas aeruginosa analyzed by GC-MS. *Baghdad Science Journal*, **21**(7), 2222–36. DOI: 10.21123/bsj.2023.8692.

Danneels, B., Pinto-Carbó, M. and Carlier, A. (2018). Patterns of nucleotide deletion and insertion inferred from bacterial pseudogenes. *Genome Biology and Evolution*, **10**(7), 1792–802. DOI: 10.1093/gbe/evy140.

Egamberdieva, D., Wirth, S.J., Alqarawi, A.A., Abd_Allah, E.F. and Hashem, A. (2017). Phytohormones and beneficial microbes: Essential components for plants to balance stress and fitness. *Frontiers in Microbiology*, **8**(n/a), 2104. DOI: 10.3389/fmicb.2017.02104.

El-Mokhtar, M.A., Hassanein, K.M., Ahmed, A.S., Gad, G.F., Amin, M.M. and Hassanein, O.F. (2020). Antagonistic activities of cell-free supernatants of lactobacilli against extended-spectrum β-lactamase-producing *Klebsiella pneumoniae* and *Pseudomonas aeruginosa*. *Infection and Drug Resistance*, **n/a**(n/a)543–52. DOI: 10.2147/IDR.S235603.

Esteban-Herrero, G., Álvarez, B., Santander, R.D. and Biosca, E.G. (2023). Screening for novel beneficial environmental bacteria for an antagonism-based biological control. *Microorganisms*, **11**(7), 1795. DOI: 10.3390/microorganisms11071795.

Gaurav, A., Bakht, P., Saini, M., Pandey, S. and Pathania, R. (2023). Role of bacterial efflux pumps in antibiotic resistance, virulence and strategies to discover novel efflux pump inhibitors. *Microbiology*, **169**(5), 001333. DOI: 10.1099/mic.0.001333.

Gleckman, R., Blagg, N. and Joubert, D.W. (1981). Trimethoprim: mechanisms of action, antimicrobial activity, bacterial resistance, pharmacokinetics, adverse reactions and therapeutic indications. *Pharmacotherapy: The Journal of Human Pharmacology and Drug Therapy*, **1**(1), 14–9. DOI: 10.1002/j.1875-9114.1981.tb03548.x.

Goad, C.L. (2020). *SAS Programming for Elementary Statistics: Getting Started*. 1st Edition. Chapman and Hall/CRC. DOI: 10.1201/9780429491900

Gopal, M.A. and Thirupathi, A. (2020). Isolation and identification of Pseudomonas aeruginosa FROM UROPATHOGENS. *University of Yangon Research Journal*, **7**(11), n/a.

Hefetz, I., Israeli, O., Bilinsky, G., Plaschkes, I., Hazkani-Covo, E., Havouka, Z. and Helman, Y. (2023). A reversible mutation in a genomic hotspot saves bacterial swarms from extinction. *Iscience*, **26**(2). 106043 DOI: 10.1016/j.isci.2023.106043.

Hooykaas, P.J. (2023). The Ti plasmid, driver of *Agrobacterium* pathogenesis. *Phytopathology*, **113**(4), 594–604. DOI: 10.1094/PHYTO-11-22-0432-IA.

Horton, J.S. and Taylor, T.B. (2023). Mutation bias and adaptation in bacteria. *Microbiology*, **169**(11), 001404. DOI: 10.1099/mic.0.001404.

Iglesias-Bernabé, L., Madloo, P., Rodríguez, V.M., Francisco, M. and Soengas, P. (2019). Dissecting quantitative resistance to *Xanthomonas campestris* pv. *campestris* in leaves of *Brassica oleracea* by QTL analysis. *Scientific Reports*, **9**(1), n/a. DOI: 10.1038/s41598-019-38527-5.

Islam, M.S., Akter, M.M., Rahman, M.A., Rahman, M.M., Akhtar, M. and Alam, M.F. (2010). Isolation of *Agrobacterium tumefaciens* strains from crown gall sample of dicot plants in Bangladesh. *Current Research in Bacteriology*, **3**(n/a), 27–36. DOI: 10.3923/crb.2010.27.36.

Jumaah, O., Sultan, R. and Assafi, M. (2022). Antimicrobial activity of local rhizobial isolates against some fungi. *Journal of Education and Science*, **31**(2), 141–9. DOI: 10.33899/edusj.2022.133511.1230.

Kiran, G.S., Priyadharsini, S., Sajayan, A., Ravindran, A. and Selvin, J. (2018). An antibiotic agent pyrrolo[1,2-a] pyrazine-1,4-dione, hexahydro isolated from a marine bacteria *Bacillus tequilensis* MSI45 effectively controls multi-drug-resistant *Staphylococcus aureus*. *RSC Advances*, **8**(32), 17837–46. DOI: 10.1039/C8RA00820E.

Li, J.H., Qin, S.Y., Shi, Y.X., Xie, X.W., Chai, A.L., Wang, Y.H. and Li, L. (2025). First report of *Lelliottia amnigena* causing soft rot on purple stem mustards in China. *Plant Disease*, **109**(1), 228. DOI: 10.1094/PDIS-01-24-0180-PDN.

Liang, J.H. and Han, X. (2013). Structure-activity relationships and mechanism of action of macrolides derived from erythromycin as antibacterial agents. *Current Topics in Medicinal Chemistry*, **13**(24), 3131–64. DOI: 10.2174/15680266113136660223.

Long, H., Sung, W., Miller, S.F., Ackerman, M.S., Doak, T.G. and Lynch, M. (2015). Mutation rate, spectrum, topology and context-dependency in the DNA mismatch repair-deficient *Pseudomonas fluorescens* ATCC948. *Genome Biology and Evolution*, **7**(1), 262–71. DOI: 10.1093/gbe/evu284.

Lynch, M. (2006). Streamlining and simplification of microbial genome architecture. *Annual Review of Microbiology*, **60**(1), 327–49. DOI: 10.1146/annurev.micro.60.080805.142300.

Mokrani, S., Nabti, E.H. and Cruz, C. (2020). Current advances in plant growth promoting bacteria alleviating salt stress for sustainable agriculture. *Applied Sciences*, **10**(20), 7025. DOI:10.3390/app10207025.

Morcillo, R.J.L., Baroja-Fernández, E., López-Serrano, L., Leal-López, J., Muñoz, F.J., Bahaji, A. and Pozueta-Romero, J. (2022). Cell-free microbial culture filtrates as candidate biostimulants to enhance plant growth and yield and activate soil-and plant-associated beneficial microbiota. *Frontiers in Plant Science*, **13**(n/a), 1040515. DOI: 10.3389/fpls.2022.1040515.

Naseem, H., Ahsan, M., Shahid, M.A. and Khan, N. (2018). Exopolysaccharides produce rhizobacteria and their role in plant growth and drought tolerance. *Journal of Basic Microbiology*, **58**(12), 1009–22. DOI: 10.1002/jobm.201800309.

Nilsson, A.I., Koskiniemi, S., Eriksson, S., Kugelberg, E., Hinton, J.C.D. and Andersson, D.I. (2005). Bacterial genome size reduction by experimental evolution. *Proceedings of the National Academy of Sciences*, **102**(34), 12112–6. DOI: 10.1073/pnas.0503654102.

Osei, R., Yang, C., Cui, L., Ma, T., Li, Z. and Boamah, S. (2022). Isolation, identification and pathogenicity of *Lelliottia amnigena* causing soft rot of potato tuber in China. *Microbial Pathogenesis*, **164**(6), 105441. DOI: 10.1016/j.micpath.2022.105441.

Pantigoso, H.A., Newberger, D. and Vivanco, J.M. (2022). The rhizosphere microbiome: Plant–microbial interactions for resource acquisition. *Journal of Applied Microbiology*, **133**(5), 2864–76. DOI: 10.1111/jam.15686.

Payne, J.L., Menardo, F., Trauner, A., Borrell, S., Gygli, S.M., Loiseau, C. and Hall, A.R. (2019). Transition bias influences the evolution of antibiotic resistance in *Mycobacterium tuberculosis*. *PLoS Biology*, **17**(5), e3000265. DOI: 10.1371/journal.pbio.3000265

Pellegrini, M., Pagnani, G., Bernardi, M., Mattedi, A., Spera, D.M. and Gallo, M.D. (2020). Cell-free supernatants of plant growth-promoting bacteria: a review of their use as biostimulant and microbial biocontrol agents in sustainable agriculture. *Sustainability*, **12**(23), 9917. DOI: 10.3390/su12239917.

Popović, T., Jošić, D., Starović, M., Milovanović, P., Dolovac, N., Poštić, D. and Stanković, S. (2013). Phenotypic and genotypic characterization of *Xanthomonas campestris* strains isolated from cabbage, kale and broccoli. *Archives of Biological Sciences*, **65**(2), 585–93. DOI: 10.2298/ABS1302585P.

Rashad, Y.M., Al Tami, M.S. and Abdalla, S.A. (2023). Eliciting transcriptomic and antioxidant defensive responses against *Rhizoctonia* root rot of sorghum using the endophyte *Aspergillus oryzae* YRA3. *Scientific Reports*, **13**(1), 19823. DOI: 10.1038/s41598-023-46696-7.

Riseh, R.S., Vatankhah, M., Hassanisaadi, M. and Ait Barka, E. (2024). Unveiling the role of hydrolytic enzymes from soil biocontrol bacteria in sustainable phytopathogen management. *Frontiers in Bioscience-Landmark*, **29**(3), 105. DOI: 10.31083/j.fbl2903105.

Rudolf, I., Mendel, J., Šikutová, S., Švec, P., Masaříková, I., Nováková, D. and Hubálek, Z. (2009). *16S rRNA* gene-based identification of cultured bacterial flora from host-seeking *Ixodes ricinus, Dermacentor reticulatus* and *Haemaphysalis concinna* ticks, vectors of vertebrate pathogens. *Folia Microbiologica*, **54**(5), 419–28. DOI: 10.1007/s12223-009-0059-9.

Selveshwari, S., Lele, K. and Dev, S. (2021). Genomic signatures of UV resistance evolution in *Escherichia coli* depend on the growth phase during exposure. *Journal of Evolutionary Biology*, **34**(6), 953–67. DOI: 10.1111/jeb.13764.

Ser, H.L., Palanisamy, U.D., Yin, W.F., Abd Malek, S.N., Chan, K.G., Goh, B.H. and Lee, L.H. (2015). Presence of antioxidative agent, pyrrolo[1,2-a] pyrazine-1,4-dione, hexahydro-in newly isolated *Streptomyces mangrovisoli* sp. nov. *Frontiers in Microbiology*, **6**(n/a), 854. DOI: 10.3389/fmicb.2015.00854.

Skowronek, M., Sainaga, E., Pleszczyńska, M., Kazimierczak, W., Lis, M. and Wiater, A. (2020). Bacteria from the midgut of common cockchafer (*Melolontha melolontha* L.) larvae exhibiting antagonistic activity against bacterial symbionts of entomopathogenic nematodes: isolation and molecular identification. *International Journal of Molecular Sciences*, **21**(2), 580. DOI: 10.3390/ijms21020580.

Soriful, I.M., Akter, M.M., Rahman, M.M., Akhtar, M.M. and Alam, M.F. (2010). Isolation of *Agrobacterium tumefaciens* strains from crown gall sample of dicot plants in Bangladesh. *Current Research in Bacteriology*, **3**(1), 27–36. DOI: 10.3923/crb.2010.27.36.

Spagnolo, F., Rinaldi, C., Sajorda, D.R. and Dykhuizen, D.E. (2016). Evolution of resistance to continuously increasing streptomycin concentrations in populations of *Escherichia coli*. *Antimicrobial Agents and Chemotherapy*, **60**(3), 1336–42. DOI: 10.1128/aac.01359-15.

Tariq, M., Khan, A., Asif, M., Khan, F., Ansari, T., Shariq, M. and Siddiqui, M.A. (2020). Biological control: a sustainable and practical approach for plant disease management. *Acta Agriculture Scandinavica, Section B-Soil and Plant Science*, **70**(6), 507–24. DOI: 10.1080/09064710.2020.1784262.

Trigui, F., Pigeon, P., Jalleli, K., Top, S., Aifa, S. and El Arbi, M. (2013). Selection of a suitable disc bioassay for the screening of anti-tumor molecules. *International Journal of Biomedical Science*, **9**(4), 230. DOI: 10.59566/IJBS.2013.9230.

Vivekanandan, K.E., Kumar, P.V., Jaysree, R.C. and Rajeshwari, T. (2025). Exploring molecular mechanisms of drug resistance in bacteria and progressions in crispr/cas9-based genome expurgation solutions. *Global Medical Genetics*, **12**(2) 100042. DOI:10.1016/j.gmg.2025.100042.

Wu, H., Guo, T., Yang, S., Guo, Z., Kang, B., Liu, L. and Peng, B. (2023). First report of bacterial soft rot caused by Enterobacter mori affecting host watermelon. *Plant Disease*, **107**(7), 2209. DOI:10.1094/PDIS-05-22-1048-PDN.

Yu, T. and Zeng, F. (2024). Chloramphenicol interferes with 50s ribosomal subunit maturation via direct and indirect mechanisms. *Biomolecules*, **14**(10), 1225. DOI: 10.3390/biom14101225.

Scientific Journal of King Faisal University:
Basic and Applied Sciences

Magneto-Exciton Energy in Cylindrical Indium Arsenide Quantum Dots Affected by External Parameters

Marwan Zuhair Elias
Department of Medical Physics, College of Science, Mosul University, Mosul, Iraq

LINK	RECEIVED	ACCEPTED	PUBLISHED ONLINE	ASSIGNED TO AN ISSUE
https://doi.org/10.37575/b/sci/250014	11/04/2025	27/05/2025	27/05/2025	01/06/2025
NO. OF WORDS	**NO. OF PAGES**	**YEAR**	**VOLUME**	**ISSUE**
3491	5	2025	26	1

ABSTRACT

The effects of temperature, pressure, and an applied magnetic field on the energies of a cylindrical layer of indium arsenide (InAs) quantum dots, with and without Coulomb interaction, are investigated. Exciton energy depends significantly on these parameters. The results show that the ground-state and excited-state energies increase with rising temperature and applied magnetic field (blue shift), but that both energy states decrease with increasing pressure (red shift). As the temperature increases for higher states, the sensitivity of magneto-exciton energy also increases. The outcomes obtained for layered and ring-shaped systems exhibit a universal quality, making them particularly interesting.

KEYWORDS
Exciton, magnetic field, nanostructures, potential, pressure, temperature

CITATION
Elias, M.Z. (2025). Magneto-exciton energy in cylindrical indium arsenide quantum dots affected by external parameters. *Scientific Journal of King Faisal University: Basic and Applied Sciences*, **26**(1), 64–8. DOI: 10.37575/b/sci/250014

1. Introduction

The fact that motion in zero-dimensional semiconductor structures is limited in all three dimensions and that their sizes are smaller than or equivalent to the bulk exciton Bohr radius has attracted significant attention. Over the past 20 years, a large number of studies have been published on the creation and decay of exciton states in nanostructures containing quantum dots (QDs), as well as on how these states interact with other quasiparticles and external fields.

Core/shell nanomaterials may be constructed primarily as a result of recent technological advancements in material growth processes; these materials' unique and improved optical and electrical characteristics make them extremely desirable from an application standpoint. The confinement of quasiparticle motion in QDs leads to an increase in binding energy (BE), oscillator strength, and exciton lifetime in such systems (Kramar, 2009).

Numerous works have addressed the topic of determining the energy and BE of an exciton in nanostructures with QDs; an imperfect list of these works is provided by Elias (2019). Bhat and Shah (2018) presented findings on exciton energies in spherical gallium arsenide (GaAs) QDs, showing that dot size affects exciton energies and that the initial excited-state exciton energy becomes five orders of magnitude larger than the ground-state exciton energy for a consistent dot radius.

Pokutnyi (2013) investigates a quasi-zero-dimensional semiconductor nano system where an electron is restricted to the outer spherical boundary between the QD and dielectric matrix while a hole navigates through the QD volume. The system produces ground-state exciton BE that exceeds the values found in zinc selenide and cadmium sulfide single crystals.

Chafai *et al.*, 2019 studied the effects an external electric field has on the exciton energy spectrum in spherical GaN/AlN core/shell nanodots. They examined how an external electric field modifies the energy spectrum of excitons. This study also considers how changes in nanodot size influence the lowest energy state of confined excitons. According to a theoretical model using variational computation, the exciton energy experiences a significant reduction when the electric field is applied. The study shows that a specific energy red shift exists between the intensity of the external electric field and specific sizes of nanodots. Further research demonstrates that increases in nanodot size lead to a decrease in the lowest exciton energy, while decreases in nanodot size result in higher, lowest exciton energy.

Pokytnyi *et al.*, (2023) studied exciton quasi-molecules existing in germanium double QDs situated in a silicon matrix nano system. When two spatially indirect excitons interact, they combine to form an exciton quasi-molecule. The production of spatially indirect excitons and exciton quasi-molecules in the nano system was shown to depend on the distance D between QD surfaces. The exciton quasi-molecule's singlet ground state exhibits BE greater than the biexciton BE in a silicon crystal by two orders of magnitude.

Standard QD confinement behavior is primarily determined by the nano system's average size as well as its composition. Zieliński *et al.* (2015) reveal that natural QDs produced in the indium arsenide (InAs)/GaAs wetting layer have their excitonic properties predominantly determined by random lattice composition fluctuations. The biexciton BE shows extreme sensitivity to lattice randomness while exhibiting almost no dependency on exciton energy.

The notable flexibility of TMDC materials permits strain to alter their fundamental exciton energies and spectral linewidths. Niehues *et al.*, 2020 provided a description of the Stokes shift, which represents the energy difference between light absorption and emission for the A exciton in TMDC mono- and bilayers. Research indicates that mechanical strain enables tuning of the Stokes shift. The Stokes shift diminishes as tensile strain levels increase. The interaction between excitons and phonons weakens due to shifts in the energy positions of various excitons.

Iris Niehues *et al.*, (2019) investigated how interlayer excitons in bilayer MoS_2 respond to uniaxial tensile strain up to a maximum of 1.6%. They measured a gauge factor of −47 meV per percent through differential transmission spectra at varying strain levels, which track the energy shift in the interlayer exciton. The intralayer A and B excitons display a gauge factor of −49 meV per percent. Their research confirms that

Corresponding Author: Marwan Zuhair Elias 009647702028210, marwanzuhairelias.1001@gmail.com

interlayer excitons originate at the K point of the Brillouin zone, where the electron remains within a single layer while the hole extends across two layers. This work creates potential opportunities for future straintronic devices utilizing interlayer excitons.

The authors explored the exciton configuration in type II QDs, where the hole resides in the barrier material and the electron remains inside the dot (Janssens *et al.*, 2001a). The Hartree–Fock mesh computation method evaluates exciton properties under a perpendicular magnetic field. A flat quantum disk serves as one component within the simulation system. Angular momentum transitions are expected to occur as the magnetic field increases. Their research analyzes how modifications in the hole's confinement potential lead to the transformation of a type I QD into a type II QD. Under strong magnetic field conditions, a re-entrant behavior emerges, resulting in a transition from type II back to type I behavior.

An exciton within a quantum disk displays ground-state energy and BE that vary with changes in the external magnetic field (Janssens *et al.*, 2001b). The confinement is modeled as a rigid wall with a finite height limitation. The study examines the diamagnetic shift when magnetic fields reach 40 T. When the light hole participates in exciton generation, researchers find strong agreement between their results and experimental data for InyAl1-yAs/AlxGa1−xAs self-assembled QDs. They analyzed the impact of dot size on the diamagnetic shift by varying the radius of the disk. Magnetic field-dependent exciton excited states were successfully identified. Since the relative angular momentum depends on magnetic field strength, it cannot serve as a valid quantum number. The ground-state properties of an exciton in a self-assembled quantum disk under a perpendicular magnetic field are reported by Janssens *et al.*, (2004).

Hsiao *et al.*, (2024) created a 4×2 germanium QD ladder and employed it to investigate the transport and generation of excitons. The authors tuned the entire array into the single-hole regime and independently controlled all of the interdot tunnel couplings and on-site potentials to design the Hamiltonian system. They discovered a significant inter-channel Coulomb interaction while suppressing tunneling between channels.

A QD with light hole–heavy hole splitting and a strong, high-energy exciton was described Wang *et al.*, (2024). According to their experimental and computational data, the oscillator strength of heavy holes decreases more than that of light holes under electric fields. This, the authors argue, is the primary cause of the strong light-hole electroluminescence. Both $CdxZn_{1-x}Se$–ZnS and CdSe–CdS core–shell QDs with substantial light hole–heavy hole splitting show this phenomenon.

The size-dependent scintillation of $CsPbBr_3$ nanocrystals was investigated both theoretically and experimentally by Fratelli *et al.*, (2025), using a combination of spectroscopic, radiometric, and Monte Carlo simulation methods. Due to their higher stopping power and lower Auger decay, the results demonstrated that the combined effects of size-dependent energy deposition, (multi-)exciton population, and light emission under ionizing excitation—all characteristic of confined particles—serve to maximize the scintillation efficiency and timing performance of larger nanocrystals. This model offers essential guidance for the rational design of nanoscale scintillators.

The ability to create spatial variations in QDs, quantum wires, and quantum wells with various geometries forms a fundamental basis for understanding the theoretical framework behind layered and ring-shaped configurations. The system functions as a quantum well when the cylindrical nanolayer maintains a constant thickness while both inner and outer radii expand. A quantum wire is formed when the cylindrical quantum layer's inner radius vanishes and height approaches infinity. The structure becomes a cylindrical QD when the height remains fixed, and the inner radius disappears (Zuhair *et al.*, 2009; Barseghyan *et al.*, 2024; Zuhair, 2012). The results obtained for both layered and ring-shaped systems show universal characteristics that make them particularly interesting. The present study investigates how temperature, pressure, and magnetic field influence exciton states in cylindrical-layer QDs.

2. Theoretical Framework

The investigation of how pressure, temperature, and magnetic field affect the exciton energy of an InAs cylindrical layer QD requires calculations of electron quantized energy (E_n), well thickness (L), dot radii (R), effective electron mass (m^*), and energy correction (ΔE_0) based on these parameters. The single-particle states are examined within a cylindrical layer QD characterized by height L and inner and outer radii R_1 and R_2, respectively, as shown in Fig. 1. Given that the radial motion of an electron is confined between the inner and outer radii, both the wave function and energy spectrum are determined under the assumption of a uniform magnetic field along the OZ-axis. The layer's confinement potential is defined by infinitely tall rectangular walls:

$$v(\rho,z,p)=\begin{cases}0,\mathrm{R}_1(p)\le\rho\le\mathrm{R}_2(p),-\frac{\mathrm{L}}{2}\le z\le+\frac{\mathrm{L}}{2}\\ \infty\quad,\rho<\mathrm{R}_1(p),\rho>\mathrm{R}_2(p),|z|>\frac{L}{2}\end{cases}. \tag{1}$$

The corresponding Schrödinger equation, in terms of the parabolic dispersion law, takes the form:

$$\frac{1}{2m^*(p,t)}\left(\vec{P}(p,t)-\frac{e}{c}\vec{A}\right)^2\Psi(\rho,\emptyset,z,p,t)=E_n(\rho,\emptyset,z,p,t)\text{-}$$
$$.\Psi(\rho,\emptyset,z,p,t), \tag{2}$$

where $\vec{P}=\hbar k,\vec{A}=\frac{1}{2}\vec{r_l}\times\vec{B}$ is the vector potential. The effective mass of the electron in InAs, as a function of pressure and temperature, is given by:

$$m^*(p,t)=\left[1+\frac{15020}{E_g(p,t)}+\frac{7510}{E_g(p,t)+341}\right]^{-1}.m_0^*. \tag{3}$$

The bulk energy gap of InAs is provided by Duque *et al.*, (2006):

$$E_g(p,t)=\left(533+7.7.p-\frac{0.276.T^2}{T+83}\right). \tag{4}$$

The fractional change in the radii of the cylindrical layer QD is expressed as:

$$R_{1(2)}(p)=R_{1(2)}(0)(S_{11}+2S_{12}).P. \tag{5}$$

Here, $R_{1(2)}(0)$ denotes the zero-pressure inner (outer) radius, and the well thickness under pressure is:

$$L[P]=[L_0.((1-P.(S_{11}-2.S_{12})^{0.5}], \tag{6}$$

where L_0 is the original height of the well. The compliance constants S_{11} and S_{12} are given by:

$$S_{11}=\frac{\mathrm{C}_{11}+\mathrm{C}_{12}}{[(\mathrm{C}_{11}-\mathrm{C}_{12}).(\mathrm{C}_{11}+2\mathrm{C}_{12})]} \tag{7}$$

$$S_{12}=\frac{-C_{12}}{[(C_{11}-C_{12}).(C_{11}+2C_{12})]}, \tag{8}$$

where C_{11} and C_{12} are the elastic constants of InAs (Kita *et al.*, 2019). The wave function must satisfy the boundary conditions:

$$\psi(\pm L/2)=\psi(R_1)=\psi(R_2)=0. \tag{9}$$

The exact solution of Eq. (2) takes the following form:

$$\Psi(\rho,\emptyset,z,p,t)=\frac{1}{\sqrt{2\pi}}.e^{im\emptyset}.\sqrt{\frac{2}{L(P)}}.\begin{pmatrix}sin\frac{\pi n}{L(P)}Z\\ cos\frac{\pi n}{L(P)}Z\end{pmatrix}.G(\rho,p,t). \tag{10}$$

Substituting Eq. (10) into Eq. (2) yields a new equation for the function G(ρ,p,t):

$$\frac{\hbar^2}{2m^*(p,t)}\left(G(\rho,p,t)'' + \frac{1}{\rho}G(\rho,p,t)' - \frac{m^*(p,t)^2}{\rho^2}.G(\rho,p,t)\right) + \left[\varepsilon - E_n(\rho,\emptyset,z,p,t) - \frac{m^*(p,t).\omega_H^2.\rho^2}{8} - \frac{\hbar.\omega_H.m^*(p,t)}{2}\right].G(\rho,p,t) = 0 \quad (11)$$

where $\omega_H = e.H/m^*(p,t).c$ is the cyclotron frequency, and $E_n(\rho,\emptyset,z,p,t) = n^2\pi^2\eta^2/2.m^*(p,t).L(P)$.

The simplest way to express the solution of Eq. (11) is using hypergeometric functions:

$$G(\rho,p,t) = \left\{c_1 F\left(-\left(\beta - \frac{|m^*(p,t)|+1}{2}\right), |m^*(p,t)|+1, \frac{\rho^2}{2a_H^2}\right) + c_2 U\left(-\left(\beta - \frac{|m^*(p,t)|+1}{2}\right), |m^*(p,t)|+1, \frac{\rho^2}{2a_H^2}\right)\right\}.e^{\frac{\rho^2}{4a_H^2}}.\rho^{|m^*(p,t)|}, \quad (12)$$

where $\beta = \frac{1}{\hbar\omega_H.(\varepsilon - E_n(\rho,\emptyset,z,p,t))} - \frac{m^*(p,t)}{2}$ and $a_H = \sqrt{\frac{\hbar}{m^*(p,t).\omega_H.}}$ represent the magnetic length.

Given that the wave function in Eq. (10) must vanish at the boundaries, the zero determinant condition $G(R_1) = G(R_2) = 0$ is required to determine the system's energy spectrum:

$$\begin{vmatrix} F\left(-\left(\beta - \frac{|m^*(p,t)|+1}{2}\right), |m^*(p,t)|+1, \frac{R_1^2}{2a_H^2}\right) & U\left(-\left(\beta - \frac{|m^*(p,t)|+1}{2}\right), |m^*(p,t)|+1, \frac{R_1^2}{2a_H^2}\right) \\ F\left(-\left(\beta - \frac{|m^*(p,t)|+1}{2}\right), |m^*(p,t)|+1, \frac{R_2^2}{2a_H^2}\right) & U\left(-\left(\beta - \frac{|m^*(p,t)|+1}{2}\right), |m^*(p,t)|+1, \frac{R_2^2}{2a_H^2}\right) \end{vmatrix} = \mathbf{0} \quad (13)$$

The energy spectrum is found by numerically solving the transcendental Eq. (13).

Now, using perturbation theory, the hole–electron interaction, or exciton effect, is examined under the assumption of strong quantization along the disk axis (OZ direction). Thus, in the present case, motion in the OZ direction is considered using the single-particle model (i.e., a two-dimensional exciton). The magneto-exciton Hamiltonian, in the limit of infinitely high walls, takes the following form:

$$\hat{H}_{ex} = \hat{H}_e + \hat{H}_h - \frac{e^2}{\varepsilon|\rho_e - \rho_h|}, \quad (14)$$

Where $\hat{H}_i = \frac{1}{m^*(p,t)}\left(\left(\hat{P}(p,t) - \frac{e}{c}\hat{A}_i\right)\right)$, (15)

and $\hat{H}_i.\Psi_i = E_i(\rho,\emptyset,z,p,t).\Psi_i$, where $(i = e = h)$.

In a first-order approximation, the magneto-exciton wave function can be expressed as:

$$\Psi_{ex}^0(r_e,r_h,p,t) = \Psi_e(\rho_e,\emptyset_e,z_e,p,t).\Psi_h(\rho_h,\emptyset_h,z_h,p,t). \quad (16)$$

This form assumes that the third term in Eq. (14) acts as a small perturbation to the Hamiltonian.

The corresponding energy correction is given by:

$$\Delta E_0 = \int \Psi_{ex}^0(r_e,r_h,p,t)\left(-\frac{e^2}{\varepsilon.\sqrt{\rho_e^2 - \rho_h^2 - 2\rho_e.\rho_h.\cos(\varphi_e - \varphi_h)}}\right)\Psi_{ex}^0.dv_e.dv_h. \quad (17)$$

Janssens *et al.*, (2002) state that this may be simplified to the following form:

$$\Delta E_0 = -\frac{8\pi e^2}{\varepsilon}.\int_{R_1(p)}^{R_2(p)}\rho_2.d\rho_2.\int_{R_1(p)}^{R_2(p)}\frac{f(\rho_1,\rho_2)}{\rho_1+\rho_2}.L\left(\frac{4\rho_1\rho_2}{(\rho_1+\rho_2)^2}\right)\rho_1.d\rho_2, \quad (18)$$

where $f(\rho_1,\rho_2) = \Psi_e^0(\rho_e,\emptyset_e,z_e,p,t).\Psi_h^0(\rho_e,\emptyset_e,z_e,p,t)$ and $L(x) = \int_0^{\pi/2}\frac{d\varphi}{\sqrt{1-x\sin^2(\varphi)}}$ is the complete elliptic integral of the first kind.

Thus, the total energy of the electron becomes:

$$E = E_e + E_h + \Delta E_0. \quad (19)$$

Figure 1: The cross-sectional area and specific features of the cylindrical layer quantum dot.

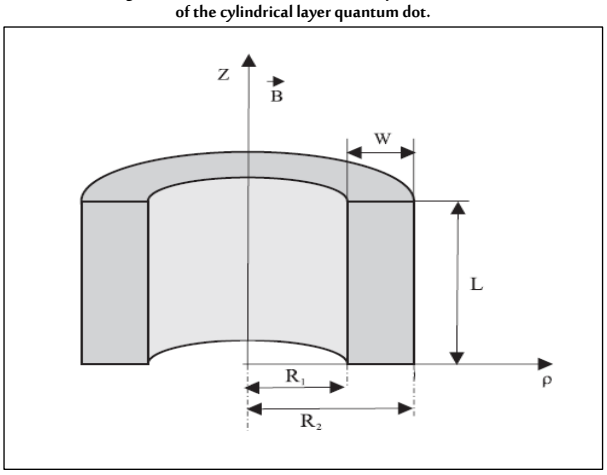

3. Analysis of the Results Obtained

Understanding how bound excitons respond to variations in external parameters is essential for the creation of tunable optical systems. The results of calculations for cylindrical InAs QDs are discussed for cases with and without Coulomb interaction. At given values of radii, pressure, and height, and under a perpendicular magnetic field directed along the OZ-axis, the energy of the exciton as a function of temperature is investigated, as shown in Fig. 2. Temperature influences the energy of excitons in cylindrical layer QDs (blue shift). As a result, the dependence of energy on temperature is found to be considerable.

Consequently, due to their interaction, electron–hole ground-state energy renormalization causes temperature-induced changes in exciton ground-state energy in QDs (Kramar, 2009). According to the observed results, nanostructured material properties may be controlled and altered through temperature via the band gap. In addition, due to their sensitivity to temperature, exciton behavior in nanostructures may be modified by adjusting the mobility and distribution of charge carriers (Zuhair, 2012). Furthermore, it is observed that at higher energy levels, relative to ground states, the sensitivity of exciton energy to temperature increases.

Figure 2: Energy (in meV) with and without Coulomb interaction versus temperature (in K) for different states at given values of radii, pressure, height, and magnetic field strength.

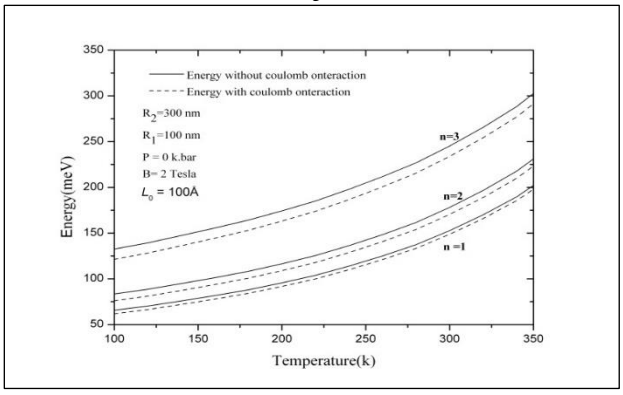

The impact of pressure on exciton energies trapped within a cylindrical QD made of InAs layers under a perpendicular magnetic field directed along the OZ-axis, for the cases with and without Coulomb interaction, is illustrated in Fig. 3. It is observed that energy is highly influenced by the applied pressure across all energy states (Bhat and Shah, 2018). Furthermore, according to Janssens *et al.*, (2004), as pressure increases, the hole moves from inside the dot to

its radial edge. This causes the BE between the electron and the hole to decrease, which, in turn, lowers the total energy.

Additionally, the results from comparing the ground-state and first excited-state curves for a given dot radius reveal that with increasing pressure, the exciton energy in the first excited state increases by approximately 25% more than the energy in the ground state.

Calculations performed for the ground-state energy as a function of the exciton's external magnetic field in InAs cylindrical layer QDs are presented in Fig. 4, considering fixed values of temperature, pressure, and radii for both cases—with and without Coulomb interaction. In good agreement with Janssens *et al.*, (2001b), the exciton ground-state energy rises under an externally applied magnetic field of up to 10 T. Additionally, it is observed that although the curves for both cases are almost parallel, the space between them gradually narrows as the magnetic field increases, in strong agreement with the findings of Ghosh *et al.*, 2024.

Figure 3: Energy (in meV) with and without Coulomb interaction versus pressure for different states at given values of radii, temperature, height, and magnetic field strength.

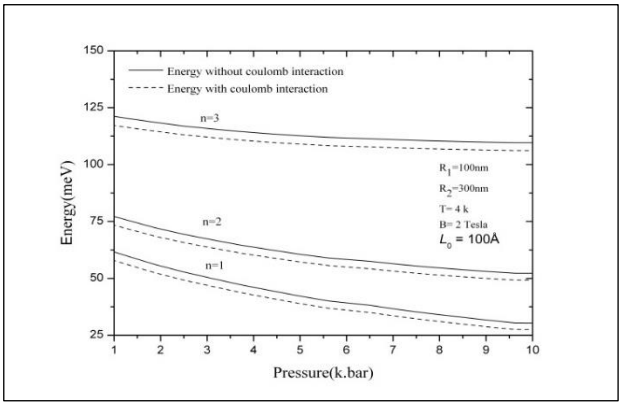

Figure 4: Exciton energy (in meV) with and without Coulomb interaction versus magnetic field strength for different states at given values of radii, pressure, temperature, and height.

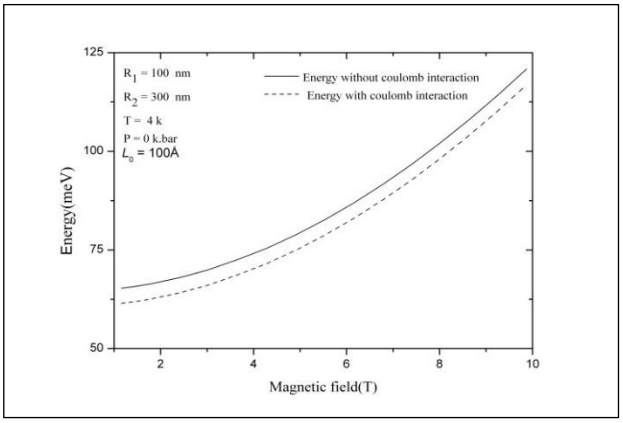

4. Conclusions

Creating layered-shaped nanostructures has led to the development of a new class of theoretical problems concerning the physical behavior of these systems, which is a noteworthy outcome. The present study examines the impact of external factors, such as temperature, pressure, and applied magnetic field, on the exciton energy of InAs cylindrical layer QDs. The findings show that, at a given dot size, energy increases with rising temperature and applied magnetic field but decreases with increasing pressure. These results have several applications in nanoelectronics and are significant from both applied and fundamental standpoints.

Data Availability Statement

The data supporting this study's findings are available on request from the corresponding author.

Acknowledgments

We extend our heartfelt thanks to the University of Mosul for its encouragement and support of our research work

Funding

This research did not receive a specific grant from any funding agency in the public, commercial, or not-for-profit sectors.

Conflicts of Interest

No conflicts of interest exist.

Biographies

Marwan Zuhair Elias

Department of Medical Physics, College of Science, Mosul University, Mosul, Iraq, 009647702028210, marwanzuhairelias.1001@gmail.com

Marwan is an Iraqi lecturer and researcher specializing in Semiconductor Nanophysics. He earned his B.Sc. in Physics in 1993, followed by a M.Sc. in 1996 and a Ph.D. in 2010, all from the University of Mosul. His research focuses on the electronic, optical, and structural properties of nanomaterials, with an emphasis on their applications in medical and energy technologies. He has published over 20 peer-reviewed articles and continues to contribute to the advancement of nanoscale science and its real-world applications.

ORCID: 0000-0001-6521-3136

References

Barseghyan, M.G., Hakimyfard, A., Zuhair, M., Duque, C.A. and Kirakosyan, A.A. (2011). Binding energy of hydrogen-like donor impurity and photoionization cross-section in lnAs Pöschl–Teller quantum ring under applied magnetic field. *Physica E: Low-dimensional Systems and Nanostructures*, **44**(2), 419–24. DOI: 10.1016/j.physe.2011.09.013

Bhat, B.M.U.D. and Shah, K.A. (2018). Effect of dot size on exciton energy states confined in a spherical gallium arsenide quantum dot. *Nanosystem, Nanomaterial, Nanotechnology*, **16**(1), 175–9. DOI: 10.15407/nnn.16.01.175

Chafai, A., Essaoudi, I., Ainane, A., Dujardin, F. and Ahuja, R. (2019). Binding energy of an exciton in a GaN/AlN nanodot: Role of size and external electric field. *Physica B: Condensed Matter*, **559**(n/a), 23–8. DOI: 10.1016/j.physb.2019.01.047

Duque, C.A., Porras-Montenegro, N., Barticevic, Z., Pacheco, M. and Oliveira, L.E. (2006). Effects of applied magnetic fields and hydrostatic pressure on the optical transitions in self-assembled InAs/GaAs quantum dots. *Journal of Physics: Condensed Matter*, **18**(6), 1877. DOI: 10.1088/0953-8984/18/6/005

Elias, M.Z. (2019). Scattering by interface roughness of InAs/GaAs quantum well under some external influences. *Physica E: Low-dimensional Systems and Nanostructures*, **108**(n/a), 96–9. DOI: 10.1016/j.physe.2018.12.011

Fratelli, A., Zaffalon, M.L., Mazzola, E., Dirin, D.N., Cherniukh, I., Otero-Martínez, C. and Brovelli, S. (2025). Size-Dependent multiexciton dynamics governs scintillation from perovskite quantum dots. *Advanced Materials*, **37**(5), 2413182. DOI: 10.1002/adma.202413182

Ghosh, O.S.N., Gayathri, S., Allam, S.R., Sharan, A., Lal, S.S., Reddy, M.J.K. and Viswanath, A.K. (2024). Bound exciton engineering approach for tuning the thermal lensing phenomenon in anatase TiO2: Gd nanosystems. *Chemical Physics Impact*, **9**(n/a), 100679. DOI: 10.1016/j.chphi.2024.100679

Hsiao, T.K., Cova Fariña, P., Oosterhout, S.D., Jirovec, D., Zhang, X., van Diepen, C.J. and Vandersypen, L.M.K. (2024). Exciton transport in a germanium quantum dot ladder. *Physical Review X*, **14**(1), 011048. DOI: 10.1103/PhysRevX.14.011048

Janssens, K.L., Partoens, B. and Peeters, F.M. (2001a). Magnetoexcitons in planar type-II quantum dots in a perpendicular magnetic field. *Physical Review B*, **64**(15), 155324. DOI: 10.1103/PhysRevB.64.155324

Janssens, K.L., Partoens, B. and Peeters, F.M. (2002). Magneto‐exciton in single and coupled type ii quantum dots. *Physica Status Solidi (A)*, **190**(2), 571–6. DOI: 10.1002/1521-396X(200204)190:2<571::AID-PSSA571>3.0.CO;2-K

Janssens, K.L., Partoens, B. and Peeters, F.M. (2004). Magnetoexciton in vertically coupled InP/ GaInP quantum disks: Effect of strain on the exciton ground state. *Physical Review B—Condensed Matter and Materials Physics*, **69**(23), 235320. DOI: 10.1103/PhysRevB.69.235320

Janssens, K.L., Peeters, F.M. and Schweigert, V.A. (2001b). Magnetic-field dependence of the exciton energy in a quantum disk. *Physical Review B*, **63**(20), 205311. DOI: 10.1103/PhysRevB.63.205311

Kita, T., Harada, Y. and Asahi, S. (2019). Fundamentals of semiconductors. In: *Energy Conversion Efficiency of Solar Cells. Green Energy and Technology*. Springer, Singapore. DOI: 10.1007/978-981-13-9089-0_8

Kramar, V.M. (2009). Temperature dependence of the excitonic transition energy in flat semiconductor nanofilms. Ukr. J. *Phys.*, **54**(12), 1225–33.

Niehues, I., Blob, A., Stiehm, T., de Vasconcellos, S.M. and Bratschitsch, R. (2019). Interlayer excitons in bilayer MoS 2 under uniaxial tensile strain. *Nanoscale*, **11**(27), 12788–92. DOI: 10.1039/C9NR03332G

Niehues, I., Marauhn, P., Deilmann, T., Wigger, D., Schmidt, R., Arora, A. and Bratschitsch, R. (2020). Strain tuning of the Stokes shift in atomically thin semiconductors. *Nanoscale*, **12**(40), 20786–96. DOI: 10.1039/D0NR04557H

Pokutnyi, S.I. (2013). Binding energy of the exciton of a spatially separated electron and hole in quasi-zero-dimensional semiconductor nanosystems. *Technical Physics Letters*, **39**(n/a), 233–5. DOI: 10.1134/S1063785013030139

Pokytnyi, S.I., Gayvoronsky, V.Y. and Poroshin, V.N. (2023). Spatially indirect excitons and exciton quasimolecules in nanosystems with double quantum dots. *Molecular Crystals and Liquid Crystals*, **752**(1), 103–11. DOI: 10.1016/j.rinp.2025.108191

Wang, X., Gao, Y., Liu, X., Xu, H., Liu, R., Song, J. and Fan, F. (2024). Strong high-energy exciton electroluminescence from the light holes of polytypic quantum dots. *Nature Communications*, **15**(1), 6334. DOI: 10.1038/s41467-024-50432-8

Zieliński, M., Gołasa, K., Molas, M.R., Goryca, M., Kazimierczuk, T., Smoleński, T. and Babiński, A. (2015). Excitonic complexes in natural InAs/GaAs quantum dots. *Physical Review B*, **91**(8), 085303. DOI: 10.1103/PhysRevB.91.085303

Zuhair, M. (2012). Hydrostatic pressure and electric-field effects on the electronic and optical properties of InAs spherical layer quantum dot. *Physica E: Low-dimensional Systems and Nanostructures*, **46**(n/a), 232–5. DOI: 10.1016/j.physe.2012.09.017

Zuhair, M., Manaselyan, A. and Sarkisyan, H. (2009). Magneto-and electroabsorption in narrow-gap InSb cylindrical layer quantum dot. *Physica E: Low-dimensional Systems and Nanostructures*, **41**(8), 1583–90. DOI: 10.1016/j.physe.2009.05.002.

Scientific Journal of King Faisal University:
Basic and Applied Sciences

Controllability of Nonlocal Impulsive Semilinear Differential Inclusions with Fractional Sectorial Operators and Infinite Delay

Feryal Abdullah Al Adsani and Ahmed Gamal Ibrahim
Department of Mathematics, College of Science, King Faisal University, AlAsa, Saudi Arabia

LINK	RECEIVED	ACCEPTED	PUBLISHED ONLINE	ASSIGNED TO AN ISSUE
https://doi.org/10.37575/b/sci/250010	11/03/2025	29/05/2025	29/05/2025	01/06/2025
NO. OF WORDS	**NO. OF PAGES**	**YEAR**	**VOLUME**	**ISSUE**
6084	12	2025	26	1

ABSTRACT

This paper demonstrates the controllability of two fractional nonlocal impulsive semilinear differential inclusions with infinite delay, where the linear part is a fractional sectorial operator and the nonlinear term is a multivalued function. The operator families generated by the linear part are not assumed to be compact. The objective is achieved using the properties of fractional sectorial operators and the Hausdorff measure of noncompactness. The results generalise several recent findings, and the method can be used to extend further contributions to cases where the linear term is a fractional sectorial operator and the nonlinear term is a multivalued function, in the presence of instantaneous impulses and infinite delays. The novelty of this work lies in initiating the study of the controllability of a system involving a fractional Caputo derivative under infinite impulses and delays. An example is presented to verify the theoretical developments. Given the wide-ranging applications of fractional calculus in medicine, energy and other scientific fields, this work contributes to those domains.

KEYWORDS
Caputo derivative, mazur's lemma, mild solutions, multivalued functions, noncompact measure, phase space

CITATION
Al Adsani, F.A and Ibrahim, A.G. (2025). Controllability of nonlocal impulsive semilinear differential inclusions with fractional sectorial operators and infinite delay. *Scientific Journal of King Faisal University: Basic and Applied Sciences*, **26**(1), 69–80. DOI: 10.37575/b/sci/250010

1. Introduction

Fractional calculus has many applications in industry, energy, fluid flow, control theory, electrical circuits, electrochemistry, engineering, polymer science, organic dielectric materials, viscoelastic materials, rheology, diffusive transport, electrical networks, electromagnetic theory and physics (Baleanu and Lopes, 2019; Butt *et al.*, 2023; Sudsutad *et al.*, 2024). Many phenomena in real life are characterised by sudden changes in state and are modelled by impulsive differential equations and impulsive differential inclusions. For example, consider the motion of an elastic ball bouncing vertically on a surface. The instants of impulses occur when the ball meets the surface and its velocity changes rapidly. One of the recent works on this topic was presented by Aladsani and Ibrahim (2024).

Sectorial operators have many applications in partial differential equations. In Wang *et al.* (2015), the existence of mild solutions for fractional differential inclusions with fractional sectorial operators, impulsive effects and nonlocal conditions was demonstrated. It is known that nonlocal Cauchy problems are motivated by physical problems and various phenomena, such as nonlocal neural networks and nonlocal pollution. Many findings on nonlocal differential equations and inclusions have been reported (Hassan *et al.*, 2022; Zhang *et al.*, 2019).

A system is said to be controllable if a control function exists that directs the solution of the system from its initial state to its final state. This subject is of interest because many control processes can be represented as differential equations or inclusions. Approximate controllability means that the system can be steered to an arbitrarily small neighbourhood of the desired final state. In recent years, several achievements have been made regarding exact controllability (Almarri and Elshenhab, 2022; Alsaroria and Ghadle, 2022; Alsheekhhussain and Ibrahim, 2021) and approximate controllability (Varun *et al.*, 2022; Dineshkumar and Udhayakumar, 2022; Dineshkumar *et al.*, 2022; Kumar, 2023).

Wang *et al.* (2020) studied the finite controllability of Hilfer fractional semilinear differential equations, while Chalishajar *et al.* (2024) discussed the null controllability of Hilfer fractional stochastic differential equations with nonlocal conditions. Some authors have considered the controllability of problems with finite delay (Almarri and Elshenhab, 2022; Karthikeyan *et al.*, 2021), infinite delay (Bose and Udhayakumar, 2023; Slama and Boudaoui, 2017) and impulses (Wang *et al.*, 2019).

Different kinds of controllability have been investigated when the linear part is the infinitesimal generator of a semigroup of operators (Wang *et al.*, 2019), a fractional sectorial operator (Alsaroria and Ghadle, 2022; Raja *et al.*, 2022), or a fractional almost sector operator (Varun *et al.*, 2022).

Furthermore, some authors have treated problems involving integer-order systems (Karthikeyan *et al.*, 2021), and others have addressed systems with the fractional Caputo derivative (Almarri and Elshenhab, 2022; Wang *et al.*, 2019), the Atangana–Baleanu derivative (Dineshkumar *et al.*, 2022), the Riemann–Liouville derivative (Yang and Wang, 2016) and the Hilfer–Katugampola derivative (Hassan *et al.*, 2022). For contributions concerning the controllability of problems with nonlocal conditions, see Kumar *et al.* (2020) and Slama and Boudaoui (2017).

Nonetheless, the number of works in the literature on the controllability of problems involving infinite state-dependent delay and impulsive effects is limited, particularly when the right-hand side is a multi-valued function. To the best of current knowledge, the controllability of Caputo fractional differential inclusions generated by fractional sectorial operators in the presence of nonlocal conditions, impulsive effects and infinite delay has not yet been addressed.

The objective of this article is to examine the existence of mild solutions and to study the exact controllability of two impulsive fractional differential inclusions with fractional sectorial operators in the presence of infinite delay and nonlocal conditions, with the following structures:

Corresponding Author: Feryal Abdullah Al Adsani 00966665059341 44, faladsani@kfu.edu.sa

$$(1)\quad \begin{cases} {}^{c}D^{\gamma}w(\vartheta) \in Aw(\vartheta) + \mathcal{F}(\vartheta, w_\vartheta) + Q\big(\mathfrak{U}(\vartheta)\big), a.e.\, on\, T - \{\vartheta_1, \vartheta_2, \dots, \vartheta_m\}, \\ w(\vartheta_k^+) = w(\vartheta_k^-) + I_k\big(w(\vartheta_k^-)\big), k = 1,2, \dots, m, \\ w(\vartheta) = \Psi(\vartheta) - g(w)(\vartheta), \vartheta \in (-\infty, 0]. \end{cases}$$

and

$$(2)\quad \begin{cases} {}^{c}D^{\gamma}w(\vartheta) \in Aw(\vartheta) + \mathcal{F}(\vartheta, w_\vartheta) + (Vz)(\vartheta), a.e.\, on\, T - \{\vartheta_1, \vartheta_2, \dots, \vartheta_m\}, \\ w(\vartheta_k^+) = w(\vartheta_k^-) + I_k\big(w(\vartheta_k^-)\big), k = 1,2, \dots, m, \\ w(\vartheta) = \Psi(\vartheta) - g(w)(\vartheta), \vartheta \in (-\infty, 0], \end{cases}$$

where $m \geq 2$ is a natural number, $\gamma \in (0,1), T = [0, \varpi], \varpi > 0$, ${}^{c}D^{\gamma}w(\vartheta)$ is the Caputo derivative of order γ(Kilbas *et al.*, 2006), E is a real Banach space with $dim(E) = \infty, \omega: T \to E, A: D(A) \subseteq E \to E$ is a fractional sectorial operator as in Wang *et al.* (2015), and the function $w_\vartheta(s) = w(\vartheta + s), s \in (-\infty, 0]$, belongs to some abstract phase space $\beta, \mathcal{F}: T \times \beta \to 2^E$ is a multi-valued function with non-empty values, $0 = \vartheta_0 < \vartheta_1 < \cdots < \vartheta_m < \vartheta_{m+1} = \varpi$, $I_k: E \to E$ $(k = 1,2, \dots, m)$ are impulsive functions characterising the jump of the solutions at impulse points, $\Psi \in \beta$ and $g: \beta_\varpi \to \beta$ is a nonlinear function related to the nonlocal condition, and β_ϖ will be defined later.

In Problem (1), the control function $\mathfrak{U} \in L^\infty(T, X)$, where X is a real Banach space and $Q: X \longrightarrow E$ is a bounded linear operator. In Problem (2), the control function $z \in L^p(T, X), p > \frac{1}{\gamma}$ and $V: L^p(T, X) \to L^p(T, E)$ is a bounded linear operator. The spaces β_ϖ and $PC(T, E)$ will be defined later.

It is worth noting that we do not assume that the operator families generated by $A, \{\kappa_1(\vartheta): \vartheta > 0\}$ and $\{\kappa_2(\vartheta): \vartheta > 0\}$, are compact, and this increases the importance of this work.

Recently, Alsaroria and Ghadle (2022) studied the controllability of Problem (1) without delay, assuming that the operator families generated by $A, \{\kappa_1(\vartheta): \vartheta > 0\}$ and , $\{\kappa_2(\vartheta): \vartheta > 0\}$, are compact.

To compare with related work, Alsaroria and Ghadle (2022) examined the controllability of Problem (1) in a special case without delay, assuming the families of operators generated by $A, \{\kappa_1(\vartheta): \vartheta > 0\}$ and $\{\kappa_2(\vartheta): \vartheta > 0\}$ are compact. Johnsona *et al.* (2023) showed the existence of a mild solution to Problem (1) when $Q = 0$. Raja *et al.* (2022) obtained sufficient conditions for approximate control of nonlinear fractional differential integral embeddings of degree $1 < \alpha < 2$, similar to Problem (1) in the case without delay. Wang *et al.* (2015) showed the existence of moderate solutions to Problem (1) when $Q = 0$ and there is no delay. Furthermore, no studies were found on Problem (2).

The main contributions of this paper are summarised as follows:

- A new class of differential inclusions (with the right-hand side as a multi-valued function) generated by sectorial operators with infinite delay, impulsive effects and nonlocal conditions in infinite-dimensional Banach spaces is formulated.
- Unlike other works, such as Alsaroria and Ghadle (2022), this study does not assume that the operator families $\{\kappa_1(\vartheta): \vartheta > 0\}$ and $\{\kappa_2(\vartheta): \vartheta > 0\}$, generated by A, are compact, thereby increasing the importance of the work.
- The discussions are based on the properties of phase spaces, sectorial operators, multi-valued functions, and the Hausdorff measure of noncompactness.
- The existence of mild solutions and the controllability of systems (1) and (2) are established.
- Wang *et al.* (2015) studied Problem (1) in the special case where $Q \equiv 0$ and delay is absent. Alsaroria and Ghadle (2022) addressed Problem (1) with finite delay, assuming the compactness of the operator families $\{\kappa_1(\vartheta): \vartheta > 0\}$ and $\{\kappa_2(\vartheta): \vartheta > 0\}$. This assumption is not adopted in the present study. Therefore, the results generalise Theorem 3.1 in Wang *et al.* (2015) and Theorem 3.4 in Alsaroria and Ghadle (2022).
- The technique presented here can be used to generalise the results obtained in Almarri and Elshenhab (2022), Bedi, Varun *et al.* (2022), Dineshkumar and Udhayakumar (2022), Kumar *et al.* (2022), Salem and Alharbi (2023), and Varun and Bose (2023), particularly when the right-hand side is a multi-valued function instead of a single-valued function and in the presence of instantaneous impulses.
- Finally, an example is provided to demonstrate the applicability of the theoretical results.

For directions on future work, refer to the Discussion and Conclusion section.

Structure of the paper: Section 2 presents the background material required for later development. Section 3 establishes sufficient conditions for the controllability of Problem (1). Section 4 discusses the controllability of Problem (2), based on different sufficient conditions from those in Section 3. Finally, an example is provided.

2. Preliminaries and Notation

Let $P_{ck}(E) = \{Z \subseteq E: Z\ is\ non-empty, convex\ and\ compact\}$, $\mathbb{N} = \{1,2,3, \dots\}$, $\Pi_0 = \{0,1,2, \dots, m\}$ and $\Pi_1 = \{1,2, \dots, m\}$.

Let $D(A) = \{x \in E: A(x)\ is\ defined\}$, $\sigma(A)$ its spectrum, $\rho(A) = \mathbb{C} - \sigma(A)$, and $R(\zeta, A) = (\zeta I - A)^{-1}, \zeta \in \rho(A)$ the resolvent operators of A.

For any function $w: (-\infty, \varpi] \to E$ and $\vartheta \in T$, let $w_\vartheta: (-\infty, 0] \to E;\ w_\vartheta(\tau) = w(\vartheta + \tau); \tau \in (-\infty, 0]$.

Let $T_0 = [0, \vartheta_1], T_i = (\vartheta_i, \vartheta_{i+1}]; i \in \Pi_1$ and consider the Banach space $PC(T, E) = \{w: T \to E: \omega_{|_{T_i}}$ is continuous and $w(\vartheta_i^+)$ and $w(\vartheta_i^-)$ are finite for all $i \in \Pi_0\}$, where $||w||_{PC(T,E)} = sup\{||w(\vartheta)||: \vartheta \in T\}$. Moreover, the Hausdorff measure of noncompactness on $PC(T, E)$ is given by (Cardinali and Rubbioni 2012):

$$\chi PC(\Upsilon) = \max_{i=0,1,\dots,m} \chi_{C(\overline{T}_i, E)}\big(\Upsilon_{|\overline{T}_i}\big),$$

where $\Upsilon \subseteq PC(T, E)$ is bounded,

$$\Upsilon_{|\overline{T}_i} = \{f^* \in C(\overline{T}_i, E): f^*(\vartheta) = f(\vartheta);\ \vartheta \in T_i, f^*(\vartheta_i) = f(\vartheta_i^+), f \in \Upsilon\},$$

and $\chi_{C(\overline{T}_i, E)}$ is the Hausdorff measure of noncompactness on $C(\overline{T}_i, E)$ defined by (Kamenskii *et al.*, 2011):

$$\chi_{C(\overline{T}_i, E)}\big(\Upsilon_{|\overline{T}_i}\big) = \frac{1}{2} \lim_{\delta \to 0} sup_{f \in \Upsilon} \max_{|t-s| < \delta} ||f(t) - f(s)||.$$

It is known (example 2.1.3 in (Kamenskii et al., 2011) that if $Z_{|\overline{T}_i}$ is equicontinuous, then

$$\chi_{C(\overline{T}_i, E)}\big(\Upsilon_{|\overline{T}_i}\big) = sup_{t \in \overline{T}_i} \chi_E\{f(t): f \in \Upsilon_{|\overline{T}_i}\},$$

where χ_E denotes the Hausdorff measure of noncompactness on E.

Definition 1. (Hale and Kato, 1978). A phase space is a vector space β consisting of functions

$w: (-\infty, 0] \to E$, equipped with a seminorm $||.||_\beta$ such that:

1- If $w: (-\infty, \varpi] \to E$ is such that $w_{|T} \in PC(T, E)$ and $w_0 \in \beta$, the following properties hold:

$w_\vartheta \in \beta, \forall \vartheta \in T$.

There exists $C > 0$ such that $||w(\vartheta)|| \leq C||w_\vartheta||_\beta, \forall \vartheta \in T$.

There exist a continuous function $L_1: [0, \infty) \to [0, \infty)$ and a locally bounded function L2: $[0,\infty) \longrightarrow [1,\infty)$ such that

$$(3)\quad ||\omega_\vartheta||_\beta \leq L_1(\vartheta)\, sup\{||\omega(\tau)||: \tau \in [0, \vartheta]\} + L_2(\vartheta)||\omega_0||_\beta, \forall \vartheta \in T.$$

2- The function $t \to w_t$ is continuous from T into β.

3- β is complete.

For any $\vartheta \in T = [0, \varpi], the\ fucntion\ w_\vartheta: (-\infty, 0] \to E;\ is\ defined\ by\ w_\vartheta(\tau) = w(\vartheta + \tau)$. .

We now introduce the vector space

$$\beta_\varpi := \{w: (-\infty, \varpi] \to E\ such\ that\ w_0 \in \beta, w_{|T} \in PC(T, E)\},$$

endowed with the seminorm $||w||_{\beta_\omega} = ||w_0||_\beta + sup_{\tau \in T}||w(\tau)||$.

Moreover, let

$\mathcal{H} := \{w \in \beta_\varpi : w_0(\tau) = 0, \forall \tau \in (-\infty, 0]\}$.

It may be noted that $(\mathcal{H}, ||.||_\mathcal{H})$ is a Banach space, where $||w||_\mathcal{H} = sup_{\vartheta \in T}||w(\vartheta)||$, and the Hausdorff measure of noncompactness on it is defined by:

$\chi_\mathcal{H}(D) := \max_{i=0,1,2,\ldots,m} \chi_i(D_{|\bar{I}_i})$,

where D is a bounded subset of $\mathcal{H}$.

Remark that, if $\in \mathcal{H}$, then $||w||_{\beta_\varpi} = sup_{t\in J}||w(t)|| = ||w||_\mathcal{H}$.

Definition 2. (Kilbas *et al.*, 2006) The Riemann–Liouville fractional integral of order $q > 0$ with the lower limit zero for a function $f \in L^p(T, E), P \in [1, \infty)$ is defined as follows:

$$I^q f(\vartheta) = \frac{1}{\Gamma(q)} \int_0^\vartheta (\vartheta - s)^{q-1} f(s)\, ds, \qquad t \in T,$$

where the integration is in the sense of Bochner and Γ is the Euler gamma function.

Definition 3. (Kilbas *et al.*, 2006) Let $q \in (k-1, k)$ and k be a non-negative integer. The Caputo derivative of order q with the lower limit zero for a given function $f \in C^k(T, E)$ is defined by

$${}^c D^\gamma f(\vartheta) = I^{q-k} f(\vartheta) = \frac{1}{\Gamma(q-k)} \int_0^t (\vartheta - s)^{q-k-1} f(s)\, ds.$$

Let us list some properties of the Riemann–liouville integral and Caputo derivative.

Lemma 1. Let $q \in (k-1, k)$ and k be a non-negative integer. The following properties hold.

1. ${}^c D^q(a) = 0$,where a is a constant.
2. If $f \in L^p(T, E), P > \left(\frac{1}{q}\right)$, then ${}^c D^q I^q f(\vartheta) = f(\vartheta), a.e. \vartheta \in T$.
3. ${}^c D^q(\vartheta^\beta) = \frac{\Gamma(\beta+1)}{\Gamma(\beta+1-\alpha))} \vartheta^{\beta-\alpha}\wedge, \beta > k-1$.
4. If $f \in C^k(T, E)$, then
5. $I^q\ {}^c D^q f(\vartheta) = f(\vartheta) - f(0) - \sum_{n=1}^{n=k-1} \frac{f^{(n)}(0)\vartheta^n}{n!}$.

For more information about the fractional calculus we refer to, (Az-Zo'bi *et al.* 2024), (Al Zubi *et al.* 2024) and (Kilbas *et al.*, 2006).

Next, we recall the notation of fractional sectorial operators (Wang *et al.*, 2015). Let $\emptyset_0 \in (0, \frac{\pi}{2}]$ and $t_0 \in \mathbb{R}$. We denote by $M^\gamma(\emptyset_0, t_0)$ to the family of linear closed densely defined operators A satisfying:

$\kappa^\gamma \in \rho(A)$ for any $\kappa \in \sum_{\theta_0+\frac{\pi}{2}}(t_0) = \{\kappa \in \mathbb{C} - \{0\} : |arg(\kappa - t_0)| < \phi_0 + \frac{\pi}{2}\}$.

For any $t > t_0$ and $\emptyset < \emptyset_0$, there is a constant $C = C(t, \emptyset)$ such that $\left|\left|\kappa^{\gamma-1} R(\kappa^\gamma, A)\right|\right| \le \frac{C}{|\kappa - t|}$, $for\ \lambda \in \kappa \in \sum_{\theta_0+\frac{\pi}{2}}(t_0)$.

Now, according to Def. 2.20 in (Wang *et al.*, 2015), we have the following definition:

Definition 4. Let $A \in M^\gamma(\emptyset_0, t_0), \emptyset_0 \in \left(0, \frac{\pi}{2}\right], t_0 \in \mathbb{R}\ and\ \mho \in L^\infty(T, X)$. A function $w^\mho \in \beta_\varpi$ is called a mild solution for problem (1) if and only if there exists a function $\xi \in L^1(T, E)$ with $\xi(\vartheta) \in \mathcal{F}(\vartheta, (w^\mho)_\vartheta), a.e.$ such that

$$(4) \quad \omega^u(\vartheta) = \begin{cases} \Psi(\vartheta) - g(w^\mho)(\vartheta);\ \vartheta \in (-\infty, 0], \\ \kappa_1(\vartheta)\left(\Psi(0) - g(w^\mho)(0)\right) + \int_0^\vartheta \kappa_2(\vartheta - \tau)\left(\xi(\tau) + Q(\mho(\tau))\right) d\tau, v \in T_0, \\ \kappa_1(\vartheta)\left(\Psi(0) - g(w^\mho)(0)\right) + \kappa_1(\vartheta - \vartheta_1) I_1\left(w^\mho(\vartheta_1^-)\right) \\ \quad + \int_0^\vartheta \kappa_2(\vartheta - \tau)\left(\xi(\tau) + Q(\mho(\tau))\right) d\tau, v \in T_1, \\ \quad \vdots \\ \kappa_1(\vartheta)\left(\Psi(0) - g(w^\mho)(0)\right) + \sum_{k=1}^{k=m} \kappa_1(\vartheta - \vartheta_k) I_k\left(w^\mho(\vartheta_k^-)\right) \\ \quad + \int_0^\vartheta \kappa_2(\vartheta - \tau)\left(\xi(\tau) + Q(\mho(\tau))\right) d\tau, v \in T_m, \end{cases}$$

where

$$\kappa_1(\vartheta) = \frac{1}{2\pi i} \int_\Upsilon e^{\xi\vartheta} \zeta^{\gamma-1} R(\zeta^{\gamma-1}, A) d\zeta,$$

$$\kappa_2(\vartheta) = \frac{1}{2\pi i} \int_\Upsilon e^{\xi\vartheta} R(\zeta^{\gamma-1}, A) d\zeta,$$

and Υ is a suitable path lying in $\sum_{\theta_0+\frac{\pi}{2}}(w_0)$.

Lemma 2. (Wang *et al.*, 2015). The operators $\kappa_1(\vartheta)$ and $\kappa_2(\vartheta)$ satisfy the properties:

There are $M \ge 1, w > w_0$ and $C > 0$ such that $||\kappa_1(\vartheta)|| \le Me^{w\vartheta}$ and $||\kappa_2(\vartheta)|| \le Ce^{w\vartheta}(1 + \vartheta^{\gamma-1})$ for each $\vartheta > 0$.

For any $\vartheta \in T$.

$$(5) \qquad ||\kappa_1(\vartheta)||_{L(E)} \le M_1\ and\ ||\kappa_2(\vartheta)||_{L(E)} \le \vartheta^{\gamma-1} M_2,$$

where

$$(6) \qquad M_1 := \sup_{0\le\vartheta\le\varpi} ||\kappa_1(\vartheta)||_{L(E)}\ and\ M_2 := \sup_{0\le\vartheta\le\varpi} Ce^{w\vartheta}(1 + \vartheta^{1-\gamma}).$$

Definition 5. Let $A \in M^\gamma(\phi_0, t_0), \phi_0 \in \left(0, \frac{\pi}{2}\right], t_0 \in \mathbb{R}$ and $\in L^p(T, X); p > \frac{1}{\gamma}$. A function $w^z \in \beta_\omega$ is called a mild solution for problem (2) if there exists $\xi \in L^1(T, E)$ with $\xi(\vartheta) \in \mathcal{F}(\vartheta, (w^z)_\vartheta), a.e.$ such that

$$(7) \quad \omega^z(\vartheta) = \begin{cases} \Psi(\vartheta) - g(w^z)(\vartheta);\ \vartheta \in (-\infty, 0], \\ \kappa_1(\vartheta)\left(\Psi(0) - g(w^z)(0)\right) + \int_0^\vartheta \kappa_2(\vartheta - \tau)(\xi(\tau) + (V_z)(\tau)) d\tau, v \in T_0, \\ \kappa_1(\vartheta)\left(\Psi(0) - g(w^z)(0)\right) + \kappa_1(\vartheta - \vartheta_1) I_1(\vartheta - \vartheta_1^-) \\ \quad + \int_0^\vartheta \kappa_2(\vartheta - \tau)(\xi(\tau) + (V_z)(\tau)) d\tau, v \in T_1, \\ \quad \vdots \\ \kappa_1(\vartheta)\left(\Psi(0) - g(w)(0)\right) + \sum_{k=1}^{k=m} \kappa_1(\vartheta - \vartheta_k) I_k\left(w(\vartheta_k^-)\right) \\ \quad + \int_0^\vartheta \kappa_2(\vartheta - \tau)(\xi(\tau) + (V_z)(\tau)) d\tau, v \in T_m \end{cases}$$

Definition 6. The Problem (1) is called nonlocal controllable on $T = [0, \varpi]$, if for each $w_1 \in E$, there exists a control function $\mho \in L^\infty(T, E)$ such that any corresponding mild solution $w^\mho \in \beta_\varpi$ to Problem (1) must satisfy $w^\mho(0) = \Psi(0) - g(w^\mho)(0)$ and $w^\mho(\varpi) = w_1 - g(w^\mho)(0)$.

Definition 5. The system (2) is said to be nonlocal controllable on the interval $T = [0, \varpi]$ if for each $w_1 \in E$, there exists a control function $z \in L^p(T, X), p > \frac{1}{\gamma}$ such that any corresponding mild solution $w^z \in \beta_\varpi$ for Problem (2) must satisfy $w^z(0) = \Psi(0) - g(w)(0)$ and $w^z(\varpi) = w_1 - g(w^z)(0)$.

Lemma 3. (O'Regan and Precup, 2000, Theorem 3.1). Let D be a closed convex subset of a Banach space and $R: D \to \wp_c(D)$ with a closed graph and maps compact sets into relatively compact sets. Assume that there is $w_0 \in D$ such that, for any $\subseteq D$, with $K = conv(\{w_0\} \cup R(K)), \bar{K} = \bar{Z}$, $Z \subseteq D$ countable, we get K is relatively compact. Then R has a fixed point.

2.1. Controllability of the system (1):

Theorem 1. Assume the following conditions:

$(H\mathcal{F})$ $\mathcal{F}: T \times \beta \to P_{ck}(E)$ such that

$(H\mathcal{F}_1)$ For each $z \in \beta$, the multifunction $\vartheta \to \mathcal{F}(\vartheta, z)$ admits a strongly measurable selection, and for almost each $\vartheta \in T$, the multifunction $z \to \mathcal{F}(\vartheta, z)$ is upper semicontinuous.

$(H\mathcal{F}_2)$ For any $n \in \mathbb{N}$, there exists a $\varrho_n \in L^p(T, \mathbb{R}^+)$ satisfying $sup_{||w||_{\beta\le n}} ||\mathcal{F}(\vartheta, w)|| \le \varrho_n(\vartheta)$, for $a.e. \vartheta \in T$ and

(8) $$\liminf_{n\to\infty}\frac{||\varrho_n||_{L^p(T,\mathbb{R}^+)}}{n}=0.$$

$(H\mathcal{F}_3)$ There is a $\varsigma\in L^p(T,E), p>\frac{1}{\gamma}$ such that, for each bounded subset $Z\subset\beta$ we have

(9) $$\chi_E(\mathcal{F}(\tau,Z))\le\varsigma(\tau)\sup_{\vartheta\in(-\infty,0]}\chi_E\{\psi(\vartheta):\psi\in Z\},$$

$a.e. for\ \tau\in T$.

(H_g) The function $g:\beta_\varpi\to\beta$ verifies:

(Hg_1)

(10) $$liminf_{||w||_{\beta_\varpi}\to\infty}\frac{||g(w)(0)||_E}{||w||_{\beta_\varpi}}=0.$$

(Hg_2) If $w_n\to w\ in\ \beta_\varpi$, then $\lim_{n\to\infty}g(w)(0)_E=g(w)(0)$.

(Hg_3) $\overline{\{g(z)(0):z\in D\}}$ is compact in E whenever $D\subseteq\beta_\varpi$ is bounded.

(HI) For any $i\in\Pi_1, I_i:E\to E$ is continuous and compact, and there are non-decreasing functions $h_i:\mathbb{R}^+\to\mathbb{R}$ such that $\big||I_i(w)|\big|\le h_i\big(||w||\big), w\in E$ and

(11) $$\liminf_{n\to\infty}\frac{|h_i(n)|}{n}=0, i\in\Pi_1.$$

$(H\Delta)$ The operator $\Delta:L^\infty(T,X)\to E$, defined by

(12) $$\Delta(\mho)=\int_0^\varpi\kappa_2(\varpi-\tau)Q\big(\mho(\tau)\big)d\tau,$$

is linear, bounded and has a bounded inverse Δ^{-1}.

Then, the system (1.1) is controllable on T if the following inequality is satisfied:

(13) $$2M_{2^\eta}||\beta||_{L^p(T,\mathbb{R}^+)}\left[1+N^2M_2\frac{\varpi^\gamma}{\gamma}\right]<1,$$

where $\eta=\left(\frac{p-1}{p\gamma-1}\right)^{\frac{p-1}{p}}\varpi^{\gamma-\frac{1}{p}}$ and $N>0$ with $||\Delta^{-1}||\le N$ and $||Q||\le N$.

Proof. Note that, for any $\mho\in L^\infty(T,X)$,

$$||\Delta(\mho)||\le M_2N\int_0^\varpi(\varpi-\tau)^{\gamma-1}\big|\mho(\tau)\big|d\tau$$
$$\le M_2N||\mho||_{L^\infty(T,\omega)}\frac{\varpi^\gamma}{\gamma},$$

which means that Δ is well defined. Let $w\in\beta$ be fixed. In view of $(H\mathcal{F}_1)$ and $(H\mathcal{F}_2)$, there is $\xi\in L^p(T,E)$ with $\xi(\vartheta)\in\mathcal{F}(\vartheta,w_\vartheta), a.e.$ Then, thanks to $(H\Delta)$ we can define a control function $\mho_{w,\xi}\in L^\infty(T,\omega)$ as:

(14)
$$\begin{aligned}\mho_{w,\xi}=\Delta^{-1}[&w_1g(w)(0)-\kappa_1(\varpi)(\Psi(0)-g(w)(0))\\&-\sum_{k=1}^{k=m}\kappa_1(\varpi-\vartheta_k)I_k\big(w(\vartheta_k^-)\big)-\int_0^\varpi\kappa_2(\varpi-\tau)\xi(\tau)d\tau].\end{aligned}$$

Thus, a multifunction $R:\mathcal{H}\to2^{\mathcal{H}}$ can be defined as follows: $y\in R(w)$ if and only if

(15)
$$y(\vartheta)=\begin{cases}0,\vartheta\in(-\infty,0],\\ \kappa_1(\vartheta)\big(\Psi(0)-g(w)(0)\big)+\int_0^\vartheta\kappa_2(\vartheta-\tau)\Big(\xi(\tau)+Q\left(\mho_{w,\xi}(\tau)\right)\Big)d\tau, v\in T_0,\\ \kappa_1(\vartheta)\big(\Psi(0)-g(\omega)(0)\big)+\kappa_1(\vartheta-\vartheta_1)I_1\left(w^{\mho}(\vartheta_1^-)\right)\\ +\int_0^\vartheta\kappa_2(\vartheta-\tau)\Big(\xi(\tau)+Q\left(\mho_{w,\xi}(\tau)\right)\Big)d\tau, v\in T_1,\\ \vdots\\ \kappa_1(\vartheta)\big(\Psi(0)-g(w)(0)\big)+\sum_{k=1}^{k=m}\kappa_1(\vartheta-\vartheta_k)I_k\left(w^{\mho}(\vartheta_k^-)\right)\\ +\int_0^\vartheta\kappa_2(\vartheta-\tau)\Big(\xi(\tau)+Q\left(\mho_{w,\xi}(\tau)\right)\Big)d\tau, v\in T_m,\end{cases}$$

where $\xi\in\tau^1_{\mathcal{F}(.,w(.))}=\{v\in L^p(T,E):v(t)\in\mathcal{F}(t,w_t),a.e.\}$. Notice that, if W is a fixed point for R, then from $(H\Delta)$, (14) and (15)

$$\begin{aligned}\omega(\varpi)&=\kappa_1(\varpi)\big(\Psi(0)-g(w)(0)\big)\\&\quad+\sum_{k=1}^{k=m}\kappa_1(\varpi-\vartheta_k)I_k\big(w(\vartheta_k^-)\big)\\&\quad+\int_0^\varpi\kappa_2(\varpi-\tau)\xi(\tau)d\tau\\&\quad+\int_0^\varpi\kappa_2(\varpi-\tau)Q\left(\mho_{w,\xi}(\tau)\right)d\tau\\&=\kappa_1(\varpi)\big(\Psi(0)-g(w)(0)\big)+\sum_{k=1}^{k=m}\kappa_1(\varpi-\vartheta_k)I_k\big(w(\vartheta_k^-)\big)\\&\quad+\int_0^\varpi\kappa_2(\varpi-\tau)\xi(\tau)d\tau+\Delta(\mho_{w,\xi})\\&=\kappa_1(\varpi)\big(\Psi(0)-g(w)(0)\big)+\sum_{k=1}^{k=m}\kappa_1(\varpi-\vartheta_k)I_k\big(w(\vartheta_k^-)\big)\\&\quad+\int_0^\varpi\kappa_2(\varpi-\tau)\xi(\tau)d\tau+w_1-g(w)(0)\\&\quad-\kappa_1(\varpi)\big(\Psi(0)-g(w)(0)\big)\\&\quad-\sum_{k=1}^{k=m}\kappa_1(\varpi-\vartheta_k)I_k\big(w(\vartheta_k^-)\big)\\&\quad-\int_0^\varpi\kappa_2(\varpi-\tau)\xi(\tau)d\tau=w_1-g(w)(0).\end{aligned}$$

Thus, the function $\overline{w}:(-\infty,\varpi]\to E$ defined by

$$\overline{w}(\vartheta)=\begin{cases}\Psi(\vartheta)-g(w)(\vartheta),\vartheta\in(-\infty,0],\\ w(\vartheta),\vartheta\in[0,\varpi],\end{cases}$$

is a mild solution of system (1) and satisfies $\overline{w}(0)=\Psi(0)-g(w)(0)$ and $\overline{w}(\varpi)=w_1-g(w)(0)$.

Our goal is to prove, using Lemma 2, that R has a fixed point. Clearly $R(w);w\in\mathcal{H}$ is convex.

Step1. In this step, we demonstrate the existence of $n_0\in\mathbb{N}$ such that $R\big(D_{n_0}\big)\subseteq D_{n_0};D_{n_0}=\{w\in\mathcal{H}:||w||_{\mathcal{H}}\le n_0$. Assume, by contradiction, that for each $r\in\mathbb{N}$, there exist $w_r,k_r\in\mathcal{H}$ with $k_r\in R(w_r),||w_r||_{\mathcal{H}}\le r$ and $||k_r||_{\mathcal{H}}>0$. So, there exists a sequence $(\xi_r)_{r\ge1}\in\tau^p_{\mathcal{F}(.,(w_r)_\vartheta)}$ such that:

(16)
$$k_r(\vartheta)=\begin{cases}0,\vartheta\in(-\infty,0],\\ \kappa_1(\vartheta)\big(\Psi(0)-g(w_r)(0)\big)+\int_0^\vartheta\kappa_2(\vartheta-\tau)\Big(\xi_r(\tau)+Q\left(\mho_{w_r,\xi_r}(\tau)\right)\Big)d\tau, v\in T_0,\\ \kappa_1(\vartheta)\big(\Psi(0)-g(w_r)(0)\big)+\kappa_1(\vartheta-\vartheta_1)I_1\big(w_r(\vartheta_1^-)\big)\\ +\int_0^\vartheta\kappa_2(\vartheta-\tau)\Big(\xi_r(\tau)+Q\left(\mho_{w_r,\xi_r}(\tau)\right)\Big)d\tau, v\in T_1,\\ \vdots\\ \kappa_1(\vartheta)\big(\Psi(0)-g(w_r)(0)\big)+\sum_{k=1}^{k=m}\kappa_1(\vartheta-\vartheta_k)I_k\big(w_r(\vartheta_k^-)\big)\\ +\int_0^\vartheta\kappa_2(\vartheta-\tau)\Big(\xi_r(\tau)+Q\left(\mho_{w_r,\xi_r}(\tau)\right)\Big)d\tau, v\in T_m,\end{cases}$$

Notably, (3) yields $\big||(w_r)_\vartheta|\big|_\beta\le\xi r,\forall\vartheta\in T\ and\ r\ge1$. Then, by $(H\mathcal{F}_2)$ for all $r\ge1$,

(17) $$\big||\xi_r(\tau)|\big|\le\xi\varphi_r(\tau),a.e.\vartheta\in T,$$

where $\xi=\sup\{L_1(\vartheta):\vartheta\in T\}$. Since $p>\frac{1}{\gamma}$, the function $\tau\to(\vartheta-\tau)^{\gamma-1}$ belongs to $L^{\frac{p}{p-1}}(T,\mathbb{R}^+)$. Consequently, using (17) and Holder's inequality, we obtain, for any $r\in\mathbb{N}$ and $\vartheta\in T$

$$
\begin{aligned}
\Big\|\int_0^{\vartheta}\kappa_2(\vartheta-\tau)\xi_r(\tau)d\tau\Big\| &\le \xi M_2\int_0^{\vartheta}(\vartheta-\tau)^{\gamma-1}\varphi_r(\tau)d\tau\\
&\le \xi M_2\big\|\varphi_r\big\|_{L^p(T,\mathbb{R}^+)}\Big(\int_0^{\vartheta}(\vartheta-\tau)^{\frac{(\gamma-1)p}{p-1}}d\tau\Big)^{\frac{p-1}{p}}\\
&= \xi M_2\big\|\varphi_r\big\|_{L^p(T,\mathbb{R}^+)}\Big(\frac{p-1}{p\gamma-1}\Big)^{\frac{p-1}{p}}\vartheta^{\gamma-\frac{1}{p}}\\
&\le \xi M_2\eta\big\|\varphi_r\big\|_{L^p(T,\mathbb{R}^+)}.
\end{aligned}
\tag{18}
$$

Next, since $\mathfrak{V}_{w,\xi}\in L^{\infty}(T,w)$, then for any $w\in\mathcal{H}$ and any $\xi\in\tau^p_{\mathcal{F}(.,w(.))}$, we have, for almost every $\tau\in T$

$$
\begin{aligned}
\big\|\mathfrak{V}_{w,\xi}(\tau)\big\| &\le \big\|\mathfrak{V}_{w,\xi}\big\|_{L^{\infty}(T,X)}\\
&\le \|\Delta^{-1}\|\big[\|w_1\|+\big|g(w)(0)\big|+\|\kappa_1(\varpi)\|\big(\big\|\Psi(0)\big\|+\big|g(w)(0)\big|\big)\\
&\quad+\sum_{k=1}^{k=m}\big\|\kappa_1(\varpi-\vartheta_k)\big\|\big\|I_k\big(w(\vartheta_k^-)\big)\big\|\\
&\quad+\Big\|\int_0^{\varpi}\kappa_2(\varpi-\tau)\xi(\tau)d\tau\Big\|\big].
\end{aligned}
\tag{19}
$$

This inequality gives us,

$$
\begin{aligned}
\Big\|\int_0^{\vartheta}\kappa_2(\vartheta-\tau)Q\big(\mathfrak{V}_{w_r,\xi_r}(\tau)\big)d\tau\Big\| &\le M_2N\int_0^{\vartheta}(\vartheta-\tau)^{\gamma-1}\big\|\mathfrak{V}_{w_r,\xi_r}(\tau)\big\|d\tau\\
&\le M_2N\frac{\varpi^{\gamma}}{\gamma}N\big[\|w_1\|+\big|g(w_r)(0)\big|+\|\kappa_1(\varpi)\|\big(\big\|\Psi(0)\big\|+\big|g(w_r)(0)\big|\big)\\
&\quad+\sum_{k=1}^{k=m}\big\|\kappa_1(\varpi-\vartheta_k)\big\|\big\|I_k\big(w_r(\vartheta_k^-)\big)\big\|\\
&\quad+\Big\|\int_0^{\varpi}\kappa_2(\varpi-\tau)\xi_r(\tau)d\tau\Big\|\big].
\end{aligned}
\tag{20}
$$

Consequently, if $\vartheta\in T_0$, then from (Hg_1), (HI), (16) and (20), it follows:

$$
\begin{aligned}
\big\|\kappa_r(\vartheta)\big\| &\le M_1\big(\big\|\Psi(0)\big\|+\big\|g(w_r)(0)\big\|\big)+M_2\xi\big\|\varphi_r\big\|_{L^p(T,\mathbb{R}^+)}\eta\\
&\quad+M_2N\frac{\varpi^{\gamma}}{\gamma}N\big[\big\|w_1\big\|+\big\|g(w_r)(0)\big\|+M_1\big(\big\|\Psi(0)\big\|+\big\|g(w_r)(0)\big\|\big)\\
&\quad+M_1\sum_{k=1}^{k=m}h_k\big(\big\|w_r\big\|\big)+M_2\xi\big\|\varphi_r\big\|_{L^p(T,\mathbb{R}^+)}\eta\big].
\end{aligned}
$$

Likewise, when $\vartheta\in T_{\xi}$, $\xi\in\Pi_1$, we have:

$$
\begin{aligned}
\big\|\kappa_r(\vartheta)\big\| &\le M_1\big(\big\|\Psi(0)\big\|+\big\|g(w_r)(0)\big\|\big)+M_1\sum_{k=1}^{k=m}h_k\big(\big\|w_r\big\|\big)+\eta M_2\xi\big\|\varphi_r\big\|_{L^p(T,\mathbb{R}^+)}\\
&\quad+\frac{\varpi^{\gamma}}{\gamma}N^2M_2\big[\big\|w_1\big\|+\big\|g(w_r)(0)\big\|+M_1\big(\big\|\Psi(0)\big\|+\big\|g(w_r)(0)\big\|\big)\\
&\quad+M_1\sum_{k=1}^{k=m}h_k\big(\big\|w_r\big\|\big)+\eta M_2\xi\big\|\varphi_r\big\|_{L^p(T,\mathbb{R}^+)}\big].
\end{aligned}
$$

Then,

$$
\begin{aligned}
r<\big\|\kappa_r\big\| &\le M_1\big(\big\|\Psi(0)\big\|+\big\|g(w_r)(0)\big\|\big)+M_1\sum_{k=1}^{k=m}h_k(r)+\eta M_2\xi\big\|\varphi_r\big\|_{L^p(T,\mathbb{R}^+)}\\
&\quad+\frac{\varpi^{\gamma}}{\gamma}N^2M_2\big[\big\|w_1\big\|+\big\|g(w_r)(0)\big\|+M_1\big(\big\|\Psi(0)\big\|+\big\|g(w_r)(0)\big\|\big)\\
&\quad+M_1\sum_{k=1}^{k=m}h_k(r)+\eta M_2\xi\big\|\varphi_r\big\|_{L^p(T,\mathbb{R}^+)}\big].
\end{aligned}
$$

By dividing both sides by r and taking the $\lim inf$ as $r\to\infty$, and using (8), (10), and (11), we obtain the contradiction 1<0. Thus, there exists $n_0\in\mathbb{N}$ such that $R(D_{n_0})\subseteq D_{n_0}$.

Step 2. Let $K=R(D_{n_0})$. We claim, in this step, that the set $K_{|\overline{T_i}}$ is equicontinuous for each $i\in\Pi_m$, where

$K_{|\overline{T_i}}=\{y^*\in C(\overline{T_i},E)\colon y^*(\vartheta)=y(\vartheta),\vartheta\in T_i,y^*(\vartheta_i)=y(\vartheta_i^+),y\in K\}$.

Let $y\in K$, Then, there exists $w\in D_{n_0}$ such that $y\in R(w)$. Hence, there exists $\xi\in\tau^p_{\mathcal{F}(.,w_{\vartheta})}$ such that

$$
y(\vartheta)=\begin{cases}
0,\vartheta\in(-\infty,0],\\
\kappa_1(\vartheta)\big(\Psi(0)-g(w)(0)\big)+\int_0^{\vartheta}\kappa_2(\vartheta-\tau)\Big(\xi(\tau)+Q\Big(\mathfrak{V}_{w,\xi}(\tau)\Big)\Big)d\tau,\upsilon\in T_0,\\
\kappa_1(\vartheta)\big(\Psi(0)-g(w)(0)\big)+\kappa_1(\vartheta-\vartheta_1)I_1\big(w(\vartheta_1^-)\big)\\
\quad+\int_0^{\vartheta}\kappa_2(\vartheta-\tau)\Big(\xi(\tau)+Q\Big(\mathfrak{V}_{w,\xi}(\tau)\Big)\Big)d\tau,\upsilon\in T_1,\\
\cdot\\
\cdot\\
\kappa_1(\vartheta)\big(\Psi(0)-g(w)(0)\big)+\sum_{k=1}^{k=m}\kappa_1(\vartheta-\vartheta_k)I_k\big(w(\vartheta_k^-)\big)\\
\quad+\int_0^{\vartheta}\kappa_2(\vartheta-\tau)\Big(\xi(\tau)+Q\Big(\mathfrak{V}_{w,\xi}(\tau)\Big)\Big)d\tau,\upsilon\in T_m,
\end{cases}
$$

Case 1. Let $\vartheta,\vartheta+\delta\in\overline{T_0}=T_0$. Then,

$$
\begin{aligned}
&\big\|y^*(\vartheta+\delta)-y^*(\vartheta)\big\|=\big\|y(\vartheta+\delta)-y(\vartheta)\big\|\\
&\le\big\|\kappa_1(\vartheta+\delta)\big(\Psi(0)-g(w)(0)\big)-\kappa_1(\vartheta)\big(w_0-g(w)(0)\big)\big\|\\
&+\Big\|\int_0^{\vartheta+\delta}\kappa_2(\vartheta+\delta-\tau)\Big(\xi(\tau)+Q\Big(\mathfrak{V}_{w,\xi}(\tau)\Big)\Big)d\tau\\
&\qquad-\int_0^{\vartheta}\kappa_2(\vartheta-\tau)\Big(\xi(\tau)+Q\Big(\mathfrak{V}_{w,\xi}(\tau)\Big)\Big)d\tau\\
&+\big\|\kappa_1(\vartheta+\delta)\big(\Psi(0)-g(w)(0)\big)-\kappa_1(\vartheta)\big(w_0-g(w)(0)\big)\big\|\\
&\quad+\Big\|\int_{\vartheta}^{\vartheta+\delta}\kappa_2(\vartheta+\delta-\tau)\Big(\xi(\tau)+Q\Big(\mathfrak{V}_{w,\xi}(\tau)\Big)\Big)d\tau\Big\|\\
&+\Big\|\int_0^{\vartheta}[\kappa_2(\vartheta+\delta-\tau)\\
&\qquad-\kappa_2(\vartheta-\tau)]\Big(\xi(\tau)+Q\Big(\mathfrak{V}_{w,\xi}(\tau)\Big)\Big)d\tau\Big\|\\
&=G_1+G_2+G_3,
\end{aligned}
$$

where

$G_1=\big\|\kappa_1(\vartheta+\delta)\big(w_0-g(w)(0)\big)-\kappa_1(\vartheta)\big(w_0-g(w)(0)\big)\big\|$,

$G_2=\big\|\int_{\vartheta}^{\vartheta+\delta}\kappa_2(\vartheta+\delta-\tau)\Big(\xi(\tau)+Q\Big(\mathfrak{V}_{w,\xi}(\tau)\Big)\Big)d\tau\big\|$,

and

$G_3=\big\|\int_0^{\vartheta}[\kappa_2(\vartheta+\delta-\tau)-\kappa_2(\vartheta-\tau)]\Big(\xi(\tau)+Q\Big(\mathfrak{V}_{w,\xi}(\tau)\Big)\Big)d\tau\big\|$.

Thanks to (Hg_3), there exists a constant $k>0$ such that $\big\|g(w)(0)\big\|\le k,\forall w\in B_{n_0}$. Thus,

$$
\begin{aligned}
\lim_{\delta\to0}G_1&=\lim_{\delta\to0}\big\|\kappa_1(\vartheta+\delta)\big(\Psi(0)-g(w)(0)\big)-\kappa_1(\vartheta)\big(\Psi(0)-g(w)(0)\big)\big\|\\
&\le\|\Psi(0)-g(w)(0)\|\lim_{\delta\to0}\|\kappa_1(\vartheta+\delta)-\kappa_1(\vartheta)\|\\
&\le\big(\big\|\Psi(0)\big\|+k\big)\lim_{\delta\to0}\|\kappa_1(\vartheta+\delta)-\kappa_1(\vartheta)\|=0,
\end{aligned}
$$

and this limit is independent of the choice of $w\in B_{n_0}$.

Next, by (19) and Hölder's inequality, it follows that:

$$
\lim_{\delta\to0}G_2\le M_2\lim_{\delta\to0}\int_{\vartheta}^{\vartheta+\delta}(\vartheta+\delta-\tau)^{\gamma-1}\big(\|\xi(\tau)\|+\|Q\|\big\|\mathfrak{V}_{w,\xi}(\tau)\big\|\big)d\tau
$$

$$\leq M_2[\lim_{\delta\to 0}\int_{\vartheta}^{\vartheta+\delta}(\vartheta+\delta-\tau)^{\gamma-1}\varphi_{n_0}(\tau)d\tau + N\lim_{\delta\to 0}\int_{\vartheta}^{\vartheta+\delta}(\vartheta+\delta-\tau)^{\gamma-1}||\mho_{w,\xi}(\tau)||d\tau]$$

$$\leq M_2||\varphi_{n_0}||_{L^p(T,\mathbb{R}^+)}\lim_{\delta\to 0}\left(\int_{\vartheta}^{\vartheta+\delta}(\vartheta+\delta-\tau)^{\frac{p(\gamma-1)}{p-1}}d\tau\right)^{\frac{p-1}{p}} + M_2N||\mho_{w,\xi}||_{L^\infty(T,W)}\lim_{\delta\to 0}\int_{\vartheta}^{\vartheta+\delta}(\vartheta+\delta-\tau)^{\gamma-1}d\tau = 0,$$

and this limit is independent of the choice of $w \in B_{n_0}$.

For G_3, note that for almost every $\vartheta \in T$, $||\xi(\vartheta)|| \leq \varphi_{n_0}(\vartheta)$. Moreover, from (19), for almost every $\vartheta \in T$, we obtain:

$$\begin{aligned}&\left\|Q\left(\mho_{w,\xi}(\vartheta)\right)\right\| \leq ||Q||\left\|\mho_{w,\xi}(\vartheta)\right\| \\ &\leq N^2[||w_1|| + ||g(w)(0)|| + M_1(||w_0|| + ||g(w)(0)||) \\ &+M_1\sum_{k=1}^{k=m}h_k(||w||) + \int_0^{\vartheta}\kappa_2(\vartheta-\tau)\xi(\tau)d\tau] \\ &\leq N^2[||w_1|| + k + M_1(||w_0|| + k) + M_1\sum_{k=1}^{k=m}h_k(n_0) + M_2\eta\left\|\varphi_{n_0}\right\|_{L^p(T,\mathbb{R}^+)}]\end{aligned} \tag{21}$$

Then, in view of (21), we have:

$$\lim_{\delta\to 0}G_3 \leq \int_0^{\vartheta}\lim_{\delta\to 0}||\kappa_2(\vartheta+\delta-\tau)-\kappa_2(\vartheta-\tau)]\xi(\tau)d\tau|| + N\int_0^{\vartheta}\lim_{\delta\to 0}||[\kappa_2(\vartheta+\delta-\tau)-\kappa_2(\vartheta-\tau)]Q\left(\mho_{w,\xi}(\vartheta)\right)||d\tau$$

In view of the definition of κ_2, we conclude that $\lim_{\delta\to 0}G_3 = 0$, independently of the choice of W.

Case 2. Let $\vartheta, \vartheta+\delta \in T_i, i \in \Pi_1$.

$$\begin{aligned}&\left||y^*(\vartheta+\delta)-y^*(\vartheta)\right|| = \left||y(\vartheta+\delta)-y(\vartheta)\right| \\ &\leq ||\kappa_1(\vartheta+\delta)\big(\Psi(0)-g(w)(0)\big) - \kappa_1(\vartheta)\big(\Psi(0)-g(w)(0)\big)|| \\ &+\sum_{k=1}^{k=i}||\kappa_1(\vartheta+\delta-\vartheta_k)-\kappa_1(\vartheta-\vartheta_k)||h_k(n_0)|| \\ &+||\int_0^{\vartheta+\delta}\kappa_2(\vartheta+\delta-\tau)\left(\xi(\tau)+Q\left(\mho_{w,\xi}(\tau)\right)\right)d\tau - \int_0^{\vartheta}\kappa_2(\vartheta-\tau)\left(\xi(\tau)+Q\left(\mho_{w,\xi}(\tau)\right)\right)d\tau\end{aligned}$$

As in the previous case, we get $\lim_{\delta\to 0}\left||y(\vartheta+\delta)-y(\vartheta)\right|| = 0$.

Case 3. Let $\vartheta = \vartheta_i;\ i \in \Pi_1, \delta > 0$ and $\tau > 0$ such that $\vartheta_i + \delta \in T_i$ and $\vartheta_i < \tau < \vartheta_i + \delta \leq \vartheta_{i+1}$. Then,

$$\left||y^*(\vartheta_i+\delta)-y^*(\vartheta_i)\right|| = \lim_{\tau\to\vartheta_i^+}\left||y(\vartheta_i+\delta)-y(\tau)\right||.$$

Note that,

$$\begin{aligned}&\left||y(\vartheta_i+\delta)-y(\tau)\right|| \\ &\leq ||\kappa_1(\vartheta_i+\delta)\big(\Psi(0)-g(w)(0)\big) - \kappa_1(\tau)\big(\Psi(0)-g(w)(0)\big)|| \\ &+\sum_{k=1}^{k=T}||\kappa_1(\vartheta_i+\delta-\vartheta_k)I_k(w(\vartheta_k^-)) - \kappa_1(\lambda-\vartheta_k)I_k(w(\vartheta_k^-))||\end{aligned}$$

$$+||\int_0^{\vartheta_i+\delta}\kappa_2(\vartheta_i+\delta-\tau)\left(\xi(\tau)+Q\left(\mho_{w,\xi}(\tau)\right)\right)d\tau - \int_0^{\vartheta_i}\kappa_2(\tau-\tau)\left(\xi(\tau)+Q\left(\mho_{w,\xi}(\tau)\right)\right)d\tau.$$

As in the first case, we get $\lim_{\substack{\delta\to 0\\ \tau\to\vartheta_i^+}}\left||y(\vartheta_i^+ + \delta)-y(\tau)\right|| = 0$. As a consequence of this discussion, the set $K_{|\overline{T_i}}$ is Equi continuous for every $i \in \Pi_0$.

Step 3. The graph of $R_{|B_{n_0}}$ is closed.

Let $w_n \to w$ in B_{n_0} and $z_n \in R(w_n)$ with $z_n \to z\ in\ \mathcal{H}$. We must show that $z \in R(w)$. For each $n \geq 1$, let $\xi_n \in \tau^p_{\xi(.,(w_n)_\vartheta)}$ be such that:

$$z_n(\vartheta) = \begin{cases} 0, \vartheta \in (-\infty, 0], \\ \kappa_1(\vartheta)\big(\Psi(0)-g(w_n)(0)\big) + \int_0^{\vartheta}\kappa_2(\vartheta-\tau)\left(\xi_n(\tau)+Q\left(\mho_{w_n,\xi_n}(\tau)\right)\right)d\tau, v \in T_0, \\ \kappa_1(\vartheta)\big(\Psi(0)-g(w_n)(0)\big) + \kappa_1(\vartheta-\vartheta_1)I_1\big(w_n(\vartheta_1^-)\big) + \int_0^{\vartheta}\kappa_2(\vartheta-\tau)\left(\xi_n(\tau)+Q\left(\mho_{w_n,\xi_n}(\tau)\right)\right)d\tau, v \in T_1, \\ \vdots \\ \kappa_1(\vartheta)\big(\Psi(0)-g(w_n)(0)\big) + \sum_{k=1}^{k=m}\kappa_1(\vartheta-\vartheta_k)I_k\big(w_n(\vartheta_k^-)\big) + \int_0^{\vartheta}\kappa_2(\vartheta-\tau)\left(\xi_n(\tau)+Q\left(\mho_{w_n,\xi_n}(\tau)\right)\right)d\tau, v \in T_m, \end{cases}$$

In view of $(H\mathcal{F}_2)$, $\left||\xi_n(\vartheta)|\right| \leq \xi\varphi_{n_0}(\vartheta), \forall n \geq 1$, and for $a.e.\ \vartheta \in T$. Hence, the set $\{\xi_n : n \geq 1\}$ is weakly compact in $L^p(T,E)$. Since $p > 1$, we can assume that ξ_n converges weakly to a function $\xi \in L^p(T,E)$. Thanks to Mazur's lemma, there exists a sequence $(\varsigma_n)_{n\geq 1}$, where each ς_n is a convex combination of $\xi_j\ with\ j \geq n$, and $\varsigma_n \to \xi$ strongly in $L^1(T,E)$. Let

$$\overline{z_n}(\vartheta) = \begin{cases} 0, \vartheta \in (-\infty, 0], \\ \kappa_1(\vartheta)\big(\Psi(0)-g(w_n)(0)\big) + \int_0^{\vartheta}\kappa_2(\vartheta-\tau)\left(\varsigma_n(\tau)+Q\left(\mho_{w_n,z_n}(\tau)\right)\right)d\tau, v \in T_0, \\ \kappa_1(\vartheta)\big(\Psi(0)-g(w_n)(0)\big) + \kappa_1(\vartheta-\vartheta_1)I_1\big(w_n(\vartheta_1^-)\big) + \int_0^{\vartheta}\kappa_2(\vartheta-\tau)\left(\varsigma_n(\tau)+Q\left(\mho_{w_n,z_n}(\tau)\right)\right)d\tau, v \in T_1, \\ \vdots \\ \kappa_1(\vartheta)\big(w_0-g(w_n)(0)\big) + \sum_{k=1}^{k=m}\kappa_1(\vartheta-\vartheta_k)I_k\big(w_n(\vartheta_k^-)\big) + \int_0^{\vartheta}\kappa_2(\vartheta-\tau)\left(\varsigma_n(\tau)+Q\left(\mho_{w_n,z_n}(\tau)\right)\right)d\tau, v \in T_m, \end{cases}$$

Note that, $\overline{z_n} \to z$ and for each $\vartheta \in T$, and each $\tau \in (0,\vartheta]$, we get:

$\left||\kappa_2(\vartheta-\tau)\varsigma_n(\tau)|\right| \leq M_2(\vartheta-\tau)^{\gamma-1}\varphi_{n_0}(\tau);\ \forall n \geq 1.$

Because κ_2 is continuous, it follows that,

$$\lim_{n\to\infty}\int_0^{\vartheta}\kappa_2(\vartheta-\tau)\varsigma_n(\tau)d\tau = \int_0^{\vartheta}\kappa_2(\vartheta-\tau)\xi(\tau)d\tau. \tag{22}$$

From (22), (Hg_2), the continuity of Δ^{-1}, κ_1 and (14), we obtain $\lim_{n\to\infty}\mho_{w_n,z_n} = \mho_{w,\xi}$, in $L^\infty(T,w)$. So, $\lim_{n\to\infty}\mho_{w_n,z_n}(\vartheta) = \mho_{w,\xi}(\vartheta), a.e.\ \vartheta \in T$. Because Q is continuous, it follows that $\lim_{n\to\infty}Q(\mho_{w_n,z_n}(\vartheta)) = Q\left(\mho_{w,\xi}(\vartheta)\right), a.e.\ \vartheta \in T, in\ E$. Therefore, by the Lebesgue dominated convergence theorem, we conclude,

$$z(\vartheta) = \begin{cases} 0, \vartheta \in (-\infty, 0], \\ \kappa_1(\vartheta)\big(\Psi(0) - g(w)(0)\big) + \int_0^{\vartheta} \kappa_2(\vartheta-\tau)(\xi(\tau) + Q\left(\mho_{w,\xi}(\tau)\right))d\tau, v \in T_0, \\ \kappa_1(\vartheta)\big(\Psi(0) - g(w)(0)\big) + \kappa_1(\vartheta-\vartheta_1)I_1\big(w(\vartheta_1^-)\big) \\ + \int_0^{\vartheta} \kappa_2(\vartheta-\tau)\left(\xi(\tau) + Q\left(\mho_{w,\xi}(\tau)\right)\right)d\tau, v \in T_1, \\ \cdot \\ \cdot \\ \kappa_1(\vartheta)\big(\Psi(0) - g(w_n)(0)\big) + \sum_{k=1}^{k=m} \kappa_1(\vartheta-\vartheta_k)I_k\big(w(\vartheta_k^-)\big) \\ + \int_0^{\vartheta} \kappa_2(\vartheta-\tau)\left(\xi(\tau) + Q\left(\mho_{w,\xi}(\tau)\right)\right)d\tau, v \in T_m, \end{cases}$$

Notice that, thanks to (3) it follows for $\vartheta \in T$ that

$\lim_{n\to\infty} ||(w_n)_\vartheta - w_\vartheta||_B = \lim_{n\to\infty} ||(w_n - w)_\vartheta||_B \le \xi \lim_{n\to\infty} ||w_n - w||_{\mathcal{H}} = 0.$

This implies with the upper semi continuity of $\mathcal{F}(\vartheta, .)$; $a.e. \vartheta \in T, \xi(\vartheta) \in \mathcal{F}(\vartheta, w_\vartheta), a.e. \vartheta \in T$. This proves that the graph of R is closed.

Step 4. Let $K \subseteq B_{n_0}$ *be defined as* $K = conv\big(\{0\} \cup R(K)\big), with\ \overline{K} = \overline{B}$ where $B \subseteq K$ is countable. We claim that K is relatively compact. From Step 2, we know that K is equicontinuous on each $\overline{T}_i; i \in \Pi_0$. It remains to show that the set $\{K(\vartheta);\ \vartheta \in T\}$ is relatively compact in E. Since $B \subseteq K = conv(\{0\} \cup R(K))$ is countable, we can find a countable set $H = \{y_n : n \ge 1\} \subseteq R(K)$ such that $B \subseteq conv(\{0\} \cup H)$. Then, for any $\vartheta \in T$,

$$\chi\big(K(\vartheta)\big) = \chi\big(\overline{B}(\vartheta)\big)\chi\big(H(\vartheta)\big) = \chi\{y_n(\vartheta) : n \ge 1\}. \quad (23)$$

Now, for any $n \ge 1$, let $w_n \in K \subseteq B_{n_0}$ with $y_n \in R(w_n)$. Then, there exists $\xi_n(\vartheta) \in \tau^p_{\mathcal{F}(\vartheta,(w_n)_\vartheta)}$ such that $\big||\xi_n(\vartheta)|\big| \le \varphi_{n_0}(\vartheta), a.e., \forall n \ge 1$. Moreover,

$$y_n(\vartheta) = \begin{cases} 0, \vartheta \in (-\infty, 0], \\ \kappa_1(\vartheta)\big(w_0 - g(w)(0)\big) + \int_0^{\vartheta} \kappa_2(\vartheta-\tau)(\xi_n(\tau) + Q\left(\mho_{w_n,\xi_n}(\tau)\right))d\tau, v \in T_0, \\ \kappa_1(\vartheta)\big(w_0 - g(w)(0)\big) + \kappa_1(\vartheta-\vartheta_1)I_1\big(w(\vartheta_1^-)\big) \\ + \int_0^{\vartheta} \kappa_2(\vartheta-\tau)\left(\xi_n(\tau) + Q\left(\mho_{w_n,\xi_n}(\tau)\right)\right)d\tau, v \in T_1, \\ \cdot \\ \cdot \\ \kappa_1(\vartheta)\big(w_0 - g(w)(0)\big) + \sum_{k=1}^{k=m} \kappa_1(\vartheta-\vartheta_k)I_k\big(w(\vartheta_k^-)\big) \\ + \int_0^{\vartheta} \kappa_2(\vartheta-\tau)\left(\xi_n(\tau) + Q\left(\mho_{w_n,\xi_n}(\tau)\right)\right)d\tau, v \in T_m. \end{cases}$$

Then, by using the properties of the measure of noncompactness (Kamenskii *et al.*, 2011) we obtain:

$$\chi\{y_n(\vartheta) : n \ge 1\} \le \begin{cases} 0, \vartheta \in (-\infty, 0], \\ \chi\{\kappa_1(\vartheta)\big(w_0 - g(w_n)(0)\big) : n \ge 1\} \\ +\chi\left\{\int_0^{\vartheta} \kappa_2(\vartheta-\tau)\left(\xi_n(\tau) + Q\left(\mho_{w_n,\xi_n}(\tau)\right)\right)d\tau : n \ge 1\right\}, \\ v \in T_0, \\ \chi\{\kappa_1(\vartheta)\big(w_0 - g(w_n)(0)\big) : n \ge 1\} \\ + \sum_{k=1}^{k=m} \chi\{\kappa_1(\vartheta-\vartheta_k)I_k\big(w_n(\vartheta_k^-)\big) : n \ge 1\} \\ +\chi\{\int_0^{\vartheta} \kappa_2(\vartheta-\tau)\left(\xi_n(\tau) + Q\left(\mho_{w_n,\xi_n}(\tau)\right)\right)d\tau : n \ge 1\}, \\ v \in T_i, i \in \Pi_m. \end{cases}$$

Now, by (Hg_3), the set $\{g(w_n)(0) : n \ge 1\}$ is relatively compact. Hence, for each $\vartheta \in T$,

$$\chi\{\kappa_1(\vartheta)\big(\Psi(0) - g(w_n)(0)\big) : n \ge 1\} = 0. \quad (24)$$

Furthermore, since each I_K is compact for $k \in \Pi_1$, it follows that for each $\vartheta \in T$,

$$\chi\{\kappa_1(\vartheta - \vartheta_k)(I_k(w_n(\vartheta_n^-))) : n \ge 1\} = 0. \quad (25)$$

Next, we estimate the quantity $\chi\left\{\int_0^{\vartheta} \kappa_2(\vartheta-\tau)\xi_k(\tau)d\tau : k \ge 1\right\}$, where $\vartheta \in T$ is fixed. Note that, from $(H\mathcal{F}_3)$, it holds for $a.e. \vartheta \in T$

$$\begin{aligned} \chi\left\{\xi_k(\vartheta) : k \ge 1\right\} &\le \chi\left\{\xi\big(\vartheta, (w_k)_\vartheta\big) : k \ge 1\right\} \\ &\le \beta(\vartheta) \sup_{\theta\in(-\infty,0]} \chi\{(w_k)_\vartheta(\theta) : k \ge 1\} \\ &= \beta(\vartheta) \sup_{\theta\in(-\infty,0]} \chi\{w_k(\vartheta+\theta) : k \ge 1\} \\ &= \beta(\vartheta) \sup_{\delta\in[0,\vartheta]} \chi\{w_k(\delta) : k \ge 1\} \le \beta(\vartheta)\chi(K(\vartheta)) \\ &\le \beta(\vartheta)\chi\big(K(\vartheta)\big) = \rho(\vartheta)\ . \end{aligned} \quad (26)$$

Note that, $\rho \in L^p(T, R^+)$. According to Bader *et al.* (2001), for every $\varepsilon > 0$, there exists a compact set K_ε, a measurable set $T_\varepsilon \subset T$ with measure less than $\mathcal{E}$, and a sequence of functions $\{\varsigma_k^{\mathcal{E}}\} \subset L^p(T, E)$ such that $\{\varsigma_k^{\varepsilon}(\tau) : k \ge 1\} \subseteq K_\varepsilon, \tau \in T$ and

$$\big||\xi_k(\tau) - \varsigma_k^{\varepsilon}(\tau)|\big| \le 2\rho(\tau) + \varepsilon, for\ each\ k \ge 1\ and\ each\ \tau \in T - T_\varepsilon. \quad (27)$$

Next, consider the linear continuous operator $G: L^p(T, E) \to C(T, E)$ defined by:

$$G(z)(\vartheta) = \int_0^{\vartheta} \kappa_2(\vartheta-\tau)z(\tau)d\tau, \forall \vartheta \in T. \quad (28)$$

Combine (26)–(28), for all $\vartheta \in T$ and all $k \ge 1$, we obtain:

$$\begin{aligned} ||G(\xi_k(\vartheta) - G(\varsigma_k^{\varepsilon})(\vartheta)|| &\le \eta M_2 \left(\int_0^{\vartheta} ||\xi_k(\tau) - \varsigma_k^{\varepsilon}(\tau)||^p\, d\tau\right)^{\frac{1}{p}} \\ &= \eta M_2 [\int_{[0,\vartheta]-T_\varepsilon} \big||\xi_k(\tau) - \varsigma_k^{\varepsilon}(\tau)|\big|^p\, d\tau \\ &\quad + \int_{[0,\vartheta]\cap T_\varepsilon} \big||\xi_k(\tau) - \varsigma_k^{\varepsilon}(\tau)|\big|^p\, d\tau]^{\frac{1}{p}} \\ &\le \eta M_2 [\int_{[0,\vartheta]-T_\varepsilon} (2\rho(\tau) + \varepsilon)^p\, d\tau \\ &\quad + \int_{[0,\vartheta]\cap T_\varepsilon} \big||\xi_k(\tau) - \varsigma_k^{\varepsilon}(\tau)|\big|^p\, d\tau]^{\frac{1}{p}} \end{aligned}$$

By taking into account that $\mathcal{E}$ is arbitrary, we get for all $\vartheta \in T$ and all $r \ge 1$

$$||G(\xi_k(\vartheta) - G(\varsigma_k^{\varepsilon})(\vartheta)|| \le 2\eta M_2 \left(\int_0^{\vartheta} (\rho(\tau))^p\, d\tau\right)^{\frac{1}{p}}.$$

Since $\{\varsigma_k^{\varepsilon}(\tau) : k \ge 1\} \subseteq K_\varepsilon, \chi\{G(\varsigma_k^{\varepsilon})(\vartheta) : r \ge 1\} = 0$. Thus, for all $\vartheta \in T$

$$\begin{aligned} &\chi\left(\left\{\int_0^{\vartheta} \kappa_2(\vartheta-\tau)\xi_r(\tau)d\tau : r \ge 1\right\}\right) \\ &= \chi\{G(\xi_r)(\vartheta) : r \ge 1\} \\ &\le \chi\{G(\xi_r)(\vartheta) - G(\varsigma_r^{\varepsilon})(\vartheta) : r \ge 1\} \\ &\le \chi\{G(\xi_r)(\vartheta) - G(\varsigma_r^{\varepsilon})(\vartheta) : r \ge 1\} \\ &\le 2\eta M_2 \left(\int_0^{\vartheta} \big(\rho(\tau)\big)^p\, d\tau\right)^{\frac{1}{p}} \\ &\le 2\eta M_2 \chi_{\mathcal{H}}(Z)||\beta||_{L^p(T,\mathbb{R}^+)}. \end{aligned} \quad (29)$$

Next, we estimate the quantity $\chi\left(\left\{\int_0^{\vartheta}\kappa_2(\vartheta-\tau)Q(\mho_{w_r,\xi_r}(\tau)d\tau: r\geq 1\right\}\right)$. From (24), (25), (29) and the fact that Δ^{-1} is linear and bounded, we have:

$$\begin{aligned}\chi_{L^{\infty}(T,w)}\{\mho_{w_r,\xi_r}: r\geq 1\}&\leq N\chi\{w_1-g(w_r)-\kappa_1(\varpi)\big(w_0-g(w_r)\big)\\&\quad-\sum_{k=1}^{k=m}\kappa_1(\varpi-\vartheta_k)I_k\big(w_r(\vartheta_k^-)\big)\\&\quad-\int_0^{\varpi}\kappa_2(\varpi-\tau)\xi_r(\tau)d\tau: r\geq 1\}\\&=N\chi\{\int_0^{\varpi}\kappa_2(\varpi-\tau)\xi_r(\tau)d\tau: r\in\mathbb{N}\}\end{aligned}$$

$$\leq 2NM_2\eta\chi_{\mathcal{H}}(Z)||\beta||_{L^p(T,\mathbb{R}^+)}. \tag{30}$$

Now, consider the linear continuous operator $\Theta: L^{\infty}(T,w)\to C(T,E)$, where $\Theta(h)(\vartheta)=\int_0^{\vartheta}\kappa_2(\vartheta-\tau)Q\big(h(\tau)\big)d\tau$. Then, by (30), we obtain:

$$\begin{aligned}\chi\left(\left\{\int_0^{\vartheta}\kappa_2(\vartheta-\tau)Q(\mho_{w_r,\xi_r}(\tau)d\tau: r\geq 1\right\}\right)&=\chi\{\Theta\big(\mho_{w_r,\xi_r}\big): r\geq 1\}\\&\leq||\Theta||\chi_{L^{\infty}(T,w)}\{\mho_{w_r,\xi_r}: r\geq 1\}\\&\leq 2\frac{\varpi^{\gamma}}{\gamma}N^2M_2^2\eta\chi_{\mathcal{H}}(Z)||\beta||_{L^p(T,\mathbb{R}^+)}.\end{aligned} \tag{31}$$

By combining (24), (25), (29) and (31) we obtain:

$$\chi_{PC}(K)=\max_{i=0,1,..,m}\chi_{C(\overline{T_i},E)}(K_{|\overline{T_i}})\leq\max_{i=0,1,..,m}\max_{\vartheta\in\overline{T_i}}\chi(K(\vartheta))$$

$$=\max_{\vartheta\in T}\chi(K(\vartheta))\leq\max_{\vartheta\in T}\chi\big(H(\vartheta)\big)=\max_{\vartheta\in T}\chi\{y_r(\vartheta): r\geq 1\}$$

$$\leq\chi_{\mathcal{H}}(K)2M_2\eta\big||\beta|\big|_{L^p(T,\mathbb{R}^+)}\left[1+N^2\overline{M_{\vartheta}}\frac{\varpi}{\gamma}\right]<\chi_{PC}(K).$$

This leads to $\chi_{PC}(K)$, and consequently, K is relatively compact.

Step 5. In this step, we demonstrate that, if $\Theta\subseteq B_{n_0}$ is compact, then $R(\Theta)$ is relatively compact. Let $y_n\in R(\Theta), n\geq 1$. Then, there exists $w_n, n\geq 1$, such that $y_n\in R(w_n)$. Hence, there exists $\xi_n\in\tau^p_{\mathcal{F}(.,(w_n)_{\vartheta})}$ such that, for $\vartheta\in T$,

$$y_n(\vartheta)=\begin{cases}\kappa_1(\vartheta)\big(w_0-g(w)(0)\big)+\int_0^{\vartheta}\kappa_2(\vartheta-\tau)\Big(\xi_n(\tau)+Q\left(\mho_{w_n,\xi_n}(\tau)\right)\Big)d\tau, \upsilon\in T_0,\\ \kappa_1(\vartheta)\big(w_0-g(w)\big)+\kappa_1(\vartheta-\vartheta_1)I_1\big(w(\vartheta_1^-)\big)\\ \quad+\int_0^{\vartheta}\kappa_2(\vartheta-\tau)\Big(\xi_n(\tau)+Q\left(\mho_{w_n,\xi_n}(\tau)\right)\Big)d\tau, \upsilon\in T_1,\\ \quad\vdots\\ \kappa_1(\vartheta)\big(w_0-g(w)(0)\big)+\sum_{k=1}^{k=m}\kappa_1(\vartheta-\vartheta_k)I_k\big(w(\vartheta_k^-)\big)\\ \quad+\int_0^{\vartheta}\kappa_2(\vartheta-\tau)\Big(\xi_n(\tau)+Q\left(\mho_{w_n,\xi_n}(\tau)\right)\Big)d\tau, \upsilon\in T_m.\end{cases}$$

We must show that the set $Z=\{y_n: n\geq 1\}$ is relatively compact in $\mathcal{H}$. As in Step 2, it follows that the set $Z_{|\overline{T_i}}$ is equicontinuous for each $i\in\Pi_0$. In addition, since Θ is compact in $\mathcal{H}$, we have $\sup_{\delta\in[0,\vartheta]}\chi\{w_k(\delta): k\geq 1\}=0$, and hence, from $(H\mathcal{F}_3)$ we get for $a.e.\ \vartheta\in T$:

$$\begin{aligned}\chi\{\xi_k(\vartheta): k\geq 1\}&\leq\chi\{\mathcal{F}(\tau,(w_k)_{\vartheta}): k\geq 1\}\\&\leq\beta(\vartheta)\sup_{\theta\in(-\infty,0]}\chi\{(w_k)_{\vartheta}(\theta): k\geq 1\}\\&=\beta(\vartheta)\sup_{\theta\in(-\infty,0]}\chi\{w_k(\vartheta+\theta): k\geq 1\}\\&=\beta(\vartheta)\sup_{\delta\in[0,\vartheta]}\chi\{w_k(\delta): k\geq 1\}=0.\end{aligned}$$

Following the arguments in Step 4, we obtains for all $\vartheta\in T$, $\chi\{y_n(\vartheta): n\geq 1\}=0$, which shows that $R(\Theta)$ is relatively compact.

As a consequence of Steps 1 to 5 and Lemma 2, we conclude that the operator R has a fixed point. Therefore, the problem (1.1) is controllable.

2.2. Controllability result for the system (2):

Consider the following assumptions:

$(H\mathcal{F}_2)^*$ There exists a function $\varphi\in L^p(T,\mathbb{R}^+)$ such that for any $w\in\beta$

$$||\mathcal{F}(\vartheta,w)||\leq\varphi(\vartheta)(1+\big||w|\big|), \text{for } a.e.\ \vartheta\in T. \tag{32}$$

$(Hg_1)^*$ There are $a,d\in(0,\infty)$ with

$$||g(w)(0)||_E\leq a\big||w|\big|_{\beta_{\varpi}}+d, \forall w\in\beta_{\varpi}. \tag{33}$$

$(HI)^*$ For each $i\in\Pi_1$, I_i is continuous and compact and there is $\sigma_i>0$, such that

$$||I_i(w)\big||\leq\sigma_i\big||w||, w\in E. \tag{34}$$

$(H\Delta)^*$ The linear bounded operator $\Delta: L^p(T,X)\to E$ defined by

$$\Delta(z)=\int_0^{\varpi}\kappa_2(\varpi-\tau)\big(V_z(\tau)\big)d\tau$$

has a bounded inverse Δ^{-1}.

Theorem 2. Assume that $(H\mathcal{F}_1)$, $(H\mathcal{F}_2)^*, (H\mathcal{F}_3), (Hg_1)^*, (Hg_2), (Hg_3), (HI)^*$ and $(H\Delta)$ are verified. Then, the system (2) is controllable on T provided that

$$2\overline{M_{\vartheta}}\eta||\beta||_{L^p(T,\mathbb{R}^+)}\left[1+\aleph^2\overline{M_{\vartheta}}\frac{\varpi^{\gamma}}{\gamma}\right]<1, \tag{35}$$

and

$$M_1(a+\sigma)+M_2||\varphi||_{L^p(T,\mathbb{R}^+)}\eta+M_2\frac{\varpi^{\gamma}}{\gamma}\aleph^2\Big[a+M_1(a+\sigma)+M_2\eta||\varphi|\big|_{L^p(T,\mathbb{R}^+)}\Big]<1, \tag{36}$$

where η is defined in the statement of Theorem 1, $\sigma=\sum_{i=1}^{i=m}\sigma_i$ and $\aleph>0$ such that $||\Delta^{-1}||\leq\aleph$ and $||V||\leq\aleph$.

Proof. Since the proof is similar to the proof of Theorem1, we will focus on the difference. Using $(H\Delta)$, for any $w\in\mathcal{H}$ and any $\xi\in L^1(T,E)$ with $\xi(\vartheta)\in\mathcal{F}(\vartheta,w_{\vartheta}), a.e.$, we define the control function $z_{w,\xi}\in L^p(T,w)$ by:

$$\begin{aligned}z_{w,\xi}=\Delta^{-1}[&w_1-g(w)(0)-\kappa_1(\varpi)\big(\Psi(0)-g(w)(0)\big)\\&-\sum_{k=1}^{k=m}\kappa_1(\varpi-\vartheta_k)I_k(w(\vartheta_k^-))\\&-\int_0^{\varpi}\kappa_2(\varpi-\tau)\xi(\tau)d\tau].\end{aligned} \tag{37}$$

Therefore, we can define a multi valued operator $\mathcal{R}:\mathcal{H}\to 2^{\mathcal{H}}$ as follows: let $w\in\mathcal{H}$. A function $y\in\mathcal{R}(w)$ if and only if

$$y(\vartheta)=\begin{cases}0, \vartheta\in(-\infty,0],\\ \kappa_1(\vartheta)\big(\Psi(0)-g(w)(0)\big)+\int_0^{\vartheta}\kappa_2(\vartheta-\tau)(\xi(\tau)+\big(V_{z_w,\xi}\big)(\tau))d\tau, \upsilon\in T_0,\\ \kappa_1(\vartheta)\big(w_0-g(w)(0)\big)+\kappa_1(\vartheta-\vartheta_1)I_1\big(w(\vartheta_1^-)\big)\\ \quad\vdots\\ \kappa_1(\vartheta)\big(\Psi(0)-g(w)(0)\big)+\sum_{k=1}^{k=m}\kappa_1(\vartheta-\vartheta_k)I_k\big(w(\vartheta_k^-)\big)\\ \quad+\int_0^{\vartheta}\kappa_2(\vartheta-\tau)\Big(\xi(\tau)+\big(V_{z_w,\xi}\big)(\tau)\Big)d\tau, \upsilon\in T, i=1,\dots,m,\end{cases} \tag{38}$$

where $\xi\in\tau^1_{\mathcal{F}(.,w_{(.)})}$. As above, we can show that if $\mathcal{W}$ is a fixed point for $\mathcal{R}$, then the function $\overline{w}:(-\infty,\varpi]\to E$, defined by:

$$\overline{w}(\vartheta)=\begin{cases}\Psi(\vartheta)-g(w)(\vartheta), \vartheta\in(-\infty,0],\\ w(\vartheta), \vartheta\in[0,\varpi],\end{cases}$$

is a mild solution for Problem (2) and satisfies $w(0)=\Psi(0)-g(w)(0)$ and $w(\varpi)=w_1-g(w)(0)$. Let $Z_0=\{w\in\mathcal{H}: \big||w|\big|\leq r\}$, where r is a positive real number such that

(39) $\frac{\varrho}{1-w} < r,$

where

$\varrho = M_1\big(||w_0|| + d\big) + M_2||\varphi||_{L^p(T,\mathbb{R}^+)}\eta + M_2\frac{\varpi^\gamma}{\gamma}\aleph^2[||w_1|| + d + M_1\big(||w_0|| + d\big)],$

and

$w = M_1(a+\sigma) + M_2||\varphi||_{L^p(T,\mathbb{R}^+)}\eta + M_2\frac{\varpi^\gamma}{\gamma}\aleph^2[a + M_1(a+\delta) + M_2\eta||\varphi||_{L^p(T,\mathbb{R}^+)}].$

Step1. In this step we claim that $\mathcal{R}(Z_0) \subseteq Z_0$. Suppose $w \in Z_0$ and $y \in \mathcal{R}(w)$. Then, there exists $\xi \in \tau^1_{\mathcal{F}(.,w_{(.)})}$ such that $\mathcal{Y}$ satisfies (38). Since $p > \frac{1}{\gamma}$, the function $\tau \to (\vartheta-\tau)^{\gamma-1}$ belongs to $L^{\frac{p}{p-1}}(T - \mathbb{R}^+)$, hence, using $(H\mathcal{F}_2)^*$ and Hölder's inequality, we get:

$$||\int_0^\vartheta \kappa_2(\vartheta-\tau)\xi(\tau)d\tau|| \le M_2(1+r)\int_0^\vartheta(\vartheta-\tau)^{\gamma-1}\varphi(\tau)d\tau$$
$$\le (1+r)M_2||\varphi||_{L^p(T,\mathbb{R}^+)}\left(\int_0^\vartheta(\vartheta-\tau)^{\frac{(\gamma-1)p}{p-1}}d\tau\right)^{\frac{p-1}{p}}$$
(40) $$\le (1+r)M_2\eta||\varphi||_{L^p(T,\mathbb{R}^+),\vartheta\in T}.$$

and

$$||\int_0^\vartheta \kappa_2(\vartheta-\tau)\big(V_{z_w,\xi}\big)(\tau)d\tau||$$
$$\le M_2\int_0^\vartheta(\vartheta-\tau)^{\gamma-1}||\big(V_{z_w,\xi}\big)(\tau)||d\tau$$
(41) $$\le M_2\big|V_{z_w,\xi}\big|_{L^p(T,E)}\eta.$$

Next, according to the definition of $z_{w,\xi}$ and (40), we get:

$$\big|\big|V_{z_w,\xi}\big|\big|_{L^p(T,E)} \le ||V||||z_w,\xi||_{L^p(T,X)}$$
$$\le ||V||\Delta^{-1}[||w_1|| + ||g(w)(0)||$$
$$+ ||\kappa_1(\varpi)||\big(||\Psi(0)|| + ||g(w)(0)||\big)$$
$$+ \sum_{k=m}^{k_{\vartheta}-1}||\kappa_1(\varpi-\vartheta_k)||\,\big|\big|I_k\big(w(\vartheta_k^-)\big)\big|\big|$$
$$+ \int_0^{\varpi}||\kappa_2(\varpi-\tau)||||\xi(\tau)||d\tau]$$
$$\le \aleph^2[||w_1|| + ar + d + M_1\big(||\Psi(0)|| + ar + d\big) + M_1 r\,\sigma$$
$$+ (1+r)M_2\eta||\varphi||_{L^p(T,\mathbb{R}^+)}]$$
(42) $$= \varsigma.$$

Combine (41) and (42) to get

(43) $$||\int_0^\vartheta \kappa_2(\vartheta-\tau)\big(V_{z_w,\xi}\big)(\tau)d\tau|| \le M_2\frac{\varpi^\gamma}{\gamma}\varsigma.$$

Let $\vartheta \in T_0$. By using (40), (43) and $(H_g)^*$, we get:

(44) $$\big||y(\vartheta)|\big| \le M_1\big(||\Psi(0)|| + ar + d\big) + M_2(1+r)\big||\varphi|\big|_{L^p(T,\mathbb{R}^+)}\eta + M_2\frac{\varpi^\gamma}{\gamma}\varsigma.$$

Likewise, by using $(H_g)^*$ and $(HI)^*$, we get for all $\vartheta \in T_i, i = 1,2,\dots,m,$

$$||y(\vartheta)|| \le M_1\big(||w_0|| + ar + d + \sigma r\big)$$
$$+ M_2(1+r)\big||\varphi|\big|_{L^p(T,\mathbb{R}^+)}\eta + M_2\frac{\varpi^\gamma}{\gamma}\varsigma$$
$$= M_1\big(||w_0|| + d\big) + M_2\big||\varphi|\big|_{L^p(T,\mathbb{R}^+)}\eta + M_2\frac{\varpi^\gamma}{\gamma}\aleph^2[||w_1|| + d$$
$$+ M_1\big(||w_0|| + d\big)$$
$$+M_2\eta\big||\varphi|\big|_{L^p(T,\mathbb{R}^+)} + r[M_1(a+\sigma) + M_2\big||\varphi|\big|_{L^p(T,\mathbb{R}^+)}\eta$$
(45) $$+M_2\frac{\varpi^\gamma}{\gamma}\aleph^2[a + M_1(a+\sigma) + M_2\eta\big||\varphi|\big|_{L^p(T,\mathbb{R}^+)}].$$

In view of (39) and (45), we conclude that $\mathcal{R}(Z_0) \subseteq Z_0$.

Step 2. Let $\kappa = \mathcal{R}(Z_0)$. By following the same arguments from Step 2 and 3 in the proof of Theorem1, one can show that the set $\kappa_{|\overline{T}_i}$ is equicontinuous for each $i \in \Pi_0$, where

$\kappa_{|\overline{T}_i} = \{y^* \in C(\overline{T}_i, E): y^*(\vartheta) = y(\vartheta), \vartheta \in T_i \quad , \quad y^*(\vartheta_i) = y(\vartheta_i^+), y \in \kappa\},$

and the graph of the multivalued function $\mathcal{R}_{|Z_0}: Z_0 \to 2^{Z_0}$ is closed.

Step 3. Let $\mathcal{M} \subseteq Z_0, \mathcal{M} = conv\big(\{w_0\} \cup \mathcal{R}(\mathcal{M})\big), \overline{and\ \mathcal{M}} = \bar{C}$ with $C \subseteq \mathcal{M}$ countable. We demonstrate that $\mathcal{M}$ is relatively compact. Because $\mathcal{M}$ is equicontinuous on each $\overline{T}_i, i \in \Pi_0$, we only need to show that $\mathcal{M}(\vartheta)$ is relatively compact in E. From the countability of C and $C \subseteq \mathcal{M} = conv(\{w_0\} \cup \mathcal{R}(\mathcal{M}))$, we can find a countable set $H = \{y_n: n \ge 1\} \subseteq \mathcal{R}(\mathcal{M})$ with $C \subseteq conv(\{w_0\} \cup H)$. Therefore,

$\chi\big(\mathcal{M}(\vartheta)\big) \le \chi\big(\bar{C}(\vartheta)\big) \le \chi\big(H(\vartheta)\big) = \chi\{y_n(\vartheta): n \ge 1\}, \vartheta \in T.$

In the same manner as in the fourth step of the proof of Theorem 1, we can demonstrate that

$\chi\{y_n(\vartheta): n \ge 1\} \le \chi_{\mathcal{H}}(Z)2\,\overline{M_\vartheta}\eta\big||\beta|\big|_{L^p(T,\mathbb{R}^+)}[1 + \aleph^2\overline{M_\vartheta}\frac{\varpi^\gamma}{\gamma}],$

Thus, by (35), $\chi_{PC}(\mathcal{M}) = 0$.

Step 4. $\mathcal{R}$ maps compact sets into relatively compact sets.

This can be proven by following the same arguments as in Step 5 of the proof of Theorem 1.

Finally, by applying Lemma 2, the proof is complete.

Corollary 1. If we replaced $(H\mathcal{F}_2)^*$ with:

$(H\mathcal{F}_2)^{**}$ There is a $\varphi \in L^p(T,\mathbb{R}^+)$ such that for any $w \in E$ $\big||\mathcal{F}(\vartheta,w)|\big| \le \varphi(\vartheta),\ a.e.\,\vartheta \in T.$

then, the condition (36) becomes

(46) $$M_1(a+\sigma) + M_2\frac{\varpi^\gamma}{\gamma}\aleph^2[a + M_1(a+\sigma)] < 1.$$

Proof. Let $r > 0$ and suppose it satisfies

(47) $$\frac{\xi}{1-M_1(a+\sigma)+M_2\frac{\varpi^\gamma}{\gamma}\aleph^2[a+M_1(a+\sigma)]} < r,$$

where

$$\xi = M_1\big(\big|\Psi(0)\big| + d\big) + M_2\eta||\varphi||_{L^p(T,\mathbb{R}^+)}$$
(48) $$+ M_2\frac{\varpi^\gamma}{\gamma}\aleph^2[\big||w_1|\big| + d + M_1\big(\big|\Psi(0)\big| + d\big) + M_2\eta\big||\varphi|\big|_{L^p(T,\mathbb{R}^+)}].$$

We just need to check $\mathcal{R}(B_0) \subseteq B_0$, where $B_0 = \{w \in \mathcal{H}: ||w|| \le r\}$. Let $w \in B_0$ and $y \in R(w)$. Then, there is $\xi \in \tau^p_{\mathcal{F}(.,w(.))}$ such that $\mathcal{Y}$ satisfies (38). As in Step 1 of the proof of Theorem 2, we obtain the estimate:

$$\big||y(\vartheta)|\big| \le M_1\big(\big|\Psi(0)\big| + ar + d + \sigma r\big) + M_2\big||\varphi|\big|_{L^p(T,\mathbb{R}^+)}\eta$$
$$+ M_2\frac{\varpi^\gamma}{\gamma}\varsigma$$
$$= M_1\big(\big|\Psi(0)\big| + ar + d + \sigma r\big) + M_2\big||\varphi|\big|_{L^p(T,\mathbb{R}^+)}\eta$$
$$+M_2\frac{\varpi^\gamma}{\gamma}\aleph^2[\big||w_1|\big| + ar + d + M_1\big(\big|\Psi(0)\big| + ar + d\big)$$
$$+ M_1 r\sigma + M_2\eta\big||\varphi|\big|_{L^p(T,\mathbb{R}^+)}].$$
$$= M_1\big(\big|\Psi(0)\big| + d\big) + M_2\big||\varphi|\big|_{L^p(T,\mathbb{R}^+)}\eta$$
$$+M_2\frac{\varpi^\gamma}{\gamma}\aleph^2[\big||w_1|\big| + d + M_1\big(\big|\Psi(0)\big| + d\big) + M_2\eta\big||\varphi|\big|_{L^p(T,\mathbb{R}^+)}].$$
(49) $$+r\left[M_1(a+\sigma) + M_2\frac{\varpi^\gamma}{\gamma}\aleph^2\big(a + M_1(a+\sigma)\big)\right];\ \vartheta \in T.$$

It follows from (46)–(49) that $\mathcal{R}(\varpi_0) \subseteq B_0$.

Remark 1. The controllability of (2) can be achieved by adopting the assumptions and arguments used in Theorem 1. The same applies to the controllability of (1).

Example

Assume that $\varrho: (-\infty, 0] \to (-\infty, 0]$ is a continuous function with $L = \int_{-\infty}^0 \varrho(\tau)d\tau < \infty$, and let B_ϱ be the vector space of all functions

$w:(-\infty,0]\to E$ which is bounded and measurable on $[-r,0]$ for each $r>0$, and satisfy $\int_{-\infty}^{0}\varrho(\tau)\sup_{\vartheta\in[\tau,0]}||w(\vartheta)||\,d\tau<\infty$. It is known that, B_ϱ is a phase space that fulfils all assumptions of Definition 1, with the norm given by $||w||_{B_\varrho}=\int_{-\infty}^{0}\varrho(\tau)\sup_{\vartheta\in[\tau,0]}||w(\vartheta)||\,d\tau$ (Karthikeyan *et al.*, 2021).

Let $\Omega=\{\tau=(\tau_1,\tau_2):\tau_1^2+\tau_2^2\le 1\}$, and $E=w=L^2(\Omega)$. Define an operator $A:D(A)\subseteq E\to E$ by

$$A(u):=\Delta u-u, \tag{50}$$

with $D(A)=H^2(\Omega)\cap H_0^1(\Omega)$. It is known that (Ren *et al.*, 2019) A is a sectorial operator. Let $T=[0,1], m=2, 0=\vartheta_0<\vartheta_1=\frac{1}{3}<\vartheta_2=\frac{2}{3}<\vartheta_3=1, Z$ be a non-empty, compact and convex subset of $E, \upsilon=sup_{z\in Z}||z||$. Consider $\mathcal{F}:T\times B_\varrho\longrightarrow P_{ck}(E)$ defined by:

$$\mathcal{F}(\delta,\psi)=\{z\in E: z(\tau)=\frac{e^{-r\vartheta}\sqrt{\tau_1^2+\tau_2^2}||\psi||}{\delta\left(1+||\psi||\right)}Z,\tau=(\tau_1,\tau_2)\}, \tag{51}$$

where $r>1$ then,

$$\begin{aligned}||\mathcal{F}(\delta,\psi)||&=\sup_{z\in\mathcal{F}(\delta,\psi)}||z||_E=\sup_{z\in\mathcal{F}(\vartheta,\psi)}[\int_\Omega||z(\tau)||^2\,d\tau]^{\frac{1}{2}}\\&=\frac{e^{-r\vartheta}||\psi||}{(1+||\psi||)}[\int_\Omega(\tau_1^2+\tau_2^2)\,d\tau]^{\frac{1}{2}}\\&\le e^{-r\vartheta}||\psi||<e^{-r\vartheta}(||\psi||+1).\end{aligned} \tag{52}$$

In addition, let $\vartheta\in T,\psi_1,\psi_2\in B_\varrho$ and $z_1\in\mathcal{F}(\vartheta,\psi_1)$. Then,

$$z_1=\frac{e^{-r\vartheta}\sqrt{\tau_1^2+\tau_2^2}\sup_{\theta\in(-\infty,0]}||\psi_1(\theta)||w}{\upsilon},w\in Z.$$

Put $z_2=\frac{e^{-r\vartheta}\sqrt{\tau_1^2+\tau_2^2}\sup_{\theta\in(-\infty,0]}||\psi_2(\vartheta)||w}{\upsilon},w\in Z$. Obviously, $z_2\in\mathcal{F}(\vartheta,\psi_2)$ and

$$\begin{aligned}||z_1-z_2||&\le e^{-r\vartheta}[\sup_{\theta\in(-\infty,0]}||\psi_1(\theta)||\\&\quad-\sup_{\theta\in(-\infty,0]}||\psi_2(\theta)||][\int_\Omega|\tau|d\tau]^{\frac{1}{2}}\\&=e^{-r\vartheta}\sup_{\theta\in(-\infty,0]}(||\psi_1(\theta)||-||\psi_2(\theta)||)\\&\le e^{-r\vartheta}\sup_{\theta\in(-\infty,0]}||\psi_1(\theta)-\psi_2(\theta)||,\end{aligned}$$

which yields

$$\begin{aligned}&h(\mathcal{F}(\vartheta,\Phi_1),\mathcal{F}(\vartheta,\Phi_2))\\&\le e^{-r\vartheta}\sup_{\theta\in(-\infty,0]}||\psi_1(\theta)-\psi_2(\theta)||,\forall\vartheta\in\end{aligned} \tag{53}$$

$T,\Phi_1,\Phi_2\in B_\varrho$.

It follows from (52) that, for any bounded subset, Ω, of B_ϱ one has

$$\chi(\mathcal{F}(\vartheta,\Omega)\le e^{-r\vartheta}\sup_{\theta\in(-\infty,0]}\chi\{\psi(\theta):\psi\in\Omega\}.$$

Then, assumptions $(H\mathcal{F}_1),(H\mathcal{F}_2)^*$ and $(H\mathcal{F}_3)$ are satisfied. Let $g:B_\varpi\longrightarrow B$ be defined by

$$g(w)(\vartheta)=\lambda\Upsilon(w(\vartheta));\ \vartheta\in(-\infty,0],w\in B_\varpi, \tag{54}$$

where $\lambda>0$ and $\Upsilon:E\to E$ is a linear, bounded and compact operator. Notice that $||g(w)(0)||\le\lambda||\Upsilon||||w(0)||\le||\Upsilon||||w||_{B_\varpi}$. Therefore, $(Hg_1)^*$ is verified with $a=\lambda||\Upsilon||$ and $d=0$. Let $w_n\to w$ in B_ϖ. Then, $w_n(0)\longrightarrow w(0)$ in E, and hence $g(w_n)(0)\to g(w)(0)$. Moreover, if D is a bounded subset in B_ϖ, then, from the compactness of ϑ, the set $\{g(w)(0):w\in D\}$ is relatively compact in E. So, (Hg_2) and (Hg_3) are satisfied. Let $I_i:E\to E\ (i=1,2)$ be defined by

$$I_i(w)=\sigma_i\Upsilon(w), \tag{55}$$

where σ_i are positive real numbers. Next, suppose $V:L^p(T,w)\to L^p(T,E)$ is a bounded linear operator such that the operator $\Delta:L^p(T,w)\to E$ defined by

$$\Delta(z)=\int_0^\varpi\kappa_2(\varpi-\tau)(V_z)(\tau))d\tau, \tag{56}$$

has a bounded inverse $\Delta^{-1}:E\to L^p(T,w)/Ker(\Delta)$. Let $\aleph>0$ with $||\Delta^{-1}||\le\aleph$ and $||V||\le\aleph$. By choosing $r,\lambda,\vartheta,\sigma_1,\sigma_2$ such that the inequalities (35) and (36) are satisfied, we can apply Theorem 2. Therefore, the system (2) is controllable, where $A,\mathcal{F},g,I_i,V$ and Δ are given by (51) and (53)– (56).

3. Discussion and Conclusion

In recent years, there have been many contributions concerning various kinds of controllability of different types of differential equations and inclusions involving fractional derivatives. Some of these works have considered problems with finite or infinite delay, infinite delay and impulsive effects. Others have treated problems generated by semigroups of operators, sectorial operators and almost sectorial operators. However, to the best of our knowledge, the controllability of Caputo fractional differential inclusions generated by sectorial operators and in the presence of nonlocal conditions, impulses and infinite delay has not yet been treated.

In this paper, we fill this gap and prove the exact controllability of two fractional differential inclusions generated by sectorial operators in infinite-dimensional spaces and with impulses, infinite delay and nonlocal conditions.

We did not assume, similar to Alsaroria and Ghadle (2022), that the families of operators $\{\kappa_1(\vartheta):\vartheta>0\}$ and $\{\kappa_2(\vartheta):\vartheta>0\}$, which are generated by A, are compact, and this increases the importance of this work.

Our technique was based on the properties of phase spaces, fractional sectorial operators, multi-valued functions, the Hausdorff measure of noncompactness and a fixed-point theorem for multi-valued functions.

Since fractional calculus has many applications in medicine, energy and other fields of science, this work contributes to these applications.

Many directions for future work are possible. Indeed, our technique can be used to:

a. Generalise the results in Alsheekhhussain and Ibrahim (2021) and Kumar *et al.* (2022) to the case when the nonlinear term is a multi-valued function.
b. Extend the obtained results in Abbas (2020), Almarri and Elshenhab (2022), Varun *et al.* (2022) and Mohan *et al.* (2024), in the presence of impulses, nonlocal conditions and infinite delay, and when the linear term is a fractional sectorial operator and the nonlinear term is a multi-valued function.
c. Extend the work in both Almarri and Elshenhab (2022) and Karthikeyan *et al.* (2021) when the delay is infinite.
d. Study the controllability of the considered problem in Raja *et al.* (2025).

Data Availability Statement

The data that support the findings of this study are available on request from the corresponding author.

Acknowledgments

We extend our sincere appreciation to King Faisal University.

Funding

This research received no specific grant from any funding agency in the public, commercial, or not-for-profit sectors.

Conflicts of Interest

No conflicts of interest exist.

Biographies

Feryal Abdullah Al Adsani

Department of Mathematics, College of Science, King Faisal University, Al Ahsa, Saudi Arabia, 0096666505934144, faladsani@kfu.edu.sa

Al Adsani is a graduate of King Faisal University (KFU) and currently serves as an assistant professor in Saudi Arabia. In 2011, she was appointed Head of the Mawhiba Program at KFU. She also chaired the Qiyas Testing Committee affiliated with the National Center for Assessment and Evaluation at Al-Kifah Schools during 2014 and 2015. Throughout her career, she has published several research articles, held various leadership roles within the university, and actively contributed to numerous committees at the departmental, college, and university levels.

ORCID ID: 0000-0003-3549-5587

Ahmed Gamal Ibrahim

Independent Researcher, Faculty of Science, Cairo University, Cairo, Egypt, 00201019429069, agamal2000@yahoo.com

Prof. Ibrahim, an Egyptian mathematician with a Ph.D. from Cairo University, specializes in functional analysis and differential inclusions. With over 45 years of academic experience, he has authored 72 publications, supervised 15 theses, and co-authored a widely used Functional Analysis textbook. He served as a professor at KFU and visiting professor at MIU. An active reviewer for international journals, he regularly participates in global conferences. His research focuses on functional analysis, set-valued functions, and integer/fractional-order differential inclusions.

ORCID ID: 0000-0001-7416-5973

References

Abbas, M.I. (2020). On the controllability of Hilfer-Katugampola fractional differential equations. *Acta et Commentationes Universitatis Tartuensis de Mathematica*, **24**(2), 195–204. DOI: 10.12697/ACUTM.2020.24.13

Al Zubi, M.A., Afef, K. and Az-Zo'bi, E.A. (2024). Assorted spatial optical dynamics of a generalized fractional quadruple nematic liquid crystal system in non-local media. *Symmetry*, **16**(6), 778. DOI: 10.3390/sym16060778

Aladsani, F. and Ibrahim, A.G. (2024). Existence and stability of solutions for p-proportional ω-weighted κ-hilfer fractional differential inclusions in the presence of non-instantaneous impulses in banach spaces. *Fractal and Fractional*, **8**(8), 475. DOI: 10.3390/fractalfract8080475

Almarri, B. and Elshenhab, A.M. (2022). Controllability of fractional stochastic delay systems driven by the Rosenblatt process. *Fractal and Fractional*, 6(11), 664. DOI: 10.3390/fractalfract6110664

Alsarori, N. and Ghadle, K. (2022). Existence and controllability of fractional evolution inclusions with impulse and sectorial operator. *Results in Nonlinear Analysis*, **5**(3), 235–49. DOI: 10.53006/rna.1018780

Alsheekhhussain, Z. and Ibrahim, A.G. (2021). Controllability of Semilinear Multi-Valued Differential Inclusions with Non-Instantaneous Impulses of Order $\alpha \in (1, 2)$ without Compactness. *Symmetry*, **13**(4), 566. DOI: 10.3390/sym13040566

Az-Zo'bi, E.A., Afef, K., Ur Rahman, R., Akinyemi, L., Bekir, A., Ahmad, H. and Mahariq, I. (2024). Novel topological, non-topological, and more solitons of the generalized cubic p-system describing isothermal flux. *Optical and Quantum Electronics*, **56**(1), 84. DOI: 10.1007/s11082-023-05642-7

Bader, R., Kamenskiĭ, M. and Obukhovskiĭ, V. (2001). On some classes of operator inclusions with lower semicontinuous nonlinearities. *Topological Methods in Nonlinear Analysis Journal of the Juliusz Schauder Center*. **17**(1): 143–56

Baleanu, D. and Lopes, A.M. (2019). Handbook of fractional calculus with applications. *Applications in Engineering, Life and Social Sciences, Part A, Southampton: Comput Mech Publicat, 7. De Gruyter*. DOI: 10.1515/9783110571929

Bose, C.V. and Udhayakumar, R. (2023). Analysis on the controllability of Hilfer fractional neutral differential equations with almost sectorial operators and infinite delay via measure of noncompactness. *Qualitative Theory of Dynamical Systems*, **22**(1), 22. DOI: 10.1007/s12346-022-00719-2

Butt, A.I.K., Imran, M., Batool, S. and Nuwairan, M.A. (2023). Theoretical analysis of a COVID-19 CF-fractional model to optimally control the spread of pandemic. *Symmetry*, **15**(2), 380. DOI: 10.3390/sym15020380

Cardinali, T. and Rubbioni, P. (2012). Impulsive mild solutions for semilinear differential inclusions with nonlocal conditions in Banach spaces. *Nonlinear Analysis: Theory, Methods and Applications*, **75**(2), 871–9. DOI: 10.1016/j.na.2011.09.023

Chalishajar, D., Ravikumar, K., Ramkumar, K. and Anguraj, A. (2024). Null controllability of Hilfer fractional stochastic differential equations with nonlocal conditions. *Numerical Algebra, Control and Optimization*, **14**(2), 322–38. DOI: 10.3934/naco.2022029

Dineshkumar, C. and Udhayakumar, R. (2022). Results on approximate controllability of fractional stochastic Sobolev-type Volterra–Fredholm integro-differential equation of order $1< r< 2$. *Mathematical Methods in the Applied Sciences*, **45**(11), 6691–704. DOI: **1**0.1002/mma.8200

Dineshkumar, C., Udhayakumar, R., Vijayakumar, V., Nisar, K.S. and Shukla, A. (2022). A note concerning to approximate controllability of Atangana-Baleanu fractional neutral stochastic systems with infinite delay. *Chaos, Solitons and Fractals*, **157**(n/a), 111916. DOI: 10.1016/j.chaos.2022.111916

Hale, J.K. and Kato, J. (1978). Phase spaces for retarded equations with infinite delay. *Funkcialaj Ekvacioj*, **21**(n/a), 11–41.

Hassan, T.S., Gamal Ahmed, R., El-Sayed, A.M., El-Nabulsi, R.A., Moaaz, O. and Mesmouli, M.B. (2022). Solvability of a State–Dependence Functional Integro-Differential Inclusion with Delay Nonlocal Condition. *Mathematics*, **10**(14), 2420. DOI: 10.3390/math10142420

Kamenskii, M.I., Obukhovskii, V.V. and Zecca, P. (2011). *Condensing Multivalued Maps and Semilinear Differential Inclusions in Banach Spaces* (Vol. 7). Germany: Walter de Gruyter.

Karthikeyan, K., Tamizharasan, D., Nieto, J.J. and Nisar, K.S. (2021). Controllability of second-order differential equations with state-dependent delay. *IMA Journal of Mathematical Control and Information*, **38**(4), 1072–83. DOI: 10.1093/imamci/dnab027

Kilbas, A.A., Srivastava, H.M. and Trujillo, J.J. (2006). *Theory and Applications of Fractional Differential Equations* (Vol. 204). Netherland: Elsevier.

Kumar, A., Jeet, K. and Vats, R.K. (2022). Controllability of Hilfer fractional integro-differential equations of Sobolev-type with a nonlocal condition in a Banach space. *Evolution Equations and Control Theory*, **11**(2), 605–19. DOI: 10.3934/eect.2021016

Kumar, A., Vats, R.K., Kumar, A. and Chalishajar, D.N. (2020). Numerical approach to the controllability of fractional order impulsive differential equations. *Demonstratio Mathematica*, **53**(1), 193–207. DOI: 10.1515/dema-2020-0015

Kumar, S. (2023). On approximate controllability of non-autonomous measure driven systems with non-instantaneous impulse. *Applied Mathematics and Computation*, **441**(n/a), 127695. DOI: 10.1016/j.amc.2022.127695

Mohan Raja, M., Vijayakumar, V., Udhayakumar, R. and Nisar, K.S. (2024). Results on existence and controllability results for fractional evolution inclusions of order $1< r< 2$ with Clarke's subdifferential type. *Numerical Methods for Partial Differential Equations*, **40**(1), e22691. DOI: 10.1002/num.22691

O'Regan, D. and Precup, R. (2000). Fixed point theorems for set-valued maps and existence principles for integral inclusions. *Journal of Mathematical Analysis and Applications*, **245**(2), 594–612. DOI: 10.1006/jmaa.2000.6789

Raja, M.M., Vijayakumar, V. and Veluvolu, K.C. (2025). Higher-order caputo fractional integrodifferential inclusions of Volterra–Fredholm type with impulses and infinite delay: existence results. *Journal of Applied Mathematics and Computing*, **n/a**(n/a)1–26. DOI: 10.1007/s12190-025-02412-4

Raja, M.M., Vijayakumar, V., Shukla, A., Nisar, K.S. and Baskonus, H.M. (2022). On the approximate controllability results for fractional integrodifferential systems of order 1< r< 2 with sectorial operators. *Journal of Computational and Applied Mathematics*, **415**(n/a), 114492. DOI: 10.1016/j.cam.2022.114492

Ren, L., Wang, J. and O'Regan, D. (2019). Asymptotically periodic behavior of solutions of fractional evolution equations of order 1< α< 2. *Mathematica Slovaca*, **69**(3), 599–610. DOI: 10.1515/ms-2017-0250

Salem, A. and Alharbi, K.N. (2023). Controllability for fractional evolution equations with infinite time-delay and non-local conditions in compact and noncompact cases. *Axioms*, **12**(3), 264. DOI: 10.3390/axioms12030264

Slama, A. and Boudaoui, A. (2017). Approximate controllability of fractional nonlinear neutral stochastic differential inclusion with nonlocal conditions and infinite delay. *Arabian Journal of Mathematics*, **6**(n/a), 31–54. DOI: 10.1007/s40065-017-0163-7

Sudsutad, W., Thaiprayoon, C., Kongson, J. and Sae-dan, W. (2024). A mathematical model for fractal-fractional monkeypox disease and its application to real data. *AIMS Mathematics*, **9**(4), 8516–8563. DOI: 10.3934/math.2024414

Varun Bose, C.S., Udhayakumar, R., Elshenhab, A.M., Kumar, M.S. and Ro, J.S. (2022). Discussion on the approximate controllability of Hilfer fractional neutral integro-differential inclusions via almost sectorial operators. *Fractal and Fractional*, **6**(10), 607. DOI: 10.3390/fractalfract6100607

Wang, J., Ibrahim, A.G. and Fečkan, M. (2015). Nonlocal impulsive fractional differential inclusions with fractional sectorial operators on Banach spaces. *Applied Mathematics and Computation*, **257**(n/a), 103–18. DOI: 10.1016/j.amc.2014.04.093

Wang, J., Ibrahim, G. and O'Regan, D.D. (2019). Controllability of Hilfer fractional noninstantaneous impulsive semilinear differential inclusions with nonlocal conditions. *Nonlinear Analysis: Modelling and Control*, **24**(6), 958–84. DOI: 10.15388/NA.2019.6.7

Wang, J., IbrahimA, A.G. and O'Regan, D. (2020). Finite approximate controllability of Hilfer fractional semilinear differential equations. *Miskolc Mathematical Notes*, **21**(1), 489–507. DOI: 10.18514/MMN.2020.2921

Yang, M. and Wang, Q. (2016). Approximate controllability of Riemann–Liouville fractional differential inclusions. *Applied Mathematics and Computation*, **274**(n/a), 267–81. DOI: 10.1016/j.amc.2015.11.017

Zhang, X., Chen, P., Abdelmonem, A. and Li, Y. (2019). Mild solution of stochastic partial differential equation with nonlocal conditions and noncompact semigroups. *Mathematica Slovaca*, **69**(1), 111–24. DOI: 10.1515/ms-2017-0207

إرشادات التسليم (المجلة العلمية لجامعة الملك فيصل)

Submission Guidelines (The Scientific Journal of King Faisal University)

1. General Information

- The Journal publishes in English and Arabic.
- There are no submission or publication fees.
- It takes up to 100 days from submission to publication.
- Manuscripts must be submitted to the appropriate managing editor:
  - The Managing Editor of Basic and Applied Sciences: secretary-b@kfu.edu.sa. The associate editor will check if the author has followed the Submission Instructions. If not, the manuscript will be sent back to the author. If the instructions are followed, the associate editor will create an account and send the author the username and password to log in using our online submission system (ScholarOne): https://mc04.manuscriptcentral.com/sjkfub.
  - The Managing Editor of Humanities and Management Sciences (educational manuscripts only): sjkfu-assed@kfu.edu.sa. The associate editor will check if the author has followed the Submission Instructions. If not, the manuscript will be returned to the author. If followed, the associate editor will create an account and send the author the username and password to log in using our online submission system (ScholarOne): https://mc04.manuscriptcentral.com/sjkfuh.
  - The Managing Editor of Humanities and Management Sciences (non-educational manuscripts): sjkfu-hm@kfu.edu.sa. The associate editor will check if the author has followed the Submission Instructions. If not, the manuscript will be returned to the author. If followed, the associate editor will create an account and send the author the username and password to log in using our online submission system (ScholarOne): https://mc04.manuscriptcentral.com/sjkfuh.

2. Pre-Submission Guidelines

- **Content**: Authors must ensure a clearly articulated academic contribution to the field, clarity of abstracts, quality of and conformity to the stated aims and scope of the Journal and readability of their manuscripts.
- **Manuscript Word Limit**: Manuscripts must not exceed 8,000 words, considering all inclusions (e.g. references, tables, figures).
- **Abstract Word Limit**: Abstracts must not exceed 200 words.
- **Title Word Limit**: Manuscript titles must not exceed 15 words.
- **Keyword Limit**: Keywords must not exceed six words and must not be used in the manuscript title.
- **Number of Tables and Figures**: Tables, figures, abbreviations and footnotes must be kept to a minimum. Tables and figures must not exceed six, each.
- **Reference Limit**: There must be no more than 40 references unless the manuscript is a review article or equivalent.
- **Quotations**: A quotation must not exceed 50 words. Longer quotations required due to the nature of the academic field must be justified in the cover letter.
- **Appendixes**: Appendixes are not allowed. If readers would like to access appendixes, they can reach out to corresponding authors.
- **Linguistic Quality**: Manuscripts must be written at an acceptable language level.
- **Plagiarism**: The Journal maintains a strict plagiarism policy.
- **Reviewers**: Authors must suggest five reviewers, who are specialised in the field of the manuscript, are not affiliated with authors' institutions, are at least associate professors and have not worked on joint projects with authors. Reviewers' names, phone numbers, email addresses, academic field, academic rank and institutions must be provided.
- **Documents Required**: Title page (with author details) and main document (without author details):
  - **Title Page**: It must consist of the following: the manuscript title, author details, minor and major field of the topic, 80-word bio and acknowledgements (optional). Below are explanations of how the author details and bio are written.
  - **Main Manuscript**: It must be submitted in MSWord format. It must consist of the following: manuscript title, abstract, keywords, main body and references.
- **Author Details**: Author details must be included in the following order: full name, department, college, university, city and country (or the equivalent). In the absence of an employer, one may write 'Independent Researcher'. Ranks (e.g. Dr and Prof.) must not be included. A star '*' should be placed next to the corresponding author's name. Below is an example:

  Abdulrahman Essa Al Lily*
  Department of Curriculum and Teaching Methods, College of Education, King Faisal University, Al Ahsa, Saudi Arabia
- **Bio**: The bio must be in the following format: the author's name, under which is written the author's department, college, university, city, country (or equivalent), the author's contact number and email address, under which is written an 80-word description of the author. Author's names and affiliations are not part of the 80-word count. If the author has an ORCID number or personal website, this can be included at the end of the description. Below is an example:

  Abdulrahman Essa Al Lily
  Department of Curriculum and Teaching Methods, College of Education, King Faisal University, Al Ahsa, Saudi Arabia, 00966000000000, scijkfu@kfu.edu.sa
  Prof. Al Lily is an Oxford graduate, Saudi professor, a former national-centre director, editor-in-chief (Scopes) and bestselling author (Amazon). He has coined 4 theories (e.g. 'Multiple Stupidities', "Retroactivism' and 'On-the-Go Sourcing') and 3 notions ('Crowd-Authoring', 'Crowd-Reflecting' and 'Door-Knocking'). His work is translated into 7 languages (including Spanish, Filipino, Indonesian, Chinese and Italian). His interviews is in 5 languages (including, French, Spanish and German). He has published 24 ISI/Scopus-indexed articles with the globally largest publishers (Elsevier, Springer, Taylor & Francis, Wiley, SAGE, Cogent, Palgrave, Nature Research & Oxford). His work is cited by 35 countries (Including Hungary, Serbia, Russia, Peru, Korea, Colombia, Switzerland, Netherlands, Sweden, Finland and Latvia) in 6 languages (including Turkish and Lithuanian). He has worked as a consultant for such institutions as Wikipedia and the University of Hanover. He worked during the summer in New Zealand and Italy. He has participated in conferences in Singapore, Greece, Spain, US, Japan & Bulgaria.
  ORCID: 0000-0002-5116-422X.
  Website: https://abdulallily.wordpress.com/

3. Post-Reviewing Guidelines

- **Page Settings**: Page size is A4. Margins are 2.5 cm, each side. Any standard font is acceptable.
- **Headings**: There must be no more than three levels of headings. The first level of headings must be numbered: 1., 2., 3., etc. The second level of headings must be numbered: 1.1., 1.2., 1.3., etc. The third level of headings must be numbered: 1.1.1., 1.1.2., 1.1.3, etc. The headings for abstracts, bios and references must not be numbered.
- **Tables and Figures**: Captions must be above tables and figures. In the body, 'see above' or 'see below' must not be used. Instead, use 'see Table 1' or 'see Figure 1'.
- **Measuring Units**: In the case of using local measuring units in the manuscript, the equivalent of international units must be included. Scientific rather than provincial terms must be used. Currencies must be in U.S. dollars.
- **Footnotes**: Footnotes must be kept to a minimum. They must be referred to in the text in uppercase numbers. Footnotes must appear at the bottom of the page on which they are introduced.
- **References**: Authors must follow the APA style of referencing. References must be arranged alphabetically. The reference list must not be numbered. Non-English references must be "romanised" into English.
- **Digital Object Identifier (DOI)**: If a reference has a DOI, it must be included.

Proofreading Certificates: Once accepted, manuscripts must be sent by authors to an accredited proofreading company. A proofreading certificate must be submitted to the Journal. A suggested company is: proofreadmyessay.co.uk

1. معلومات عامة

- **أخلاقيات البحث**: لا تقبل المجلة استلام أي ورقة أو تحكيم يتضمن أي نوع من أنواع التحامل أو العدوانية أو التطرف أو التشدق الأيديولوجي (سواء كان ذلك موجها لشخص، أو مدرسة فكرية، أو طائفة، أو جنس، أو أيديولوجية بعينها). كما لا تقبل استلام الأبحاث أو تقييمات المحكمين التي تحمل أفكاراً تناهض الأمن الفكري والمجتمعي، أو تُعزز الإرهاب والأفكار المتطرفة، أو تحضّ عليها تصريحاً أو تلميحاً.
- **أوقات العمل**: تقوم المجلة بمهمة استلام الأوراق العلمية على مدار العام، وفي حالة وجود توقف سيتم وضع رد تلقائي على البريد الإلكتروني.
- **رسوم النشر**: المجلة لا تتقاضى أي أجر أو رسوم مالية مقابل عملية النشر العلمي وإجراءاته (النشر مجانًا لجميع الباحثين).
- **لغة النشر**: تقبل المجلة أبحاثاً مكتوبة باللغة العربية أو اللغة الإنجليزية.
- **مدة النشر**: بعد انضمام المجلة إلى المعرف الرقمي العالمي الموحد (DOI) أصبح بإمكان أي بحث جديد مرسل للمجلة أن ينشر على الموقع الإلكتروني للمجلة برقم المعرف الرقمي (DOI) في غضون فترة لا تزيد عن 100 يوم عمل منذ تسليمه للمجلة وأعطائه رقم قيد.
- **آلية تسليم الورقة**: يجب تسليم الورقة للمحرر المناسب، وفقاً للآتي:
  - تسلم أوراق العلوم الأساسية والتطبيقية إلى سعادة محرر فرع العلوم الأساسية والتطبيقية: secretary-b@kfu.edu.sa. سيقوم المحرر بتدقيق الورقة للتأكد من اتباعها لـ "تعليمات النشر". في حال عدم اتباع التعليمات، فستعاد الورقة للمؤلف. في حال اتباع التعليمات، فسيقوم المحرر بإنشاء حساب للمؤلف وتزويده باسم المستخدم وكلمة السر لتسليم ورقته من خلال نظام التسليم الإلكتروني (ScholarOne): https://mc04.manuscriptcentral.com/sjkfub.
  - تسلم أوراق العلوم الإنسانية والإدارية (الأبحاث التربوية فقط) إلى سعادة محرر فرع العلوم الإنسانية والإدارية للقضايا التربوية: sjkfu-assed@kfu.edu.sa. سيقوم المحرر بتدقيق الورقة للتأكد من اتباعها لـ "تعليمات النشر". في حال عدم اتباع التعليمات، فستعاد الورقة للمؤلف. في حال اتباع التعليمات، فسيقوم المحرر بإنشاء حساب للمؤلف وتزويده باسم المستخدم وكلمة السر لتسليم ورقته من خلال نظام التسليم الإلكتروني (ScholarOne): https://mc04.manuscriptcentral.com/sjkfuh.
  - تسلم أوراق العلوم الإنسانية والإدارية (الأبحاث غير التربوية) إلى سعادة محرر فرع العلوم الإنسانية والإدارية للقضايا غير التربوية: sjkfu-hm@kfu.edu.sa. سيقوم المحرر بتدقيق الورقة للتأكد من اتباعها لـ "تعليمات النشر". في حال عدم اتباع التعليمات، فستعاد الورقة للمؤلف. في حال اتباع التعليمات، فسيقوم المحرر بإنشاء حساب للمؤلف وتزويده باسم المستخدم وكلمة السر لتسليم ورقته من خلال نظام التسليم الإلكتروني (ScholarOne): https://mc04.manuscriptcentral.com/sjkfuh.
- **الرسائل العلمية**: تقبل المجلة الأوراق المستلة من الرسائل العلمية، على أن يتم النص على ذلك.
- **الحقوق الفكرية**: جميع حقوق الطبع والنشر محفوظة للمجلة، ولا يسمح بإعادة طبع أو نشر أي جزء من المجلة أو نسخه بأي شكل وبأي وسيلة كانت إلكترونية أو آلية بما في ذلك التصوير والتسجيل والإدخال في أي نظام حفظ معلومات أو استعادتها دون الحصول على موافقة كتابية من رئيس هيئة التحرير.
- **آراء المؤلفين**: الآراء المضمنة في الأوراق المنشورة تعبر عن وجهات نظر كتابها ولا تعبر بالضرورة عن وجهة نظر المجلة.
- **فلسفة الأوراق العلمية**: لا تستقبل المجلة الأوراق العلمية التي لا تراعي المحاور الآتية ولا تحقق مدى عاليا في كل محور:
  - مدى احتمالية اقتباس الورقة من قبل بحوث أخرى في كلاريفيت وسكوبس خلال عامين قادمين؛ حيث إن هذا يعد أحد المتطلبات المهمة لتصنيف المجلة في قاعدة بيانات سكوبس.
  - مدى فائدة الورقة للقارئ الدولي ومدى اتساع جمهور الورقة خارج نطاق المكان والزمان واللغة. يُعرف القارئ الدولي هنا بأنه "شخصية اعتبارية محايدة (سواء شخص، مجموعة، جهة، مؤسسة أو مُنظمة) لا تشترك مع المؤلف في الحدود الزمانية والمكانية واللغوية التي كُتبت بها الورقة".
- **ضرورة اتباع الإرشادات**: وفقاً لسياسة المجلة، فإنه يتوجب على أصحاب السعادة الباحثين ضبط ورقتهم وفقاً لملف "إرشادات التسليم"، واتباعها حرفياً وبدقة متناهية وعالية جداً، حيث إن عدم الالتزام بها بأي وجه من الأوجه سيمثل عائقاً لنشر الورقة. نؤكد الضرورة القصوى للاتباع الحرفي والدقيق لهذه الإرشادات. إن المجلة تسعى جاهدة أن تكون مصنفة في عدد من قواعد البيانات المتميزة عالمياً مما يتطلب دقة عالية في ضبط الورقة، وعليه وجب توخي الحذر التام في كيفية ضبط الورقة وفقاً للمطلوب، حيث إن آلية صياغة المراجع، على سبيل المثال، هي العنصر الأهم لقواعد البيانات العالمية. في حالة قيام المؤلف بإرسال الورقة إلى المجلة، وتبين لهيئة التحرير وجود بعض الإرشادات لم يتم اتباعها، فإنه سيتم إرجاع الورقة للمؤلف، وسيتم إخباره بعدم اتباعه للإرشادات، بدون تحديد أي من الإرشادات لم يتم اتباعها، وذلك لأن الوقت للأسف لا يتسع للمجلة لأن تزود كل مؤلف بتغذية فردية عن أي من الإرشادات لم يتم مراعاتها، كما أنه بناء على سياسة المجلة فإن السادة الباحثين هم المعنيون بالدرجة الأولى من التأكد من اتباع كافة الإرشادات. ولذلك ننصح سعادة المؤلف الرئيس، بعد الانتهاء من ضبط الورقة، بأن يقوم بإرسال الورقة للمؤلفين الآخرين (وأيضاً لزميل من غير المؤلفين) للتأكد من أن جميع الإرشادات قد اتبعت. كما ننصح أصحاب السعادة المؤلفين أن يقوموا أيضاً بالاستعانة بطرق واستراتيجيات أخرى يرون أنها قد تساعدهم في التأكد من اتباع كافة الإرشادات؛ فعلى سبيل المثال، القيام بطباعة ملف "إرشادات التسليم"، ثم وضع علامة "صح" بجانب كل فقرة من الإرشادات للتأكد من تغطية جميع الإرشادات. تؤكد المجلة لأصحاب السعادة المؤلفين أنها من خلال خطتها الاستراتيجية الحالية تسعى لأن تكون منار التميز في العالم العربي (بجميع ما يتطلبه التميز من عمل شاق ودقة)، وهذا قد يزيد العبء على المجلة والمؤلف والمحكمين وجميع "أصحاب الشأن" على حد سواء. سيمنح المؤلف فرصين كحد أعلى لاتباع التعليمات، وفي حالة عدم قيامه بذلك، فإن هيئة التحرير ستقوم بطي قيد البحث، حتى وإن أوصى المحكمين بقبول البحث. اتباع التعليمات تحمل نفس الماهية التي تحملها القيمة العلمية للورقة.
- **متعارضات**: في حالة تضارب توصيات المحكمين مع إرشادات النشر، فيتم استبعاد توصيات المحكمين وتعتمد إرشادات النشر، مع ضرورة إعلام المحرر بهذا التضارب.

2. شروط لا يتم استلام الورقة دونها

- **المستندات المطلوبة**: يجب تسليم ملفين على صيغة الوورد (DOC)، وهما كالتالي:
  - الملف الأول تحت مسمى "بيانات الباحث" (Title Page): يجب ترتيب هذا الملف كالتالي:
    - عنوان الورقة بالعربي (غير مطلوب إذا كانت الورقة باللغة الإنجليزية).
    - بيانات المؤلف بالعربي (على أن يتضمن اسم المؤلف، اسم القسم، اسم الكلية، اسم الجامعة، اسم المدينة، واسم الدولة، البريد الإلكتروني، رقم الواتساب). في حالة عدم وجود قسم أو كلية أو جامعة، يكتب ما يعادلها. في حالة عدم الانتساب لجامعة، يكتب "باحث مستقل" (غير مطلوب إذا كانت الورقة باللغة الإنجليزية).
    - عنوان الورقة بالإنجليزي.
    - بيانات المؤلف بالإنجليزي (على أن يتضمن اسم المؤلف، اسم القسم، اسم الكلية، اسم الجامعة، اسم المدينة، واسم الدولة، البريد الإلكتروني، رقم الواتساب). في حالة عدم الانتساب لجامعة، يكتب "Independent Researcher".
    - تحديد تخصص الورقة: 1) التخصص العام، 2) التخصص الدقيق ، 3) التخصص الأدق من الدقيق.
    - نبذة من 80 كلمة عن كل مؤلف. أدناه توضيح عن كيفية كتابة النبذ (إذا كانت الورقة بالعربي فتكتب النبذة بالعربي، وإذا كانت الورقة بالإنجليزي، فتكتب النبذة بالإنجليزي).
    - شكر وتقدير (اختياري).

- الملف الثاني تحت عنوان "ملف البحث" (Main Document): تتبع المجلة سياسة التحكيم المزدوج مجهول الهوية، وعليه يجب على المؤلف عدم تضمين ما يكشف هويته في "ملف البحث"، حيث ان "ملف البحث" سيرسل كما هو للمحكمين. يجب ترتيب الملف كالتالي:
  - عنوان الورقة بالعربي (غير مطلوب إذا كانت الورقة باللغة الإنجليزية).
  - ملخص الورقة بالعربي (غير مطلوب إذا كانت الورقة باللغة الإنجليزية).
  - الكلمات المفتاحية بالعربي (غير مطلوب إذا كانت الورقة باللغة الإنجليزية).
  - عنوان الورقة بالإنجليزي.
  - ملخص البحث بالإنجليزي.
  - الكلمات المفتاحية بالإنجليزي.
  - مضمون البحث.
  - المراجع.

- **"نبذة عن المؤلف"**: يجب تزويد نبذة عن كل مشارك في البحث. تتضمن النبذة الاسم، ثم أدناه اسم القسم، الكلية، الجامعة، المدينة، الدولة (أو ما يوازيه)، رقم الواتساب مع فتح الخط الدولي، البريد الإلكتروني، ثم أدناه نبذة عن الباحث (من 80 كلمة لكل باحث، علماً أن اسم الباحث و مكان العمل لا يحسب من هذه الـ 80 كلمة). إذا كان لدى الباحث رقم أوركيد و/أو صفحة شخصية، فيدرج في نهاية النبذة. يجب أن تتضمن النبذة جنسية المؤلف، وأعلى درجة علمية حصل عليها (مثلاً، ماجستير، دكتوراه) واسم الجامعة التي حصل منها على هذه الدرجة. يمكن للمؤلف الكتابة في النبذة عن نشاطه البحثي واهتماماته البحثية ومدى التأثير الوطني والعالمي الذي حققه ومدى قدرته على التواصل خارج نطاق مكان عمله وشيء من نشاطه في المؤتمرات والدورات التدريبية. النبذة هي وسيلة مهمة يستطيع الباحث من خلالها التعريف بنفسه وتسويق ذاته؛ فينبغي أن تحظى باهتمام عال من قبل المؤلف. ترتب النبذ وفقاً لترتيب المؤلفين. أدناه مثال على ذلك:

  عبدالرحمن عيسى الليلي
  قسم المناهج وطرق التدريس، كلية التربية، جامعة الملك فيصل، الأحساء، المملكة العربية السعودية، 00966000000000، scijkfu@kfu.edu.sa
  أ.د. الليلي دكتوراه (أكسفورد)، سعودي، أستاذ دكتور، مدير مركز وطني، رئيس هيئة تحرير (سكوبس)، أعماله في 7 لغات (منها، إسباني، فلبيني، إندونيسي، صيني، إيطالي)، مقابلاته في 5 لغات (منها، فرنسي، إسباني، ألماني)، مؤسس 4 نظريات (منها، "Multiple Stupidities" و"Retroactivism" و"On-the-Go Sourcing") و 3 منهجيات ("Crowd-Authoring" و"Crowd-Reflecting" و"Door-Knocking")، أكثر مبيعاً (أمازون)، نشر مع أكبر دور نشر (Nature Research, Cogent, Palgrave, Elsevier, Springer, Taylor & Francis, Wiley, Sage, Oxford)، نشر 24 ورقة في ISI و/أو سكوبس، أبحاثه مقتبسة من قبل 35 دولة (منها المجر، صربيا، روسيا، بيرو، كوريا، كولومبيا، سويسرا، هولندا، السويد، فنلندا، لاتفيا) في 6 لغات (منها، التركية و الليتوانية)، عمل خلال الصيف في نيوزلندا وايطاليا. شارك بأوراق في مؤتمرات سنغافورة، اليونان، اليابان، بلغاريا وغيرها. عمل مستشاراً لمؤسسات منها الويكيبيديا و جامعة هانوفر.
  رقم الأوركيد (ORCID): 0000-0002-5116-422x
  الموقع الشخصي: https://abdulrahmanallily.wordpress.com

- **عدد كلمات الورقة**: ألا يتجاوز عدد كلمات الورقة 8000 كلمة في أي حال من الأحوال (شاملة كل شيء، بما في ذلك المراجع والجداول والأشكال والملخص وبيانات المؤلفين والهوامش والرومنة وكل شيء).
- **الملخص**: ألا يزيد الملخص عن 200 كلمة. لا يسمح بإدراج مراجع أو اقتباسات في الملخص.
- **عدد كلمات العنوان**: ألا يزيد عنوان الورقة عن 15 كلمة.
- **عدد الكلمات المفتاحية**: أن تحتوي الورقة على ست كلمات مفتاحية باللغة العربية وترجمتها بالإنجليزية، ويجب ألا يكون قد سبق ذكرها في العنوان، كما يجب ألا تزيد كل كلمة مفتاحية عن كلمتين.
- **عدد الجداول والرسومات**: ينبغي تقليص عدد الجداول والرسومات والاختصارات والحواشي السفلية، قدر المستطاع. يجب ألا تتضمن الورقة أكثر من (6) جداول و (6) صور/أشكال. علماً أن عدم وجود أشكال بالورقة لا يعني أن عدد الجداول يمكن أن يزيد عن (6)، وعدم وجود جداول بالورقة لا يعني أن عدد الأشكال يمكن أن يزيد عن (6). يجب ألا يزيد عدد السطور عن 20 وعدد الأعمدة عن 7 في كل جدول من الجداول.
- **الجودة اللغوية**: يجب أن يكون البحث مكتوبًا بمستوى لغوي صحيح مقبول. كما يجب على المؤلف الضغط على أيقونة "المراجعة اللغوية" في ملف الوورد للتأكد من عدم وجود أخطاء لغوية.
- **عدد المراجع**: يجب ألا يزيد عدد المراجع عن 40 مرجعًا (إلا في حالة كون الورقة "مراجعة أدبية").
- **الاقتباس**: يجب أن تكون نسبة الاقتباس غير المشروع 0%.
  - يسري ذلك على نوعي الاقتباس: الاقتباس الذاتي و الاقتباس من الآخرين. ويقصد بالاقتباس الذاتي أن ينقل الباحث من عمل آخر له قام بنشره من قبل دون أن يشير إلى النقل.
  - يستثنى من الاقتباس غير المشروع تلك العبارات والجمل المتداولة التي لا تُمثل انتهاكا لحقوق الآخرين، ولا تطعن في الأصالة العلمية؛ مثل عبارة:
    والجدول يُوضح معاملات متغيرات الدراسة التي وضعت في قائمة الاستقصاء التي اعتمد عليها الباحث في تجميع البيانات الأولية.
  - في حالة الاقتباس الحرفي ولجعل الاقتباس مشروعاً، فيجب ألا يزيد عن 30 كلمة، وتوضع في علامة تنصيص، ويذكر اسم المرجع ورقم الصفحة. مثال على ذلك:
    ويجدر الإشارة إلى أنه "يعد التعليم عن بعد في زمن الكورونا مختلفاً بشكل أساسي وجوهري عن "التعليم عن بعد" التقليدي من عدة أوجه، أولها كونه مفاجئا وغير مخطط له مسبقاً" (العلي، 2020: 15).
  - غير مسموح بالاقتباس الحرفي إلا في حالة الضرورة القصوى والمبررة؛ حيث مفترض من المؤلف أن يعيد صياغة أي اقتباس بأسلوبه الشخصي.
  - في حالة كون أن طبيعة التخصص تتطلب اقتباسات مطولة، فيجب تبرير ذلك في الخطاب الموجه للمجلة أثناء التسليم.
- **العبارات غير الأكاديمية**: يجب أن تكون اللغة المكتوب بها الورقة لغة علمية أكاديمية مباشرة تبتعد عن الإسهاب الذي لا علاقة له بالورقة من الناحية العلمية، وأيضا تبتعد عن تكرار الجمل والمعاني المعلومة بالضرورة؛ ومن الأمثلة على ذلك ما يرد في مقدمة البحث وخاتمته لدى بعض الباحثين: (فإن أكن أصبت فمن الله وحده وله المنة على ذلك، وإن تكن الثانية فمن نفسي ومن الشيطان، والله الهادي إلى سواء السبيل..)، (أحمد الله أن أعانني ويسر لي إتمام هذا البحث بعدما لاقيت فيه من عناء وجهد طيلة شهور متتابعة، فإن أصبت فإمساك بمعروف، وإن تكن الأخرى فتسريح بإحسان..)، (حفظه الله ورعاه وسدد على طريق الخير خطاه..)، (رحمه الله وطيب ثراه..)، ونحو ذلك، ويستثنى من ذلك ما يتعلق بالأنبياء والمرسلين: (صلى الله عليه وسلم)، (عليه السلام).
- **المرفقات/الملاحق**: ألا تتضمن الورقة مرفقات، وفي حال ضرورة المرفقات فإنها توضع في المتن، أو يتم وضع رابط للمرفقات على الإنترنت (يتم تزويد الملحقات فقط في حالة طلب المحكمين لها).

3. إجراءات يطلب من المؤلف عملها فقط بعد صدور قرار المحكمين

- **مقاس الصفحة**: يكون مقاس الصفحة A4، على عمود واحد، الهوامش 2.5 سم من جميع الجهات، ويكون نوع الخط من الخطوط الدارج استخدامها، ويكون حجم الخط مقبولا.
- **جودة اللغة**: يجب التأكد من الخلو التام من وجود أي ملاحظات لغوية.
- **العناوين**:
  - لا يزيد عدد مستويات العناوين عن ثلاثة. أي يسمح فقط بعناوين أساسية، وفرعية وفرعية فرعية فقط. أي كون هناك عناوين فرعية فرعية فرعية غير مسموح لتجاوزها ثلاثة مستويات. الأساسية والفرعية. يجب ترقيمها كالتالي: 1.، 2.، 3.، وتحت 1. يكون 1.1.، 1.2.، 1.3.، وتحت 1.1. يكون 1.1.1.، 1.1.2.، 1.1.3.، وهكذا. يجب ألا يتم ترقيم عنوان الملخص، والنبذة عن المؤلف والمراجع.

- المجلة لا تستقبل عناوين الأبحاث التي تدور حول فرد بعينه أو قصيدة بعينها أو كتاب بعينه؛ مثل: "المفارقة الشعرية في شعر أبي الحسن القيرواني"، "حجيّة المنجز الكلامي في مقدّمة دلائل الإعجاز لعبد القاهر الجرجاني"، "هرمية المصطلح البلاغي والنقدي عند الجاحظ"، "النسق البنيوي في قصيدة أبي ذؤيب الهذلي في رثاء أولاده الخمسة".
- نظراً لكون المجلة العلمية لجامعة الملك فيصل مجلة متعددة التخصصات تندرج ضمن المنصات العالمية للبحث العلمي فإن هذا يتطلب من الباحثين كتابة عنوان الورقة وملخصها باللغة العلمية المباشرة بصياغة سهلة بعيدة عن التعقيد مما ييسر لكل قارئ في مختلف التخصصات فهم مضمون الورقة وعنوانها وملخصها.
- لا تنشر المجلة الأوراق التي تتحدد بذكر مدينة أو محافظة بعينها في العنوان البحثي (يمكن الاكتفاء بذكر اسم الدولة فقط إذا لزم الأمر)، وذلك لأن تخصيص اسم مدينة بعينها يحدد من نسبة الاستشهادات للورقة بعد نشرها، لأنه غالباً ما تكون هذه المدينة غير معلومة أو غير ذات اهتمام من القراء، وهذا يتعارض مع سياسة المجلة في استقطاب الأوراق ذات العمومية والانتشار الواسع. وإذا أراد الباحث أن يخصص محافظة أو مدينة ما، فيمكنه الإشارة لذلك في ملخص الورقة وحدودها المكانية وليس في العنوان.

- **التواريخ والأرقام**: يجب أن تكون جميع تواريخ الورقة بالميلادي وبأرقام إنجليزية (سواء في المتن أو المراجع).
- **الجداول**: يتم كتابة رقم وعنوان الشكل أو الجدول أعلاه. في المتن، يتم الإشارة إلى الجدول أو الشكل دائماً برقمه سواءً قبل أو بعد وضعه، وترقم الجداول تسلسليا حسب تسلسل ذكرها في المتن.
- **العملات**: يجب كتابة القيمة بالدولار بين قوسين، بعد أي قيمة مذكورة بالريال السعودي أو أي عملة أخرى.
- **الاختصارات**: عند استخدام رموز لاختصار مصطلح، فيجب أن يذكر نص المصطلح كاملا في أول مرة يرد فيها في نص البحث. علما أن المسموح به ثلاث اختصارات على الأكثر.
- **المقاييس الرياضية**: يجب استخدام الاختصارات المقننة دوليا بدلا من كتابة الكلمة كاملة مثل سم، ملم، كلم و% (لكل من سنتمتر، مليمتر، كيلومتر والنسبة المئوية، على الترتيب). يفضل استخدام المقاييس المترية وفي حالة استخدام وحدات أخرى يكتب المعادل المتري لها بين أقواس مربعة. في حالة ذكر وحدات قياس أو أسماء درجة إقليميا للكائنات الحية في المتن يذكر عقبها مباشرة المقابل لها بالوحدات القياسية أو الاسم اللاتيني للكائن. يجب أن تكون جميع العملات بالدولار الأمريكي.
- **الحواشي**: يفضل تقليص الحواشي، ولكن في حالة الحاجة لها، فيشار إلى الحاشية في المتن بأرقام بين قوسين مرتفعة عن السطر، ترقم الحواشي داخل المتن وتكتب حواشي كل صفحة أسفلها مفصولة عن المتن بخط ولا تجمع في نهاية المتن. يعاد ترقيم الحواشي ابتداءً من الرقم 1 مع بداية كل صفحة جديدة.
- **الهوامش السفلية**: تأخذ المراجع المدرجة في الحواشي السفلية ترقيماً متسلسلاً لكل صفحة بحيث يوضع رقم الحاشية بين قوسين علويين ()، وتكون جميع العناصر الببليوجرافية لكل مرجع مرتبة وفقا للترتيب المذكور في قائمة المراجع، سواء ذكرت البيانات كاملة أو مختصرة، كما يجب التأكد من أن جميع المراجع الواردة في المتن والحواشي مذكورة في قائمة المراجع، كما يجب ألا تكون هنالك مراجع بالقائمة لم يشر إليها في المتن.
- **روابط المراجع**:
  - **للمراجع العربية**: في حالة الرغبة في إدراج رابط لمرجع عربي، فيكتب بعد المرجع "متوفر بموقع:" ثم يدرج الرابط، وبعد الرابط يفتح قوس ويكتب "تاريخ الاسترجاع:" ثم يدرج التاريخ على هذه الصيغة "2020/07/27"، ثم يغلق القوس.
  - **للمراجع الإنجليزية**: في حالة الرغبة في إدراج رابط لمرجع إنجليزي، فيكتب بعد المرجع "Available at:" ثم يدرج الرابط، وبعد الرابط يفتح قوس ويكتب "accessed on" ثم يدرج التاريخ على هذه الصيغة "2020/07/27"، ثم يغلق القوس.
- **ترتيب قائمة المراجع**: يجب ترتيب المراجع هجائياً. ويجب عدم ترقيم قائمة المراجع.
- **مرجعان لمؤلف في سنة واحدة**: في حالة وجود مرجعين لمؤلف واحد في سنة واحدة، فللتمييز بينهما يكتب حرف بجانب التاريخ كالآتي: (2020أ)، (2020ب)، وبالإنجليزي (2020a)، (2020b)
- **DOI للمرجع**: عند استعمال مراجع لها رقم DOI، يجب ذكر هذا الرقم.
- **المراجع داخل المتن**: بخصوص آلية كتابة المراجع داخل المتن:
  - إذا كان المرجع في بداية الجملة، يكتب اسم عائلة الباحث/الباحثين يليها تاريخ النشر بين قوسين. مثال: "ذكر الصالح والأحمد (2020) بأن..."
  - إذا كان المرجع في نهاية الجملة، فيكتب بين قوسين اسم عائلة الباحث/الباحثين، ثم فاصلة، ثم تاريخ النشر. مثال: "وهذا هو أساس المشكلة (الصالح والأحمد، 2020)."
  - في حالة كون المرجع لأكثر من باحثين فيكتب اسم عائلة الباحث الأول متبوعا بكلمة "وآخرون". مثال: "ذكر المحمد وآخرون (2020) بأن..." أو "وهذا ما يسمى بالتعليم المدمج (العلي وآخرون، 2020)."
  - يجب تدوين رقم الصفحة المقتبس منها داخل المتن. أدناه أمثلة على كيفية عمل هذا التدوين:
    - "وهذه من القضايا الأساسية التي ستساهم في تطور التعليم العالي" (المحمد، 2020: 15).
    - ذكر المحمد (2020: 15) أن هذه "من القضايا الأساسية التي ستساهم في تطور التعليم العالي".
    - ذكر المحمد (2020) أن هذه "من القضايا الأساسية التي ستساهم في تطور التعليم العالي" (ص. 15).
- **المراجع في قائمة المراجع**: لا يتم استخدام كلمة "وآخرون" (. et al) في قائمة المراجع.
- **صفحات الويكيبيديا**: لا يسمح باقتباس صفحات الويكيبيديا.
- **تعريف الرومنة**: يجب رومنة/ترجمة قائمة المراجع العربية. يقصد بالرومنة النقل الصوتي للحروف إلى الإنجليزية، أي تحويل منطوق الحروف العربية إلى حروف إنجليزية. تتم الرومنة عن طريق مترجم قوقل (http://translate.google.com)، حيث إن في كتابة أي جملة في مترجم قوقل (مثلاً: " إنجازات جامعة الملك فيصل منذ تأسيسها")، فستكون رومنة هذه الجملة متوفرة بأسفل النص " iinjazat jamieat almalik faysal mundh tasisiha"، وترجمتها متوفرة على الجنب (Achievements of King Faisal University since its foundation). رومنة المراجع العربية لا يعني حذف المراجع العربية. فالمراجع العربية والمرومنة تبقى سوياً. توضع أولاً المراجع العربية، يليها المراجع المرومنة والإنجليزية. تدمج المراجع المرومنة والإنجليزية سوياً وترتب هجائياً.
- **تعديلات هيئة التحرير على عنوان الورقة**: يحقّ لهيئة التحرير إعادة صياغة عنوان الورقة في المرحلة الأخيرة للنشر (قبل الإحالة لعدد)، وذلك وفقاً لمقتضيات التوجه التطويري العام للمجلة حالياً، والذي يتطلب الاقتصار على نشر العناوين: "الموجزة، والبسيطة، والواضحة، والعامة التي لا تشتمل على صف دراسي بعينه أو جامعة أو محافظة أو مدينة بعينها في العنوان" وبالتالي سيتم استبعاد أية كلمة غير ضرورية من العنوان لأن هذه المصطلحات تحدّ من نسبة انتشار البحث، وشموليته، وتقلل من نسبة اقتباسه واستشهاداته من قبل الباحثين.
- **شهادة مراجعة لغوية**: في حالة قبول الورقة للنشر، فإنه سيطلب من المؤلف إرسال ورقته لشركة معتمدة لمراجعة الورقة من قبل متحدثي اللغة الإنجليزية كلغة أم، وموافاة المجلة بشهادة إثبات مراجعة لغوية من قبل الشركة. إذا كانت الورقة باللغة العربية، فإن المراجعة تكون لعنوان الورقة والملخص باللغة الإنجليزية. وإذا كانت الورقة باللغة الإنجليزية، فإن المراجعة تكون على الورقة كاملة. تكون هذه المراجعة اللغوية كمرحلة أخيرة قبل نشر الورقة وبعد إدخال كامل ملاحظات المحكمين والمحررين وهيئة التحرير. أدناه إحدى هذه الشركات والتي تقوم بالمراجعة اللغوية خلال 24 ساعة:
https://proofreadmyessay.co.uk

4. آلية كتابة الدوريات والمجلات في المراجع (يطلب عملها فقط في حالة قبول الورقة للنشر)

4.1. كتابة الدوريات والمجلات العربية في قائمة المراجع

يبدأ كل مرجع باسم العائلة للمؤلف الأول، ثم فاصلة، ثم الاسم الأول واسم الأب للمؤلف الأول، ثم فاصلة، ثم اسم العائلة للمؤلف الثاني، ثم فاصلة، ثم الاسم الأول واسم الأب للمؤلف الثاني، ثم حرف العطف "و" ثم اسم العائلة للمؤلف الثالث، ثم فاصلة، ثم الاسم الأول واسم الأب للمؤلف الثالث، ثم نقطة، ثم فتح قوس، ثم التاريخ، ثم إغلاق القوس، ثم نقطة، ثم عنوان البحث، ثم نقطة، ثم اسم المجلة يكون مكتوبا بشكل مائل، ثم فاصلة، ثم رقم المجلد مكتوبا بشكل عريض، ثم فتح قوس، ثم

يكتب رقم العدد، ثم يغلق القوس، علماً أنه لا يوجد مسافة بين رقم المجلد ورقم العدد، ثم فاصلة، ثم رقم أول صفحة للبحث، ثم علامة "-" ثم رقم آخر صفحة للبحث. (مع مراعاة أن حرف العطف "و" يوضع دائما قبل المؤلف الأخير أيًّا كان عدد المؤلفين). أدناه مثال على ذلك:

الأحمد، محمد عبدالرحمن، العلي، إسماعيل صلاح والصالح، أحمد محمد. (2020). إنجازات جامعة الملك فيصل منذ تأسيسها. *المجلة العلمية لجامعة الملك فيصل: فرع العلوم الإنسانية والإدارية*، **13**(2)، 213-223.

في حالة عدم وجود تاريخ، فتكتب العبارة التالية "د.ت." في مكان التاريخ، سواء في المتن أو المرجع. على سبيل المثال:

الأحمد، محمد عبدالرحمن، العلي، إسماعيل صلاح والصالح، أحمد محمد. (د.ت.). إنجازات جامعة الملك فيصل منذ تأسيسها. *المجلة العلمية لجامعة الملك فيصل: فرع العلوم الإنسانية والإدارية*، **13**(2)، 213-223.

في حالة عدم وجود رقم مجلد، فتكتب العبارة التالية "بدون رقم مجلد" في مكان رقم المجلد. على سبيل المثال:

الأحمد، محمد عبدالرحمن، العلي، إسماعيل صلاح والصالح، أحمد محمد. (2020). إنجازات جامعة الملك فيصل منذ تأسيسها. *المجلة العلمية لجامعة الملك فيصل: فرع العلوم الإنسانية والإدارية*، **بدون رقم مجلد** (2)، 213-223.

في حالة عدم وجود رقم عدد، فتكتب العبارة التالية "بدون رقم عدد" في مكان رقم العدد. على سبيل المثال:

الأحمد، محمد عبدالرحمن، العلي، إسماعيل صلاح والصالح، أحمد محمد. (2020). إنجازات جامعة الملك فيصل منذ تأسيسها. *المجلة العلمية لجامعة الملك فيصل: فرع العلوم الإنسانية والإدارية*، **13**(بدون رقم عدد)، 213-223.

في حالة عدم وجود أرقام صفحات، فتكتب العبارة التالية "بدون أرقام صفحات" في مكان أرقام الصفحات، أو رقم مسلسل البحث في مجلات الأونلاين. على سبيل المثال:

الأحمد، محمد عبدالرحمن، العلي، إسماعيل صلاح والصالح، أحمد محمد. (2020). إنجازات جامعة الملك فيصل منذ تأسيسها. *المجلة العلمية لجامعة الملك فيصل: فرع العلوم الإنسانية والإدارية*، **13**(2)، بدون أرقام صفحات.

4.2. كتابة الدوريات والمجلات الإنجليزية في قائمة المراجع

يبدأ كل مرجع باسم العائلة للمؤلف الأول، ثم فاصلة، ثم الحرف الأول من الاسم الأول للمؤلف الأول، ثم نقطة، ثم الحرف الأول لاسم الأب للمؤلف الأول، ثم نقطة، ثم فاصلة، ثم اسم العائلة للمؤلف الثاني، ثم فاصلة، ثم الحرف الأول من الاسم الأول للمؤلف الثاني، ثم نقطة، ثم الحرف الأول لاسم الأب للمؤلف الثاني، ثم نقطة، ثم حرف العطف "and" (وليس "&") ثم اسم العائلة للمؤلف الثالث، ثم فاصلة، ثم الحرف الأول من الاسم الأول للمؤلف الثالث، ثم نقطة، ثم الحرف الأول لاسم الأب للمؤلف الثالث، ثم نقطة، ثم فتح قوس، ثم التاريخ بالميلادي، ثم إغلاق القوس، ثم نقطة، ثم عنوان البحث بحروف صغيرة (صمول small)، ثم فتح علامة تنصيص واحدة، ثم عنوان البحث مترجما بحروف صغيرة (صمول small؛ يستثنى من ذلك الكلمة الأولى وأسماء الأشخاص وأسماء الأماكن وأسماء الجنسيات واللغات والأسابيع والشهور فيبقى الحرف الأول منها بحروف كبيرة، كابتل capital)، ثم إغلاق علامة التنصيص، ثم نقطة، ثم اسم المجلة مترجما (أو مرومن) يكون مكتوبا بشكل مائل والحرف الأول من كل كلمة يكون كبيرا (كابتل capital؛ يستثنى من ذلك أدوات التنكير والتعريف مثل "a" و "an" و "the" وحروف الجر مثل "to" و "of" و "in" وأدوات الربط "and" و "but" و "or" فيبقى الحرف الأول منها بحروف صغيرة، إلا إذا كانوا في بداية اسم المجلة فيكون الحرف الأول منها بحروف كبيرة)، ثم فاصلة، ثم رقم المجلد مكتوبا بشكل عريض، ثم فتح قوس، ثم يكتب رقم العدد، ثم يغلق القوس، علماً أنه لا يوجد مسافة بين رقم المجلد ورقم العدد، ثم رقم أول صفحة للبحث، ثم علامة "-" ثم رقم آخر صفحة للبحث، ثم نقطة، ثم تكتب "[in Arabic]" أدناه مثال على رومنة المرجع العربي:

Al Ahmed, M.A., Al Ali, I.S. and Al Salah, A.M. (2020). Iinjazat jamieat almalik faysal mundh tasisiha 'Achievements of King Faisal University since its foundations'. *The Scientific Journal of King Faisal University: Humanities and Management Sciences*, **13**(2), 213-223. [in Arabic]

في حالة كون المرجع بلغة غير العربية وغير الإنجليزية، وهذه اللغة تستخدم حروف غير إنجليزية، فتتم رومنة العنوان بالطريقة نفسها التي تتم بها رومنة العناوين العربية. ولكن، في حالة كون الدورية بلغة غير العربية وغير الإنجليزية، ولكن هذه اللغة تستخدم الحروف الإنجليزية نفسها، فلا حاجة لرومنة عنوان البحث، ويكتفى بإبقاء العنوان في لغته الأصل ووضع الترجمة في علامة تنصيص. فعلى سبيل المثال، في حالة كون الدورية باللغة

Al Ahmed, K.A., Al Muhammed, S.F. and Al Saleh, A.F. (2020). The history of agriculture in Al Ahsa. *The Scientific Journal of King Faisal University: Humanities and Management Sciences*, **13**(2), 213-222.

في حالة عدم وجود تاريخ، فيكتب "n/a". على سبيل المثال:

Al Ahmed, K.A., Al Muhammed, S.F. and Al Saleh, A.F. (n/a). The history of agriculture in Al Ahsa. *The Scientific Journal of King Faisal University: Humanities and Management Sciences*, **13**(2), 213-222.

في حالة عدم وجود رقم مجلد، فيكتب "n/a". على سبيل المثال:

Al Ahmed, K.A., Al Muhammed, S.F. and Al Saleh, A.F. (2020). The history of agriculture in Al Ahsa. *The Scientific Journal of King Faisal University: Humanities and Management Sciences*, **n/a**(2), 213-222.

في حالة عدم وجود رقم عدد، فيكتب "n/a". على سبيل المثال:

Al Ahmed, K.A., Al Muhammed, S.F. and Al Saleh, A.F. (2020). The history of agriculture in Al Ahsa. *The Scientific Journal of King Faisal University: Humanities and Management Sciences*, **13**(n/a), 213-222.

في حالة عدم وجود أرقام صفحات، فيكتب "n/a". على سبيل المثال:

Al Ahmed, K.A., Al Muhammed, S.F. and Al Saleh, A.F. (2020). The history of agriculture in Al Ahsa. *The Scientific Journal of King Faisal University: Humanities and Management Sciences*, **13**(2), n/a.

4.3. رومنة/ترجمة الدوريات والمجلات غير الإنجليزية في قائمة المراجع

يبدأ كل مرجع باسم العائلة للمؤلف الأول، ثم فاصلة، ثم الحرف الأول من الاسم الأول للمؤلف الأول، ثم نقطة، ثم الحرف الأول لاسم الأب للمؤلف الأول، ثم نقطة، ثم فاصلة، ثم اسم العائلة للمؤلف الثاني، ثم فاصلة، ثم الحرف الأول من الاسم الأول للمؤلف الثاني، ثم نقطة، ثم الحرف الأول لاسم الأب للمؤلف الثاني، ثم نقطة، ثم حرف العطف "and" (وليس "&") ثم اسم العائلة للمؤلف الثالث، ثم فاصلة، ثم الحرف الأول من الاسم الأول للمؤلف الثالث، ثم نقطة، ثم الحرف الأول لاسم الأب للمؤلف الثالث، ثم نقطة، ثم فتح قوس، ثم التاريخ بالميلادي، ثم إغلاق القوس، ثم نقطة، ثم عنوان البحث (مرومن) بحروف صغيرة (صمول small)، ثم فتح علامة تنصيص واحدة، ثم عنوان البحث مترجما بحروف صغيرة (صمول small؛ يستثنى من ذلك الكلمة الأولى وأسماء الأشخاص وأسماء الأماكن وأسماء الجنسيات واللغات والأسابيع والشهور فيبقى الحرف الأول منها بحروف كبيرة، كابتل capital)، ثم إغلاق علامة التنصيص، ثم نقطة، ثم اسم المجلة مترجما (أو مرومن) يكون مكتوبا بشكل مائل والحرف الأول من كل كلمة يكون كبيرا (كابتل capital؛ يستثنى من ذلك أدوات التنكير والتعريف مثل "a" و "an" و "the" وحروف الجر مثل "to" و "of" و "in" وأدوات الربط "and" و "but" و "or" فيبقى الحرف الأول منها بحروف صغيرة، إلا إذا كانوا في بداية اسم المجلة فيكون الحرف الأول منها بحروف كبيرة)، ثم فاصلة، ثم رقم المجلد مكتوبا بشكل عريض، ثم فتح قوس، ثم يكتب رقم العدد، ثم يغلق القوس، علماً أنه لا يوجد مسافة بين رقم المجلد ورقم العدد، ثم فاصلة، ثم رقم أول صفحة للبحث، ثم علامة "-" ثم رقم آخر صفحة للبحث. أدناه مثال على ذلك:

الألمانية، فيبدأ المرجع باسم العائلة للمؤلف الأول، ثم فاصلة، ثم الحرف الأول من الاسم الأول للمؤلف الأول، ثم نقطة، ثم الحرف الأول لاسم الأب للمؤلف الأول، ثم نقطة، ثم فاصلة، ثم اسم العائلة للمؤلف الثاني، ثم فاصلة، ثم الحرف الأول من الاسم الأول للمؤلف الثاني، ثم نقطة، ثم الحرف الأول لاسم الأب للمؤلف الثاني، ثم نقطة، ثم حرف العطف "and" (وليس "&") ثم اسم العائلة للمؤلف الثالث، ثم فاصلة، ثم الحرف الأول من الاسم الأول للمؤلف الثالث، ثم نقطة، ثم الحرف الأول لاسم الأب للمؤلف الثالث، ثم نقطة، ثم فتح قوس، ثم التاريخ بالميلادي، ثم إغلاق القوس، ثم نقطة، ثم عنوان البحث باللغة الألمانية (صمول small)، ثم فتح علامة تنصيص واحدة، ثم عنوان البحث مترجما بحروف صغيرة (صمول small؛ يستثنى من ذلك الكلمة الأولى وأسماء الأشخاص وأسماء الأماكن وأسماء الجنسيات واللغات والأسابيع والشهور فيبقى الحرف الأول منها بحروف كبيرة، كابتل capital)، ثم إغلاق علامة التنصيص، ثم نقطة، ثم اسم المجلة مترجما يكون مكتوبا بشكل مائل والحرف الأول من كل كلمة يكون كبيرا (كابتل capital؛ يستثنى من ذلك أدوات التنكير والتعريف مثل "a" و "an" و "the" وحروف الجر مثل "to" و "of" و "in" وأدوات الربط "and" و "but" و "or" فيبقى الحرف الأول منها بحروف صغيرة، إلا إذا كانوا في بداية اسم المجلة فيكون الحرف الأول منها بحروف كبيرة)، ثم فاصلة، ثم رقم المجلد ورقم العدد، ثم رقم أول صفحة للبحث، ثم علامة "-" ثم رقم آخر صفحة للبحث، ثم نقطة، ثم تكتب "[in German]" أدناه مثال على ذلك:

Al Ahmed, M.A., Al Ali, I.S. and Al Salah, A.M. (2020). Erfolge der King Faisal University seit ihrer gründung 'Achievements of King Faisal University since its foundations'. *The Scientific Journal of King Faisal University: Humanities and Management Sciences*, **13**(2), 213-223. [in German]

5. آلية كتابة المؤتمرات والندوات والملتقيات في المراجع (يطلب عملها فقط في حالة قبول الورقة للنشر)

5.1. كتابة المؤتمرات والندوات والملتقيات العربية في قائمة المراجع

يبدأ كل مرجع باسم العائلة للمؤلف الأول، ثم فاصلة، ثم الاسم الأول واسم الأب للمؤلف الأول، ثم فاصلة، ثم اسم العائلة للمؤلف الثاني، ثم فاصلة، ثم الاسم الأول واسم الأب للمؤلف الثاني، ثم حرف العطف "و" ثم اسم العائلة للمؤلف الثالث، ثم فاصلة، ثم الاسم الأول واسم الأب للمؤلف الثالث، ثم نقطة، ثم فتح قوس، ثم التاريخ، ثم إغلاق القوس، ثم نقطة، ثم عنوان البحث، ثم نقطة، ثم يكتب "في:" ثم يكتب اسم المؤتمر بشكل مائل، ثم فاصلة، ثم اسم مكان انعقاد المؤتمر، ثم فاصلة، ثم اسم مدينة المؤتمر، ثم فاصلة، ثم اسم دولة المؤتمر، ثم فاصلة، ثم تاريخ انعقاد المؤتمر، ثم نقطة. (مع مراعاة أن حرف العطف "و" يوضع دائما قبل المؤلف الأخير أيًا كان عدد المؤلفين). أدناه مثال على ذلك:

الأحمد، محمد عبدالرحمن، العلي، إسماعيل صلاح والصالح، أحمد محمد. (2020). الموهبة في التعليم العالي. في: *الملتقى الوطني الأولى لمنسقي الموهوبين، جامعة الملك فيصل*، الأحساء، المملكة العربية السعودية، 2020/03/05-03.

5.2. كتابة المؤتمرات والندوات والملتقيات الإنجليزية في قائمة المراجع

يبدأ كل مرجع باسم العائلة للمؤلف الأول، ثم فاصلة، ثم الحرف الأول من الاسم الأول للمؤلف الأول، ثم نقطة، ثم الحرف الأول لاسم الأب للمؤلف الأول، ثم نقطة، ثم فاصلة، ثم اسم العائلة للمؤلف الثاني، ثم فاصلة، ثم الحرف الأول من الاسم الأول للمؤلف الثاني، ثم نقطة، ثم الحرف الأول لاسم الأب للمؤلف الثاني، ثم نقطة، ثم حرف العطف "and" (وليس "&") ثم اسم العائلة للمؤلف الثالث، ثم فاصلة، ثم الحرف الأول من الاسم الأول للمؤلف الثالث، ثم نقطة، ثم الحرف الأول لاسم الأب للمؤلف الثالث، ثم نقطة، ثم فتح قوس، ثم التاريخ بالميلادي، ثم إغلاق القوس، ثم نقطة، ثم عنوان البحث بالإنجليزية (صمول small؛ يستثنى من ذلك الكلمة الأولى وأسماء الأشخاص وأسماء الأماكن وأسماء الجنسيات واللغات والأسابيع والشهور فيبقى الحرف الأول منها بحروف كبيرة، كابتل capital)، ثم يكتب "In:"، ثم يكتب اسم المؤتمر يكون مكتوبا بشكل مائل والحرف الأول من كل كلمة يكون كبيرا (كابتل capital؛ يستثنى من ذلك أدوات التنكير والتعريف مثل "a" و "an" و "the" وحروف الجر مثل "to" و "of" و "in" وأدوات الربط "and" و "but" و "or" فيبقى الحرف الأول منها بحروف صغيرة، إلا إذا كانوا في بداية اسم المجلة فيكون الحرف الأول منها بحروف كبيرة)، ثم فاصلة، ثم اسم مكان المؤتمر، ثم فاصلة، ثم اسم مدينة المؤتمر، ثم فاصلة، ثم اسم دولة المؤتمر، ثم فاصلة، ثم تاريخ انعقاد المؤتمر، ثم نقطة. أدناه مثال على ذلك:

Al Ahmed, K.A., Al Muhammed, S.F. and Al Saleh, A.F. (2020). Giftedness and creativity. In: *The First National Symposium for the Coordinators of the Gifted*, King Faisal University, Al Ahsa, Saudi Arabia, 03-05/03/2020.

5.3. رومنة/ترجمة المؤتمرات والندوات والملتقيات غير الإنجليزية في قائمة المراجع

يبدأ كل مرجع باسم العائلة للمؤلف الأول، ثم فاصلة، ثم الحرف الأول من الاسم الأول للمؤلف الأول، ثم نقطة، ثم الحرف الأول لاسم الأب للمؤلف الأول، ثم نقطة، ثم فاصلة، ثم اسم العائلة للمؤلف الثاني، ثم فاصلة، ثم الحرف الأول من الاسم الأول للمؤلف الثاني، ثم نقطة، ثم حرف العطف "and" ثم اسم العائلة للمؤلف الثالث، ثم فاصلة، ثم الحرف الأول من الاسم الأول للمؤلف الثالث، ثم نقطة، ثم الحرف الأول لاسم الأب للمؤلف الثالث، ثم نقطة. ثم فتح قوس، ثم التاريخ بالميلادي، ثم إغلاق القوس، ثم نقطة، ثم عنوان البحث (مرومن) بحروف صغيرة (صمول small)، ثم فتح علامة تنصيص واحدة، ثم عنوان البحث مترجما بحروف صغيرة (صمول small؛ يستثنى من ذلك الكلمة الأولى وأسماء الأشخاص وأسماء الأماكن وأسماء الجنسيات واللغات والأسابيع والشهور فيبقى الحرف الأول منها بحروف كبيرة، كابتل capital)، ثم إغلاق علامة التنصيص، ثم نقطة، ثم يكتب "In:"، ثم يكتب اسم المؤتمر مترجما (أو مرومن) يكون مكتوبا بشكل مائل والحرف الأول من كل كلمة يكون كبيرا (كابتل capital؛ يستثنى من ذلك أدوات التنكير والتعريف مثل "a" و "an" و "the" وحروف الجر مثل "to" و "of" و "in" وأدوات الربط "and" و "but" و "or" فيبقى الحرف الأول منها بحروف صغيرة، إلا إذا كانوا في بداية اسم المجلة فيكون الحرف الأول منها بحروف كبيرة)، ثم فاصلة، ثم اسم مكان المؤتمر مترجما (أو مرومن)، ثم فاصلة، ثم يكتب اسم مدينة المؤتمر بالإنجليزي، ثم فاصلة، ثم اسم دولة المؤتمر بالإنجليزي، ثم فاصلة، ثم تاريخ انعقاد المؤتمر، ثم نقطة، ثم يكتب "[in Arabic]" أدناه مثال على رومنة المرجع العربي:

Al Ahmed, K.A., Al Muhammed, S.F. and Al Saleh, A.F. (2020). Al'iibdae fi altaelim aleali 'Creativity in higher education'. In: *The First National Symposium for the Coordinators of the Gifted*, King Faisal University, Al Ahsa, Saudi Arabia, 03-05/03/2020. [in Arabic]

في حالة كون المرجع بلغة غير العربية وغير الإنجليزية، وهذه اللغة تستخدم حروف غير إنجليزية، فتتم رومنة العنوان بالطريقة نفسها التي تتم بها رومنة العناوين العربية. أما في حالة كون المرجع بلغة غير العربية وغير الإنجليزية، ولكن هذه اللغة تستخدم الحروف الإنجليزية، فلا حاجة لرومنة عنوان البحث، ويكتفى بإبقاء العنوان في لغته الأصل ووضع الترجمة في علامة تنصيص. فعلى سبيل المثال، في حالة كون المرجع باللغة الفرنسية، فيبدأ المرجع باسم العائلة للمؤلف الأول، ثم فاصلة، ثم الحرف الأول من الاسم الأول للمؤلف الأول، ثم نقطة، ثم الحرف الأول لاسم الأب للمؤلف الأول، ثم نقطة، ثم فاصلة، ثم اسم العائلة للمؤلف الثاني، ثم فاصلة، ثم الحرف الأول من الاسم الأول للمؤلف الثاني، ثم نقطة، ثم الحرف الأول لاسم الأب للمؤلف الثاني، ثم نقطة، ثم حرف العطف "and" ثم اسم العائلة للمؤلف الثالث، ثم فاصلة، ثم الحرف الأول من الاسم الأول للمؤلف الثالث، ثم نقطة، ثم الحرف الأول لاسم الأب للمؤلف

الثالث، ثم نقطة. ثم فتح قوس، ثم التاريخ بالميلادي، ثم إغلاق القوس، ثم نقطة، ثم عنوان البحث باللغة الفرنسية (صمول small)، ثم فتح علامة تنصيص واحدة، ثم عنوان البحث مترجما بحروف صغيرة (صمول small؛ يستثنى من ذلك الكلمة الأولى وأسماء الأشخاص وأسماء الأماكن وأسماء الجنسيات واللغات والأسابيع والشهور فيبقى الحرف الأول منها بحروف كبيرة، كابتل capital)، ثم إغلاق علامة التنصيص، ثم نقطة، ثم يكتب "In:"، ثم يكتب اسم المؤتمر مترجما يكون مكتوبا بشكل مائل والحرف الأول من كل كلمة يكون كبيرا (كابتل capital؛ يستثنى من ذلك أدوات التنكير والتعريف مثل "a" و "an" و "the" وحروف الجر مثل "to" و "of" و "in" وأدوات الربط "and" و "but" و "or" فيبقى الحرف الأول منها بحروف صغيرة، إلا إذا كانوا في بداية اسم المجلة فيكون الحرف الأول منها بحروف كبيرة)، ثم فاصلة، ثم اسم مكان المؤتمر مترجما، ثم فاصلة، ثم يكتب اسم مدينة المؤتمر بالإنجليزي، ثم فاصلة، ثم اسم دولة المؤتمر بالإنجليزي، ثم فاصلة، ثم تاريخ انعقاد المؤتمر، ثم نقطة، ثم يكتب "[in French]". أدناه مثال على رومنة المرجع الفرنسي:

Al Ahmed, K.A., Al Muhammed, S.F. and Al Saleh, A.F. (2020). Créativité dans l'enseignement supérieur 'Creativity in higher education'. In: *The First National Symposium for the Coordinators of the Gifted*, King Faisal University, Al Ahsa, Saudi Arabia, 03-05/03/2020. [in French]

6. آلية كتابة الكتب في قائمة المراجع (يطلب عملها فقط في حالة قبول الورقة للنشر)

ملاحظات:

- إذا كانت طبعة الكتاب هي الطبعة الأولى، فلا يكتب أي شيء بخصوص رقم الطبعة.
- تصاغ مراجع التقارير والدراسات الصادرة عن وزارات ومؤسسات حكومية وغير حكومية بالطريقة نفسها التي تصاغ بها الكتب.

6.1. كتابة الكتب العربية في قائمة المراجع

يبدأ كل مرجع باسم العائلة للمؤلف الأول، ثم فاصلة، ثم الاسم الأول واسم الأب للمؤلف الأول، ثم فاصلة، ثم اسم العائلة للمؤلف الثاني، ثم فاصلة، ثم الاسم الأول واسم الأب للمؤلف الثاني، ثم حرف العطف "و" ثم اسم العائلة للمؤلف الثالث، ثم فاصلة، ثم الاسم الأول واسم الأب للمؤلف الثالث، ثم نقطة، ثم فتح قوس، ثم التاريخ، ثم إغلاق القوس، ثم نقطة، ثم عنوان الكتاب بخط مائل، ثم نقطة، ثم اسم مدينة الناشر، ثم فاصلة، ثم اسم دولة الناشر، ثم نقطتين رأسيتين، ثم اسم الناشر. (مع مراعاة أن حرف العطف "و" يوضع دائما قبل المؤلف الأخير أيًا كان عدد المؤلفين). أدناه مثال على ذلك:

الأحمد، محمد عبدالرحمن، العلي، إسماعيل صلاح والصالح، أحمد محمد. (2020). *إنجازات جامعة الملك فيصل منذ تأسيسها*. السعودية: مكتبة جرير.

في حالة وجود رقم طبعة، فيكتب التالي:

الأحمد، محمد عبدالرحمن، العلي، إسماعيل صلاح والصالح، أحمد محمد. (2020). *إنجازات جامعة الملك فيصل منذ تأسيسها*. الطبعة الثانية. الرياض، السعودية: مكتبة جرير.

في حالة كون الكتاب مترجمًا، فيكتب بعد اسم المؤلف: "ترجمة: اسم العائلة، الاسم الأول اسم الأب". أدناه مثال على ذلك:

وايت، جولي. ترجمة: الأحمد، محمد عبدالرحمن، العلي، إسماعيل صلاح والصالح، أحمد محمد. (2020). *إنجازات جامعة الملك فيصل منذ تأسيسها*. الطبعة الثانية. الرياض، السعودية: مكتبة جرير.

في حالة كون الكتاب محققاً، فيكتب بعد اسم المؤلف: "تحقيق: اسم العائلة، الاسم الأول اسم الأب". أدناه مثال على ذلك:

الخالد، محمد. تحقيق: الأحمد، محمد عبدالرحمن. (2020). *إنجازات جامعة الملك فيصل منذ تأسيسها*. الطبعة الثانية. الرياض، السعودية: مكتبة جرير.

6.2. كتابة الكتب الإنجليزية في قائمة المراجع

يبدأ كل مرجع باسم العائلة للمؤلف الأول، ثم فاصلة، ثم الحرف الأول من الاسم الأول للمؤلف الأول، ثم نقطة، ثم الحرف الأول لاسم الأب للمؤلف الأول، ثم نقطة، ثم فاصلة، ثم اسم العائلة للمؤلف الثاني، ثم فاصلة، ثم الحرف الأول من الاسم الأول للمؤلف الثاني، ثم نقطة، ثم الحرف الأول لاسم الأب للمؤلف الثاني، ثم نقطة، ثم حرف العطف "and" (وليس "&") ثم اسم العائلة للمؤلف الثالث، ثم فاصلة، ثم الحرف الأول من الاسم الأول للمؤلف الثالث، ثم نقطة، ثم الحرف الأول لاسم الأب للمؤلف الثالث، ثم نقطة، ثم فتح قوس، ثم التاريخ بالميلادي، ثم إغلاق القوس، ثم نقطة، ثم عنوان الكتاب بحروف مائلة والحرف الأول من كل كلمة يكون كبيرا (كابتل capital؛ يستثنى من ذلك أدوات التنكير والتعريف مثل "a" و "an" و "the" وحروف الجر مثل "to" و "of" و "in" وأدوات الربط "and" و "but" و "or" فيبقى الحرف الأول منها بحروف صغيرة، إلا إذا كانوا في بداية اسم المجلة فيكون الحرف الأول منها بحروف كبيرة)، ثم نقطة، ثم اسم مدينة الناشر، ثم فاصلة، ثم اسم دولة الناشر، ثم نقطتين رأسيتين، ثم اسم الناشر، ثم نقطة. أدناه مثال على ذلك:

Al Ahmed, K.A., Al Muhammed, S.F. and Al Saleh, A.F. (2020). *The History of Agriculture in Al Ahsa*. Saudi Arabia: Jarir Bookstore.

في حالة وجود رقم طبعة، فيكتب التالي:

Al Ahmed, K.A., Al Muhammed, S.F. and Al Saleh, A.F. (2020). *The History of Agriculture in Al Ahsa*. 2nd edition. Riyadh, Saudi Arabia: Jarir Bookstore.

6.3. رومنة/ترجمة الكتب غير الإنجليزية في قائمة المراجع

ملاحظة: عند رومنة/ترجمة مراجع الكتب العربية فإنه لا يكتب اسم المحقق.

يبدأ كل مرجع باسم العائلة للمؤلف الأول، ثم فاصلة، ثم الحرف الأول من الاسم الأول للمؤلف الأول، ثم نقطة، ثم الحرف الأول لاسم الأب للمؤلف الأول، ثم نقطة، ثم فاصلة، ثم اسم العائلة للمؤلف الثاني، ثم فاصلة، ثم الحرف الأول من الاسم الأول للمؤلف الثاني، ثم نقطة، ثم الحرف الأول لاسم الأب للمؤلف الثاني، ثم نقطة، ثم حرف العطف "and" (وليس "&") ثم اسم العائلة للمؤلف الثالث، ثم فاصلة، ثم الحرف الأول من الاسم الأول للمؤلف الثالث، ثم نقطة، ثم الحرف الأول لاسم الأب للمؤلف الثالث، ثم نقطة، ثم فتح قوس، ثم التاريخ بالميلادي، ثم إغلاق القوس، ثم نقطة، ثم عنوان الكتاب (مرومن) بحروف مائلة والحرف الأول من كل كلمة يكون كبيرا (كابتل capital)، ثم فتح علامة تنصيص واحدة، ثم عنوان الكتاب مترجما والحرف الأول من كل كلمة يكون كبيرا (كابتل capital؛ يستثنى من ذلك أدوات التنكير والتعريف مثل "a" و "an" و "the" وحروف الجر مثل "to" و "of" و "in" وأدوات الربط "and" و "but" و "or" فيبقى الحرف الأول منها بحروف صغيرة، إلا إذا كانوا في بداية اسم المجلة فيكون الحرف الأول منها بحروف كبيرة) والكلمة غير مائلة، ثم إغلاق علامة التنصيص، ثم نقطة، ثم اسم مدينة الناشر مترجمة، ثم فاصلة، ثم اسم دولة الناشر مترجمة، ثم نقطتين رأسيتين، ثم اسم الناشر مترجما (أو مرومن)، ثم نقطة، ثم تكتب "[in Arabic]" أدناه مثال على رومنة المرجع العربي:

Al Ahmed, M.A., Al Ali, I.S. and Al Salah, A.M. (2020). *Iinjazat Jamieat Almalik Faysal Mundh Tasisiha* 'Achievements of King Faisal University since its Foundations'. Riyadh, Saudi Arabia: Jarir Bookstore. [in Arabic]

في حالة كون الكتاب بلغة غير العربية وغير الإنجليزية، ولكن هذه اللغة تستخدم حروف غير إنجليزية، فتتم رومنة العنوان بالطريقة نفسها التي تتم بها رومنة العناوين العربية. ولكن، في حالة كون الكتاب بلغة غير العربية وغير الإنجليزية، ولكن هذه اللغة تستخدم الحروف الإنجليزية

نفسها، فلا حاجة لرومنة عنوان الكتاب، ويكتفى بإبقاء العنوان في لغته الأصل ووضع الترجمة في علامة تنصيص. فعلى سبيل المثال، في حالة كون الكتاب باللغة الألمانية، فيبدأ المرجع باسم العائلة للمؤلف الأول، ثم فاصلة، ثم الحرف الأول من الاسم الأول للمؤلف الأول، ثم نقطة، ثم الحرف الأول لاسم الأب للمؤلف الأول، ثم نقطة، ثم فاصلة، ثم اسم العائلة للمؤلف الثاني، ثم فاصلة، ثم الحرف الأول من الاسم الأول للمؤلف الثاني، ثم نقطة، ثم الحرف الأول لاسم الأب للمؤلف الثاني، ثم نقطة، ثم حرف العطف "and" (وليس "&") ثم اسم العائلة للمؤلف الثالث، ثم فاصلة، ثم الحرف الأول من الاسم الأول للمؤلف الثالث، ثم نقطة، ثم الحرف الأول لاسم الأب للمؤلف الثالث، ثم نقطة، ثم فتح قوس، ثم التاريخ بالميلادي، ثم إغلاق القوس، ثم نقطة، ثم عنوان الكتاب باللغة الألمانية بحروف مائلة والحرف الأول من كل كلمة يكون كبيرا (كابتل capital)، ثم فتح علامة تنصيص واحدة، ثم عنوان الكتاب مترجما والحرف الأول من كل كلمة يكون كبيرا (كابتل capital؛ يستثنى من ذلك أدوات التنكير والتعريف مثل "a" و "an" و "the" وحروف الجر مثل "to" و "of" و "in" وأدوات الربط "and" و "but" و "or" فيبقى الحرف الأول منها بحروف صغيرة، إلا إذا كانوا في بداية اسم المجلة فيكون الحرف الأول منها بحروف كبيرة) والكلمة غير مائلة، ثم إغلاق علامة التنصيص، ثم نقطة، ثم اسم مدينة الناشر مترجمة للإنجليزي، ثم فاصلة، ثم اسم دولة الناشر مترجمة للإنجليزي، ثم نقطتين رأسيتين، ثم اسم الناشر مترجما للإنجليزي، ثم نقطة، ثم تكتب "[in German]" أدناه مثال على رومنة المرجع الألماني:

Al Ahmed, M.A., Al Ali, I.S. and Al Salah, A.M. (2020). *Erfolge der King Faisal University seit ihrer Gründung* 'Achievements of King Faisal University since its Foundations'. Riyadh, Saudi Arabia: Jarir Bookstore. [in German]

7. آلية كتابة فصل من كتاب في قائمة المراجع (يطلب عملها فقط في حالة قبول الورقة للنشر)

7.1. كتابة فصل في كتاب عربي في قائمة المراجع

يبدأ كل مرجع باسم العائلة للمؤلف الأول، ثم فاصلة، ثم الاسم الأول واسم الأب للمؤلف الأول، ثم فاصلة، ثم اسم العائلة للمؤلف الثاني، ثم فاصلة، ثم الاسم الأول واسم الأب للمؤلف الثاني، ثم حرف العطف "و" ثم اسم العائلة للمؤلف الثالث، ثم فاصلة، ثم الاسم الأول واسم الأب للمؤلف الثالث، ثم نقطة، ثم فتح قوس، ثم التاريخ، ثم إغلاق القوس، ثم نقطة، ثم عنوان الفصل، ثم نقطة، ثم يكتب "في:" ثم يكتب الاسم الأول، ثم اسم الأب، ثم اسم العائلة للمؤلف الأول، ثم فاصلة، ثم يكتب الاسم الأول، ثم اسم الأب، ثم اسم العائلة للمؤلف الثاني، ثم حرف العطف "و"، ثم يكتب الاسم الأول، ثم اسم الأب، ثم اسم العائلة للمؤلف الثالث، ثم يفتح قوس ويكتب "محررون" (أو محرر إذا كان مفردا)، ثم يغلق القوس، ثم اسم الكتاب بخط مائل، ثم نقطة، ثم اسم مدينة الناشر، ثم فاصلة، ثم اسم دولة الناشر، ثم نقطتين رأسيتين، ثم اسم الناشر. (مع مراعاة أن حرف العطف "و" يوضع دائما قبل المؤلف الأخير أيًّا كان عدد المؤلفين). أدناه مثال على ذلك:

الأحمد، محمد عبدالرحمن، العلي، إسماعيل صلاح والصالح، أحمد محمد. (2020). الموهبة في التعليم العالي. في: محمد الصالح، إبراهيم العبدالرحمن وصلاح الخالد (محررون) *الإبداع في العالم العربي*. الرياض، السعودية: مكتبة العبيكان.

7.2. كتابة فصل في كتاب إنجليزي في قائمة المراجع

يبدأ كل مرجع باسم العائلة للمؤلف الأول، ثم فاصلة، ثم الحرف الأول من الاسم الأول للمؤلف الأول، ثم نقطة، ثم الحرف الأول لاسم الأب للمؤلف الأول، ثم نقطة، ثم فاصلة، ثم اسم العائلة للمؤلف الثاني، ثم فاصلة، ثم الحرف الأول من الاسم الأول للمؤلف الثاني، ثم نقطة، ثم الحرف الأول لاسم الأب للمؤلف الثاني، ثم نقطة، ثم حرف العطف "and" (وليس "&") ثم اسم العائلة للمؤلف الثالث، ثم فاصلة، ثم الحرف الأول من الاسم الأول للمؤلف الثالث، ثم نقطة، ثم الحرف الأول لاسم الأب للمؤلف الثالث، ثم نقطة، ثم فتح قوس، ثم التاريخ بالميلادي، ثم إغلاق القوس، ثم نقطة، ثم عنوان الفصل بحروف صغيرة (صمول small؛ يستثنى من ذلك الكلمة الأولى وأسماء الأماكن وأسماء الأشخاص وأسماء الجنسيات واللغات والأسابيع والشهور فيبقى الحرف الأول منها بحروف كبيرة، كابتل capital)، ثم نقطة، ثم يكتب "In:"، ثم يكتب الحرف الأول من الاسم الأول للمؤلف الأول، ثم نقطة، ثم الحرف الأول لاسم الأب للمؤلف الأول، ثم نقطة، ثم اسم العائلة كاملاً للمؤلف الأول، ، ثم فاصلة، ثم يكتب الحرف الأول من الاسم الأول للمؤلف الثاني، ثم نقطة، ثم الحرف الأول لاسم الأب للمؤلف الثاني، ثم نقطة، ثم حرف العطف "and" (وليس "&")، ثم يكتب الحرف الأول من الاسم الأول للمؤلف الثالث، ثم نقطة، ثم الحرف الأول لاسم الأب للمؤلف الثالث، ثم نقطة، ثم اسم العائلة كاملاً للمؤلف الثالث، ثم يفتح قوس ويكتب "eds." (أو "ed." إذا كان مفردا)، ثم يغلق القوس، ثم اسم الكتاب بخط مائل والحرف الأول من كل كلمة يكون كبيرا (كابتل capital؛ يستثنى من ذلك أدوات التنكير والتعريف مثل "a" و "an" و "the" وحروف الجر مثل "to" و "of" و "in" وأدوات الربط "and" و "but" و "or" فيبقى الحرف الأول منها بحروف صغيرة، إلا إذا كانوا في بداية اسم المجلة فيكون الحرف الأول منها بحروف كبيرة)، ثم نقطة، ثم اسم مدينة الناشر، ثم فاصلة، ثم اسم دولة الناشر، ثم نقطتين رأسيتين، ثم اسم الناشر. أدناه مثال على ذلك:

Al Ahmed, K.A., Al Muhammed, S.F. and Al Saleh, A.F. (2020). Giftedness and creativity. In: A.E. Al Ibrahim, A.L. Al Salim and R.E. Al Rashid (eds.) *Creativity in the Arab World*. Riyadh, Saudi Arabia: Obeikan Bookstore.

7.3. رومنة/ترجمة فصل في كتاب غير إنجليزي في قائمة المراجع

يبدأ كل مرجع باسم العائلة للمؤلف الأول، ثم فاصلة، ثم الحرف الأول من الاسم الأول للمؤلف الأول، ثم نقطة، ثم الحرف الأول لاسم الأب للمؤلف الأول، ثم نقطة، ثم فاصلة، ثم اسم العائلة للمؤلف الثاني، ثم فاصلة، ثم الحرف الأول من الاسم الأول للمؤلف الثاني، ثم نقطة، ثم الحرف الأول لاسم الأب للمؤلف الثاني، ثم نقطة، ثم حرف العطف "and" (وليس "&") ثم اسم العائلة للمؤلف الثالث، ثم فاصلة، ثم الحرف الأول من الاسم الأول للمؤلف الثالث، ثم نقطة، ثم الحرف الأول لاسم الأب للمؤلف الثالث، ثم نقطة، ثم فتح قوس، ثم التاريخ بالميلادي، ثم إغلاق القوس، ثم نقطة، ثم عنوان الفصل (مرومن) بحروف صغيرة (صمول small)، ثم فتح علامة تنصيص واحدة، ثم عنوان الفصل مترجما بحروف صغيرة (صمول small؛ يستثنى من ذلك الكلمة الأولى وأسماء الأشخاص وأسماء الأماكن وأسماء الجنسيات واللغات والأسابيع والشهور فيبقى الحرف الأول منها بحروف كبيرة، كابتل capital)، ثم إغلاق علامة التنصيص، ثم نقطة، ثم يكتب "In:"، ثم يكتب الحرف الأول من الاسم الأول للمؤلف الأول، ثم نقطة، ثم الحرف الأول لاسم الأب للمؤلف الأول، ثم نقطة، ثم اسم العائلة كاملاً للمؤلف الأول، ، ثم فاصلة، ثم يكتب الحرف الأول من الاسم الأول للمؤلف الثاني، ثم نقطة، ثم الحرف الأول لاسم الأب للمؤلف الثاني، ثم نقطة، ثم اسم العائلة كاملاً للمؤلف الثاني، ثم حرف العطف "and" (وليس "&")، ثم يكتب الحرف الأول من الاسم الأول للمؤلف الثالث، ثم نقطة، ثم الحرف الأول لاسم الأب للمؤلف الثالث، ثم نقطة، ثم اسم العائلة كاملاً للمؤلف الثالث، ثم يفتح قوس ويكتب "eds." (أو "ed." إذا كان مفردا)، ثم يغلق القوس، ثم اسم الكتاب (مرومن) بخط مائل والحرف الأول من كل كلمة يكون كبيرا (كابتل capital)، ثم فتح علامة تنصيص واحدة، ثم عنوان الكتاب مترجما والحرف الأول من كل كلمة يكون كبيرا (كابتل capital؛ يستثنى من ذلك أدوات التنكير والتعريف مثل "a" و "an" و "the" وحروف الجر مثل "to" و "of" و "in" وأدوات الربط "and" و "but" و "or" فيبقى الحرف الأول منها بحروف صغيرة، إلا إذا كانوا في بداية اسم المجلة فيكون الحرف الأول منها بحروف كبيرة)، ثم نقطة، ثم اسم مدينة الناشر مترجمة، ثم فاصلة، ثم اسم دولة الناشر مترجما، ثم نقطتين رأسيتين، ثم اسم الناشر مترجما (أو مرومن)، ثم نقطة، ثم تكتب "[in Arabic]" أدناه مثال على رومنة المرجع العربي:

Al Ahmed, K.A., Al Muhammed, S.F. and Al Saleh, A.F. (2020). Al'iibdae fi altaelim aleali 'Creativity in higher education'. In: M. Al Saleh, I. Al

Abdulrahman and S. Al Khalid (eds.) *Al'iibdae Fi Alealam Alearabii'* Creativity in the Arab World'. Riyadh, Saudi Arabia: Obeikan Bookstore. [in Arabic]

في حالة كون الفصل بلغة غير العربية وغير الإنجليزية، ولكن هذه اللغة تستخدم حروف غير إنجليزية، فتتم رومنة العنوان بالطريقة نفسها التي تتم بها رومنة العناوين العربية. ولكن، في حالة كون الفصل بلغة غير العربية وغير الإنجليزية، ولكن هذه اللغة تستخدم الحروف الإنجليزية نفسها، فلا حاجة لرومنة عنوان الفصل والكتاب، ويكتفى بإبقاء العنوان في لغته الأصل ووضع الترجمة في علامة تنصيص. فعلى سبيل المثال، في حالة كون الفصل باللغة الألمانية، فيبدأ المرجع باسم العائلة للمؤلف الأول، ثم فاصلة، ثم الحرف الأول من الاسم الأول للمؤلف الأول، ثم نقطة، ثم الحرف الأول لاسم الأب للمؤلف الأول، ثم نقطة، ثم فاصلة، ثم اسم العائلة للمؤلف الثاني، ثم فاصلة، ثم الحرف الأول من الاسم الأول للمؤلف الثاني، ثم نقطة، ثم الحرف الأول لاسم الأب للمؤلف الثاني، ثم نقطة، ثم حرف العطف "and" (وليس "&") ثم اسم العائلة للمؤلف الثالث، ثم فاصلة، ثم الحرف الأول من الاسم الأول للمؤلف الثالث، ثم نقطة، ثم الحرف الأول لاسم الأب للمؤلف الثالث، ثم نقطة، ثم فتح قوس، ثم التاريخ بالميلادي، ثم إغلاق القوس، ثم نقطة، ثم فتح علامة تنصيص واحدة، ثم عنوان الفصل مترجما للإنجليزية بحروف صغيرة (صمول small؛ يستثنى من ذلك الكلمة الأولى وأسماء الأشخاص وأسماء الأماكن وأسماء الجنسيات واللغات والأسابيع والشهور فيبقى الحرف الأول منها بحروف كبيرة، كابتل capital)، ثم إغلاق علامة التنصيص، ثم نقطة، ثم يكتب "In:"، ثم يكتب الحرف الأول من الاسم الأول للمؤلف الأول، ثم نقطة، ثم الحرف الأول لاسم الأب للمؤلف الأول، ثم نقطة، ثم اسم العائلة كاملاً للمؤلف الأول، ، ثم فاصلة، ثم يكتب الحرف الأول من الاسم الأول للمؤلف الثاني، ثم نقطة، ثم الحرف الأول لاسم الأب للمؤلف الثاني، ثم نقطة، ثم اسم العائلة كاملاً للمؤلف الثاني، ثم حرف العطف "and" (وليس "&")، ثم يكتب الحرف الأول من الاسم الأول للمؤلف الثالث، ثم نقطة، ثم الحرف الأول لاسم الأب للمؤلف الثالث، ثم نقطة، ثم اسم العائلة كاملاً للمؤلف الثالث، ثم يفتح قوس ويكتب "eds." (أو "ed." إذا كان مفردا)، ثم يغلق القوس، ثم اسم الكتاب باللغة الألمانية بخط مائل والحرف الأول من كل كلمة يكون كبيرا (كابتل capital)، ثم فتح علامة تنصيص واحدة، ثم عنوان الكتاب مترجما للإنجليزية والحرف الأول من كل كلمة يكون كبيرا (كابتل capital؛ يستثنى من ذلك أدوات التنكير والتعريف مثل "a" و "an" و "the" وحروف الجر مثل "to" و "of" و "in" وأدوات الربط "and" و "but" و "or" فيبقى الحرف الأول منها بحروف صغيرة، إلا إذا كانوا في بداية اسم المجلة فيكون الحرف الأول منها بحروف كبيرة)، ثم فتح قوس، ثم اسم مدينة الناشر مترجمة للإنجليزية، ثم فاصلة، ثم اسم دولة الناشر مترجما للإنجليزية، ثم نقطتين رأسيتين، ثم اسم الناشر مترجما للإنجليزية، ثم نقطة، ثم تكتب "[in German]" أدناه مثال على رومنة المرجع الألماني:

Al Ahmed, K.A., Al Muhammed, S.F. and Al Saleh, A.F. (2020). Kreativität in der hochschulbildung 'Creativity in higher education'. In: M. Al Saleh, I. Al Abdulrahman and S. Al Khalid (eds.) *Kreativität in der Arabischen Welt* 'Creativity in the Arab World'. Riyadh, Saudi Arabia: Obeikan Bookstore. [in German]

8. آلية كتابة رسائل الماجستير والدكتوراه في قائمة المراجع (يطلب عملها فقط في حالة قبول الورقة للنشر)

8.1. كتابة رسائل الماجستير والدكتوراه العربية في قائمة المراجع

يبدأ كل مرجع باسم العائلة للمؤلف، ثم فاصلة، ثم الاسم الأول واسم الأب للمؤلف، ثم نقطة، ثم فتح قوس، ثم التاريخ، ثم إغلاق القوس، ثم نقطة، ثم عنوان الرسالة بخط مائل، ثم نقطة، ثم يكتب "رسالة ماجستير" أو "رسالة دكتوراه"، ثم فاصلة، ثم اسم الجامعة، ثم فاصلة، ثم اسم المدينة، ثم فاصلة، ثم اسم الدولة، ثم نقطة. أدناه مثال على ذلك:

الأحمد، محمد عبدالرحمن. (2020). *تأملات في الإبداع*. رسالة دكتوراه، جامعة الملك فيصل، الأحساء، السعودية.

8.2. كتابة رسائل الماجستير والدكتوراه الإنجليزية في قائمة المراجع

يبدأ كل مرجع باسم العائلة للمؤلف، ثم فاصلة، ثم الحرف الأول من الاسم الأول للمؤلف، ثم نقطة، ثم الحرف الأول لاسم الأب للمؤلف، ثم نقطة، ثم فتح قوس، ثم التاريخ بالميلادي، ثم إغلاق القوس، ثم نقطة، ثم عنوان الرسالة بحروف مائلة والحرف الأول من كل كلمة يكون كبيرا (كابتل capital؛ يستثنى من ذلك أدوات التنكير والتعريف مثل "a" و "an" و "the" وحروف الجر مثل "to" و "of" و "in" وأدوات الربط "and" و "but" و "or" فيبقى الحرف الأول منها بحروف صغيرة، إلا إذا كانوا في بداية اسم المجلة فيكون الحرف الأول منها بحروف كبيرة)، ثم نقطة، ثم يكتب " Master's Dissertation" إذا كانت رسالة ماجستير أو "PhD Thesis" إذا كانت رسالة دكتوراه، ثم فاصلة، ثم اسم الجامعة، ثم فاصلة، ثم اسم المدينة، ثم فاصلة، ثم اسم الدولة، ثم نقطة. أدناه مثال على ذلك:

Al Ahmed, K.A. (2020). *The History of Agriculture in Al Ahsa*. PhD Thesis, King Faisal University, Al Ahsa, Saudi Arabia.

8.3. رومنة/ترجمة رسائل الماجستير والدكتوراه غير الإنجليزية في قائمة المراجع

يبدأ كل مرجع باسم العائلة للمؤلف الأول، ثم فاصلة، ثم الحرف الأول من الاسم الأول للمؤلف الأول، ثم نقطة، ثم الحرف الأول لاسم الأب للمؤلف الأول، ثم نقطة، ثم فتح قوس، ثم التاريخ بالميلادي، ثم إغلاق القوس، ثم نقطة، ثم عنوان الرسالة (مرومن) بحروف مائلة والحرف الأول من كل كلمة يكون كبيرا (كابتل capital)، ثم فتح علامة تنصيص واحدة، ثم عنوان الرسالة مترجما والحرف الأول من كل كلمة يكون كبيرا (كابتل capital؛ يستثنى من ذلك أدوات التنكير والتعريف مثل "a" و "an" و "the" وحروف الجر مثل "to" و "of" و "in" وأدوات الربط "and" و "but" و "or" فيبقى الحرف الأول منها بحروف صغيرة، إلا إذا كانوا في بداية اسم المجلة فيكون الحرف الأول منها بحروف كبيرة) والكلمة غير مائلة، ثم إغلاق علامة التنصيص، ثم نقطة، ثم يكتب "Master's Dissertation" إذا كانت رسالة ماجستير أو "PhD Thesis" إذا كانت رسالة دكتوراه، ثم فاصلة، ثم اسم الجامعة، ثم فاصلة، ثم اسم المدينة، ثم فاصلة، ثم اسم الدولة، ثم نقطة، ثم تكتب "[in Arabic]" أدناه مثال على رومنة المرجع العربي:

Al Ahmed, M.A. (2020). *Tamalat Fi Al'iibdae* 'Reflections on Creativity'. PhD Thesis, King Faisal University, Al Ahsa, Saudi Arabia. [in Arabic]

في حالة كون الرسالة بلغة غير العربية وغير الإنجليزية، ولكن هذه اللغة تستخدم حروف غير إنجليزية، فتتم رومنة العنوان بالطريقة نفسها التي تتم بها رومنة العناوين العربية. ولكن، في حالة كون الرسالة بلغة غير العربية وغير الإنجليزية، ولكن هذه اللغة تستخدم الحروف الإنجليزية نفسها، فلا حاجة لرومنة عنوان الرسالة، ويكتفى بإبقاء العنوان في لغته الأصل ووضع الترجمة في علامة تنصيص. فعلى سبيل المثال، في حالة كون الرسالة باللغة الألمانية، فيبدأ المرجع باسم العائلة للمؤلف الأول، ثم فاصلة، ثم الحرف الأول من الاسم الأول للمؤلف الأول، ثم نقطة، ثم الحرف الأول لاسم الأب للمؤلف الأول، ثم نقطة، ثم فتح قوس، ثم التاريخ بالميلادي، ثم إغلاق القوس، ثم نقطة، ثم عنوان الرسالة باللغة الألمانية بحروف مائلة والحرف الأول من كل كلمة يكون كبيرا (كابتل capital)، ثم فتح علامة تنصيص واحدة، ثم عنوان الرسالة مترجما والحرف الأول من كل كلمة يكون كبيرا (كابتل capital؛ يستثنى من ذلك أدوات التنكير والتعريف مثل "a" و "an" و "the" وحروف الجر مثل "to" و "of" و "in" وأدوات الربط "and" و "but" و "or" فيبقى الحرف الأول منها بحروف صغيرة، إلا إذا كانوا في بداية اسم المجلة فيكون الحرف الأول منها بحروف كبيرة) والكلمة غير مائلة، ثم إغلاق علامة التنصيص، ثم نقطة، ثم يكتب "Master's Dissertation" إذا كانت رسالة ماجستير أو "PhD Thesis" إذا كانت رسالة دكتوراه، ثم فاصلة، ثم اسم الجامعة بالإنجليزي، ثم فاصلة، ثم اسم المدينة بالإنجليزي، ثم فاصلة، ثم اسم الدولة بالإنجليزي، ثم نقطة،

ثم تكتب "[in German]" أدناه مثال على ذلك:

Al Ahmed, M.A. (2020). *Überlegungen zur Kreativität* 'Reflections on Creativity'. PhD Thesis, King Faisal University, Al Ahsa, Saudi Arabia. [in German]

9. آلية كتابة موقع إلكتروني في قائمة المراجع (يطلب عملها فقط في حالة قبول الورقة للنشر)

ملاحظة: المراجع المأخوذة من شبكة المعلومات يلزم فيها كتابة العنوان التفصيلي الذي يفتح الصفحة الخاصة بالمرجع مباشرة وليست الصفحة العامة للموقع. يجب ألا يزيد عدد حروف الرابط عن 120 حرف.

9.1. كتابة موقع إلكتروني عربي في قائمة المراجع

يبدأ كل مرجع باسم العائلة للمؤلف الأول، ثم فاصلة، ثم الاسم الأول واسم الأب للمؤلف الأول، ثم فاصلة، ثم اسم العائلة للمؤلف الثاني، ثم فاصلة، ثم الاسم الأول واسم الأب للمؤلف الثاني، ثم حرف العطف "و" ثم اسم العائلة للمؤلف الثالث، ثم فاصلة، ثم الاسم الأول واسم الأب للمؤلف الثالث، ثم نقطة، ثم فتح قوس، ثم التاريخ، ثم إغلاق القوس، ثم نقطة، ثم العنوان بخط مائل، ثم نقطة، ثم يكتب "متوفر بموقع:" ثم يدرج الرابط، وبعد الرابط يفتح قوس ويكتب "تاريخ الاسترجاع:" ثم يدرج التاريخ على هذه الصيغة "2020/07/27"، ثم يغلق القوس. (مع مراعاة أن حرف العطف "و" يوضع دائما قبل المؤلف الأخير أيًا كان عدد المؤلفين). أدناه مثال على ذلك:

الأحمد، محمد عبدالرحمن، العلي، إسماعيل صلاح والصالح، أحمد محمد. (2020). *إنجازات جامعة الملك فيصل منذ تأسيسها*. متوفر بموقع: https://www.kfu.edu.sa/ar/Departments/Sjournal/Pages/home.aspx (تاريخ الاسترجاع: 2020/07/27)

9.2. كتابة موقع إلكتروني إنجليزي في قائمة المراجع

يبدأ كل مرجع باسم العائلة للمؤلف الأول، ثم فاصلة، ثم الحرف الأول من الاسم الأول للمؤلف الأول، ثم نقطة، ثم الحرف الأول لاسم الأب للمؤلف الأول، ثم نقطة، ثم فاصلة، ثم اسم العائلة للمؤلف الثاني، ثم فاصلة، ثم الحرف الأول من الاسم الأول للمؤلف الثاني، ثم نقطة، ثم الحرف الأول لاسم الأب للمؤلف الثاني، ثم نقطة، ثم حرف العطف "and" (وليس "&") ثم اسم العائلة للمؤلف الثالث، ثم فاصلة، ثم الحرف الأول من الاسم الأول للمؤلف الثالث، ثم نقطة، ثم الحرف الأول لاسم الأب للمؤلف الثالث، ثم نقطة، ثم فتح قوس، ثم التاريخ بالميلادي، ثم إغلاق القوس، ثم نقطة، ثم العنوان بحروف مائلة والحرف الأول من كل كلمة يكون كبيرا (كابتل capital)؛ يستثنى من ذلك أدوات التنكير والتعريف مثل "a" و "an" و "the" وحروف الجر مثل "to" و "of" و "in" وأدوات الربط "and" و "but" و "or" فيبقى الحرف الأول منها بحروف صغيرة، إلا إذا كانوا في بداية اسم المجلة فيكون الحرف الأول منها بحروف كبيرة) والكلمة غير مائلة، ثم إغلاق علامة التنصيص، ثم نقطة، ثم يكتب "Available at:" ثم يدرج الرابط، وبعد الرابط يفتح قوس ويكتب "accessed on" ثم يدرج التاريخ على هذه الصيغة "2020/07/27"، ثم يغلق القوس. أدناه مثال على ذلك:

Al Ahmed, K.A., Al Muhammed, S.F. and Al Saleh, A.F. (2020). *The History of Agriculture in Al Ahsa*. Available at: https://www.kfu.edu.sa/ar/Departments/Sjournal/Pages/home.aspx (accessed on 10/12/2020)

9.3. رومنة/ترجمة موقع إلكتروني غير إنجليزي في قائمة المراجع

يبدأ كل مرجع باسم العائلة للمؤلف الأول، ثم فاصلة، ثم الحرف الأول من الاسم الأول للمؤلف الأول، ثم نقطة، ثم الحرف الأول لاسم الأب للمؤلف الأول، ثم نقطة، ثم فاصلة، ثم اسم العائلة للمؤلف الثاني، ثم فاصلة، ثم الحرف الأول من الاسم الأول للمؤلف الثاني، ثم نقطة، ثم الحرف الأول لاسم الأب للمؤلف الثاني، ثم نقطة، ثم حرف العطف "and" (وليس "&") ثم اسم العائلة للمؤلف الثالث، ثم فاصلة، ثم الحرف الأول من الاسم الأول للمؤلف الثالث، ثم نقطة، ثم الحرف الأول لاسم الأب للمؤلف الثالث، ثم نقطة، ثم فتح قوس، ثم التاريخ بالميلادي، ثم إغلاق القوس، ثم نقطة، ثم العنوان (مرومن) بحروف مائلة والحرف الأول من كل كلمة يكون كبيرا (كابتل capital)، ثم فتح علامة تنصيص واحدة، ثم العنوان مترجما والحرف الأول من كل كلمة يكون كبيرا (كابتل capital؛ يستثنى من ذلك أدوات التنكير والتعريف مثل "a" و "an" و "the" وحروف الجر مثل "to" و "of" و "in" وأدوات الربط "and" و "but" و "or" فيبقى الحرف الأول منها بحروف صغيرة، إلا إذا كانوا في بداية اسم المجلة فيكون الحرف الأول منها بحروف كبيرة) والكلمة غير مائلة، ثم إغلاق علامة التنصيص، ثم نقطة، ثم يكتب "Available at:" ثم يدرج الرابط، وبعد الرابط يفتح قوس ويكتب "accessed on" ثم يدرج التاريخ على هذه الصيغة "2020/07/27"، ثم يغلق القوس، ثم تكتب "[in Arabic]". أدناه مثال على رومنة المرجع العربي:

Al Ahmed, M.A., Al Ali, I.S. and Al Salah, A.M. (2020). *Iinjazat Jamieat Almalik Faysal Mundh Tasisiha* 'Achievements of King Faisal University since its Foundations'. Available at: https://www.kfu.edu.sa/ar/Departments/Sjournal/Pages/home.aspx (accessed on 10/12/2020) [in Arabic]

في حالة كون الموقع بلغة غير العربية وغير الإنجليزية، ولكن هذه اللغة تستخدم حروف غير إنجليزية، فتتم رومنة العنوان بالطريقة نفسها التي تتم بها رومنة العناوين العربية. ولكن، في حالة كون الموقع بلغة غير العربية وغير الإنجليزية، ولكن هذه اللغة تستخدم الحروف الإنجليزية نفسها، فلا حاجة لرومنة عنوان الموقع، ويكتفى بإبقاء العنوان في لغته الأصل ووضع الترجمة في علامة تنصيص. فعلى سبيل المثال، في حالة كون الموقع باللغة الألمانية، فيبدأ المرجع باسم العائلة للمؤلف الأول، ثم فاصلة، ثم الحرف الأول من الاسم الأول للمؤلف الأول، ثم نقطة، ثم الحرف الأول لاسم الأب للمؤلف الأول، ثم نقطة، ثم فاصلة، ثم اسم العائلة للمؤلف الثاني، ثم فاصلة، ثم الحرف الأول من الاسم الأول للمؤلف الثاني، ثم نقطة، ثم الحرف الأول لاسم الأب للمؤلف الثاني، ثم نقطة، ثم حرف العطف "and" (وليس "&") ثم اسم العائلة للمؤلف الثالث، ثم فاصلة، ثم الحرف الأول من الاسم الأول للمؤلف الثالث، ثم نقطة، ثم الحرف الأول لاسم الأب للمؤلف الثالث، ثم نقطة، ثم فتح قوس، ثم التاريخ بالميلادي، ثم إغلاق القوس، ثم نقطة، ثم العنوان باللغة الألمانية بحروف مائلة والحرف الأول من كل كلمة يكون كبيرا (كابتل capital)، ثم فتح علامة تنصيص واحدة، ثم العنوان مترجما للإنجليزية والحرف الأول من كل كلمة يكون كبيرا (كابتل capital؛ يستثنى من ذلك أدوات التنكير والتعريف مثل "a" و "an" و "the" وحروف الجر مثل "to" و "of" و "in" وأدوات الربط "and" و "but" و "or" فيبقى الحرف الأول منها بحروف صغيرة، إلا إذا كانوا في بداية اسم المجلة فيكون الحرف الأول منها بحروف كبيرة) والكلمة غير مائلة، ثم إغلاق علامة التنصيص، ثم نقطة، ثم يكتب "Available at:" ثم يدرج الرابط، وبعد الرابط يفتح قوس ويكتب "accessed on" ثم يدرج التاريخ على هذه الصيغة "2020/07/27"، ثم يغلق القوس، ثم تكتب "[in German]". أدناه مثال على ذلك:

Al Ahmed, M.A., Al Ali, I.S. and Al Salah, A.M. (2020). *Erfolge der King Faisal University seit ihrer Gründung* 'Achievements of King Faisal University since its Foundations'. Available at: https://www.kfu.edu.sa/ar/Departments/Sjournal/Pages/home.aspx (accessed on 10/12/2020) [in German]